Fatigue modelling in tooth root of surface-hardened gears

Čular, Ivan

Doctoral thesis / Disertacija

2022

Degree Grantor / Ustanova koja je dodijelila akademski / stručni stupanj: **University of Zagreb, Faculty of Mechanical Engineering and Naval Architecture / Sveučilište u Zagrebu, Fakultet strojarstva i brodogradnje**

Permanent link / Trajna poveznica: https://urn.nsk.hr/urn:nbn:hr:235:093779

Rights / Prava: In copyright/Zaštićeno autorskim pravom.

Download date / Datum preuzimanja: **2024-12-24**

University of Zagreb

Faculty of Mechanical Engineering and Naval Architecture

Ivan Čular

FATIGUE MODELLING IN TOOTH ROOT OF SURFACE-HARDENED GEARS

DOCTORAL THESIS

Zagreb, 2022.

University of Zagreb

Faculty of Mechanical Engineering and Naval Architecture

Ivan Čular

FATIGUE MODELLING IN TOOTH ROOT
OF SURFACE-HARDENED GEARS

DOCTORAL THESIS

Supervisor:
Assoc. prof. Krešimir Vučković, PhD

Zagreb, 2022.

Sveučilište u Zagrebu

Fakultet strojarstva i brodogradnje

Ivan Čular

MODELIRANJE ZAMORA U KORIJENU ZUBA POVRŠINSKI OTVRDNUTIH ZUPČANIKA

DOKTORSKI RAD

Mentor:
Izv. prof. dr. sc. Krešimir Vučković

Zagreb, 2022.

Bibliography data

Acknowledgment

Prije svega, zahvalio bih se mentoru izv. prof. dr. sc. Krešimiru Vučkoviću na neizmjernom strpljenju, vodstvu te pruženoj pomoći prilikom izrade ovog rada.

Zahvaljujem se doc. dr. sc. Ivici Galiću, prof. dr. sc. Srečku Glodežu, prof. dr. sc. Zdenku Tonkoviću te izv. prof. dr. sc. Draganu Žeželju na dobronamjernim komentarima koji su značajno pomogli pri objavi članaka kao i na sugestijama koje su doprinijeli kvaliteti doktorskog rada.

Veliko hvala kumu Josipu, kao i prijateljima te kolegama Robertu i Danielu na svim korisnim savjetima prilikom izrade ovog rada. Također, za isto bih se zahvalio i svim ostalim kolegama sa Zavoda za konstruiranje.

Enormnu zahvalu dugujem svojim roditeljima i uzorima, ocu Siniši te majci Mirjani, za sva odricanja i žrtve bez kojih danas ne bih bio gdje jesam.

Od srca se zahvaljujem najboljem poklonu koji su mi roditelji ikad dali, sestri Katarini. Hvala ti jer si uvijek tu kad te trebam. Sada je na tebi red.

U konačnici, vječnu zahvalu dugujem supruzi Ivani, svojem najvećem osloncu koja je svakodnevno imala strpljenja slušati o elementima konstrukcija, zamoru materijala i numeričkim simulacijama. Sva postignuća ostvarena u proteklih deset godina ne bi bila moguća bez tvoje bezuvjetne podrške te inspiracije. Ovo je i tvoj rad.

Mojoj baki Ani, koja je uvijek imala osmijeh za svakoga.

Table of Contents

Abstract

Spur gears are one of the most commonly employed machine elements for power transmission. During their operating life, they are subjected to variable and cyclic loading. Consequently, material fatigue may occur in the tooth root region, commonly referred to as bending fatigue. Steel gears are typically subjected to heat treatment processes such as carburizing to reduce wear. Additionally, the gears may be shot peened to induce a beneficial, fatigue-resistant surface layer of compressive residual stresses. However, this may result in bending fatigue crack initiation below the surface, i.e., subsurface bending failure. This type of crack is hardly detectable during regular service intervals. Hence, it may go unnoticed, grow, and propagate rapidly through the brittle carburized layer, resulting in tooth breakage and gear failure.

This doctoral thesis establishes a computational model for predicting the bending fatigue crack location (surface vs. subsurface) and the required number of cycles for surface-hardened spur gears. Due to the relative complexity of the gear's geometry and loading conditions, the finite element method is employed to obtain load-induced stresses and strains. The multilayer method is employed to account for inhomogeneous material, while the strain life approach ($\varepsilon - N$) is used to predict the bending fatigue life.

The research is divided into multiple stages. During the initial stages, bending fatigue with surface/subsurface crack initiation is investigated on relatively simple geometry, such as surface-hardened gear steel specimens. Then, the model is gradually upgraded to account for more complex loading conditions, residual stress distributions, and inhomogeneous material until the final model applicable to the running gear pair is acquired.

According to the obtained numerical results and confirmed by the experimental investigations from the available literature, subsurface bending fatigue crack initiation tends to occur only in carburized and additionally shot-peened gears. The critical region for subsurface failure is located in the proximity of sharp loss of compressive residual stresses and still relatively high load-induced stresses. The probability of subsurface crack initiation can be reduced by modifying the gear's geometry (choosing a smaller normal module) or increasing the beneficial compressive residual stresses by prolonging the carburization time.

Keywords: *spur gear; bending fatigue; finite element method; subsurface crack initiation; multilayer method; residual stress*

Prošireni sažetak

Zupčanici su jedni od najčešće korištenih strojnih elemenata u prijenosnicima snage i gibanja. Vođeni strogim proračunskim kriterijima prema relevantnim standardima kao što je ISO 6336, čelični zupčanici s ravnim zubima u pravilu zadovoljavaju minimalni očekivani radni vijek. Međutim, postojeći standardi ne uzimaju u obzir zajednički utjecaj dodatnih postupaka površinskog otvrdnjavanja, kao što su cementiranje i sačmarenje, na pojavu zamora materijala u korijenu zuba. U takvim slučajevima, javlja se potreba za računskim modelom koji može procijeniti ne samo broj ciklusa do pojave zamorne pukotine, već i mjesto nastanka spomenute pukotine (površinski naspram potpovršinski nastanak). Mjesto nastanka zamorne pukotine od posebne je važnosti zbog njene otežane detekcije tijekom redovnih servisnih intervala.

U okviru rada razvijen je računski model temeljen na metodi slojeva (eng: *multilayer method*) te metodi konačnih elemenata (eng: *finite element method – FEM*) koji predviđa mjesto te broj ciklusa do nastanka zamorne pukotine u korijenu zuba zupčanika. Zbog relativne kompleksnosti modela, istraživanje je započeto na uzorcima izrađenim od materijala tipično korištenim za izradu čeličnih zupčanika. Predloženi model postepeno je unaprijeđen kako bi se simulirala stvarna geometrija te opterećenje zupčanog para.

Ciljevi i hipoteze

Cilj istraživanja je razviti računski model za predviđanje mjesta i broja ciklusa do nastanka zamorne pukotine korijena zuba površinski otvrdnutih cilindričnih zupčanika s vanjskim evolventnim ozubljenjem ravnim zubima temeljen na metodi slojeva. Kako bi se potvrdila primjena računskog modela u stvarnim situacijama, dobiveni rezultati validirani su usporedbom s postojećim eksperimentalnim istraživanjima.

Hipoteza rada glasi:

> *Primjenom metode slojeva moguće je predvidjeti mjesto i broj ciklusa do nastanka zamorne pukotine u korijenu zuba površinski otvrdnutih cilindričnih zupčanika s vanjskim evolventnim ozubljenjem ravnim zubima.*

Ponajprije, očekivani znanstveni doprinos očituje se u razvoju računskog modela za predviđanje mjesta i broja ciklusa do nastanka zamorne pukotine u korijenu zuba površinski otvrdnutih zupčanika. Nadalje, razlučeni su uvjeti površinskog od potpovršinskog nastanka zamorne pukotine što poboljšava konstruiranje kao i procjenu servisnog intervala zupčanika s obzirom

katastrofalni lom zuba. U konačnici, postavljene su teoretske osnove za unaprjeđenje razvijenog računskog modela te primjenu na drugim vrstama zupčanika, kao i na ostalim strojnim elementima koji su često površinski otvrdnuti, npr. osovine.

Struktura rada

Doktorski rad oblikovan je prema tzv. skandinavskom modelu te se sastoji od četiri znanstvena članka koji su međusobno povezani u cjelinu pregledom literature, diskusijom te kritičkim osvrtom. Kao što je već napomenuto, u prvom radu (Članak I) uspostavljen je analitički model za procjenu mjesta i broja ciklusa do nastanka zamorne pukotine na ispitnim uzorcima izrađenim od tipičnih materijala korištenim za izradu metalnih zupčanika. U drugom radu (Članak II), istražena je primjena postojećih metoda procjene zamornog ponašanja materijala na sam zupčanik s pretpostavkom površinskog nastanka zamorne pukotine u korijenu zuba. Iako je zamor materijala jedna od glavnih tema u Članku II, glavni cilj ovog rada je uspostava numeričkog modela koristeći metodu konačnih elemenata kako bi se simulirala naprezanja i deformacije uslijed stvarnog opterećenja zupčanog para. Nadalje, istražen je utjecaj susjednog zuba na stanje naprezanja u korijenu promatranog zuba. U Članku III, pozivajući se na metode iz prethodna dva članka, po prvi put je istražen nastanak potpovršinske zamorne pukotine kod površinski otvrdnutih zupčanika primjenom metodom slojeva. Međutim, zbog jednostavnosti opterećenja, umjesto simulacije zupčanog para kao prijenosnika snage i gibanja, simuliran je tzv. *single tooth bending fatigue* (STBF) postav. U konačnici, u Članku IV, postojeći numerički model zupčanog para u radu razvijen u Članku II integriran je s metodama procjene zamornog ponašanja predloženima u Članku III kako bi se dobio konačni računski model za predviđanje mjesta i broja ciklusa za nastanak zamorne pukotine u korijenu površinski otvrdnutih zupčanika.

Metode

Postojeća istraživanja u pravilu pretpostavljaju površinski nastanak zamorne pukotine u korijenu zuba. Iako je navedeno istina u većini slučajeva pojave zamorne pukotine u korijenu, kod cementiranih i dodatno sačmarenih zupčanika zamorna pukotina može nastati i ispod površine, što je potvrđeno brojnim eksperimentalnim istraživanjima u postojećoj literaturi.

Zbog nehomogenosti površinski otvrdnutih zupčanika, u sklopu ovog doktorskog rada istražena je primjena metode slojeva pomoću koje se materijal "homogenizira". Shodno tome je u Članku I korištena navedena metoda kako bi se presjek ispitnog uzorka podijelio u određeni broj

slojeva. Uslijed nehomogenosti materijala, svaki potpovršinski sloj karakteriziran je pripadajućom otpornosti na zamor materijala. Iz tog razloga je istražena i primjena metode tvrdoće (eng: *hardness method*) koja aproksimira zamorno ponašanje materijala na bazi njegove tvrdoće. U konačnici, korišten je princip lokalne deformacije ($\varepsilon - N$) za procjenu broja ciklusa do nastanka zamorne pukotine svakog sloja, gdje je sloj s najmanjim brojem ciklusa označen kao kritičan (čime se ujedno i predviđa mjesto nastanka pukotine – površinski/potpovršinski nastanak). Predloženi model potvrđen je validacijom s postojećim eksperimentalnim istraživanjima.

Naprezanja i deformacije u ispitnim uzorcima mogu se analitički odrediti zbog relativno jednostavne geometrije istih. Međutim, kako bi se povećala točnost određivanja naprezanja i deformacija kod zupčanika, uspostavljen je numerički model zupčanog para koristeći metodu konačnih elemenata (Članak II). Promatran je utjecaj susjednog zuba na ciklus naprezanja u korijenu zuba, gdje se pokazalo da navedeno modificira broj ciklusa do nastanka zamorne pukotine i do 22 %. Slično prethodnom istraživanju, korišteni su princip lokalne deformacije i metoda tvrdoće, dok metoda slojeva nije primijenjena zbog pretpostavke površinskog nastanka pukotine.

Numeričke metode i metode procjene broja ciklusa do nastanka zamorne pukotine povezane su u zajedničku cjelinu u Članku III. Osim predviđanja broja ciklusa, predviđeno je i mjesto nastanka pukotine (površinski ili potpovršinski nastanak) te dubina na kojoj nastaje potpovršinska pukotina. U ovom radu, kako se bi razlikovalo ponašanje površinskog (krtog ali čvrstog) sloja od potpovršinskog (elastičnijeg) sloja, predložena je metoda koja zajedno s metodom tvrdoće povećava točnost simuliranja razlike u ponašanju slojeva koristeći različite pristupe korekcije srednjeg naprezanja. Usporedbom s eksperimentalnim rezultatima, potvrđeno je dobro poklapanje ne samo broja ciklusa već i mjesta nastanka pukotine kao i opterećenja pri kojem pukotina nastaje ispod površine.

U konačnici, Članak IV integrira metode iz prethodna dva istraživanja kako bi se dobio konačni računski model za predviđanje broja ciklusa i mjesta nastanka zamorne pukotine kod površinski otvrdnutih zupčanika s ravnim zubima. Dodatno, predložena je metoda korekcije nominalnih naprezanja u korijenu zuba zupčanika dobivenih pomoću metode konačnih elemenata temeljena na IS0 6336 standardu koja uzima u obzir utjecaj dinamičkih efekata. Slično prethodnim istraživanjima, dobiveni rezultati validirani su usporedbom s postojećim eksperimentalnim istraživanjima.

Diskusija

Kako je potvrđeno eksperimentalnom validacijom, razvijeni računski model uspješno predviđa ne samo broj ciklusa već i mjesto nastanka zamorne pukotine u korijenu zuba površinski otvrdnutih zupčanika s ravnim zubima i evolventnim ozubljenjem.

Međutim, budući da sam model koristi više aproksimacijskih metoda, moguće je poboljšati njegovu točnost. Primjerice, povećanjem broja slojeva u metodi slojeva poboljšava se i točnost same procjene broja ciklusa do nastanka pukotine, a posebice mjesta nastanka pukotine, kao što je demonstrirano u Članku III. Međutim, budući da relativno velik broj slojeva povećava računsku zahtjevnost i vrijeme potrebno za izradu modela, u budućim istraživanjima razmotrila bi se primjena metode bez konačnih elemenata, tzv. *meshless* ili *phase-field* metoda. Primjernom navedenog pristupa eliminirala bi se greška uprosječivanja tvrdoće te čvrstoće materijala, kao i zaostalih naprezanja po dubini ispod površine korijena zuba.

Nadalje, kako je model razvijen na makroskopskoj razini, kao takav ne promatra utjecaj specifičnog broja te rasporeda mikroskopskih nepravilnosti koje su jedan od primarnih začetnika potpovršinskog nastanka zamorne pukotine u legiranim čelicima (kao što su aluminijski i sumporovi oksidi). Razmatranje njihovog utjecaja zahtijeva mikroskopsko modeliranje korijena zuba, što bi dodatno doprinijelo točnosti modela.

Kao što je demonstrirano u Članku II, utjecaj susjednog zuba na naprezanja u korijenu zuba zupčanika može smanjiti vrijeme do nastanka zamorne pukotine do 22%, što je značajni postotak u području zamora materijala. Navedeni postotak može varirati ovisno o geometriji, opterećenju te materijalu zupčanog para, što će biti detaljno istraženo u budućim radovima.

Sukladno rezultatima iz Članka III i IV te kao što je potvrđeno eksperimentalnim istraživanjima iz relevantne literature, kritično mjesto za nastanak potpovršinske pukotine je mjesto gdje poželjna tlačna zaostala naprezanja (po pitanju otpornosti prema zamoru materijala) naglo iščezavaju dok su naprezanja uslijed opterećenja i dalje relativno visoka. Vjerojatnost nastanka potpovršinske pukotine može se potencijalno umanjiti smanjenjem modula zupčanika kao i produljenjem vremena cementiranja, vodeći računa da se pri tome ne poveća šansa površinskog nastanka zamorne pukotine u korijenu zuba. Točni parametri će biti istraženi u budućim radovima.

Zaključak

Validacijom razvijenog računskog modela s postojećim eksperimentalnim rezultatima može se potvrditi hipoteza doktorskog rada. Drugim riječima, razvijeni model moguće je primijeniti za procjenu mjesta i broja ciklusa do nastanka zamorne pukotine u korijenu zuba površinski otvrdnutih zupčanika s ravnim zubima i evolventnim ozubljenjem. Prema rezultatima razvijenog računskog modela te postojećim eksperimentalnim istraživanjima, može se zaključiti kako su zupčanici koji su cementirani i dodatno površinski otvrdnuti sačmarenjem skloni nastanku potpovršinske zamorne pukotine. Kritično područje za nastanak potpovršinske pukotine je mjesto naglog gubitka tlačnih zaostalih naprezanja gdje su naprezanja uslijed opterećenja i dalje relativno visoka. Parametri koji potencijalno smanjuju vjerojatnost nastanka potpovršinske pukotine na spomenutoj lokaciji predmet su budućeg istraživanja.

Provedeno istraživanje omogućava bolju procjenu redovnih servisnih intervala te mjesta nastanka zamorne pukotine. Također, pridonosi se učinkovitosti samog procesa konstruiranja zupčanog para. Nadalje, razlučivanjem uvjeta površinskog od potpovršinskog nastanka pukotine predložene su smjernice pomoću kojih se umanjuje vjerojatnost potpovršinskog nastanka zamorne pukotine. U konačnici, razvijeni računski model predstavlja teoretsku osnovu za daljnje unaprjeđivanje te potencijalnu primjenu na druge (u pravilu površinski otvrdnute) elemente konstrukcija, kao što su osovine.

Ključne riječi: *zupčanici s ravnim zubima; zamor u korijenu zuba; metoda konačnih elemenata; potpovršinski nastanak pukotine; metoda slojeva; zaostala naprezanja*

Abbreviations

AGMA	American Gear Manufacturers Association
AISI	American Iron and Steel Institute
DIN	German: *Deutsches Institut für Normung*
FE	Finite Element
GBF	Granular Bright Facet
HPSTC	Highest Point of a Single Tooth Contact
ISO	International Organization for Standardization
LEFM	Linear-Elastic Fracture Mechanics
LBB	Leak-Before-Break
NDT	Non-Destructive Testing
RoM	Rule of Mixture
RPM	Revolutions Per Minute
STBF	Single Tooth Bending Fatigue

List of Figures

Nomenclature

A	total cross-section area of a surface-hardened specimen, mm^2
A_{case}	cross-section area of the case layer of a surface-hardened specimen, mm^2
A_{core}	cross-section area of the core layer of a surface-hardened specimen, mm^2
a	crack length in fracture mechanics, mm
a_d	smallest crack length unable to be detected by non-destructive testing, mm
a_i	crack initiation length, mm
a_0	initial crack size, mm
C	experimentally obtained material coefficient depending on loading frequency, stress ratio, temperature, and environmental effects, (mm/cycle) / (MPa·m$^{1/2}$)
Eht_{max}	maximum effective case depth of a gear according to ISO 6336-5, mm
Eht_{min}	minimum effective case depth of a gear according to ISO 6336-5, mm
Eht_{Hopt}	recommended case depth of a gear to avoid pitting according to ISO 6336-5, mm
Eht_{Fopt}	recommended case depth of a gear to avoid tooth root breakage due to surface-initiated bending fatigue according to ISO 6336-5, mm
K	stress intensity factor in fracture mechanics, MPa·m$^{1/2}$
K_C	combined factor used in Paper IV to account for various dynamic effects in a running gear pair (not to be confused with fracture toughness K_c), -
K_c	fracture toughness (critical stress intensity factor) in fracture mechanics, MPa·m$^{1/2}$
m	experimentally obtained material exponent depending on loading frequency, stress ratio, temperature, and environmental effects in fracture mechanics (not to be confused with normal gear module m), -
m	normal module of a gear, mm
N	number of loading cycles, -
N_f	number of loading cycles until failure, -
N_f'	number of loading cycles until failure, -
N_i	number of cycles required for crack initiation, -

N_p	number of cycles required for crack propagation, -
R_e	yield strength of a material, MPa
R_m	tensile strength of a material, MPa
$R_{p0.2}$	material stress at which plastic strain of 0.2% occurs, MPa
S_e	endurance limit in the $S - N$ approach, MPa
S_a	nominal stress amplitude in the $S - N$ approach, MPa
S_a'	nominal stress amplitude in the $S - N$ approach based on the safe-life design, MPa
s	time, s
x	distance (depth) below the gear's tooth root surface, mm
Z	number of gear teeth, -
$2N_f$	number of cycles until fatigue failure in the strain-life ($\varepsilon - N$) approach (here, N_f represents the number of reversals until failure), -

Greek symbols

ΔK	range of the stress intensity factor in fracture mechanics, MPa·m$^{1/2}$
ε	strain, -
ε_a	total strain amplitude, -
ε_{el}	elastic strain, -
ε_{pl}	plastic strain, -
σ	stress, MPa
σ_{avg}	averaged bending stress in the rule of mixture, MPa
σ_{case}	stress at the case layer according to the rule of mixture, MPa
σ_{core}	stress at the core layer according to the rule of mixture, MPa
σ_{max}	maximum stress in a cycle, MPa
σ_{min}	minimum stress in a cycle, MPa
σ_1	major principal load-induced stress at the tooth root, MPa

1

Introduction

Metal gears are one of the most commonly used machine elements for power transmission. Variable load-induced stresses occur in the tooth root region when the power is transferred from the driving to the driven gear. Due to gear rotation, the stresses in the tooth root region are also cyclic (more specifically periodic). This results in bending fatigue of the gear, which may cause potentially hazardous fatigue crack initiation. In practice, metal gears are frequently surface hardened through processes such as carburizing, nitriding, or shot peening. These methods result in a high-strength, wear-resistant case layer while the core remains relatively ductile and tough, thus ensuring partial dampening of the dynamic forces ensuing from the power transmission. While surface hardening processes enhance gear's mechanical properties, tooth breakage due to material fatigue is still possible. In surface-hardened gears, besides surface initiation, a crack may even initiate below the surface [1], making it harder to detect and successfully prevent tooth failure. Therefore, proper gear design accounting for surface and subsurface crack initiation is required to avert sudden crack growth across high-strength yet brittle case layer and possibly complete gear failure. Therefore, a computational model that can predict the location (surface vs. subsurface) and the number of cycles required for fatigue crack initiation in the tooth root of a surface-hardened gear is necessary.

1.1 Motivation

In the previous section, it was mentioned that metal gears are used for power transmission, and their application can be found in almost any industry branch. Relatively high load capacity with regard to their size makes metal gears suitable for transferring large torques at high rotational speeds. A catastrophic failure such as tooth breakage can have considerable repercussions, i.e., severe damage to the rest of the machinery within which the gear is operating. Even if the observed gear represents a relatively small fraction of the entire mechanism, its failure may cease the operation of the entire device, resulting in a loss of productiveness due to the idleness of the machine. Since gears can be found in almost all major drive mechanisms, such as automobiles and helicopters, fatigue-related gear failures can even cause human injuries.

Three major approaches are usually considered in gear design: analytical, experimental, and numerical. Analytical approaches are mostly based on existing standards. The most widely utilized ones include ISO (International Organization for Standardization) [2], DIN (german: *Deutsches Institut für Normung*) [3], and AGMA (American Gear Manufacturers Association) [4] standards. Compared to more complex methods, these norms are often mainly employed to calculate the bending fatigue strength of gears due to their simplicity. They provide users with referent values upon which gear design can be based. However, the aforementioned calculations estimate bending fatigue strength by assuming a single force that acts on the tooth flank, usually located at the HPSTC (highest point of a single tooth contact). Moreover, the effect of surface-hardening treatments such as carburizing and additional shot peening on subsurface bending fatigue failure is not accounted for. In addition, the highest value of principal bending stresses is assumed to occur at a fixed point located at the tooth root fillet [2], whereas the existing investigations have proven that such an assumption can be somewhat inaccurate [5–7]. Lastly, since bending tooth root stress is observed at a fixed point in time, the existing standards fail to recognize the effect of elastic deformations of teeth, which affects gear mesh and, subsequently, principal stress cycles occurring at a critical point in the tooth root.

To summarize, conventional methods based on the existing standards or norms represent somewhat rough approximations, neglecting certain parameters that affect the bending fatigue life of the gear. Relatively high safety factors are applied to compensate for such approximations, which results in overdesigned gears. In addition, these methods estimate bending fatigue lives by employing complete failure criteria, i.e., complete tooth breakage.

From a safety standpoint, it would be beneficial if fatigue damage initiation, instead of complete failure, could be accurately estimated. This coincides with the fact that gears are machine elements that usually operate for a relatively high ($< 10^6$) number of cycles, where fatigue damage or crack initiation time is almost equal to the time required for complete failure [8].

The main issue with the experimental bending fatigue life investigations of gears is the immense experimental setup complexity and cost. In addition to high torques and rotational speeds that typically range from a couple of hundred to a few thousand rotations per minute, metal gear pairs are almost exclusively partially immersed in or splashed upon by a lubricant. This substantially increases the difficulty of an experimental investigation, as housing must be completely sealed to prevent any oil leakage, thereby increasing the monitoring difficulty. Hence, researchers often resort to model experiments, such as STBF (single tooth bending fatigue) tests, where a dynamic pulsator acts upon the gear tooth flank [9–11]. In studies where actual gear rotation is involved (i.e., the running gear pair investigations), a single gear tooth is often purposely weakened to ensure its breakage due to bending fatigue [12]. Although providing some insight into the bending fatigue behavior of the gear, the investigations mentioned above are not accurate representations of the actual operating conditions of a gear. In addition, they are mostly focused on complete tooth breakage and surface crack initiation, whereas subsurface initiation is dominant and challenging to detect in high cycle fatigue regimes of surface-hardened gears that have been carburized and additionally shot peened [13].

With demonstrated disadvantages of analytical and experimental investigations, it is somewhat expected that the numerical approach would be the one showing the most promise. Be that as it may, numerical bending fatigue simulations of gears are still not sufficiently accurate when validated against experimental data. This can be partially attributed to the experimental validation itself, which is, as described in the previous paragraph, relatively hard to conduct adequately. On the other hand, the existing numerical studies are primarily directed toward computational simulations of tests based on the STBF principle, where gear meshing and consequent elastic deformations affecting the contact ratio are unaccounted for [14–17]. Furthermore, friction [18] and centrifugal forces [19] are often omitted in numerical simulations, while the material properties of surface-hardened gears are challenging to model [20, 21].

The above demonstrates the need for a computational model for bending fatigue life prediction with a reasonable estimate for the location and number of cycles required for fatigue crack initiation. This model should account for as many real-life effects as possible, such as

modification of contact ratio due to elastic deformations of the gear teeth, compressive bending stresses due to the adjacent tooth, and residual stresses from the surface hardening processes. The computational model could then be employed for gear monitoring under operating conditions or optimizing geometrical, material, and operating parameters during the gear design process regarding the bending fatigue life.

1.2   Defining the research gap

As portrayed in the previous section, a computational model is required for bending fatigue estimation of surface-hardened gears, especially because one-third of all gear tooth failures are related to material fatigue [22], and most of the industry application gears are surface-hardened by carburizing, nitriding, and/or shot peening.

Many studies that deal with bending stresses and fatigue behavior of gears can be found in the existing literature. Podrug et al. [23] conducted numerical investigations of spur gear tooth root stresses and deformations by altering the position of a concentrated force along the tooth flank, while Vučković [24] numerically modeled contact between the tooth flanks of the gear pair. Both authors proposed methods for estimating the bending fatigue lives but did not account for elastic deformations due to gear meshing. Zhan et al. [25] conducted a quasi-static analysis of the gear mesh to obtain characteristic stress curves at both the tooth root and flank regions. The authors simulated gear meshing by observing substantial points in time (increments) as static cases while rotating the gear, hence the term quasi-static analysis. This method accounts for elastic deformations of teeth due to gear meshing and reasonably approximates bending stress and strain cycles without considering dynamic effects. Dai and Parker [26] experimentally investigated tooth root deformation. They concluded that different contact conditions and extremely high rotational speeds could significantly impact dynamic tooth root strains. Perez and Aznar [27] investigated the effect of numerical modeling on attained tooth root stress values to optimize the model with regard to computational complexity and accuracy of the results. The authors concluded that their multi-point constraint elements considerably reduce computational costs while simulating the entire mesh cycle. Moreover, the authors observed that an increase in the rigid behavior of the teeth lowers bending stresses by approximately 10% compared to previous models with no mesh refinement. Kumar et al. [28] conducted a finite element numerical analysis to optimize the geometrical parameters of the tooth root fillet with consideration of maximal thermal and mechanical loads. The authors verified their simulations against theoretical values of Lewis bending stress.

Gasparini et al. [16] researched the influence of material, design, and manufacturing parameters on the fatigue behavior of gears used in helicopters. The authors developed a custom-made STBF experimental fixture, where they investigated and numerically verified the bending stresses and fatigue lives of different variants of spur gears. Concli et al. [29] studied the fatigue strength of carburized and nitrided gears used in aeronautical applications. The authors investigated the effect of surface hardening and shot-peening processes on the bending fatigue lives of spur gears through numerical and experimental investigations. The aforementioned investigations were conducted employing an STBF test. The authors concluded that surface hardening processes such as carburizing, nitriding, and even shot peening could significantly increase bending fatigue lives. However, Concli et al. did not account for the adjacent tooth effect (change of the observed bending stress once the following pair of teeth come into contact). Furthermore, frictionless contact was assumed, and case and core layers (layers characterized by different hardness and material properties due to surface-hardening treatments) were not modeled. These simplifications can also be noticed in the remainder of the literature review, where authors numerically investigated bending fatigue stresses and the lives of spur gears. Manojkumar et al. [30] compared the fatigue behavior of aluminum alloy and steel alloy gears during fully reversed loading. A finite element model was created, and contact between the gear pair was simulated, but no gear meshing was observed. The authors confirmed their initial assumption, i.e., steel alloy gears demonstrated consistently higher bending fatigue life when compared to aluminum alloy ones with regard to variation in cyclic stress amplitudes and mean stresses.

When investigating surface-hardened gears, it is extremely important to consider a change in the material structure of the gear due to surface-hardening processes such as carburizing or shot-peening. After such processes, two primary layers can be typically distinguished in the tooth root of gear: the case and the core layer [31]. The case layer is a carbon-enriched surface layer characterized by its strength and beneficial wear resistance, while the core layer is a subsurface layer or the original material of the gear, which remains ductile yet tough [32]. While the geometry of the gear after carburizing remains roughly the same (ergo, it does not affect bending stresses and strains), the process itself results in residual stresses that can affect bending fatigue life [33]. Compressive residual stresses, induced via surface hardening treatments and present in the surface (case) layer of the machine element [34], are beneficial for prolonging fatigue lives. This is also one of the main reasons why gears are often additionally shot-peened. With an increase in depth below the surface, compressive residual stresses eventually become

tensile, which adversely impacts fatigue crack initiation [35]. Residual stresses can mostly or even fully relax during low-cycle fatigue (fatigue region characterized by relatively high loads, local plastic deformations, and low failure cycles) [33]. This can negatively affect the case layer, which is strong but brittle. Combined with the presence of stress concentrators in the form of inclusions, partial or full relaxation of beneficial, compressive residual stresses leaves the layer unprotected against cyclic tensile loads, leading to bending fatigue crack initiation. As previously mentioned, cold working processes such as shot peening can also positively impact the fatigue behavior of the material by creating a surface layer filled with favorable (when it comes to bending fatigue) compressive residual stresses [36]. However, even though shot peening improves the fatigue resistance of the surface layer, the same might cause a shift in bending fatigue failure from the surface to the subsurface region. This is one of the main topics discussed in this thesis.

To investigate the matter of surface hardening processes and corresponding residual stresses in detail, researchers tend to study those effects on simple geometry specimens made of typical gear steel material. By employing fully reversed uniaxial loading, Jo et al. [1] defined the transition layer between the case and the core layer as the critical one, in whose proximity subsurface fatigue crack initiation during high-cycle fatigue occurs. Fatemi et al. conducted fatigue behavior tests on case-hardened specimens made from typical gear materials by employing either uniaxial [34] or multiaxial [37] cyclic loading. The authors utilized the multilayer method [38], which has shown great promise in estimating bending fatigue lives of multi-layered objects, such as case-hardened specimens. In addition, Fatemi et al. employed the rule of mixture (RoM) [39], originally developed for composite materials, to investigate carburized specimens that exhibit composite-like behavior due to different material properties within a single specimen. Yin and Fatemi [40] investigated fatigue crack initiation on case-hardened and through-hardened specimens by employing lower or upper-bound methods. Furthermore, the authors demonstrated the use of the hardness method [41] to estimate strain-life fatigue parameters from material hardness, which is a frequently used method when fatigue parameters are not available [18], [39]. Nishijima and Kanazawa [42] studied surface and subsurface fatigue crack initiation in surface-hardened metals. They concluded that residual compressive stresses in the surface layers are responsible for the high-cycle fatigue shift of the crack initiation site below the surface. Shanyavskiy [43] conducted an analytical study of subsurface fatigue crack initiation of steel alloys in the region of high-cycle fatigue. Zhang et al. [44] proposed numerical subsurface fatigue crack initiation model by conducting high-cycle

fatigue tests on a surface-hardened cubic steel specimen. The authors predicted critical depth for fatigue crack nucleation considering the gradient in material properties due to carburization, compressive residual stress distribution, and the gradient of the applied bending stress. Lastly, since the bending stress cycle for solid gears does not resemble a fully reversed cycle [45, 46], mean stresses that can influence fatigue lives are present [47]. Gaur et al. [48] studied the effect of mean stresses on fatigue crack initiation sites in steels used in riser tube connectors for offshore oil drilling. They found that both fatigue life and the slope of the *S-N* curves decreased with an increase in the load ratio.

In addition to bending fatigue life investigations related to surface-hardened gears and specimens, many studies exist in which contact fatigue occurring at the tooth flank region, as opposed to bending fatigue, is investigated [49–51]. However, tooth root crack initiation is more dangerous to catastrophic gear failure than contact fatigue phenomena such as pitting. Since bending fatigue of surface-hardened gears is the topic of this thesis, contact fatigue will not be discussed here.

After conducting a detailed overview of the existing studies related to this investigation, it can be concluded that the bending fatigue life estimation of non-hardened gears can still be significantly improved. Furthermore, no bending fatigue computational model for surface-hardened gears that distinguishes surface from subsurface failure was found in the literature.

Current investigations often neglect parameters such as variable stresses resulting from the change of contact point position between the tooth flanks. In other words, the elastic deformation of gear teeth [52] and its effect on the contact between teeth flanks is not accounted for. Moreover, the effect of the adjacent tooth on bending stresses is not considered. In addition, bending fatigue estimation of surface-hardened gears is often more demanding due to inhomogeneous material and residual stresses in the tooth root region. Another issue regarding the surface-hardened gears during high-cycle fatigue is that the required number of cycles for the crack to reach the critical length is relatively small compared to the number of cycles required for crack initiation. This may lead to a sudden appearance of hardly detectable subsurface cracks and their growth that can negatively impact the load capacity of the tooth during the high-cycle fatigue region [13] and lead to a complete failure of the tooth.

To gain additional insight into the bending fatigue behavior of the surface-hardened gears, increase the possibility of fatigue crack detection, and prevent tooth breakage, it is necessary to

differentiate the parameters of surface and subsurface fatigue crack initiation. By investigating different methods, a computational model is developed to determine the location and the required number of cycles for fatigue crack initiation in the tooth root region of surface-hardened gears. Moreover, differentiation between surface and subsurface fatigue crack initiation parameters is made. Lastly, the computational model is validated against experimental data from the available literature.

1.3 Hypothesis

The main objective of this doctoral thesis is to develop a computational model with a multilayer-based approach that estimates the location and number of cycles required for bending fatigue crack initiation of surface-hardened involute spur gears.

By employing a multilayer-based approach, it is possible to predict the location and number of cycles required for bending fatigue crack initiation of surface-hardened involute spur gears.

The computational model includes the effects of various real-life parameters, such as modification of gear meshing due to elastic deformations, the adjacent tooth effect, and residual stress distribution due to processes such as carburizing and shot peening. Case and core layers are simulated by utilizing multilayer and hardness methods. The obtained results are validated against experimental data from the available literature.

1.4 Methodology

The main idea of the research conducted within the scope of this doctoral thesis was to start by establishing a fatigue behavior prediction model for surface-hardened entities with relatively simple geometrical and loading parameters (such as surface-hardened test specimens). Then, the model is gradually upgraded to increase both geometric and loading complexity by employing the FE method until the computational model applicable to surface-hardened running spur gears is obtained. The research plan is schematically shown in Figure 1.
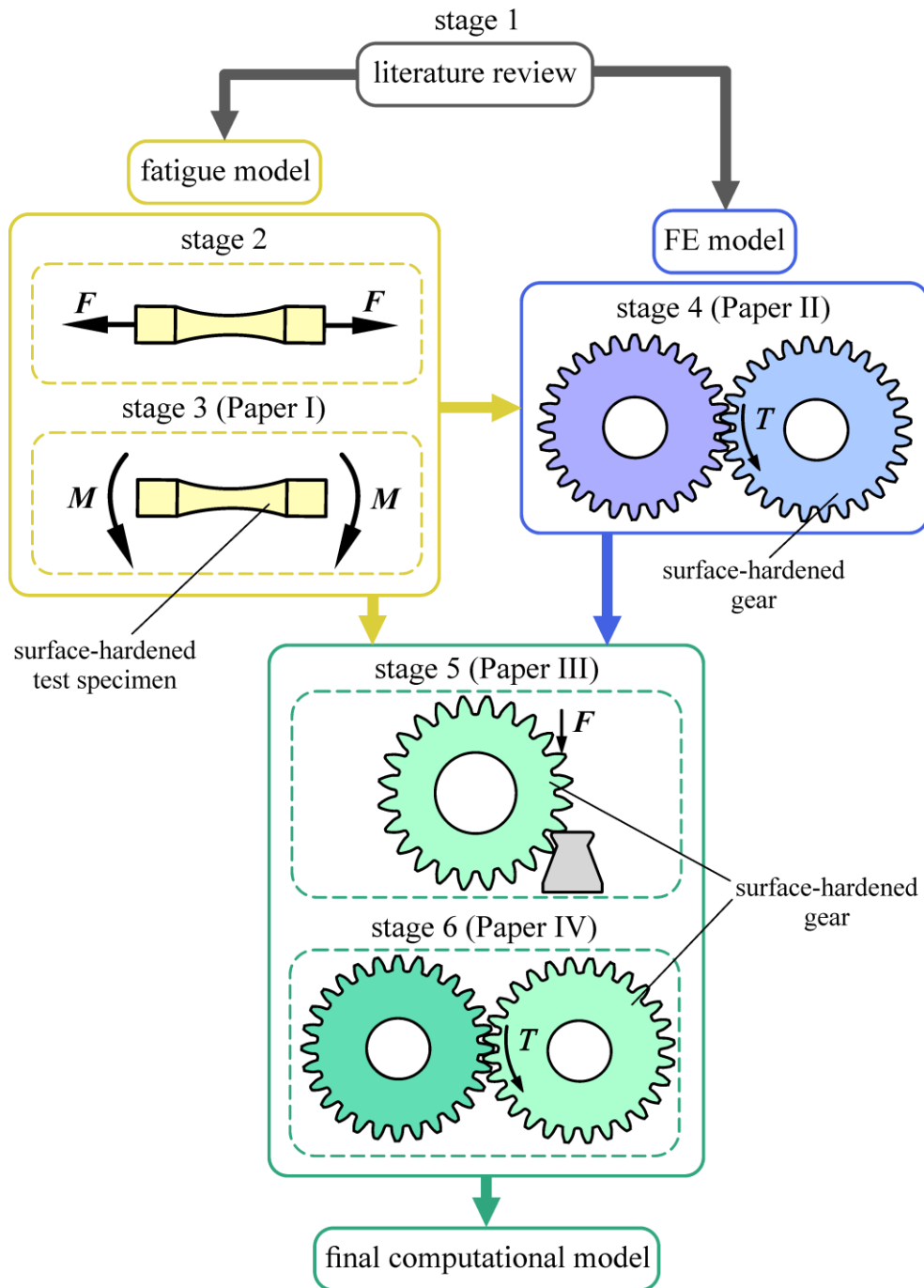
Figure 1. Schematic representation of the research plan separated into six stages

This doctoral thesis is presented in the form of a so-called Scandinavian model. In other words, the computational model is established via four scientific papers corresponding to four different research stages. The entire research is separated into six stages:

1) *The research gap (literature review)*

   Defining the research gap means choosing an area that has not been adequately answered in the field of study. This was conducted through an extensive and detailed literature overview of the relevant studies. Based on the literature overview, an idea for

developing a computational model for surface-hardened bending fatigue prediction surfaced. It should be mentioned that literature overview is a continuous process. Even though the research gap was defined, the latest and most relevant studies regarding the bending fatigue of spur gears are always kept track of.

2) *Surface-hardened test specimens under uniaxial loading*

The main idea of the second research stage was to start simple. A fatigue model of surface-hardened test specimens under relatively simplistic uniaxial alternate loading was to be developed. This stage and the following stage emphasize the *fatigue model* since loading and the corresponding stresses and strains can be expressed relatively simply via analytical relations. This fatigue model would then be incrementally upgraded to include more complex geometries and loading conditions, such as spur gears operating under typical working conditions.

However, during the initial literature review in stage 1, it was discovered that numerous studies exist that deal with uniaxial fatigue prediction of both plain and surface-hardened test specimens [34], [40], [53], [54]. Thus, this part was omitted from the original plan, and the existing methods and research findings were employed to develop a final computational model for bending fatigue prediction of surface-hardened spur gears.

3) *Surface-hardened test specimens under bending loading (Paper I)*

In the third research stage, the existing methods and models used for uniaxial fatigue prediction of surface-hardened test specimens (stage 2) are improved and applied to surface-hardened test specimens subjected to pure cyclic bending loading. Once again, due to relatively simplistic loads, the focus is placed on the *fatigue model*, i.e., describing material fatigue behavior with respect to different layers with various properties. The main purpose of this stage is to investigate surface and subsurface fatigue behavior under bending load and the corresponding stresses, which are dominant types of stresses that occur at the tooth root of a gear (bending stresses). Therefore, by investigating the effect of bending stress gradient on the surface vs. subsurface fatigue crack initiation, another step towards actual loading conditions of running gear is taken.

The research findings conducted in stage 3 are published as Paper I.

4) *Running-gear pair with surface bending fatigue crack initiation (<u>Paper II</u>)*

In the fourth research stage, the effect of typical loading conditions of a running gear pair on surface bending fatigue crack initiation is investigated via numerical simulations. This stage employs the existing findings from stages 2 and 3 to describe the fatigue behavior of the material. However, since the loading conditions of a running gear pair are relatively more complicated than those of test specimens, the emphasis in this stage is placed on developing the *FE model*, i.e., the numerical model. Within this model, the effect of the adjacent tooth on bending fatigue lives, which impacts both the amplitude and mean values of bending stresses, is explored. For simplicity, surface bending fatigue crack initiation (one of the most common types of tooth root failures in spur gears) is assumed. As a result, a quasi-static numerical model for bending fatigue estimation under the assumption of surface failure is obtained. However, a model that distinguishes between surface and subsurface fatigue crack initiation on actual gear geometry is still required.

The research in stage 4 is published as Paper II.

5) *STBF bending fatigue prediction with surface-subsurface failure distinction (<u>Paper III</u>)*

In the fifth stage, surface and subsurface bending fatigue crack initiation are investigated for the first time on actual gear geometry, i.e., on surface-hardened steel gears. For simplicity, the STBF test is chosen as the loading model, where bending fatigue of surface-hardened spur gears is investigated by applying a pulsating load at the flank of the observed tooth. Methods and models established in stage 2 and stage 3 (Paper I) are further improved to enhance the fatigue model. Moreover, the FE model similar to the one established in stage 4 (Paper II) is employed due to relatively complex tooth root stresses and strains. Therefore, the existing fatigue models (stages 2 and 3) are combined with numerical (FE) models (stage 4) to obtain a *computational model* that distinguishes surface from subsurface bending fatigue crack initiation.

The research in stage 5 is published as Paper III.

6) *Running gear pair bending fatigue prediction with surface-subsurface failure distinction (<u>Paper IV</u>)*

In the sixth and final stage, the quasi-static numerical simulation of a running gear pair established in stage 4 (Paper II) is coupled with the fatigue model established in stage 5 (Paper III). However, due to the non-proportional loading and stresses of a running-gear

pair, the multiaxial cyclic fatigue criterion is also applied. Finally, the computational model that estimates both the location (surface vs. subsurface) and the bending fatigue lives required for the crack initiation of running gear is obtained.

The research findings in stage 6 are published as Paper IV.

To summarize, after defining the research gap (stage 1) and investigating the existing methods and model for uniaxial fatigue predictions of surface-hardened specimens (stage 2), a fatigue model is developed for bending fatigue life estimation of surface-hardened test specimens made of typical gear steel material and under bending loading conditions (stage 3, Paper I). The methods and models used in stage 3 are further improved and combined with FE analysis to establish a computational model that distinguishes surface from subsurface bending failure in an STBF test (stage 5, Paper III). Lastly, the final computational model (stage 6) is obtained by combining and upgrading the numerical model of a running gear pair from stage 4 and the fatigue model from stage 5.

1.5 Expected scientific contribution

By employing the developed computational model, more accurate bending fatigue crack initiation prediction of surface-hardened spur gears will be possible. Furthermore, differentiation between surface and subsurface crack initiation will be made. If the location of possible fatigue damage can be accurately predicted, proper steps can be taken to increase the chances of early crack detection and prevention of a catastrophic fracture. Moreover, gear service intervals can be estimated with greater accuracy. This enables the users to inspect the gear for possible fatigue-related damages when prompted by the computational model and replace the components if any form of fatigue damage is observed or suspected.

By utilizing the computational model and parameterization or optimization techniques with respect to bending fatigue crack initiation, the cost-effectiveness of the gear design can also be improved. In turn, this would reduce relatively complicated and often costly experimental methods for determining the bending fatigue lives of surface-hardened gears.

Last but not least, this research will establish a theoretical basis for possible future improvements of the developed computational model to simulate crack propagation and even include other commonly employed types of gears, such as helical or bevel gears. The possibility of applying the proposed model with corresponding modifications on other surface-hardened machine elements, such as axles, should also not be dismissed.

1.6 Thesis layout

This doctoral thesis consists of six chapters. The main issues regarding bending fatigue of surface-hardened spur gears were described, and research motivation was presented in the introductory chapter. Existing studies with corresponding methodologies were portrayed, and the hypothesis was defined. Lastly, the expected scientific contribution of the doctoral thesis was conveyed.

In the second chapter, an introduction to the phenomena of material fatigue is provided, and well-known facts about this field of study are presented. Underlying physical mechanisms of material fatigue and its effects, which can be manifested through crack nucleation, initiation, propagation, and catastrophic failure, are examined. Consequences of poor fatigue design of structural components and machine elements are presented, and subsurface fatigue crack initiation is discussed. Variables that affect the component's fatigue life are analyzed, and pointers for adequate fatigue design are provided. Most importantly, the reasons behind opting for crack initiation as the main failure criteria instead of crack propagation are presented and justified.

The third chapter presents the computational model for bending fatigue prediction of surface-hardened gears by summarizing four published papers. In the first paper, a fatigue model for predicting both the location and the required number of cycles for bending fatigue crack initiation in surface-hardened gear steel specimens is established. The proposed model is validated against experimental results. In the second paper, a numerical model that simulates gear power transmission and estimates the bending fatigue life of gear is developed. The model consists of a previously verified finite element model and an already validated fatigue model. However, only surface fatigue crack initiation is assumed, whereas subsurface fatigue crack initiation is not discussed. Lastly, the effect of the adjacent tooth on estimated fatigue lives is investigated and discussed. In the third paper, a computational model that predicts surface and subsurface bending fatigue crack initiation of surface-hardened spur gears in an STBF test is established and validated against experimental results. Finally, in the fourth paper, the methods and model established in the previous three papers are combined and upgraded to account for the running gear pair conditions, thereby resulting in a final computational model, i.e., the main objective of this thesis.

In the fourth chapter, the validity of the proposed hypothesis is examined, and a critical discussion with possible improvements to the obtained results is provided. Finally, some suggestions are made for lowering the risk of subsurface bending fatigue crack initiation.

In the fifth chapter, the conclusions are drawn, and future work is discussed.

The sixth and final chapter provides a list of references cited within this thesis.

Lastly, the papers are provided in the Appendix.

2

Material fatigue in metals

If one is to talk about the strength of the materials, commonly used terms would be material's ultimate strength (R_m) and yield strength (R_e for ductile or $R_{p0,2}$ for brittle materials). These values have one thing in common: they represent parameters obtained for the material subjected to static loading. In these tests, the load is gradually applied, giving the strain an adequate amount of time to develop fully. Static testing results are usually manifested in a stress-strain diagram ($\sigma - \varepsilon$). It should be noted that, for discussion purposes, engineering stress-strain curve (which assumes constant specimen cross section) is shown in Figure 2, as opposed to the true stress-strain curve.
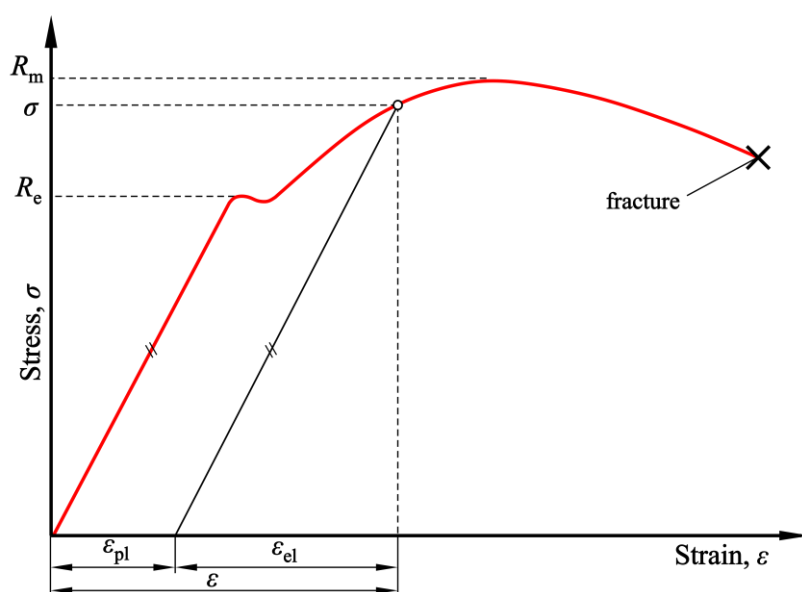
Figure 2. Schematic representation of stress-strain diagram for ductile materials under static loading

For arbitrarily chosen stress value, σ, elastic, ε_{el}, and plastic, ε_{pl}, regions of the total strain amplitude, ε, are shown. The material response shown in Figure 2 approximately correlates to the actual conditions to which many structural or machine components are exposed. An adequate example of the aforementioned can often be seen in structural engineering, where steel frames are used in various building techniques or as a reinforcement material in concrete walls. In such cases, frames are generally experiencing static loading conditions, i.e., all weight and load-induced stresses are characterized by constant direction and values with respect to time. Similarly, many machine elements are subjected to static loading conditions during their service life cycle. For example, an axle of the driven wheel of the car experiences constant values of bending-induced stress with respect to time.

Designing a new or calculating the existing mechanical components subjected to static loading is usually relatively simple. The problem arises when the component is exposed to time-varying stresses. Throughout history and even in the modern day, mechanical components have failed while exposed to variable and repetitive stress levels. After conducting thorough analyses, the researchers found that the actual levels of maximum stresses were beneath the material's ultimate strength and often even beneath the yield strength [55]. Since many cycles of repetitive stresses had to occur before the component would eventually fail, this phenomenon was called *material fatigue*.
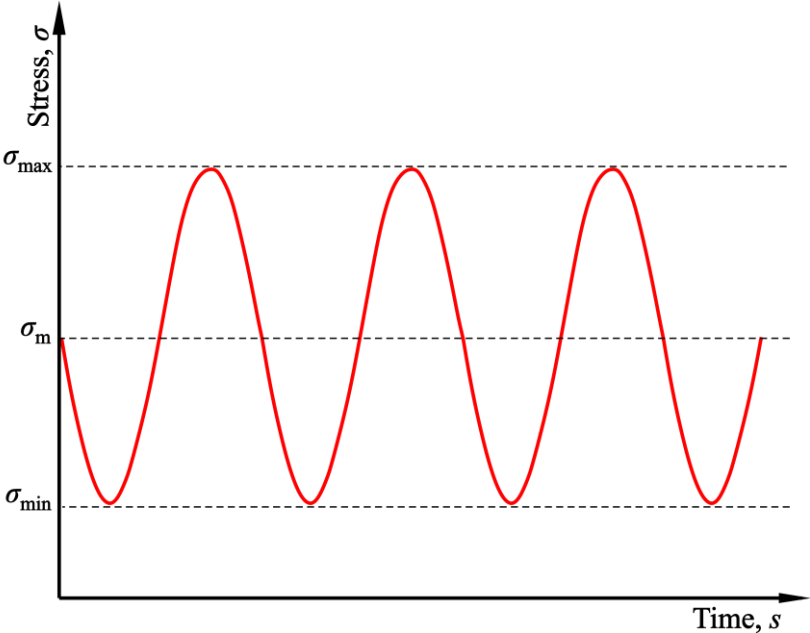
Figure 3. Schematic representation of time-varying stress

The first significant impact of fatigue-related failures was observed during the mid-19th century in the railway industry, where axles would repeatedly fail at their shoulders [56]. As opposed

to static failures, which often provide some sort of warning before a fracture occurs (such as relatively large and noticeable deflection in ductile materials), fatigue-related failures often show no visible warning. Thus, fatigue failures are considered more dangerous than static-related failures, and proper precautions must be taken when designing a component that experiences time-varying stresses. Examples of fatigue-related failures can be seen in Figure 4. In Figure 4a), crankshaft fatigue fracture due to repeated bending loading is shown [57]. Failure due to fatigue on a greater scale is shown in Figure 4b), which depicts the Taikoyama Wind Power Plant turbine accident [58].

a)   b)
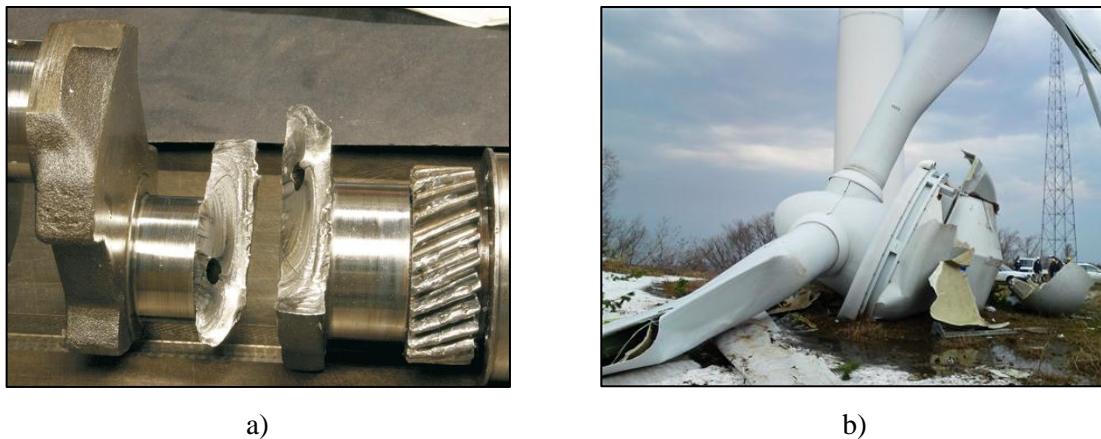
Figure 4. Fatigue failure of components: a) crankshaft [57] and b) wind turbine [58]

2.1 Stages of fatigue failure

Some dire consequences of fatigue failure have been presented in the previous section. An additional understanding of the underlying microscopic and macroscopic mechanisms of fatigue failure is required to successfully prevent potential fatigue-related damages. As previously mentioned, fatigue failure in metal materials does not occur suddenly. It is a gradual process that usually follows four dominant stages [59]: I – crack nucleation, II – growth of small cracks, III – growth of long cracks, and IV – final fracture. A schematic representation of these stages for surface-initiated fatigue failures can be seen in Figure 5.
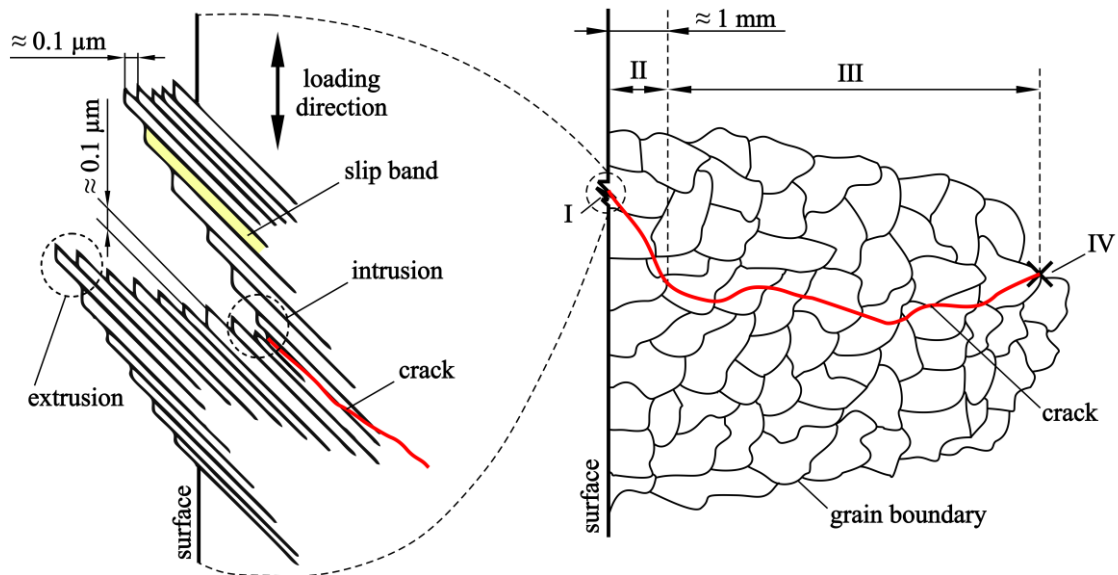
Figure 5. Stages of fatigue crack growth for metals under the assumption of surface crack initiation: I – crack nucleation, II – growth of small cracks, III – growth of long cracks, and IV – final fracture

2.1.1 Crack nucleation

The first stage of fatigue failure, crack nucleation, refers to deformation processes on a microstructural scale that transpires under cyclic loading conditions [60]. Most of the structural metals have polycrystalline microstructure. They consist of many crystals or grains with various orientations and mechanical properties. Each grain has a unique direction of movement characterized by the least resistance (more commonly known as the easy-slip plane [31]). Statistically, some microstructural grains will have easy-slip planes oriented toward the maximum applied shear stress. Due to variable and cyclic loading, localization of plastic strain (slip) ensues at critical grains and, depending upon the direction of the applied shear stress, extrusions or intrusions are formed. These extrusions and intrusions act as stress concentrators, creating possible locations for the development of cracks due to an increase in localized stresses and strains. Since extrusions and intrusions are present on a microstructural level, they are invisible to the naked eye.

2.1.2 Growth of small cracks

In the second stage, cracks on a micro-level (microcracks) are formed by interconnecting several localized deformities with multiple slip bands [61]. These microcracks tend to initially grow in the maximum shear stress plane, and their size is typically on the order of several grains. If cyclic loading continues, microcracks tend to merge and grow along the plane of maximum tensile stress. Together, stages (I) and (II) are often called the crack initiation

phase. One of the main disputes the researchers have with this stage is defining the crack initiation criterion. ASTM E606-92 standard [62] suggests many possible criteria, such as selecting a specific crack length that is typically the smallest crack length detectable via NDT (non-destructive testing) methods. Recommended by the standards and under the assumption of strain-controlled loading, failure is defined as the point at which the maximum stress or elastic modulus decreases by approximately 50% due to crack initiation. Furthermore, in [63], a more conservative approach is used, with the value of 10% being used instead of 50%. Lastly, since a crack initiation size of approximately 1 mm is equivalent to a maximum stress decrease of roughly 10%, researchers often use it as the crack initiation criteria [64].

2.1.3 Growth of large cracks

In the third stage, the growth of large cracks along the plane of maximum tensile stress is continued. Even though fatigue cracks mostly grow across grain boundaries (transcrystalline growth), they can also grow along the boundaries (intercrystalline growth). This stage of fatigue crack growth is commonly referred to as the crack propagation phase and is usually separated into three additional phases: slow, stable, and rapid (unstable) crack growth (Figure 6).
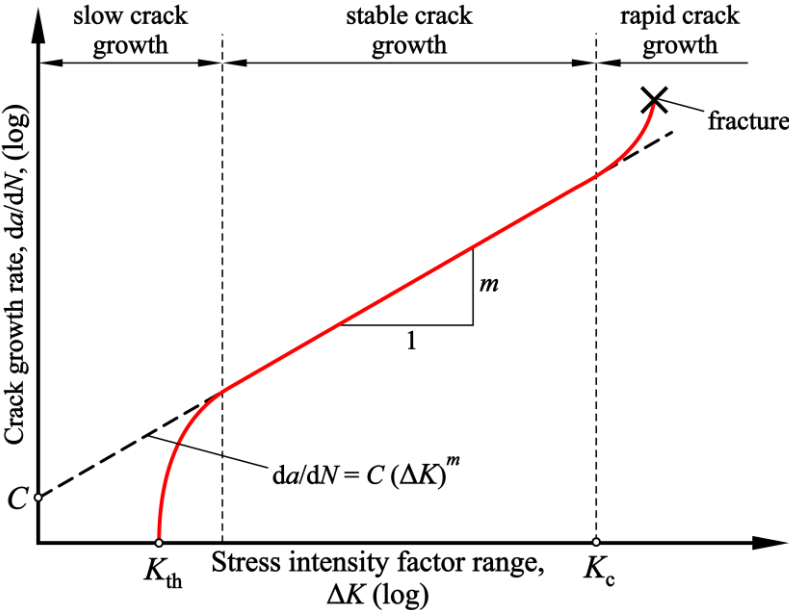
Figure 6. Schematic representation of crack growth stages according to Paris' law

Slow crack growth represents an initial crack propagation phase. In this phase, crack growth is observed only if the range of the stress intensity factor, ΔK, is higher than the value of the material's threshold stress intensity factor, K_{th}. The approximately linear crack growth rate characterizes the second phase of crack growth. Paris first observed this effect in 1961 and

proposed a power relationship (also known as the Paris-Erdogan equation) between the crack growth rate, $\dfrac{\mathrm{d}a}{\mathrm{d}N}$, and the range of the stress intensity factor, ΔK [65]:

$$\frac{\mathrm{d}a}{\mathrm{d}N} = C\left(\Delta K\right)^{m},\tag{2.1}$$

where a is the crack length, N is the number of loading cycles, and C and m are experimentally obtained material coefficients depending on loading frequency, stress ratio, temperature, and environmental effects [66]. This stage of fatigue failure is often characterized by the appearance of wavy markings, i.e., *beach marks* (Figure 7).

2.1.4 Final fracture

In the third phase of crack growth, which corresponds to the fourth and final stage of fatigue failure, the crack will rapidly start to grow in an unstable manner, ultimately leading to a complete fracture of the component. This phenomenon occurs if the range of the stress intensity factor at the crack tip surpasses the value of the critical stress intensity factor, K_c, which is more commonly known as the material's fracture toughness (shown in Figure 6).

An example of fatigue failure on an actual component is presented in Figure 7 [67], where previously described stages are shown for bending fatigue failure of an aluminum crank arm.
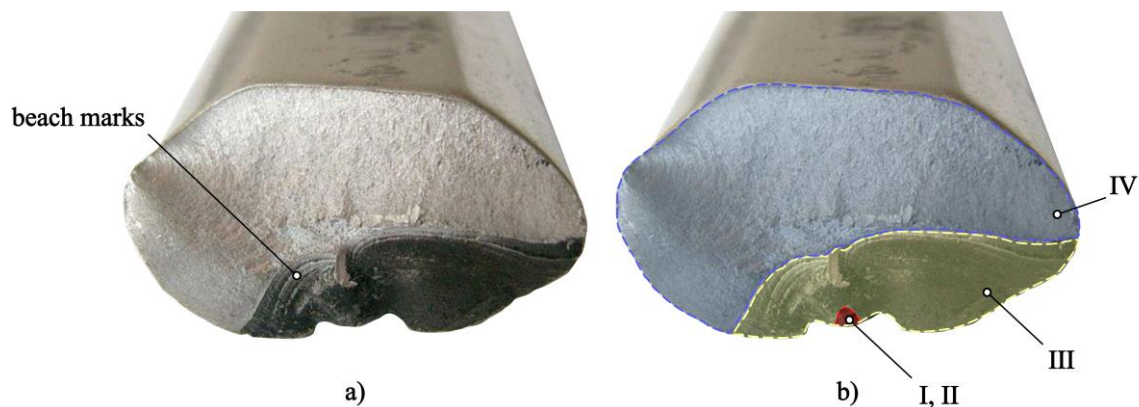
Figure 7. Fatigue failure of an aluminum crank arm [67]: a) actual cross-section, and b) cross-section with marked fatigue failure stages: I – crack initiation, II – growth of small cracks, III – growth of large cracks, and IV – final fracture

2.1.5 Subsurface crack initiation and growth

It should be mentioned that, apart from the slip bands, fatigue cracks can nucleate at or in the presence of material discontinuities, such as grain boundaries, inclusions, pores, or voids.

In such instances, a crack can even initiate below the surface. Due to its shape, this type of crack is often referred to as the fish-eye [13]. Typical fish-eye failure is shown in Figure 8.
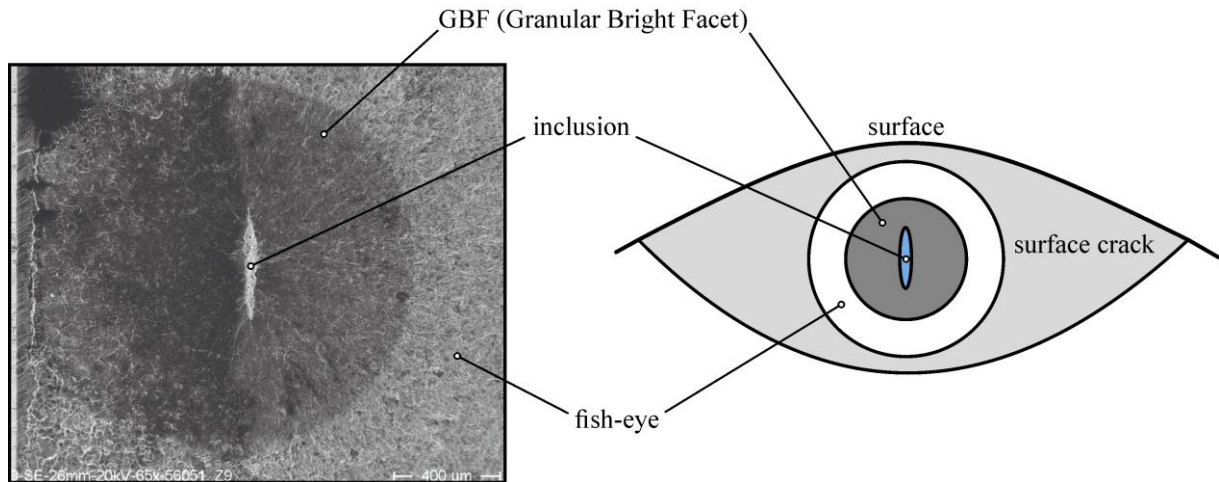
Figure 8. Subsurface fatigue failure in the form of a fish-eye: a) actual image [13], and b) schematic representation

Subsurface inclusions in steel materials, such as aluminum or sulfide oxides, represent stress concentrators that may, with time, result in crack nucleation. Multiple microcracks are then formed in the GBF (Granular Bright Facet) zone. The microcracks are evenly spread in the radial direction and create a spherical shape, i.e., the fish-eye. With time, fatigue cracks that have initiated in the form of a fish-eye may propagate to the surface and result in a catastrophic failure of a component. These cracks are especially dangerous since they often go unnoticed during regular service intervals of components.

Lastly, it should be noted that subsurface crack initiation in the form of a fish-eye is one of the most dominant subsurface bending fatigue failure modes of surface-hardened gears that were carburized and additionally shot peened. As such, it is particularly interesting for the investigation conducted within this thesis.

2.2 Fatigue design criteria

By understanding the underlying microscopic and macroscopic mechanisms and stages of fatigue failure, suitable criteria can be developed to ensure the proper safety of the component while considering the cost-effectiveness of the design. From an engineering designer's point of view, the fatigue design of a component is most often based on one or more of the following criteria: infinite–life, safe–life, fail–safe, and damage–tolerant design [31].

2.2.1 Infinite–life design

Infinite–life design is one of the oldest fatigue design criteria corresponding to unlimited safety (in theory). In this design, actual stresses and strains should be completely elastic locally and globally. They should never exceed the endurance limit (also known as the fatigue limit or fatigue strength) of the material, S_e, representing stress below which the material can theoretically withstand an infinite number of loading cycles without fatigue damage. This is presented in Figure 9 for typical steel materials, where the maximum value of the applied cyclic stress is plotted with respect to the number of cycles required for fatigue failure. This diagram is referred to as the $S - N$ diagram, more commonly known as the Wöhler curve [68].
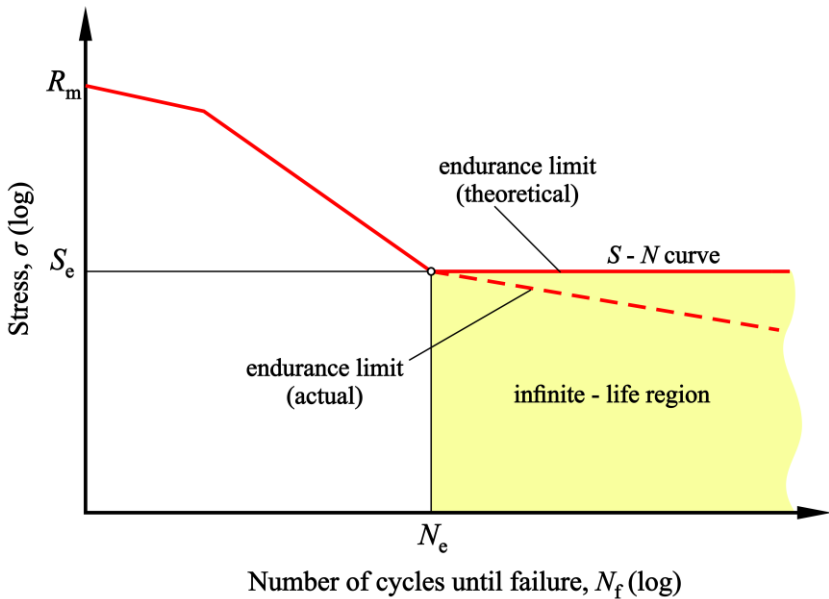
Figure 9. Schematic representation of $S - N$ curve for infinite–life design of typical metals

In recent years, researchers found that the theoretical endurance limit in metallic materials is not constant; it rather decreases with an increase in loading cycles in the very–high cycle (ultra–high cycle or giga–cycle) fatigue region [69].

Even though infinite–life design initially seems like an impeccable design criterion, mechanical components would have to be overdesigned to maintain the actual stresses at the minimum level. If one is to consider an example of an aircraft design, this would result in overdesigned components, which lead to excessive weight and impracticality when compared with the cost-effectiveness of the design.

2.2.2 Safe–life design

Safe–life design was originally proposed by automobile designers who experimentally investigated mechanical components under maximum expected load [31]. They found that the fatigue failure would occur in the ballpark of a couple of thousand cycles instead of the infinite number of loading cycles. Since maximum loads or stresses of automotive industry mechanical components would occur frequently, the engineers developed a safe–life design method. In other words, mechanical components have a finite life and should be periodically inspected and replaced when approaching their estimated fatigue lives. In other words, replacing the components once they reach their finite life is sometimes less expensive than overdesigning them for theoretically infinite fatigue life. Safe–life design can be found in numerous areas of engineering, such as pressure vessels, jet engines, gun tubes, and bearing designs.

An example of a safe–life design is presented in Figure 10 for mechanical components undergoing cyclic stress with a maximum amplitude of S_a, with the corresponding number of loading cycles required for fatigue failure, N_f. It should be mentioned that fatigue estimation is not entirely accurate due to various factors influencing fatigue life, both known and unknown. Thus, the safe–life design must include a margin of error which considers the scatter of the fatigue estimation results. This can be achieved by lowering the critical number of cycles required for fatigue failure, N_f, to the required number of cycles from the safety standpoint, N_f'. In metal fatigue engineering, a scatter factor (safety factor) of three is often employed, meaning typical values of N_f can be up to three times higher than those of N_f'.
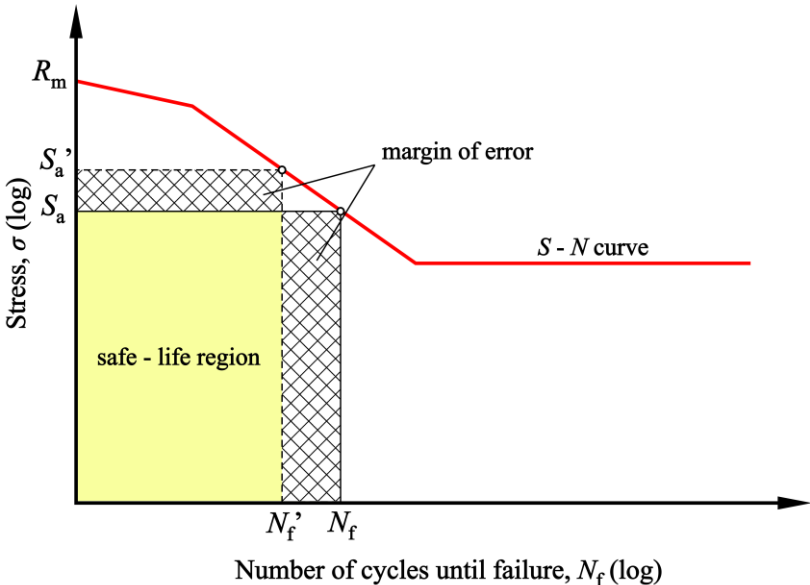
Figure 10. Schematic representation of $S – N$ curve for safe–life design of typical metals

The margin of error can also be accounted for by modifying the maximum applied stress amplitude values, S_a. Via this method, actual stress values in components are purposely overestimated (S_a'), which decreases the component's fatigue life. However, the relationship between the applied stress and the corresponding fatigue life is not linear. For example, a decrease in the applied stress of only 10% will increase fatigue lives up to three times [31]. Ergo, to arrive at the desired outcome of N_f' cycles, a valid correlation between the applied stress and the fatigue life of a component should be made.

2.2.3 Damage–tolerant design

As the expression states, damage–tolerant design assumes that fatigue-generated cracks will appear in the material that can be tolerated under specific conditions. Even though safe–life design lowers the risk of fatigue failure, it can often negatively impact the cost–effectiveness of mechanical components. Due to the uncertainty of the scatter region (margin of error) in safe–life design and consequently higher safety factors, many components will be retired from service even though they could have had substantial additional service life. Naturally, it is important to consider which components are the subject of discussion. For example, premature retirement of jet engine turbine blades will have a greater financial impact than relatively simple mechanical components in power transmission devices, such as axles. Nevertheless, if adequate and precise calculations can be made to ensure that the component can continue to operate with the existing damages, the cost–effectiveness can be significantly increased via damage–tolerant design.

2.2.4 Fail–safe design

The fail–safe fatigue design method was originally developed by aircraft engineers who could not abide with an added weight due to overdesigned components with considerable safety factors or the relatively high costs of safe–life design. Fail–safe fatigue design is based on one simple premise: if a single entity or a component in a system fails, the system itself should not. This fatigue design method, like the damage-tolerant method, accepts that fatigue damage may occur in the form of cracks. However, unlike the damage–tolerant design, a fail-safe design allows for components to fail, as long as the failure of one component does not govern the system's failure. This method considers structural and parametric alteration to ensure that fatigue cracks do not result in catastrophic system failure before they are detected, repaired, or the components replaced. One of the most commonly utilized fail–safe design methods is the

leak–before–break (LBB) method, which is often employed for pressurized components, particularly in the nuclear industry [70].

2.3 Fatigue design principles

Both fatigue design criteria and design principles have a similar goal: to ensure proper component design while considering adequate fatigue safety measurements. While design *criteria* are employed to define the end state of a component's fatigue life, design *principles* are utilized to define the initial state of the component's fatigue life. In other words, both design criteria and design principles are applied to ensure proper safety against fatigue failure. However, different approaches are used.

Fatigue design principles are based on either the total-life principle or the defect-tolerant principle [71, 72]. Both principles are based on fatigue-related crack growth. However, what differs them is the initial crack state and size within the component.

2.3.1 Total–life principle

The total–life principle assumes that no initial gaps or inclusions that serve as stress concentrators exist within the material. The initial crack size is then equal to $a_0 = 0$ mm. The total fatigue life of a component, N_f, before the fatigue-induced crack reaches its critical length, a_c, can then be described as the combination of the cycles required for crack initiation, N_i, and the cycles required for crack propagation, N_p:

$$N_f = N_i + N_p. \tag{2.2}$$

The exact crossover point between these cycles depends on the definition of the crack initiation length, a_i. The total–life principle is schematically depicted in Figure 11.
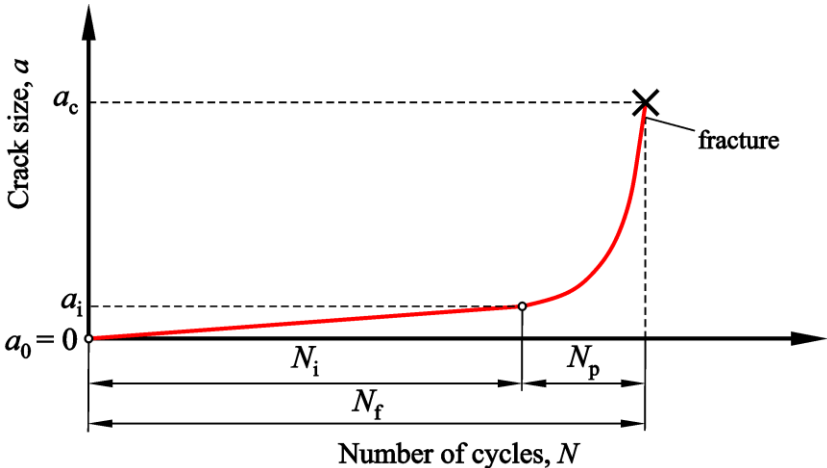
Figure 11. Schematic representation of total–life principle

In high–cycle fatigue, crack propagation time is often relatively small compared to the crack initiation time [8]. This is especially relevant for brittle materials, such as the carburized layer of the surface–hardened gear. In such materials, the brittleness promotes rapid and sudden crack growth, resulting in a negligible number of cycles required for crack propagation. Thus, total fatigue life can be expressed as:

$$N_f \approx N_i. \tag{2.3}$$

In other words, crack initiation time can be regarded as the total fatigue life of a component. This condition is often applied for relatively small mechanical components whose potential fatigue-related damages are characteristic for high–cycle fatigue regions, such as metal gears. Furthermore, the condition is frequently employed for safe–life design (Section 2.2.2), where crack initiation time serves as the safety failure criterion, thus preventing abrupt crack propagation and possible complete fracture of the component.

2.3.2 Defect–tolerant principle

Unlike the total–life principle, the defect-tolerant principle assumes initial gaps or inclusions already exist within the material. Such deformities serve as cracks with the corresponding length a_i, i.e., there is no crack initiation time N_i since cracks already exist in the material. If the number of cycles required for crack initiation is equal to zero, the total fatigue life is then equal to:

$$N_f \approx N_p. \tag{2.4}$$

The initial crack length is assumed as:

a) actual detected crack length, or

b) limiting crack length a_d, defined as the smallest crack length unable to be detected via NDT methods.

Furthermore, the defect–tolerant principle does not allow the crack to reach its critical length, a_c, during the expected lifetime. The principle also assumes that initial cracks are located and oriented in the worst possible manner, i.e., in the region of maximal stresses, while being perpendicularly oriented with respect to the stress vector. The defect–tolerant principle is schematically depicted in Figure 12.
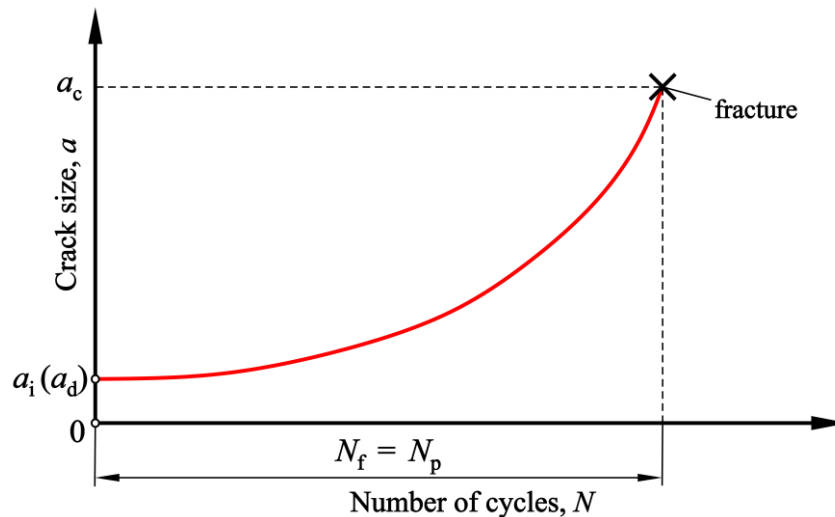
Figure 12. Schematic representation of the defect-tolerant principle

The defect–tolerant principle is applied when potential failure expenses are relatively high, e.g., for ships, pressurized containers, or airplanes. More specifically, welds are considered potential crack locations in such examples. Hence, NDT or surface inspection methods are often used for weld examinations, while fracture mechanics are employed to determine crack growth parameters and consequent service or control intervals.

2.4 Fatigue design *criteria* and *principles* in bending fatigue of surface-hardened gears

Theoretical background regarding fatigue design criteria and principles has been provided in Sections 2.2 and 2.3. However, these criteria and principles should not be universally applied to every component undergoing cyclic loading. When choosing the proper fatigue design criterion and principle, many factors should be considered, such as the component's function, its financial value, and overall failure–related risk assessment.

Since this thesis deals with gear fatigue, the applicability of each criterion and principle on bending fatigue of surface–hardened spur gears is discussed in detail.

2.4.1 Fatigue design *criteria* in bending fatigue of surface-hardened metal gears

Infinite–life design criterion of surface-hardened metal gears

When designing metal gears, which are often additionally surface-hardened to enhance their wear properties, infinite–life criterion is often employed. In theory, this would mean that the gear can withstand an infinite number of cycles without bending fatigue failure occurring.

Even if this were true, there is a question of the cost-effectiveness of the gear design. In other words, infinite-life gear design requires relatively low operating values of stresses and strains exerted on the gear. This means that the gear must be overdesigned, i.e., more material and additional treatments must be employed. For a relatively low number of gears produced, this would not cause serious manufacturing cost-effectiveness problems. However, if one is to consider the number of gears produced by a certain manufacturer in a specific period, a significant amount of funds can be saved by designing the gears according to their required service life, as opposed to a theoretically infinite number of cycles. Even if a theoretically infinite amount of service cycles can be achieved via infinite–life design, the cost of this type of design might not be effective in some cases.

Furthermore, according to Figure 9 in Section 2.2.1, the theoretically infinite number of cycles the material can withstand before fatigue damage was shown to be non-existent. Hence, fatigue-related damages can still occur in high or very high cycle fatigue regions. In these regions, the possibility of subsurface crack initiation in surface-hardened gears is increased. Subsurface fatigue initiation has often been observed in surface-hardened steels undergoing cyclic conditions. This phenomenon is more commonly known as the fish-eye [73]. This type of crack initiation is often challenging to detect and may instigate the process of rapid crack growth, culminating with a sudden and brittle fracture through the hardened layer. The aforementioned represents a potential problem for surface-hardened gear design.

To summarize, infinite–life design criterion can be employed in surface-hardened gears, whereas adequate precautions must be taken to ensure timely detection and prevention of subsurface crack initiation.

Safe–life design criterion of surface-hardened metal gears

When the safe-life design criterion is employed in surface-hardened gear design, a gear is designed according to the expected service life. In other words, inspecting and potentially replacing the gear after a certain period rather than risking a fatigue-related failure is more efficient. However, since no existing analytical or numerical methods for bending fatigue life prediction of surface-hardened gears are found in the relevant literature, it can often be challenging to provide accurate estimations. In addition, subsurface crack initiation further increases this challenge since modeling the underlying microscopic and macroscopic mechanisms of fatigue failure is quite demanding.

Briefly, the safe-life design of surface-hardened gears can be adequately utilized only if a proper model based on which relatively accurate bending fatigue estimations can be made exists, both for the location and the number of cycles required for bending fatigue failure. This is precisely the goal of this doctoral thesis.

Damage-tolerant design criterion of surface-hardened metal gears

As previously mentioned, damage – tolerant design criterion is based on a single premise, which states that some fatigue-related damage is allowable in the component as long as the component continues to operate safely. An example of the damage-tolerant design of surface-hardened gears would be an existing fatigue crack in the tooth root. The question is whether the existing crack will continue to grow when subjected to continued cyclic loading. If accurate estimations of crack growth can be made, the gear can continue to operate with the existing fatigue damage for a certain period [74–78]. On the other hand, the gear may be replaced after the first indication of fatigue-related damage. Since fatigue-related damage in operating gears infrequently occurs, replacing the entire gear is often more effective rather than seeking the benefit of additional gear exploitation. Moreover, since most of the gear-related damage occurs in the high cycle fatigue region, an additional number of operating cycles obtained is negligible compared to the gear's total service life.

The damage-tolerant design greatly depends upon the cost-effectiveness of the gear in question. If manufacturing the replacement gear and its assembly is relatively expensive, the gear can continue to operate for a certain period if accurate analytical or numerical calculations can be provided to ensure safety against rapid crack growth. On the other hand, if the replacement gear is relatively inexpensive and the replacement itself is not overly complicated, it should be replaced even if accurate estimations of the remaining fatigue life can be made.

Fail-safe design criterion of surface-hardened metal gears

As previously mentioned, the fail-safe design is based on the premise that if a single system entity fails, the system itself will not. If this principle is applied to gears, failure of a single entity can be interpreted as complete breakage of a single gear tooth due to fatigue-related damages. Since gears are often employed in power transmission devices with relatively high revolutions per minute (RPMs) and torques, the broken tooth can cause significant damage to the remainder of the system. Even if the system remains intact, the loss of the gear tooth will only hasten the fatigue process of the adjacent teeth, which will surpass their intended load capacities. Thus, it is a question of whether fail-safe design criteria should be applied to metal

surface-hardened gears used in power transmission devices with relatively high RPM and torque outputs.

In conclusion, the fatigue design criteria employed in this thesis combine the <u>infinite–life design</u> and <u>safe–life design</u>. With the developed computational model, accurate estimations of the number of cycles required for fatigue crack initiation can be made (safe-life criterion). If fatigue damage is expected in the region of high or very high cycle fatigue (infinite-life criterion), the computational model can be utilized to estimate not only the required number of cycles for fatigue failure but also the location of potential fatigue damage (surface vs. subsurface damage initiation).

2.4.2 Fatigue design *principles* in bending fatigue of surface-hardened metal gears

Total-life design principle of surface-hardened metal gears

As previously mentioned in Section 2.3.1, the total-life principle is often employed for relatively small mechanical components with potential fatigue-related damages occurring in the high cycle fatigue region, such as surface-hardened spur gears.

Spur gears are usually designed according to their corresponding material fatigue limits. However, as presented in Section 2.2.1, the fatigue limit decreases in the high cycle fatigue region. Therefore, some form of bending fatigue-related damage may be expected. Furthermore, due to the brittle material characteristics of the hardened layer, rapid crack growth is anticipated. Such growth is difficult to timely detect and properly handle before the complete fracture of the gear tooth and the failure of the gear itself. As previously mentioned, subsurface crack initiation is possible in high cycle fatigue regions of surface-hardened components. This further complicates its proper detection during service and control intervals, particularly since the crack itself is not visible via surface inspection methods. A crucial mistake may occur, in which the gear would be incorrectly placed back into operation when possibly only a relatively small amount of loading cycles would be required for the subsurface crack to propagate through the brittle, hardened layer. Thus, catastrophic failure of the gear might occur.

By applying the total-life design principle according to Eq. (2.3), the number of cycles required for crack initiation, N_i, can be designated as the failure criterion. As a result, successful prediction of the location and number of cycles required for crack initiation will ensure adequate gear withdrawal, inspection, and subsequent actions.

Defect-tolerant design principle of surface-hardened metal gears

According to Section 2.3.2, the defect-tolerant design principle is often used when expected repair or swap costs are relatively high, which is typically not the case with surface-hardened spur gears. Replacement of a single gear is relatively simple compared to heavy machinery, such as pressurized containers or transport vehicle components, e.g., airplane hubs. It should be pointed out that, even though gear replacement is relatively inexpensive and simple, this does not mean that one should wait for the complete fracture of the tooth to occur before replacing the entire component. Adequate precautions should still be taken to ensure timely detection of fatigue-related damages. Furthermore, single gear replacement costs in a specific machine may not be high, but those costs can accumulate on a monthly or yearly basis, especially if multiple machines require gear replacements.

Defect–tolerant design primarily focuses on proper crack growth estimation by employing fracture mechanics principles. As mentioned in the previous section, crack growth in surface-hardened spur gears is a relatively fast process that is difficult to describe accurately due to a continuous change in boundary conditions. From that point of view, it would be more logical to ensure an accurate estimation of the required number of cycles for crack initiation, at which point the gear would be withdrawn from the operation.

In conclusion, the focus of this thesis will be placed on estimating the gear's fatigue life from a safety standpoint, i.e., only the required number of cycles for crack initiation will be considered. This is decided based on the following standpoint: an increase in safety due to a timely gear service interval with regard to the crack initiation time outweighs the benefit of the additionally obtained (and relatively small) number of operating cycles required for the crack to reach its critical length. Hence, fatigue life estimation based on the total-life design principle is conducted in this thesis. In other words, the total number of cycles required for bending fatigue failure of the gear is equal to the number of cycles required for bending fatigue crack initiation, as presented in Eq. (2.3). Therefore, the term fatigue *failure* (or bending fatigue failure) will be used instead of bending fatigue *crack initiation* for the remainder of this thesis. Lastly, when discussing the number of cycles required for tooth root fatigue crack initiation in surface-hardened spur gears, term *fatigue life* (or *bending fatigue life*) will be employed.

3

Summary of papers

This chapter summarizes the computational model of surface-hardened spur gears that predicts both the location and the required number of cycles for bending fatigue failure. The computational model is established in the form of four published papers. As demonstrated in the introductory chapter, each paper corresponds to a single research stage.

3.1 Paper I: Analytical approach for low and high cycle bending fatigue life prediction of carburized gear steel specimens

In the first paper [79], a model for bending fatigue life prediction of carburized gear steel specimens based on a strain-life approach was proposed. The multilayer and hardness methods were used to estimate strain-life fatigue properties, whereas the rule of mixture (RoM) was employed to find average cyclic stress-strain curves of carburized specimens. In addition, an approach for converting uniaxial to bending fatigue data by utilizing Neuber's rule and modifying fatigue factors was proposed. The analytical model was validated against experimental results from the literature [80] for two types of specimens with different carburizing depths. A good correlation between the predicted and experimental data was observed for both types of specimens, with nearly all data points falling within the scatter factor of three. Furthermore, good agreement was also obtained between the predicted and the observed failure location sites (subsurface vs. surface crack initiation).

3.2 Paper II: Numerical model for bending fatigue life estimation of carburized spur gears with consideration of the adjacent tooth effect

In the second paper [81], the finite element method was used to establish the numerical model that simulates an actual running gear pair and obtains linear elastic stresses and strains at the tooth root. The accuracy of the numerical model was confirmed against the existing standards. Then, a previously validated fatigue model was employed to estimate bending fatigue lives under the assumption of surface crack initiation. Due to the relative complexity of the mathematics that closely follows numerical simulations and material fatigue investigations, computer programs Abaqus [82] and FE-Safe [83] were employed. By employing the proposed computational model, the effect of the adjacent tooth on estimated fatigue lives was also investigated. According to the obtained results, accounting for the adjacent tooth effect (which more accurately represents actual tooth root stresses and strains) decreases bending fatigue lives by approximately 22%. Lastly, a modification factor was proposed that estimates the change in bending fatigue lives due to the adjacent tooth effect.

3.3 Paper III: Computational model for bending fatigue prediction of surface hardened spur gears based on the multilayer method

In the third paper [84], surface vs. subsurface bending failure was investigated by conducting numerical simulations of an STBF test. Numerically obtained linear-elastic stresses and strains were corrected for elastic-plastic behavior via Neuber's rule. According to the multilayer method, the observed toot root region was separated into 3, 6, or 12 layers. Averaged hardness and residual stress values were assigned to each layer and the corresponding strain-life properties were obtained based on the hardness method. Finally, by employing the maximum (normal) principal strain criterion used for multiaxial fatigue and different mean stress correction approaches, bending fatigue lives were obtained for each node at the observed tooth root region. The node with the lowest bending fatigue life was designated as critical. The predicted results were then compared against experimental results from the available literature [85]. Good agreement between simulated and experimental results was observed for bending fatigue lives and critical failure locations (surface vs. subsurface failure). Lastly, it was observed that subsurface bending fatigue failure tends to occur in the region where beneficial

compressive residual stresses are sharply decreased, and load-induced tooth root stresses are still relatively high. This conclusion agrees with the experimental observations.

3.4 Paper IV: Computational model for bending fatigue life and failure location prediction of surface-hardened running gears

In the fourth paper [86], an already established and verified FE quasi-static simulation is conducted to obtain linear-elastic tooth root stresses and strains. Hence, effects such as migration of the contact point due to elastic teeth deformation and the adjacent tooth effect [80] on the fatigue life are accounted for. The influence of dynamic factors on load-induced tooth root stresses was also accounted for by proposing a modification coefficient based on the ISO 6336 standard [2]. The results are then input into the established fatigue model from the previous paper (Paper III). However, to account for non-proportional loading and stresses, incremental Neuber's rule [87] and the critical plane method [88] are employed. Lastly, the obtained predictions are validated against the experimental results from the available literature [85]. Good agreement is observed for both bending fatigue life predictions and failure location. Once again, it is confirmed that the critical location for subsurface failure is the region characterized by relatively high load-induced stresses and a sudden drop in favorable compressive residual stresses.

4

Discussion

In this chapter, the validity of the proposed hypothesis is first discussed. Then, a critical discussion of the employed methods, their effectiveness on the obtained results, and potential improvements to the model are presented. Moreover, the role of load-induced stress and residual stress profiles on bending fatigue lives is discussed. Consequently, modifications to gear geometry and surface-hardening treatments that could improve the bending fatigue resistance are considered. In addition, the role of subsurface stress concentrators in the form of non-metallic inclusions or impurities on bending fatigue failure is discussed. Lastly, the proposed computational model and obtained results are compared against the existing bending fatigue prediction models from the relevant literature.

4.1 Hypothesis

The proposed hypothesis states the following:

> *By employing a multilayer-based approach, it is possible to predict the location and number of cycles required for bending fatigue crack initiation of surface-hardened involute spur gears.*

According to the results obtained in Paper III and Paper IV, it can be concluded that the hypothesis is confirmed. In other words, it is possible to predict both the location (surface vs. subsurface) and the number of cycles required for bending fatigue crack initiation of

surface-hardened involute spur gears, as demonstrated by validating the obtained predictions against experimental results. Moreover, the proposed computational model can be applied to both STBF gears and running gear pairs.

4.2 Employed methods and potential improvements to the proposed model

In this section, some criteria and methods upon which the proposed computational model is based are discussed. Since each method is characterized by certain disadvantages, some potential improvements of the proposed model are also examined.

4.2.1 The strain-life (ε – N) and hardness methods

The strain-life ($\varepsilon - N$) method was employed in all research stages that make up the final computational model, i.e., from simple test specimens to spur gears characterized by complex geometries and loading conditions. Contrary to the popular and often employed stress-life ($S - N$) method, the strain-life method was primarily used due to low-cycle bending fatigue estimation and the hardness method.

Low-cycle bending fatigue prediction of surface-hardened spur gears

As previously mentioned, two of the most commonly employed fatigue prediction approaches are the strain-life and stress-life methods. Even though both methods can be successfully applied in the high-cycle fatigue region where linear-elastic material behavior is dominant, the strain-life method is more accurate in low-cycle fatigue that is characterized by localized plasticity effects [31]. In such instances, actual stresses and strains are somewhat different from the nominal values due to elastic-plastic material behavior.

As demonstrated by the literature review and the conducted research within this thesis, surface-hardened spur gears typically fail due to bending fatigue in the high-cycle fatigue region, where the stress-life method is considered a reasonable approach. However, the strain-life approach was chosen within this thesis to improve the accuracy of bending fatigue predictions in both low and high-cycle fatigue. The method's accuracy in low-cycle fatigue is demonstrated in Papers I – III. Lastly, the strain-life method is chosen since it is connected to the hardness method, whose applicability to non-homogenous material was investigated in this thesis.

The hardness method

Typically, fatigue data obtained from test specimens are used to predict the fatigue behavior of an actual component made of the same material. For example, if the bending fatigue behavior of steel axles made of S275J0 material is investigated, a test specimen made of the same material and subjected to reverse bending or axial cyclic loading may be employed. However, for carburized spur gears, material properties gradually change with depth below the tooth root surface, as shown in Figure 13 [89]. This is a consequence of carbon diffusion that gradually weakens with an increase in depth below the surface. After quenching, carbide and martensite regions are formed. The end result is the case layer characterized by high hardness, strength, and carbon content (%C). Below the surface, a core layer emerges with lower hardness values, strength, and carbon content. Consequently, a gradient in material properties exists between the case and core layers. In other words, the material is not homogenous.
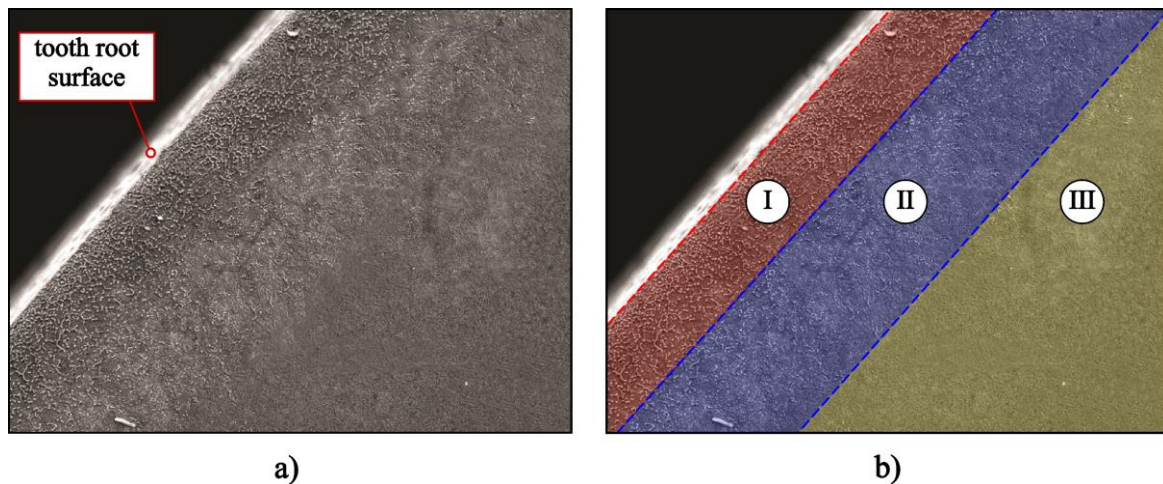
Figure 13. Microstructure of a carburized spur gear [89]: a) actual cross-section and b) cross-section with marked regions: I – carbide region, II – carbide and martensite mixed region, III – martensite region

The above-mentioned calls for multiple questions that should be adequately dealt with. If test specimens are to be used to represent the fatigue behavior of a tooth root, how many specimens should be used to represent the entire tooth root region? To what depth should these specimens be carburized? For example, if the gear made of 18CrNi8 steel with a pitch diameter of 90 mm is carburized to the nominal case depth of 1 mm, is employing a test specimen made of the same material, carburized to the same depth, but with significantly smaller dimensions justified? This might be acceptable if surface crack initiation is assumed under the condition that the surface of both the test specimen and the gear is characterized by approximately the same hardness and %C values. However, for subsurface layers, this method may not be adequate. This is because subsurface bending fatigue failure of both surface-hardened test specimens and gears is

governed by variable load-induced stresses, residual stresses, and fatigue properties of the material.

Therefore, to avoid costly, time-consuming, and complicated experiments of multiple test specimens hardened by carburizing and/or shot peening to various nominal depths, the application of the hardness method was investigated in this thesis. The hardness method [41] was proposed to approximate strain-life fatigue properties of a statistically significant number of test specimens made of various materials with respect to their hardness values. Therefore, since each point in the tooth root region is distinguished by different hardness values due to surface-hardening treatments, it is also characterized by different strain-life fatigue properties. Since no approximations were provided for the stress-life method, the strain-life method was chosen as a fatigue life prediction method within this thesis.

4.2.2 The multilayer method and the rule of mixture (RoM)

The multilayer method

As demonstrated in investigations of surface-hardened test specimens [1], [34], [39], the multilayer method can be employed to homogenize nonhomogeneous material, such as surface-hardened spur gears. The multilayer method averages residual stresses and hardness values (and consequently fatigue properties due to the hardness method) within each layer. A schematic example of the multilayer method used to partition the hardness profile of two different surface-hardened components is shown in Figure 14.
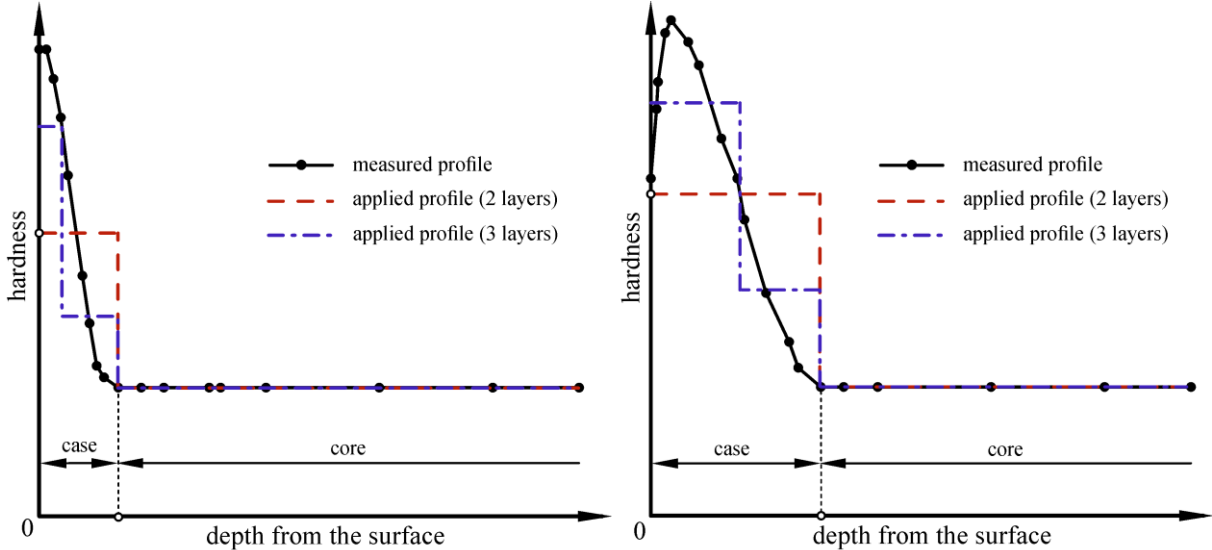
Figure 14. Multilayer partitioning of hardness profiles of surface-hardened components by employing 2- and 3-layer partitioning

According to Figure 14, it can be observed that multilayer partitioning will inevitably result in some averaging errors in hardness estimations and, consequently, due to the hardness method, in fatigue properties. Moreover, a higher number of layers will lower the averaging error. In Paper I [79], two layers were deemed adequate when simulating the bending fatigue of surface-hardened specimens to obtain good agreement with the experimental results. In Paper III [84], three, six, and 12-layer partitioning was investigated on surface-hardened spur gears. It was observed that the accuracy of estimated fatigue lives is slightly enhanced by employing 12 instead of three layers. However, the accuracy of subsurface fatigue failure location prediction was substantially improved. As a result, 12-layer partitioning was employed in Paper IV, where a running gear pair was simulated. Once again, good agreement with the experimental results was observed. It should be noted that, in addition to the hardness profile, the multilayer method can also be used to average residual stress profiles.

In future investigations, an attempt will be made to further increase the number of layers, possibly even to apply direct hardness and residual stress profiles to the gear tooth root. However, since each finite element has a specific length and width, this might not be possible via standard FE simulations. Instead, the application of different approaches, such as the meshless phase-field method [90], will be investigated.

The rule of mixture (RoM)

According to Paper I [79], in addition to the multilayer method, the RoM method was employed to average load-induced stresses and strains. The RoM was originally proposed for composite materials. Due to similarities between composites and surface-hardened materials, the RoM can be applied to the surface-hardened test specimens made of carburized steel [34], [39]. In Paper I, it was proposed that the total bending stress is averaged according to the RoM since the case layer in a test specimen accounts for a significant portion of the total cross-section:

$$\sigma_{avg} = \sigma_{case}\left(\frac{A_{case}}{A}\right) + \sigma_{core}\left(\frac{A_{core}}{A}\right), \qquad (4.1)$$

where σ_{avg} is the averaged bending stress, σ_{case} is the stress at the case layer, σ_{core} is the stress at the core layer, A_{case} is the cross-section area of the case layer, A_{core} is the cross-section area of the core layer, and A is the total cross-section area of the specimen. Then, the averaged bending stress was applied to the case and the core layers, each characterized by different fatigue properties. The layer with the lowest estimated bending fatigue life was denoted as critical, i.e., if the core layer had lower bending fatigue predictions, it was concluded that

subsurface crack had initiated at the case-core layer boundary. A detailed explanation can be found in the Appendix, Paper I.

The aforementioned, however, did not apply to gears that were carburized and additionally shot peened, as it was found that subsurface failure still occurs within the case layer [84]. Hence, the fatigue properties and load-induced stresses for the surface layer and subsurface layer failure were too similar to distinct via the RoM method established in Paper I.

4.2.3 Improving the accuracy of surface and subsurface bending fatigue failure prediction via different mean stress correction methods

Surface hardened specimens/components are characterized by somewhat inferior low-cycle fatigue behavior than non-hardened ones and excellent high-cycle fatigue behavior [40, 80]. One reason is due to highly compressive residual stresses in the case layer that may partially or fully relax when subjected to relatively high loads (low-cycle fatigue), resulting in an "unprotected" strong but brittle material prone to fatigue damage. The brittleness of the material leads to another reason for inferior low-cycle fatigue behavior, which can be attributed to non-metallic inclusions (such as aluminum or sulfide oxides) located at the critical region for bending fatigue failure (location with the most unfavorable combination of load-induced and residual stresses [84]). Those inclusions serve as stress concentrators that contribute to the initiation of the crack, which rapidly propagates through a brittle layer of surface-hardened components. In high-cycle fatigue, compressive residual stresses "protect" the brittle material, which, coupled with the high material strength, increases the fatigue life.

On the contrary, steel specimens/components that are not additionally surface hardened can generally withstand a higher number of cycles when subjected to low-cycle fatigue loading due to their relative ductility compared to brittle materials. Hence, even in the presence of stress concentrators in the form of non-metallic inclusions, relative material ductility (compared to surface-hardened materials) helps the material to withstand a higher number of cycles prior to failure. However, non-hardened specimens/components are more prone to fatigue failure in the high-cycle fatigue region since they are not "protected" by highly compressive residual stresses as surface-hardened components are.

The above-mentioned was experimentally demonstrated for AISI 4027 steel and SAE 8620 steel by Landgraf [80] and Yin and Fatemi [40], respectively, and is schematically shown in

Figure 15a). In Figure 15b), a schematic representation of Basquin-Coffin-Manson's strain life relation with two different mean stress correction methods (Morrow's and Smith-Watson-Toppers') is shown.
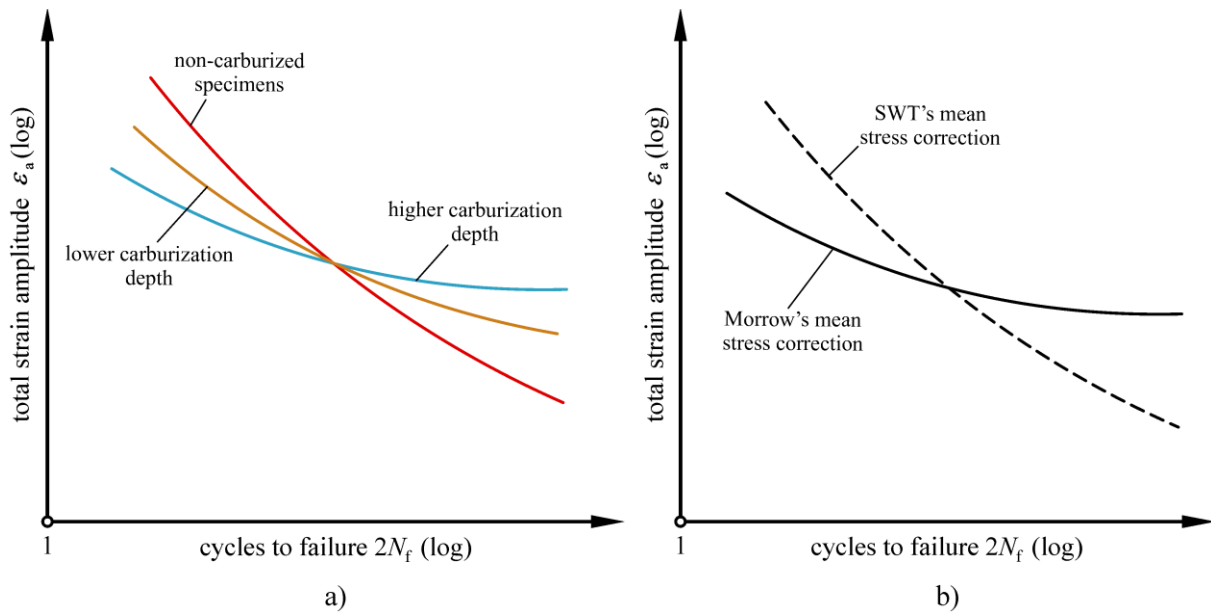
Figure 15. Schematic representation of strain-life fatigue behavior for carburized and non-carburized steel specimens: a) experimental results according to Landgraf and b) strain-life curves obtained by different mean stress correction approaches

A similarity was observed between the experimental fatigue behavior of non-carburized specimens and the fatigue behavior predicted via SWT's mean stress correction approach. The same similarity was observed between carburized specimens and Morrow's mean stress correction approach. Therefore, in Paper III, it was proposed that the fatigue behavior of brittle materials (surface layers) is simulated via Morrow's mean stress correction, and the fatigue behavior of ductile materials (subsurface layers) is simulated via SWT's mean stress correction. The above-mentioned is in accordance with the experimental data [54]. In other words, Morrow's mean stress correction method tends to provide better fatigue life estimations for steels with higher hardness values, while SWT's mean stress correction method tends to better estimate fatigue lives of steels with lower hardness values.

It should be mentioned that the hardness method employed within this thesis (Section 4.2.1) provides the same effect as the one shown in Figure 15, i.e., specimens with lower hardness values resemble the red line, while the ones with higher hardness values resemble the blue line. However, for bending fatigue prediction of surface-hardened spur gears whose surface and subsurface failure both originate at the case layer, their hardness values are not that different, i.e., the corresponding strain-life curves are similar. Therefore, different mean stress correction

methods were proposed to increase the prediction accuracy of surface and subsurface fatigue curves, as described above. A detailed explanation of the proposed approach can be found in Appendix, Paper III.

The proposed approach is an estimation based on statistical data demonstrating that a certain mean stress approach tends to estimate fatigue lives more effectively based on material characteristics (brittle vs. ductile). Consequently, some approximation errors are induced. Nevertheless, as demonstrated in both Papers III and IV, apart from the estimated bending fatigue cycles, a good agreement was observed in failure location prediction (surface vs. subsurface) and the transition point between surface and subsurface failure.

To summarize, the hardness method, the multilayer method, and employing different mean stress approaches represent a joint effort to estimate fatigue properties of inhomogeneous surface-hardened steel material. Otherwise, these properties would have to be obtained via costly, time-consuming, and still undefined experimental investigations of surface-hardened specimens with various carburizing and shot-peening depths.

4.2.4 The effect of centrifugal force and friction on load-induced stresses

As mentioned in the introductory chapter of this thesis, all known parameters should be accounted for within the computational model to improve the accuracy of the results, such as friction between teeth flanks and centrifugal force. Based on the existing research and conducted simulations, it was decided that the effects of centrifugal force and friction will not be accounted for within the established model due to their relatively minor influence. However, even though the aforementioned effects might have been irrelevant for the gear parameters investigated within this thesis, it should be emphasized that this does not mean that the centrifugal force and friction effects should always be assumed negligible.

As demonstrated in [5], the centrifugal force slightly "shifts" the load-induced bending stress cycle towards higher values. Consequently, mean and maximum stresses increase while the amplitude remains the same. According to [19, 91], major principal tooth root stresses are increased by 9 MPa, 37 MPa, and 146 MPa when the gear operates at 5 000 RPM, 10 000 RPM, and 20 000 RPM, respectively. The authors also stated that the centrifugal force does not have to be accounted for when the gear operates below 10 000 RPM. Since the gears investigated in Paper IV operated at 3 400 RPM, the centrifugal force effect was not accounted for. However,

the centrifugal force effect should be considered in gears that operate at relatively high speed, are characterized by relatively high mass, or in thin-rimmed gears [19, 24, 91]. According to the existing research, accounting for the centrifugal force effects in solid spur gears will slightly increase the load-induced stresses and decrease estimated bending fatigue lives, which minorly increases the safety of bending fatigue predictions.

As mentioned in Papers III and IV, friction coefficients for lubricated running gears range between 0.02 and 0.08 depending on the lubrication conditions, rotational speed, and the slide-to-roll ratio [92, 93]. According to the results obtained in [9], introducing a constant coefficient of friction slightly increases the maximum value of load-induced stresses during single-tooth contact due to relatively low friction coefficients in properly lubricated running gears. Moreover, as demonstrated in [92], the coefficient of friction is not constant along the path of contact; it is lower during the single-tooth contact region, which is characterized by the highest tooth root stresses. Therefore, even if a constant coefficient of friction is assumed within the computational model (which overestimates its effect and is not entirely accurate), the obtained bending fatigue lives would be slightly decreased due to increased maximum load-induced tooth root stresses. Once again, this slightly increases the safety of bending fatigue predictions by estimating somewhat lower fatigue lives.

To summarize, for the running gear pair parameters used to validate the established computational model in Paper IV, the accuracy of the model would be insignificantly increased by considering the centrifugal force and friction effects. In other words, accounting for the aforementioned effects would somewhat decrease the estimated bending fatigue lives due to an increase in maximum tooth root stresses.

4.3 Load-induced stress vs. residual stress profiles: the effect on critical bending failure locations

As demonstrated by the results of Paper III and IV, the critical location for subsurface bending fatigue failure is defined as the region where high compressive residual stresses are suddenly reduced. In other words, they no longer provide a beneficial fatigue-resistant effect, while the load-induced stresses and strains are still high. Therefore, in this section, lowering the load-induced stresses and increasing the compressive residual stresses by modifying the gear's geometry and surface-hardening treatments is discussed. This, in turn, would reduce the chance of subsurface bending fatigue failure in surface-hardened spur gears.

4.3.1 The effect of gear geometry on load-induced stresses

The gear module is one of the most important parameters affecting the gear's geometry. For a fixed number of gear teeth, Z, the effect of various spur gear modules (i.e., tooth sizes) on load-induced major principal stress profile is shown in Figure 16 [13], [94].
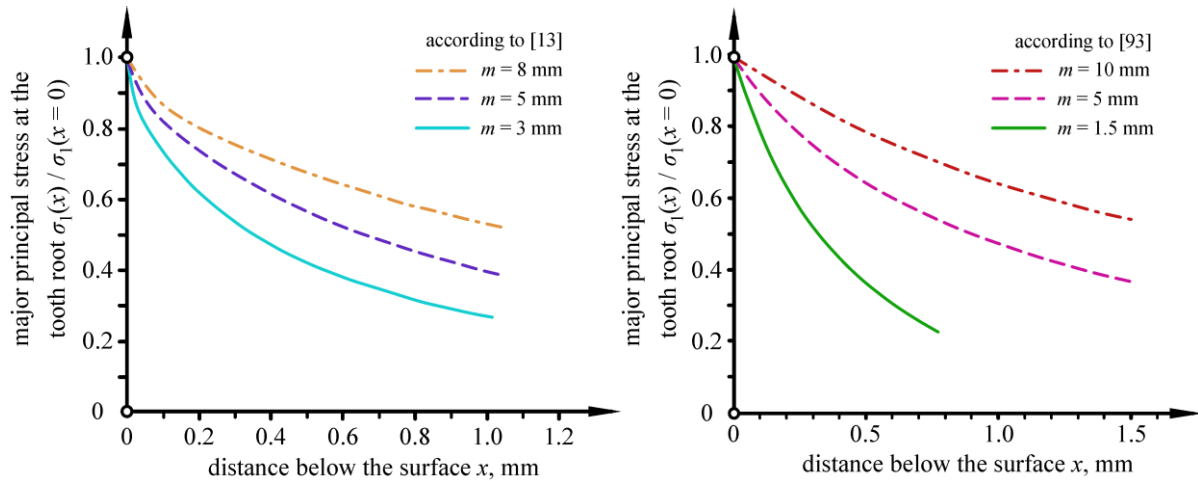
Figure 16. Schematic distributions of load-induced major principal stresses for various tooth sizes obtained via the FE method

As previously mentioned and numerically and experimentally demonstrated in Papers III and IV, the critical location for subsurface failure in surface-hardened spur gears is the region where beneficial compressive residual stresses are significantly reduced. Consequently, material strength at that location is insufficient to withstand relatively high load-induced stresses and strains.

Load-induced stresses for gears with lower modules, m, are more abruptly decreased with an increase in the distance below the surface, x, as opposed to the gears with higher modules (Figure 16). By only observing the geometry of the gear, it can be argued that the probability of subsurface bending fatigue failure can be lowered by decreasing the gear's module, which reduces the tooth root fillet radius [2]. This increases the tooth root stress concentration at the surface and sharply decreases load-induced stresses below the surface. Moreover, gear with the lower module is also characterized by a lower tooth thickness, resulting in a higher stress gradient.

It should be noted that gears with different moduli and, consequently, different tooth sizes will also have different surface-hardening treatment parameters, such as nominal carburizing and shot-peening depths. This will also affect the probability of subsurface bending fatigue failure. However, strictly from the gear's geometry point of view, choosing a lower gear module may reduce the probability of subsurface bending fatigue failure.

4.3.2 The effect of surface-hardening treatments on residual stress profiles

Two of the most commonly employed surface-hardening treatments of spur gears can be separated into thermal hardening (of which the most commonly employed one is carburizing [95]) and cold work hardening processes (one of the most commonly employed methods is shot peening). The main purpose of carburizing is to increase the wear resistance of a tooth flank, while shot peening is primarily used to induce a layer of compressive residual stresses that counteracts load-induced tensile stresses responsible for bending fatigue.

As demonstrated in this thesis and the existing experimental investigations [13, 85, 94], gears only hardened via carburizing tend to experience bending fatigue crack initiation at the surface. Apart from inclusions, this mainly occurs due to a relatively brittle case layer that is not adequately protected by compressive residual stresses that typically range from -300 MPa to -800 MPa [10], [96], [97]. Therefore, gears are often shot peened to induce even higher compressive residual stresses reaching up to -1300 MPa [13] or even -1400 MPa [98]. Even though shot-peening protects the gear tooth root surface, it makes the subsurface region vulnerable to bending fatigue failure due to a sudden loss of compressive residual stresses in the presence of high load-induced stresses, as schematically depicted in Figure 17a).
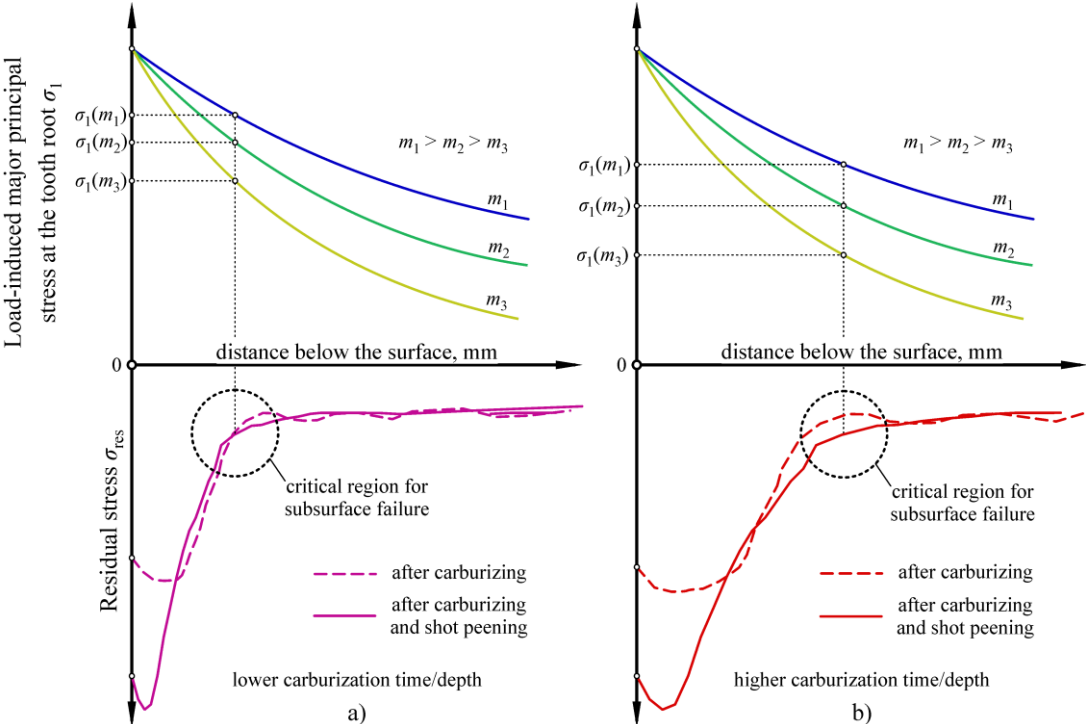
Figure 17. Schematic representation of the critical region for subsurface bending fatigue failure for surface-hardened spur gears with different moduli and carburization depths: a) lower carburization depth, and b) higher carburization depth

As mentioned in the previous section, lowering the gear module increases the gradient of the load-induced stresses, i.e., the stresses are more steeply decreased with the distance below the surface. Consequently, load-induced stresses at the critical region for subsurface failure (the region where a sudden loss of compressive residual stresses occurs) are subsided. This phenomenon is demonstrated in Figure 17a), where typical residual stress profiles after carburizing and additional shot peening are schematically depicted.

Since load-induced stresses gradually decrease with an increase in the distance below the surface, it could be argued that shifting the critical region for the subsurface failure deeper below the surface might reduce the risk of subsurface failure. This can be achieved by increasing the carburization time (which increases the effective case depth [99]) and repeating the shot peening process to induce highly compressive "protective" residual stresses at the surface layer. This process is schematically depicted in Figure 17b).

It should be mentioned that different carburization times/depths will also affect the hardness profiles of the gear's tooth root and, by extension, the obtained fatigue properties via the hardness method. However, only the effect of load-induced and residual stresses on critical location for subsurface fatigue failure is discussed in this section since their combination most significantly affects the probability of subsurface failure (if non-metallic inclusions are not considered) [13, 85, 94].

However, excessively deep effective case depth of the gear decreases its load capacity and stipulates longer carburizing times, thus increasing intergranular oxidation, lowering beneficial surface compressive residual stresses, and decreasing the bending fatigue resistance [100]. Therefore, certain recommendations regarding the effective case depth of gears provided in ISO 6336-5 standard [2] and shown in Figure 18 should be followed.
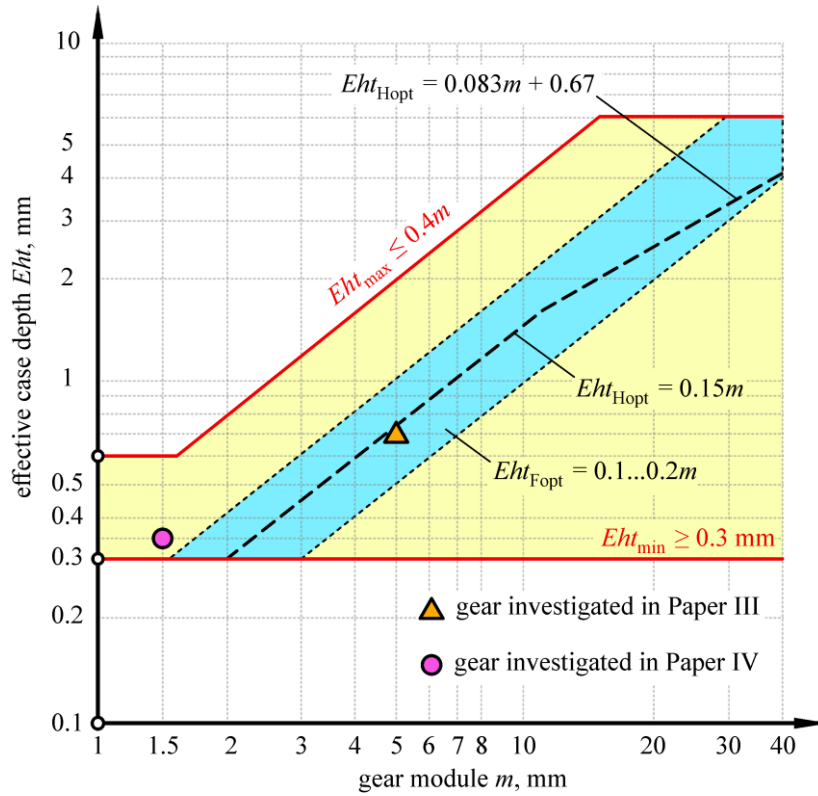
Figure 18. Recommended effective case depths for gears according to ISO 6336-5

In Figure 18, the red lines denoted by Eht_{min} and Eht_{max} represent the recommended minimum and maximum effective case depth limits, respectively. Eht_{Hopt} is the recommended effective case depth to avoid pitting, while Eht_{Fopt} is the recommended effective case depth to avoid tooth root breakage due to *surface-initiated* bending fatigue. As stated in [101], there is currently no industry standard for evaluating the risk of subsurface bending fatigue failure.

In addition, modules and effective case depths of gears investigated in Paper III (STBF tests) and Paper IV (running gear pair) are also shown in Figure 18. Specifically, the gear in Paper III has a module of $m = 5$ mm and is carburized to $Eht = 0.7$ mm, while the gear investigated in Paper IV has a module of $m = 1.5$ mm and is carburized to $Eht = 0.35$ mm. It can be observed that the effective case depth of both gears may be further increased to reduce the risk of subsurface bending fatigue failure (Figure 17) while conforming to the recommended values, i.e., staying inside the shaded (yellow or even blue) zones. The exact increase in the carburization time, the effective case depth, and the corresponding effect on lowering the risk of subsurface bending fatigue failure will be investigated in future work.

4.4 Non-metallic inclusions in surface-hardened spur gears

An unfavorable combination of load-induced stresses, material strength, and residual stresses is not the sole perpetrator of subsurface bending fatigue failure. Non-metallic inclusions (such as aluminum or sulfide oxides) have to be present at critical locations below the surface to promote subsurface bending fatigue failure [13], [31], [85], [94]. In other words, the unfavorable combination of load-induced, material strength, and residual stress profiles without inclusions will likely not cause subsurface failure and vice-versa. Typical non-metallic inclusions in surface-hardened gears are shown in Figure 19 [85].
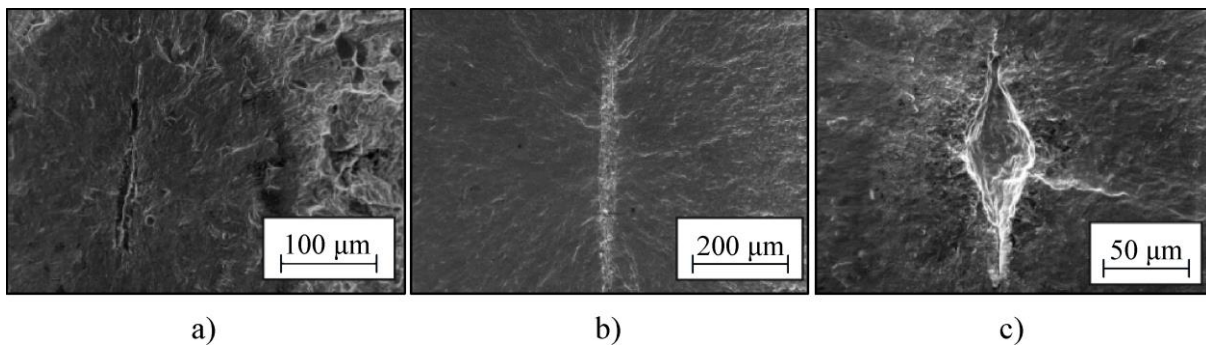
Figure 19. Common non-metallic inclusions found in surface-hardened gears [85]: a) oblong manganese sulfide (MnS) in MnCr-alloyed gear steel, b) oblong aluminum oxide (Al_2O_3) in CrNiMo-alloyed gear steel, and c) spherical Al_2O_3 in CrNiMo-alloyed gear steel

The effect of non-metallic inclusions was not considered within the scope of this thesis. Considering them would require microscopic modeling, whereas the proposed computational model was established on a macro-scale. However, even though the specific number and distribution of non-metallic inclusions were not accounted for, the hardness method was employed to obtain the fatigue properties of different layers. As previously mentioned, the hardness method is an approximation method based on the relatively large number of tested steel specimens [41], each characterized by a different degree of cleanliness (i.e., various numbers and distribution of impurities). Hence, bending fatigue lives and corresponding failure locations obtained by the proposed model accounted for some degree of impurities (and non-metallic inclusions) within the material. However, the effect of specific parameters of non-metallic inclusions, such as their size, shape, location, and distribution, was not considered in this thesis. This topic will be further explored in future investigations.

4.5 Comparison of the proposed computational model with the existing bending fatigue prediction models

In this section, the existing models most closely related to this thesis are discussed and compared against the computational model proposed in this thesis.

Fatigue life prediction of engaging spur gears using power density by Lin et al. [102]

In this work, the authors proposed a numerical model that estimates the required number of cycles for bending fatigue crack initiation and crack propagation based on the power density method. The authors conducted 3D dynamic finite element simulations to obtain tooth root stresses of carburized gears, which were then employed to predict bending fatigue lives. The results were experimentally validated, and good agreement was observed between simulated and actual results. Specifically, the estimated time for bending fatigue crack initiation was approximately 800 hours, while the simulated crack propagation time was an additional 85 hours. Within the experiment, tooth breakage was observed after 1052 hours.

Contrary to the method proposed in this thesis, the authors employed the FE method to directly simulate the dynamic conditions of a running gear pair, whereas a quasi-static simulation modified by the combined factor K_C was employed in this thesis. Moreover, the authors conducted a 3D finite element simulation of a running gear pair, which improves the accuracy of the results. However, the work in [102] does not account for residual stresses at the tooth root, and only surface-initiated bending fatigue failure was observed. Moreover, the simulated results were validated by a single experimental test.

A Computational Simulation of Bending Fatigue in Spur Gear with Profile Modification by Maifi et al. [103]

The work conducted in [103] is similar to the research from [102]. Instead of a running gear pair, a single force acting on the tooth flank was employed to investigate crack initiation and propagation times. Similar to the work conducted in this thesis, the authors employed the strain-life approach to estimate the required number of cycles for bending fatigue crack initiation. Then, they employed linear-elastic fracture mechanics (LEFM), i.e., Paris' law, to simulate the required number of cycles for crack propagation. However, homogenous gear material was assumed, and once again, no residual stress distribution was considered. In other words, only surface bending fatigue crack initiation was assumed.

Bending Fatigue Life Prediction of Spur Gear in Axial Misalignment Condition by Lias et al. [104]

In this paper, the authors investigated the effect of axial misalignment on the bending fatigue lives of gears. The authors employed the FE method by modeling three sets of teeth of spur gears and establishing the contact between them. Only surface bending fatigue failure was assumed, and no residual stresses were considered. The authors concluded that axial misalignment has a negligible effect on the bending fatigue lives of gears.

As demonstrated by the most closely related investigations, no computational model considers variable material strength due to inhomogeneous material, accounts for residual stress profiles, and distinguishes surface from subsurface-initiated bending fatigue cracks in surface-hardened spur gears. However, even though no computational model was found in the relevant literature, it should be mentioned that many *experimental* investigations can be found on both STBF and running gear pairs that explore the surface and subsurface bending fatigue failures in spur gears [13], [84], [94], [98], [101].

5

Conclusions

In this doctoral thesis, a computational model based on the multilayer method was established that predicts the location (both surface and subsurface) and the required number of cycles for bending fatigue crack initiation of surface-hardened spur gears. The proposed model is based on the strain-life approach and the multilayer method. First, the inhomogeneous tooth root region in question was divided into a specific number of homogenous layers according to the multilayer method. Then, the hardness method was employed to obtain the fatigue properties of each layer. Load-induced stresses and strains were obtained via the finite element (FE) method, and residual stresses were assigned to each layer. Bending fatigue lives and failure locations were obtained using different mean stress correction approaches to increase the accuracy of failure location predictions. The predictions were validated against experimental results from the available literature, and good agreement was observed. Lastly, it was observed that only gears that are carburized and additionally shot peened tend to experience subsurface bending fatigue crack initiation. This is mostly attributed to high compressive residual stresses induced via shot peening at the surface that increase the bending fatigue resistance of the surface layer. Consequently, the probably of surface bending fatigue crack initiation is reduced. However, shot peening shifts the critical location for bending fatigue failure to the subsurface, specifically at the region where compressive residual stresses are lowered.

The investigation was initiated on surface-hardened gear steel specimens subjected to a fully reversed bending load (Paper I). Here, the applicability of the rule of mixture (RoM) originally

proposed for composite materials was investigated, and good agreement was observed with experimental data. However, as demonstrated in Chapter 4, this rule was not applicable to spur gears. Hence, it was discarded in further investigations. Due to the relative loading and geometric complexity of spur gears, the FE method was employed in Paper II to predict surface-initiated bending fatigue lives based on the strain-life approach. The main purpose of Paper II was to establish a quasi-static FE model that would be subsequently used in further investigations of subsurface bending fatigue failure. In Paper III, subsurface bending fatigue failure was investigated for the first time on surface-hardened (carburized and additionally shot peened) spur gears in a single tooth bending fatigue (STBF) test. Here, the multilayer method was employed to explore the required number of layers for accurate predictions. Once again, the approach is based on the strain-life method, and good agreement was observed with experimental data, both in failure location and the corresponding number of cycles. Here, it was first observed that subsurface bending fatigue failure tends to occur in carburized and additionally shot-peened gears. Lastly, in Paper IV, the method established in Paper III was upgraded to the running gear pair to simulate actual operating gear conditions more accurately. Moreover, dynamic effects on load-induced stresses and estimated fatigue lives were accounted for by proposing a modification factor. Once again, good agreement was observed between the predicted and experimental results. Thus, the hypothesized computational model was finally established.

Based on the obtained predictions and experimental results from the literature, it can be concluded that carburized and shot-peened spur gears tend to experience subsurface bending fatigue crack initiation at the critical region where beneficial compressive residual stresses are suddenly reduced. Since subsurface bending fatigue failure is typically more dangerous than surface one due to hard detection, some guidelines for reducing the risk of subsurface bending fatigue failure were provided. These guidelines are based on increasing the beneficial compressive residual stresses by increasing the effective case depth of a spur gear or decreasing its module [13, 94].

5.1 Outlook and future work

The established computational model applies to surface-hardened spur gears with relatively low face widths (details can be found in Papers II, III, and IV). However, a 3D FE simulation, which was omitted in this research due to the immense computational costs of a quasi-static simulation of a running gear pair should be carried out for gears with greater

thickness and helical gears to obtain accurate load-induced stresses and strains. Thus, the application of the proposed model to helical gears with necessary corrections will be investigated in the future. It should also be noted that the established computational model has potential applications in other types of surface-hardened machine elements, such as axles.

Furthermore, as demonstrated in Chapter 4, increasing the carburization time or lowering the gear module might reduce the risk of subsurface bending fatigue failure. An additional detailed investigation will also be conducted by observing the influence of the effective case depth and gear module on estimated bending fatigue lives and failure locations (surface vs. subsurface). Lastly, due to averaging errors of the multilayer method, applying a relatively new and popular phase-field modeling approach (i.e., the meshless method) to bending fatigue predictions will be explored. This way, the exact residual stress, and hardness profiles can be assigned instead of averaged ones, thereby reducing the averaging error and increasing the prediction accuracy.

6

References

[1]   B. Jo, S. Sharifimehr, Y. Shim and A. Fatemi, "Cyclic deformation and fatigue behavior of carburized automotive gear steel and predictions including multiaxial stress states," *International Journal of Fatigue,* pp. 454-465, 2017.

[2]   ISO 6336, Calculation of Load Capacity of Spur and Helical Gears*,* 2006.

[3]   DIN 3990 Teil 3, Tragfähigkeitsberechnung von Stirnrädern, Berechnung der Zahnfußtragfähigkeit, Beut Verla*g GMBH,* Berlin, 1987.

[4]   ANSI/AGMA 2001-B88, Fundamental Rating Factors and Calculation Methods for Involute Spur and Helical Gear Teeth*,* Alexandria: American Gear Manufacturing Association, 1990.

[5]   I. Čular, Ciklus naprezanja u korijenu zuba cilindričnog zupčanika s tankim vijencem*, Bachelor's Thesis*, University of Zagreb, Zagreb, 2016.

[6]   I. Čular, Numerička analiza zamora u korijenu zuba cilindričnog zupčanika, *Master's Thesis,* University of Zagreb, Zagreb, 2017.

[7]   K. Vučković, I. Galić and I. Čular, "A Numerical Model for Estimation of Spur Gear Tooth Bending Fatigue Life," in *Proceedings of the 16th International Conference on New Trends in Fatigue and Fracture (NT2F16)*, Zagreb, 2016.

[8]   H. Deng, W. Li, T. Sakai and Z. Sun, "Very High Cycle Fatigue Failure Analysis and Life Prediction of Cr-Ni-W Gear Steel Based on Crack Initiation and Growth Behaviors," *Materials,* vol. 8, pp. 8338-8354, 2015.

[9]   Mechanical Testing and Evaluation, Volume 8*,* ASM International, 2000.

[10]   E. Conrado, C. Gorla, P. Davoli, Boniardi and M, "A comparison of bending fatigue strength of carburized and nitrided gears for industrial applications," *Engineering Failure Analysis,* 2017.

[11]   E. Olsson, A. Olander and M. Oberg, "Fatigue of gears in the finite life regime — Experiments and probabilistic modelling," *Engineering Failure Analysis,* 2016.

[12]   D. Lewicki, Crack Propagation Studies to Determine Benign or Catastrophic Failure Modes for Aerospace Thin-Rim Gears*, Technical Memo,* Cleveland, Ohio, 1996.

[13]   N. Bretl, S. Schurer, T. Tobie, K. Stahl and B. Hohn, "Investigations on Tooth Root Bending Strength of Case Hardened Gears in the Range of High Cycle Fatigue," *Thermal Processing for Gear Solutions,* pp. 52-59, 2014.

[14]   F. Cura, F. Gallo and C. Rosso, "A Study of Fatigue in High Speed Gears," *International Journal of Mechanics and Control,* vol. 14, no. 2, pp. 9-19, 2013.

[15]   P. Kumar, H. Hirani and A. Agrawal, "Fatigue failure prediction in spur gear pair using AGMA approach," *Materials Today: Proceedings,* vol. 4, pp. 2470-2477, 2017.

[16]   G. Gasparini, U. Mariani, C. Gorla, M. Filippini and F. Rosa, "Bending Fatigue Tests of Helicopter Case Carburized Gears: Influence of Material, Design and Manufacturing Parameters," *Gear Technology,* pp. 68-76, 2009.

[17]   T. Lisle, B. Shaw and R. Frazer, "External spur gear root bending stress: A comparison of ISO 6336:2006, AGMA 2101-D04, ANSYS finite element analysis and strain," *Mechanism and Machine Theory,* vol. 111, pp. 1-9, 2017.

[18]   K. Vučković, I. Galić, Ž. Božić and S. Glodež, "Effect of friction in a single-tooth fatigue test," *International Journal of Fatigue,* vol. 114, pp. 148-158, 2018.

[19]   S. Li, "Centrifugal load and its effects on bending strength and contact strength of a high speed thin-walled spur gear with offset web," *Mechanism and Machine Theory,* vol. 43, no. 2, pp. 217-239, 2008.

[20] X. Li, Q. Zhang, N. Wang, Q. Zeng and K. Hidenori, "Meshing Simulation and Strength Calculation of a Carburized Gear Pair," *International Journal of Simulation Modelling,* vol. 16, pp. 121-132, 2017.

[21] D. Liu, Y. Li, Z. Wang, Y. Wang and Y. Wang, "Modeling and Analysis of Effective Case Depth on Meshing Strength of Internal Gear Transmissions," *Computational Methods in Design and Manufacturing Processes,* vol. 2018, 2018.

[22] L. Alban, Systematic Analysis of Gear Failures, Metals Parks, Ohio: American Society for Metals, 1985.

[23] S. Podrug, D. Jelaska and S. Glodež, "Influence of different load models on gear crack path shapes and fatigue lives," *Fatigue & Fracture of Engineering Materials & Structures,* vol. 31, pp. 327-339, 2008.

[24] K. Vučković, Nastanak zamorne pukotine u korijenu zuba zupčanika s tankim vijencem, Zagreb: Doctoral Thesis, 2009.

[25] J. Zhan, M. Fard and R. Jazar, "A quasi-static FEM for estimating gear load capacity," *Measurement: Journal of the International Measurement Confederation,* vol. 75, pp. 40-49, 2015.

[26] X. Dai, C. Cooley and R. Parker, "Dynamic tooth root strains and experimental correlations in spur gear pairs," *Mechanism and Machine Theory,* vol. 101, pp. 60-74, 2016.

[27] I. Perez and A. Aznar, "mplementation of a finite element model for stress analysis of gear drives based on multi-point constraints," *Mechanism and Machine Theory,* vol. 117, pp. 35-47, 2017.

[28] M. Kumar, M. Naveenkumar, D. Gunaskeran and R. Manohar Murali, "Thermal-Stress Analysis and Gearbox Testing of Spur Gear Tooth with Relief Holes," *International Journal of Advanced Research in Basic Engineering Sciences and Technology,* vol. 3, no. 24, pp. 188-195, 2017.

[29] F. Concli, F. Rosa and E. Conrado, "Bending Fatigue Strength of Case Carburized and Nitrided Gear Steels for Aeronautical Applications," *International Journal of Applied Engineering Research,* vol. 12, no. 21, 2017.

[30] D. Manojkumar, K. Sai Sravani and B. Bharghavi, "Comparative Fatigue Life Prediction of Spur Gear Under Fully Reversed Loading by Using Finite Element Analysis," *International Journal of Research in Mechanical Engineering and Technology,* vol. 6, no. 2, pp. 12-17, 2016.

[31] R. Stephens, A. Fatemi, R. Stephens and F. HO, Metal Fatigue in Engineering, 2nd Edition, John Wiley & Sons, inc., 2001.

[32] J. Davis, Gear Materials, Properties and Manufacture, Materials Park, OH: ASM International, 2005.

[33] S. V, B. F and P. Bocher, "Predicting the effects of material properties gradient and residual stresses on the bending fatigue strength of induction hardened aeronautical gears," *International Journal of Fatigue,* vol. 85, pp. 70-84, 2016.

[34] F. Yin and A. Fatemi, "Monotonic and cyclic deformations of case-hardened steels including residual stress effects," *Strain,* vol. 47, pp. 74-83, 2011.

[35] C. Dengo, G. Meneghetti and M. Dabal, "Experimental analysis of bending fatigue strength of plain and notched case-hardened gear steels," *International Journal of Fatigue,* vol. 80, pp. 145-161, 2015.

[36] J. Wang, J. Han, W. Li, Z. Yang, Z. Li and Y. Zhao, "Analytical modelling of shot-peening residual stress on welding carbon steel surface layer," *Journal of Wuhan University of Technology-Mater Sci Ed,* vol. 31, no. 6, pp. 1352-1362, 2016.

[37] N. Gates and A. Fatemi, "Multiaxial variable amplitude fatigue life analysis using the critical plane approach, Part I: Un-notched specimen experiments and Life Estimations," *International Journal of Fatigue,* vol. 105, pp. 283-295, 2017.

[38] A. Baumel and T. Seeger, "The influence of residual stresses and surface strenghtening on components," *Fatigue 90,* vol. 1, pp. 311-316, 1990.

[39] B. Jo, Y. Shim, S. Sharifimehr and A. Fatemi, "Deformation and fatigue behaviors of carburized automotive gear steel and predictions," *Frattura ed Integrità Strutturale,* vol. 37, pp. 28-37, 2016.

[40] F. Yin and A. Fatemi, "Fatigue behaviour and life predictions of case-hardened steels," *Fatigue & Fracture of Engineering Materials & Structures,* vol. 32, no. 3, pp. 197-213, 2009.

[41] M. Roessle and A. Fatemi, "Strain-controlled fatigue properties of steels and some simple approximations," *International Journal of Fatigue,* vol. 22, pp. 495-511, 2000.

[42] S. Nishijima and K. Kanazawa, "Stepwise S-N curve and fish-eye failure in gigacycle fatigue," *Fatigue & Fracture of Engineering Materials & Structures,* vol. 22, no. 7, pp. 601-607, 1999.

[43] A. Shanyavskiy, "Mechanisms and modeling of subsurface fatigue cracking in metals," *Engineering Fracture Mechanics,* vol. 110, pp. 350-363, 2013.

[44] J. Zhang, R. Prasannavenkatesan, M. Shenoy and D. McDowell, "Modeling fatigue crack nucleation at primary inclusions in carburized and shot-peened martensitic steel," *Engineering Fracture Mechanics,* vol. 76, no. 3, pp. 315-334, 2009.

[45] M. Sanchez, M. Pleguezuelos and J. Pedrero, "Approximate equations for the meshing stiffness and the load sharing ratio of spur gears including hertzian effect," *Mechanism and Machine Theory,* vol. 109, pp. 231-249, 2017.

[46] N. Raghuwanshi and A. Parey, "Experimental measurement of gear mesh stiffness of cracked spur gear by strain gauge technique," *Measurement,* vol. 86, pp. 266-275, 2016.

[47] W. Meng, L. Xie, Y. Zhang, Y. Wang, X. Sun and S. Zhang, "Effect of Mean Stress on the Fatigue Life Prediction of Notched Fiber-Reinforced 2060 Al-Li Alloy Laminates under Spectrum Loading," *Advances in Materials Science and Engineering,* vol. Volume 2018, 2018.

[48] V. Gaur, V. Doquet, E. Persent, C. Mareau, E. Roguet and J. Kittel, "Surface Versus Internal Fatigue Crack Initiation in Steel: Influence of Mean Stress," *International Journal of Fatigue,* vol. 82, pp. 437-448, 2015.

[49] S. Li and A. Kahraman, "A micro-pitting model for spur gear contacts," *International Journal of Fatigue,* vol. 59, pp. 224-233, 2014.

[50] W. Dong, Y. Xing, T. Moan and Z. Gao, "Time domain-based gear contact fatigue analysis of a wind turbine drivetrain under dynamic conditions," *International Journal of Fatigue,* vol. 48, pp. 133-146, 2013.

[51] F. Zhao, X. Ding, X. Fan, C. Renjie, Y. Li and T. Wang, "Contact Fatigue Failure Analysis of Helical Gears with Non-Entire Tooth Meshing Tests," *Metals,* vol. 8, no. 9, 2018.

[52] I. Čular, K. Vučković, M. Vukić and M. Rastija, "Optimizing Single Tooth Bending Fatigue Fixture Rigidity for Minimizing the Effect of Friction on Nominal Tooth Root Stress Results," in *5th International Conference on Advances in Mechanical Engineering ICAME 2019*, Istanbul, 2020.

[53] K. Lee and J. Song, "Estimation methods for strain-life fatigue properties from hardness," *International Journal of Fatigue,* vol. 28, pp. 386-400, 2006.

[54] A. Ince and G. Glinka, "A modification of Morrow and Smith–Watson–Topper mean stress correction models," *Fatigue & Fracture of Engineering Materials & Structures,* vol. 34, pp. 854-867, 2011.

[55] R. G. Budynas and J. K. Nisbett, Shigley's Mechanical Engineering Design, vol. 10th Edition, New York city: McGraw-Hill Education, 2015.

[56] R. Peterson, Discussion of a Century Ago Concerning the Nature of Fatigue, and Review of Some of the Subsequent Researches Concerning the Mechanism of Fatigue, ASTM Bull, 1950.

[57] ReliaSoft, "ReliaSoft - Reliability and Maintainability Analysis," [Online]. Available: https://www.reliasoft.com/. [Accessed 23 September 2020].

[58] Y. Liu and T. Ishihara, "Accident of Wind Turbine Tower in Taikoyama Wind Farm," in *EWEA2015*, Paris, 2015.

[59] A. Vasudevan, K. Sadananda and G. Glinka, "Critical parameters for fatigue damage," *International Journal of Fatigue,* vol. 23, pp. 39-53, 2001.

[60] F. Dunne, "Fatigue crack nucleation: Mechanistic modelling across the length scales," *Current Opinion in Solid State and Materials Science,* p. 10, 2014.

[61] P. Forsyth, The Physical Basis of Metal Fatigue, New York: American Elsevier Publishing Co., 1969.

[62] A. S. E606-92, "Standard Practice for Strain-Controlled Fatigue Testing," in *Annual Book of ASTM Standards, Vol 11.03*, ASTM International, 1998.

[63] FE-Safe, Fatigue Theory Reference Manual, Safe Technologies Limited, 2002.

[64] L. Anand and D. Parks, "Defect Free Fatigue - Supplementary notes," Massachusetts Institute of Technology, Cambridge, 2004.

[65] N. Pugno, M. Ciavarella, P. Cornetti and A. Carpinteri, "A generalized Paris' law for fatigue crack growth," *Journal of the Mechanics and Physics of Solids,* vol. 54, pp. 1333-1349, 2006.

[66] D. Roylance, "Fatigue," Department of Materials Science and Engineering, Massachusetts Institute of Technology, Cambridge, MA 02139, 2001.

[67] Wikimedia.org, author: Lokilech (own work). " Ermüdungsbruch meines Fahrradpedalarmes (Kettler Alu-Rad von etwa 1990), hell: der Spröd-, Gewaltbruch, dunkel: der Ermüdungsbruch mit Rastlinien" Testing Methods for JIS Steel Materials," Total Materia, June 13th 2007. [Online]. Available: https://commons.wikimedia.org/wiki/File:Pedalarm_Bruch.jpg#filelinks [Accessed June 9th 2022].

[68] A. Wöhler, "Bericht über die Versuche, welche auf der königlichen Niederschlesischmarkischen Eisenbahn mit Apparaten zum Messen der Biegung und Verdehnung von Eisenbahnwagenachsen wahrend der Fahrt angestellt wurden," *Zeitschrift für Bauwesen,* vol. 8, pp. 641-652, 1858.

[69] C. Bathias, "There is no infinite fatigue life in metallic materials," *Fatigue & Fracture of Engineering Materials & Structures,* vol. 22, pp. 559-565, 2001.

[70] I. d. Silva, A. d. Andrade and W. Monteiro, "Leak-Before-Break methodology applied to different piping materials: a peformance evaluation," *Frattura ed Integrità Strutturale,* vol. 13, no. 50, pp. 46-53, 2019.

[71] S. Suresh, Fatigue of materials, Cambridge: University Press, 1998.

[72] C. Gagg and P. Lewis, "In-service fatigue failure of engineered products and structures," *Engineering Failure Analysis,* vol. 16, pp. 1775-1793, 2009.

[73] Š. Major, Š. Hubalovsky, J. Šedivy and J. Bryscejn, "Fatigue life of carburized steel specimens under push-pull loading," *International Journal of Materials,* vol. 1, pp. 99-104, 2014.

[74]   F. Cura, A. Mura and C. Rosso, "Effect of rim and web interaction on crack propagation paths in gears by means of XFEM technique," *Fatigue & Fracture of Engineering Materials & Structures,* vol. 38, pp. 1237-1245, 2015.

[75]   S. Zouari, M. Maatar and T. Fakhfakh, "Following Spur Gear Crack Propagation in the Tooth Foot by Finite Element Method," *Journal of Failure Analysis and Prevention,* vol. 10, no. 6, pp. 531-539, 2010.

[76]   S. Galande and R. Patil, "Spur Gear Crack Propagation Path Analysis Using Finite Element Method," *International Journal of Mechanical Engineering,* vol. 2, no. 7, 2014.

[77]   F. Cura, A. Mura and C. Rosso, "Influence of high speed on crack propagation path in thin rim gears," *Fatigue and Fracture of Engineering Materials and Structures,* vol. 40, no. 1, pp. 120-129, 2017.

[78]   Z. Chen, W. Zhai, Y. Shao, K. Wang and G. Sun, "Analytical model for mesh stiffness calculation of spur gear pair with non-uniformly distributed tooth root crack," *Engineering Failure Analysis journal,* vol. 66, pp. 502-514, 2016.

[79]   I. Čular, K. Vučković, D. Žeželj and S. Glodež, "Analytical Approach for Low and High Cycle Bending Fatigue Life Prediction," *Engineering Failure Analysis,* vol. 108, 2020.

[80]   R. Landgraf and R. Richman, "Fatigue Behavior of Carburized Steel," *Fatigue of Composite Materials,* vol. ASTM STP 569, pp. 130-144, 1975.

[81]   K. Vučković, I. Čular, R. Mašović, I. Galić and D. Žeželj, "Numerical model for bending fatigue life estimation of carburized spur gears with consideration of the adjacent tooth effect," *International Journal of Fatigue,* vol. 153, 2021.

[82]   Abaqus 6.13, Dassault Systemes, 2013.

[83]   FE-Safe, Dassault Systemes, 2013.

[84]   I. Čular, K. Vučković, S. Glodež and Z. Tonković, "Computational model for bending fatigue prediction of surface hardened spur gears based on the multilayer method," *International Journal of Fatigue,* vol. 161, 2022.

[85]   D. Fuchs, S. Schurer, T. Tobie and K. Stahl, "On the determination of the bending fatigue strength in and above the very high cycle fatigue regime of shot-peened gears," *Forschung im Ingenieurwesen/Engineering Research,* 2021.

[86]   I. Čular, K. Vučković, I. Galić and D. Žeželj, "Computational model for bending fatigue life and failure location prediction of surface-hardened running gears," *International Journal of Fatigue*, vol. 166, 2023.

[87]   G. Glinka, "An analysis of elasto-plastic strains and stresses in notched bodies subjected to cyclic non-propotional loading paths," *European Structural Integrity Society,* vol. 31, no. C, pp. 265-283, 2003.

[88]   A. Fatemi and D. Socie, "A critical plane approach to multiaxial fatigue damage including out-of-phase loading," *Fatigue & Fracture of Engineering Materials & Structures,* vol. 11, no. 3149-165, 1988.

[89]   B. Wang, Y. He, H. Wang, Y. Tian, T. Jia, B. Wang and Z. Wang, "Vacuum Low-pressure Carburization of Gear Steel 16Cr3NiWMoVNbE for Aviation," *Chinese Journal of Materials Research,* vol. 34, no. 1, pp. 35-42, 2020.

[90]   K. Seleš, Numerical phase-field modeling of damage in heterogeneous materials, Zagreb, Croatia: Doctoral Thesis, 2020.

[91]   S. Li, " Effects of centrifugal load on tooth contact stresses and bending stresses of thin-rimmed spur gears with inclined webs," *Mechanism and Machine Theory,* vol. 59, pp. 34-47, 2013.

[92]   R. Martins, J. Seabra, A. Brito, C. Seyfert, R. Luther and A. Igartua, "Friction coefficient in FZG gears lubricated with industrial gear oils: Biodegradable ester vs. mineral oil," *Tribology International,* vol. 39, no. 6, pp. 512-521, 2006.

[93]   B. R. Höhn, K. Michaelis, and A. Doleschel, "Frictional behaviour of synthetic gear lubricants," *Tribol. Ser.*, vol. 39, pp. 759–768, 2001.

[94]   D. Fuchs, S. Schurer, T. Tobie and K. Stahl, "A model approach for considering nonmetallic inclusions in the calculation of the local tooth root load-carrying capacity of high-strength gears made of high-quality steels," *Proceedings of the Institution of Mechanical Engineers, Part C: Journal of Mechanical Engineering Science,* vol. 233, no. 21-22, pp. 7309-7317, 2019.

[95] N. Bugliarello, C. Zimmerman, S. Richardson, R. Perkins, D. McCurdy, D. Giessel and B. George, "Heat Treat Processes for Gears," Gearsolutions, July 2010. [Online]. Available: https://gearsolutions.com/media/uploads/uploads/assets//PDF/Articles/July_10/0710_ Bodycote.pdf. [Accessed 25 May 2022].

[96] C. Peng, Y. Xiao, Y. Wang and W. Guo, "Effect of laser shock peening on bending fatigue performance of AISI 9310 steel spur gear," *Optics and Laser Technology,* vol. 94, pp. 15-24, 2017.

[97] K. Miyachika, W. Xue, T. Koide, H. Mada, K. Nojima, S. Oda and H. Katanuma, "Residual stress and bending fatigue strength of case-carburized thin-rimmed spur gears with asymmetric web arrangement," in *2007 Proceedings of the ASME International Design Engineering Technical Conferences and Computers and Information in Engineering Conference, DETC2007*, 2008.

[98] C. Guntner, T. Tobie and K. Stahl, "Influences of the Residual Stress Condition on the Load-Carrying Capacity of Case-Hardened Gears," *GearTechnology,* pp. 60-69, 2018.

[99] R. Rego, J. Lopenhaus, J. Gomes and F. Klocke, "Residual stress interaction on gear manufacturing," *Journal of Materials Processing Technology,* vol. 252, pp. 249-258, 2018.

[100] R. Errichello and A. Milburn, "Optimum carburized and hardened case depth," *AGMA 2019 Fall Technical Meeting, FTM 2019,* pp. 58-65, 2019.

[101] K. Winkler, S. Schurer, T. Tobie and K. Stahl, "Investigations on the tooth root bending strength and the fatigue fracture characteristics of case-carburized and shot-peened gears of different sizes," *Proceedings of the Institution of Mechanical Engineers, Part C: Journal of Mechanical Engineering Science,* vol. 233, no. 21-22, pp. 7338-7349, 2019.

[102] Y. Lin, S. Liu, X. Zhao, E. Mao, C. Cao and C. Suh, "Fatigue life prediction of engaging spur gears using power density," *Proceedings of the Institution of Mechanical Engineers, Part C: Journal of Mechanical Engineering Science,* vol. 0, no. 0, 2018.

[103] T. Maifi, R. Bourenane and R. Khelif, "A Computational Simulation of Bending Fatigue in Spur Gear with Profile Modification," *Rev. Sci. Technol., Synthèse,* vol. 37, no. 2018, pp. 209-221, 2018.

[104] M. Lias, M. Isa and A. Ahmad, "Bending Fatigue Life Prediction of Spur Gear in Axial Misalignment Condition," *IOP Conference Series: Materials Science and Engineering,* vol. 864, no. 1, 2020.

Curriculum Vitae

Ivan Čular was born on March 11th, 1993, in Šibenik, Croatia. He finished elementary school in Vodice, Croatia, and obtained a high school diploma from Brussels American School in Brussels, Belgium. He acquired his Bachelor's Degree from the University of Zagreb, Faculty of Mechanical Engineering and Naval Architecture in 2016, followed by his Master's Degree from the same faculty in 2017. Since then, he has been employed as a research assistant and Ph.D. candidate at the aforementioned Faculty, Department of Design, specializing in engineering design, machine elements, and numerical simulations. He is a member of the Croatian Society for Mechanics and an author of 16 papers, six of which were published in scientific journals indexed in the Web of Science.

List of publications:

1. Čular, Ivan; Vučković, Krešimir; Galić, Ivica; Žeželj, Dragan. Computational model for bending fatigue life and failure location prediction of surface-hardened running gears // *International Journal of Fatigue*, 166 (2023), 107300, 13, doi: 10.1016/j.ijfatigue.2022.107300.

2. Trumbić, Niko; Strelec, Ian; Čular, Ivan; Vučković, Krešimir. Multi-parameter Weight and Efficiency Optimization of a Cylindrical Gear Pair without Standard Basic Rack Geometry Limitations // *Proceedings of the 10th International Congress of Croatian Society of Mechanics* / Skozrit, Ivica; Sorić, Jurica; Tonković, Zdenko (ed.). Zagreb: Croatian Society of Mechanics, 2022. pp. 267-268.

3. Čular, Ivan; Vučković, Krešimir; Glodež, Srečko; Tonković, Zdenko. Computational Model for Bending Fatigue Prediction of Surface Hardened Spur Gears Based on the Multilayer Method // *International Journal of Fatigue*, 161 (2022), 106892, 16 doi: 10.1016/j.ijfatigue.2022.106892.

4. Mašović, R.; Breški, T.; Čular, I.; Vučković, K.; Žeželj, D. Numerical Model for Worm Gear Pair Inspection Based on 3D Scanned Data // *International Journal of Simulation Modelling*, 20 (2021), 4; 637-648 doi:10.2507/ijsimm20-4-573.

5. Mašović, Robert; Čular, Ivan; Vučković, Krešimir; Žeželj, Dragan; Breški, Tomislav. Gear Geometry Inspection Based on 3D Optical Scanning: Worm Wheel Case Study // 12th International Conference on Mechanical and Aerospace Engineering (ICMAE) /

Agarwal, Ramesh K. (ed.). Athens, Greece: IEEE, 2021. pp. 262-268 doi:10.1109/ICMAE52228.2021.9522366.

6. Vučković, Krešimir; Čular, Ivan; Mašović, Robert; Galić, Ivica; Žeželj, Dragan. Numerical model for bending fatigue life estimation of carburized spur gears with consideration of the adjacent tooth effect // *International Journal of Fatigue*, 153 (2021) (2021), 106515, 13 doi: 10.1016/j.ijfatigue.2021.106515.

7. Mašović, Robert; Čular, Ivan; Miler, Daniel; Žeželj, Dragan. Case-hardened steel surface texturing by employing electropolishing process // *Zbornik radova Desetog susreta Hrvatskog društva za mehaniku* / Damjanović, Darko; Kozak, Dražen; Konjatić, Pejo; Katinić, Marko (ed.). Slavonski Brod, 2020. pp. 157-162.

8. Miler, Daniel; Čular, Ivan; Hoić, Matija; Žeželj, Dragan. Polymer gear optimisation // *Zbornik radova Desetog susreta Hrvatskog društva za mehaniku* / Damjanović, Darko; Kozak, Dražen; Konjatić, Pejo; Katinić, Marko (ed.). Slavonski Brod, 2020. pp. 163-168.

9. Galić, Ivica; Vučković, Krešimir; Tonković, Zdenko; Čular, Ivan. Numerical simulation of initiation and crack growth on cast valve body // *Engineering failure analysis*, 117C, (2020), 104793, 19 doi: 10.1016/j.engfailanal.2020.104793.

10. Čular, Ivan; Vučković, Krešimir; Žeželj, Dragan; Glodež, Srečko. Analytical approach for low and high cycle bending fatigue life prediction of carburized gear steel specimens //*Engineering failure analysis*, 108 (2020), 104328, 12 doi: 10.1016/j.engfailanal.2019.104328.

11. Čular, Ivan; Vučković, Krešimir; Vukić, Mislav; Rastija, Marko. Optimizing single tooth bending fatigue fixture rigidity for minimizing the effect of friction on nominal tooth root stress results // *Proceedings Book of 5th International Conference on Advances in Mechanical Engineering*: ICAME 2019. Istanbul, 2019. pp. 964-972.

12. Vukic, M; Čular, I; Mašović, R; Vučković, K. Effect of friction on nominal stress results in a single tooth bending fatigue test // *IOP conference series. Materials science and engineering*, 659 (2019), 1; 012004, 8 doi:10.1088/1757-899x/659/1/012004.

13. Galić, Ivica; Čular, Ivan; Vučković, Krešimir; Tonković, Zdenko. Comparison of SIF solutions obtained by XFEM and conventional FEM for cracks in complex geometries like valve body // *Procedia Structural Integrity*, 13 (2018), 2109-2113.

14. Čular, Ivan; Vučković, Krešimir; Miler, Daniel; Žeželj, Dragan. Numerical Bending Fatigue Analysis of a Surface Hardened Spur Gears // *Proceedings of the 18th International Conference on New Trends in Fatigue and Fracture* / Reis, Luis; Freitas, Manuel; Anes, Vitor (ed.). Lisbon: Instituto Superrior Técnico, 2018. pp. 55-58.

15. Vučković, Krešimir; Čular, Ivan; Risović, Stjepan. Effects of Finite Element Type, Mesh Size and Friction on Spur Gear Nominal Tooth Root Stress Results // *Proceedings of the 3rd International Scientific Conference" Conference on Mechanical Engineering Technologies and Applications*" COMETa, 2016. / Marković, Biljana; Antunović, Ranko (ed.). University of East Sarajevo Faculty of Mechanical Engineering East Sarajevo, 2016. pp. 185-190.

16. Vučković, Krešimir; Galić, Ivica; Čular, Ivan. A Numerical Model for Estimation of Spur Gear Tooth Bending Fatigue Life // *Proceedings of the 16th International Conference on New Trends in Fatigue and Fracture* (NT2F16) / Željko Božić, Milan Vrdoljak (ed.). Zagreb, 2016.

Appendix

Paper I

The manuscript shown within this thesis is published in:
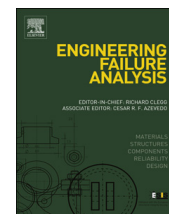
Contributions of the Ph.D. candidate:

- developing the analytical model
- validating the model against experimental data
- interpreting and discussing the results
- writing the manuscript

ELSEVIER

Analytical approach for low and high cycle bending fatigue life prediction of carburized gear steel specimens

I. Čular[a], K. Vučković[a,*], D. Žeželj[a], S. Glodež[b]

[a] University of Zagreb, Faculty of Mechanical Engineering and Naval Architecture, I. Lučića 5, 10000 Zagreb, Croatia
[b] University of Maribor, Faculty of Mechanical Engineering, Smetanova ulica 17, 2000 Maribor, Slovenia

ABSTRACT

Bending fatigue is one of the most common failure modes in spur gears. In carburized spur gears, subsurface failure initiation is characteristic for the high cycle fatigue regime, which is rather hard to detect and may cause rapid crack growth and complete failure of the tooth. Experimental testing of specimens made of the same material under comparable loading conditions is often used to gain insight into actual fatigue behavior of the component. Furthermore, in the absence of definite fatigue data of the specimens, various methods are used for estimating fatigue parameters. In this paper, analytical model for bending fatigue life prediction of carburized gear steel specimens based on strain-life approach is proposed. Multilayer method and hardness method are used for estimating strain-life fatigue properties. Rule of mixture is employed to find average cyclic stress-strain curves of carburized specimens. An approach for conversion of axial to bending fatigue data by utilizing Neuber's rule and modifying factors is suggested. Initial validation of the analytical model is carried out against experimental results from the literature of two types of specimens with different carburizing depths. Good correlation between the predicted and experimental data is observed for both types of specimens, with nearly all data points falling within the scatter factor of three.

1. Introduction

During gear meshing, a change in stress values in the tooth root region is observed. Since tooth meshing occurs once per full rotation of the gear, the stresses in the tooth root region are also cyclic. The aforesaid results in bending fatigue of the gear which may subsequently cause tooth root fatigue failure. Industrial application spur gears are often carburized. Consequently, surface wear resistance is enhanced, while induced compressive residual stresses can affect bending fatigue life. In carburized spur gears, besides the surface, a subsurface failure can also initiate [1] in the high cycle fatigue (HCF) regimes, which is often difficult to detect. In low cycle fatigue (LCF), loss of beneficial compressive residual stresses to relaxation can result in critical brittle case region. To prevent crack initiation, sudden growth and possible complete failure of the tooth, it is necessary to adequately predict the location and number of cycles required for bending fatigue failure of carburized gears. Test specimens made of typical gear steel, which can be additionally surface hardened through carburizing, are frequently used in fatigue studies and can produce beneficial fatigue data which can be used to predict bending fatigue behavior of spur gears [2,3].

There are many investigations where axial, bending or torsional fatigue is studied by employing case hardened gear steel specimens. Genel and Demirkol [4] studied the effect of case depth on bending fatigue behavior of AISI 8620 carburized gear steel. They

Nomenclature

A_{case}	cross-section area of carburized layer
A_{core}	cross-section area of core layer
A_S	total cross-section area of carburized specimen
b	fatigue strength exponent
C^*	correction factor accounting for type of loading and miscellaneous effects
C_D	modifying factor for the specimen size
C_L	modifying factor for the type of loading
C_R	modifying factor for reliability
C_S	modifying factor for the surface finish factor
c	fatigue ductility exponent
E	modulus of elasticity
K'	cyclic strength coefficient
K_f	fatigue notch factor
k_d	temperature modification factor
k_f	miscellaneous-effects modification factor
N_f	number of cycles until failure
$N_{f\ case}$	number of cycles until failure for case layer
$N_{f\ core}$	number of cycles until failure for core layer
n'	cyclic strength exponent
S_{ax}	fatigue limit for axial loading
S_{be}	fatigue limit for bending loading
S_{max}	maximum nominal stress
$\Delta\varepsilon_e$	elastic strain range
$\Delta\varepsilon_p$	plastic strain range
$\Delta\varepsilon^{be}$	true strain range for bending loading
$\Delta\sigma^{be}$	true stress range for bending loading
ΔS	nominal stress range
X_e	modification factor for elastic strain amplitude
X_p	modification factor for plastic strain amplitude
ε_a	total strain amplitude
ε_a^{ax}	total strain amplitude for axial loading
ε_a^{be}	total strain amplitude for bending loading
ε_{max}^{ax}	maximum true strain for axial loading
ε_{max}^{be}	maximum true strain for bending loading
ε_{min}^{be}	minimum true strain for bending loading
ε_f'	fatigue ductility coefficient
σ_a	true stress amplitude
σ_{avg}	average stress due to external load
σ_{case}	case layer stress
σ_{core}	core layer stress
σ_m	mean cyclic stress
σ_{max}	maximum true stress
σ_{max}^{ax}	maximum true stress for axial loading
σ_{max}^{be}	maximum true stress for bending loading
σ_{min}^{be}	minimum true stress for bending loading
σ_{res}	residual stress
σ_f'	fatigue strength coefficient

performed rotary bending fatigue tests of different case depth carburized specimens to simulate actual spur gear working conditions and concluded that a power model can be used to represent the relationship between case depth and bending fatigue behavior within the testing limits of the study. Strain-controlled uniaxial fatigue tests on Cr-Mo alloy steel under various load ratios were carried out by Gaur et al. [5]. The authors found that the fatigue lives of test specimens decreased as the load ratio increased. Liu et al. [6] investigated fatigue properties of uniaxially loaded carburized 20Cr gear steel. The authors observed that the dominant fracture mode in the high cycle fatigue region is subsurface crack initiation (commonly known as the fish-eye). Furthermore, Li et al. [7] also conducted axial fatigue tests of carburized low alloy Cr-Ni gear steel and observed that failures initiated at the subsurface level with different location sites are directly related to low and high cycle fatigue regions.

Further investigation on Cr-Ni gear steel was done by Deng et al. [8], who studied the effect of mean stress during axial loading on high cycle fatigue behavior. Dengo et al. [9] performed fatigue tests on two gas-carburized gear steels using plain and notched specimens under bending and axial loading conditions. They concluded that the case-hardening process results in a significant loss of ductility in the case region and that almost all fatigue failures originated from the surface of the specimen. Moreover, the authors indicated that ground specimens lost the beneficial fatigue behavior effect due to relatively high compressive residual stresses at the surface. Deng et al. [10] studied very high cycle fatigue (VHCF) behavior of Cr-Ni-W gear steel under fully reversed axial loading. The authors proposed VHCF prediction model which showed good agreement with the experimental results. They also observed that the predicted crack growth life in VHCF is almost negligible compared to crack initiation life, which is in accordance with material fatigue behavior in high and very high cycle fatigue regions. John et al. [11] used three-point bending fatigue tests to compare performance of four different gear steel materials, all of them subjected to the same manufacturing and carburizing processes. The authors suggested that the process of carburization and the resulting residual stresses are more important than the chemical composition of steel itself. Spice et al. [12] studied different surface hardening techniques to improve bending fatigue life of SAE 8620 steel. They concluded that shot peening process following carburization considerably increases bending fatigue life. Furthermore, the authors observed that vacuum carburized specimens showed no improvement in the high cycle fatigue region. Liu et al. [13] conducted rotary bending fatigue tests of two different carburized steels and concluded that steels with higher content of aluminum and nitrogen microalloying elements show better bending fatigue properties. In addition to carburizing, other surface hardening processes such as nitriding are also used [14] to improve bending fatigue behavior of steels.

In the absence of specimen or gear fatigue data, multilayer method [15] is often used in combination with various estimation methods [16] to predict fatigue behavior. Troshchenko and Khamaza [17] compared Basquin-Coffin-Manson fatigue parameters with those calculated by the conventional prediction methods. They demonstrated that Roessle - Fatemi hardness method [18] and the Muralidharan-Manson [19] modified universal slopes method provide relatively better results when compared to other conventional methods. Kim et al. [20] conducted uniaxial and torsional fatigue tests on different steel specimens and evaluated various methods for estimating uniaxial fatigue properties from tensile properties or material hardness. They found that the modified universal slopes method, uniform material law [21] and the hardness method predicted over 93% of test cases within the scatter factor of three when compared with the observed lives for both uniaxial and torsional loading tests. Ince and Glinka [22] proposed modified Morrow [23]

and Smith-Watson-Topper [24] mean stress correction model and applied it to fatigue life prediction of AISI 1045 and ASTM A723 steel specimens. The modified model was found superior to both SWT and Morrow models for fatigue life predictions of the latter material. The aforesaid is of particular importance to carburized gears and gear specimens, considering the typical state of load induced stresses and residual stress occurring in the tooth root region. Experimental and analytical investigation of deformation behavior of carburized gear steels under axial and torsional loading was conducted Jo et al. [25]. The authors concluded that the results obtained by using the strain-life approach in conjunction with the von Mises effective stress/strain criteria and multilayer method provided good fatigue behavior predictions. Yin and Fatemi [26] experimentally and analytically investigated fatigue behavior of carburized steels under fully reversed strain-controlled uniaxial loading. The authors used multilayer method and experimentally acquired low cycle fatigue parameters for simulated case and core regions of the specimen to predict the location and number of cycles required for fatigue crack initiation. They observed that surface crack initiation is characteristic for short life regime, while subsurface crack initiation occurs in the HCF regime. Moreover, a four-layer model combined with Smith-Watson-Topper parameter provided good predictions regarding the crack nucleation location. The aforesaid process of simulating carburized specimen's fatigue behavior is carried out through additional testing of higher and lower carbon content materials and their fatigue parameters are applied to case and core regions of the specimen, respectively. It is a common approach in estimating fatigue life of surface-hardened specimens. Finally, rule of mixture (RoM), which was originally developed for composite materials, is often applied when investigating fatigue behavior of carburized specimens with composite-like behavior, due to different material properties within single specimen [27].

During literature review, it was found that most of the studies deal with fatigue of carburized specimens under axial or torsional loading. On the other hand, bending fatigue investigations are focused on high cycle bending fatigue, where predominantly linear elastic material behavior is present. In this paper, analytical model for predicting bending fatigue behavior of carburized gear steel specimens in low and high cycle fatigue regimes, based on strain-life approach, RoM, multilayer and hardness method is proposed. Multilayer and hardness method are employed for estimating strain-life fatigue properties of corresponding material layers. RoM is employed to obtain average cyclic stress-strain curves for carburized specimens. An approach for conversion of axial to bending fatigue strain-life properties through Neuber's rule and modifying factors is suggested. Prediction results for bending fatigue lives and failure location sites are compared with the available experimental data from the literature.

2. Analytical model

2.1. Axial fatigue life

Strain-life approach (ε-N) is employed to predict axial fatigue life and failure location of a carburized specimen. The relation of the total strain amplitude, ε_a, and the fatigue life can be expressed by the Basquin- Coffin-Manson equation:

$$\varepsilon_a = \frac{\Delta\varepsilon_e}{2} + \frac{\Delta\varepsilon_p}{2} = \frac{\sigma_f'}{E}(2N_f)^b + \varepsilon_f'(2N_f)^c \tag{2.1}$$

where $\Delta\varepsilon_e$ and $\Delta\varepsilon_p$ are elastic and plastic strain range, respectively, σ_f' is the fatigue strength coefficient, E is the elasticity modulus, N_f is the number of reversals until failure, b is the fatigue strength exponent, ε_f' is the fatigue ductility coefficient and c is the fatigue ductility exponent. Basquin-Coffin-Manson equation can be modified by Morrow's mean stress method [23] to account for mean, σ_m, and residual stresses, σ_{res}:
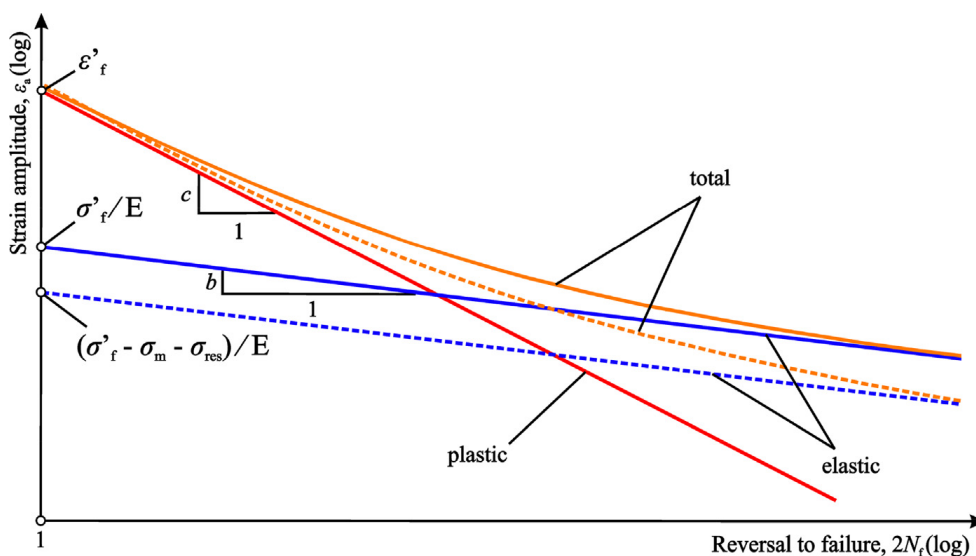

Fig. 1. Schematic representation of Morrow's mean and residual stress correction.

$$\varepsilon_a = \frac{(\sigma_f' - \sigma_m - \sigma_{res})}{E}(2N_f)^b + \varepsilon_f'(2N_f)^c \tag{2.2}$$

Basquin-Coffin-Manson relation with Morrow's mean and residual stress correction is schematically depicted in Fig. 1.

Given that carburized specimens are comprised of case and core layer with different corresponding material properties, multilayer method [15] is used for axial fatigue life predictions. Therefore, cross section of the specimen is divided in case and core layer. Case layer is defined from the surface of the specimen to the effective case depth. Core layer is defined from the effective case depth to midpoint of specimen's thickness. For both layers, uniform hardness and residual stress profiles are applied by averaging measured values.

When predicting fatigue behavior of carburized steels, a common approach consists of obtaining fatigue properties for the materials simulating case and core regions [26]. However, when such parameters are not available, other estimation methods for strain-life fatigue properties can be used [28]. In this paper, hardness method [18] is used to estimate strain-life fatigue properties of case and core layers:

$$\sigma_f' = 425HB + 225 \tag{2.3}$$

$$\varepsilon_f' = \frac{0.32(HB)^2 - 487(HB) + 191000}{E} \tag{2.4}$$

$$b = -0.56 \tag{2.5}$$

$$c = -0.09 \tag{2.6}$$

where HB is averaged Brinell hardness for each layer. Hence, according to Basquin-Coffin-Manson equation and fatigue properties obtained through Eqs. (2.3) to (2.6), while accounting for mean and residual stresses, two strain-life curves representing case and core layer axial fatigue behavior are obtained. For given total strain amplitude, layer with the inferior fatigue life is designated as critical and corresponding fatigue life is found.

2.2. Bending fatigue life

When obtaining bending fatigue limit from axial fatigue and vice-versa, typically four modifying factors are used [29]: modifying factor for the type of loading, C_L, surface finish, C_S, size, C_D and reliability C_R. Furthermore, additional modifying factors can be employed, such as temperature modification factor, k_d, and miscellaneous-effects modifying factor, k_f [30]. With an extension of factors k_f and k_d, bending fatigue limit is then estimated as:

$$S_{be} = \frac{S_{ax}}{C_L C_S C_D C_R k_d k_f} \tag{2.7}$$

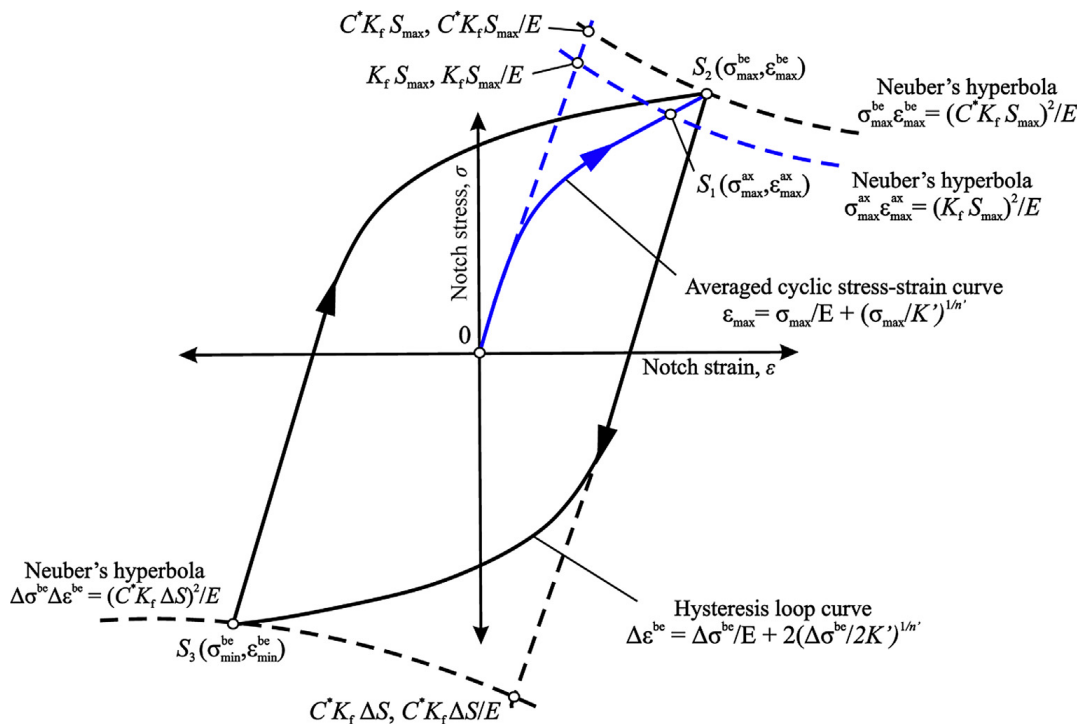Correction factor, C^* is employed to account for the combined effect of the modifying factors:

Fig. 2. Schematic representation of Neuber's rule for fully reversed loading accounting for C^*.

$$C^* = C_L C_S C_D C_R k_d k_f \tag{2.8}$$

Since test specimens are usually finely polished and their comparative size is relatively similar, the effect of surface finish and size modifying factors is assumed as negligible. The effect of reliability factor is not discussed within this research, while room temperature and absence of miscellaneous effects is presumed. In other words:

$$C_S = C_D = C_R = k_d = k_f = 1 \tag{2.9}$$

According to Eqs. (2.8) and (2.9), $C^* = C_L$. Modifying factor for the type of loading, C_L, typically varies from 0.7 for unnotched components under cyclic axial loading with slight bending to 0.9 for unnotched components under pure cyclic axial loading [29]. Correction factor, C^* is then employed to obtain bending fatigue limit, S_{be}, from axial fatigue limit, S_{ax}, for given fatigue life [29]:

$$S_{be} = \frac{S_{ax}}{C^*} \tag{2.10}$$

This value is defined for the fatigue limit or, when fatigue limit is not evident, for 10^6 load cycles [25]. Correction factor is provided for high cycle fatigue regimes where stress-strain relations are predominantly described by Hooke's law and as such it can be directly applied for stress-life (S-N) method [27]. However, it is not directly applicable for strain-life approach, which is used in this paper for bending life predictions of carburized specimens. Hence, an approach of estimating the ratio of total strain amplitude for axial fatigue loading, ε_a^{ax}, and total strain amplitude for bending fatigue loading, ε_a^{be}, in low cycle fatigue is suggested. Correction factor C^* is used in conjunction with elastoplastic correction by Neuber's rule [31]. It should be noted that elastoplastic correction is typically used for estimating true stress and strain values from linear elastic data [32]. Since C^* is directly related to nominal stresses (Eq. (2.10)), Neuber's rule is used in a reversed manner, i.e. to obtain linear elastic data from true stress and strain values (Fig. 2).

In order to employ elastoplastic correction according to Neuber's rule, averaged cyclic stress-strain curve for carburized specimen is obtained. Cyclic stress-strain curves for case and core layers of carburized specimens can be described by Ramberg-Osgood relation

$$\varepsilon_a = \frac{\sigma_a}{E} + \left(\frac{\sigma_a}{K'}\right)^{\frac{1}{n'}} \tag{2.11}$$

where σ_a is true stress amplitude, K' is cyclic strength coefficient and n' is cyclic strength exponent. According to [33], K' and n' can be roughly estimated as

$$K' = \frac{\sigma_f{}'}{(\varepsilon_f{}')^{n'}} \tag{2.12}$$

$$n' = \frac{b}{c} \tag{2.13}$$

Hence, cyclic stress-strain relations for case and core layers of carburized specimen are obtained. Next, RoM is employed to average stress values within the carburized specimen with regard to cross section surface area representation of case and core materials. According to RoM based on equilibrium conditions [27], average stress due to external load, σ_{avg}, for carburized specimens is equal to

$$\sigma_{avg} = \sigma_{case}\left(\frac{A_{case}}{A_S}\right) + \sigma_{core}\left(\frac{A_{core}}{A_S}\right) \tag{2.14}$$

where σ_{case} represents stress in the case layer, σ_{core} represents stress in the core layer, A_{case} is the cross-section area of carburized layer
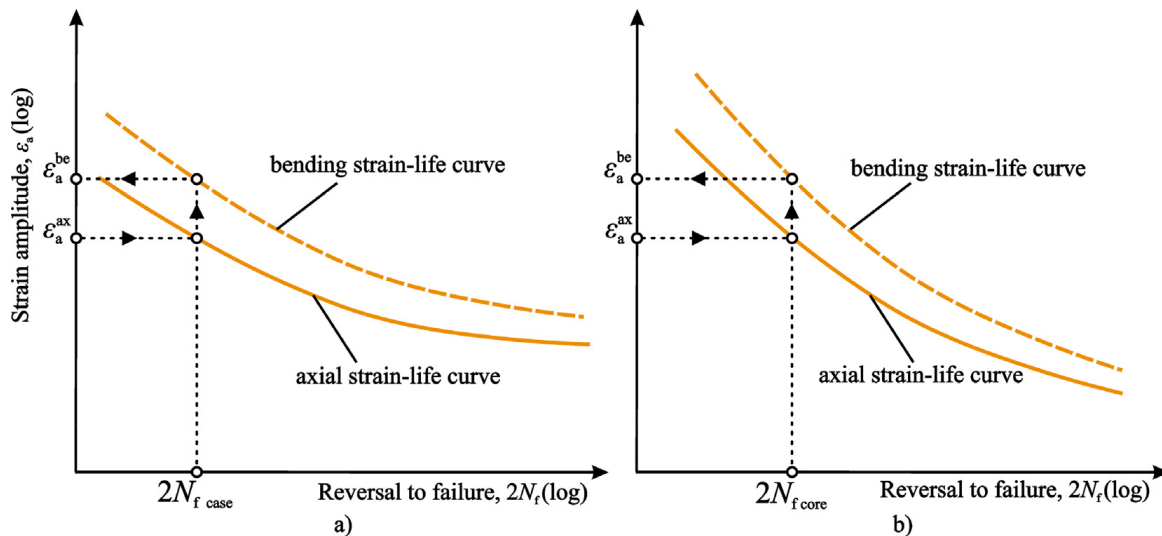

Fig. 3. Schematic representation of bending strain-life curve estimation for: (a) case layer and (b) core layer.

with respect to the effective case depth, A_{core} is the remaining cross-section area of the specimen and A_S is the total cross-section area of the specimen, such that

$$A_S = A_{case} + A_{core} \tag{2.15}$$

By substituting σ_{avg} from Eq. (2.14) for σ_a in Eq. (2.11), averaged cyclic stress-strain curve (Fig. 2) is obtained for carburized specimen. Total strain amplitude used for bending fatigue life predictions accounting for C_L is then obtained through Neuber's rule. The process is schematically depicted in Fig. 2 for fully reversed loading.

First, maximum nominal stress, S_{max}, is found from the intersection point, S_1, between averaged cyclic stress-strain curve of carburized specimen and Neuber's hyperbola for axial loading. Then, C^* is applied according to Eq. (2.10) to account for bending loading. By intersecting averaged cyclic stress-strain curve and Neuber's hyperbola for bending loading at S_2, new values of maximum true stress and strain accounting for bending loading, σ_{max}^{be} and ε_{max}^{be}, are obtained. Under assumption of Massing-type behavior [34], minimum true stress and strain, σ_{min}^{be} and ε_{min}^{be}, are acquired by intersecting hysteresis loop curve with Neuber's hyperbola for bending loading at S_3. Thus, new values for true stress and strain with consideration of C^* are obtained. Total strain amplitude used for bending fatigue life predictions, ε_a^{be}, is then equal to:

$$\varepsilon_a^{be} = \frac{\varepsilon_{max}^{be} + \varepsilon_{min}^{be}}{2} \tag{2.16}$$

For arbitrarily chosen total strain amplitude for axial loading, ε_a^{ax}, total strain amplitude for bending loading, ε_a^{be}, for given fatigue life, $2N_f$, is obtained. The procedure is repeated for different values of ε_a^{ax} and strain- life curve for bending fatigue prediction is estimated according to Eq. (2.2). This is schematically depicted in Fig. 3 for strain-life curves of case and core layers of carburized specimen.

Here, it is suggested that strain-life fatigue properties obtained from hardness according to Eqs. (2.3) to (2.6), as well as residual and mean stresses for the corresponding layer are kept constant, while elastic and plastic strain amplitudes are modified by factors X_e and X_p, respectively:

$$\varepsilon_a^{be} = X_e \frac{(\sigma_f' - \sigma_m - \sigma_{res})}{E}(2N_f)^b + X_p\varepsilon_f'(2N_f)^c \tag{2.17}$$

where X_e and X_p are estimated such that best fit is obtained for bending strain-life curve (Fig. 3) with respect to ε_a^{be} and the corresponding bending fatigue life, $2N_f$. Modified strain-life curves representing case and core layer fatigue behavior accounting for bending loading are then used to predict bending fatigue lives. The layer with lower bending fatigue life for given total strain amplitude is designated as critical and corresponding number of cycles for fatigue failure is recorded.

3. Validation of the analytical model

Experimental results from [35] are used to validate the analytical model. Test specimens were made of low carbon alloy steel commonly used for carburized gears in automotive applications [36], designated as AISI 4027. Specimens had uniform rectangular test cross section measuring 9.5 mm in height and 12.7 mm in width. Two types of specimens with different case depths are considered. Designation of the specimen, its nominal and effective case depths, and heat treatment processes are listed in Table 1.

Measured and applied hardness profiles for both type A and type B specimen, along with the corresponding case and core layer distributions, are shown in Fig. 4.

Strain-life fatigue properties estimated through hardness method for each specimen type and its corresponding layers are presented in Table 2. For the purposes of the hardness method, cross-sectional Vickers hardness of the test specimens is converted to Brinell hardness according to the conversion tables provided in [37].

Residual stress profile for type B specimen is acquired from [35]. However, residual stress profile for type A specimen was not provided in the literature, so it is approximated based on Vickers hardness and Eqs. (3.1) and (3.2) [38].

$$\sigma_{res} = -1.25(HV - HV_{core}),\ MPa \quad for\ (HV - HV_{core}) \leqslant 300 \tag{3.1}$$

$$\sigma_{res} = 0.2857(HV-HV_{core}) - 460,\ MPa \quad for\ (HV-HV_{core}) > 300 \tag{3.2}$$

Analogous to the hardness profile, uniform residual stress value is applied per layer by averaging measured residual stress profile

Table 1
Designation, nominal and effective case depth, and heat treatments of the specimens [35].

| Designation	Nominal case depth	Effective case depth (at 550 HV)	Heat treatment	Carburizing treatment		
Type A	0.4 mm	0.7 mm	austenitize: ~ 850–900 °C 30 min, oil quench temper: ~ 180 °C, 1 h	~ 900 °C, endothermic atmosphere	approx. 1 h	cool to: ~ 850 °C, oil quench; temper: ~ 180 °C, 1 h
Type B	0.9 mm	1.5 mm	austenitize: ~ 850–900 °C 30 min, oil quench temper: ~ 180 °C, 1 h	~ 900 °C, endothermic atmosphere	approx. 5 h	cool to: ~ 850 °C, oil quench; temper: ~ 180 °C, 1 h
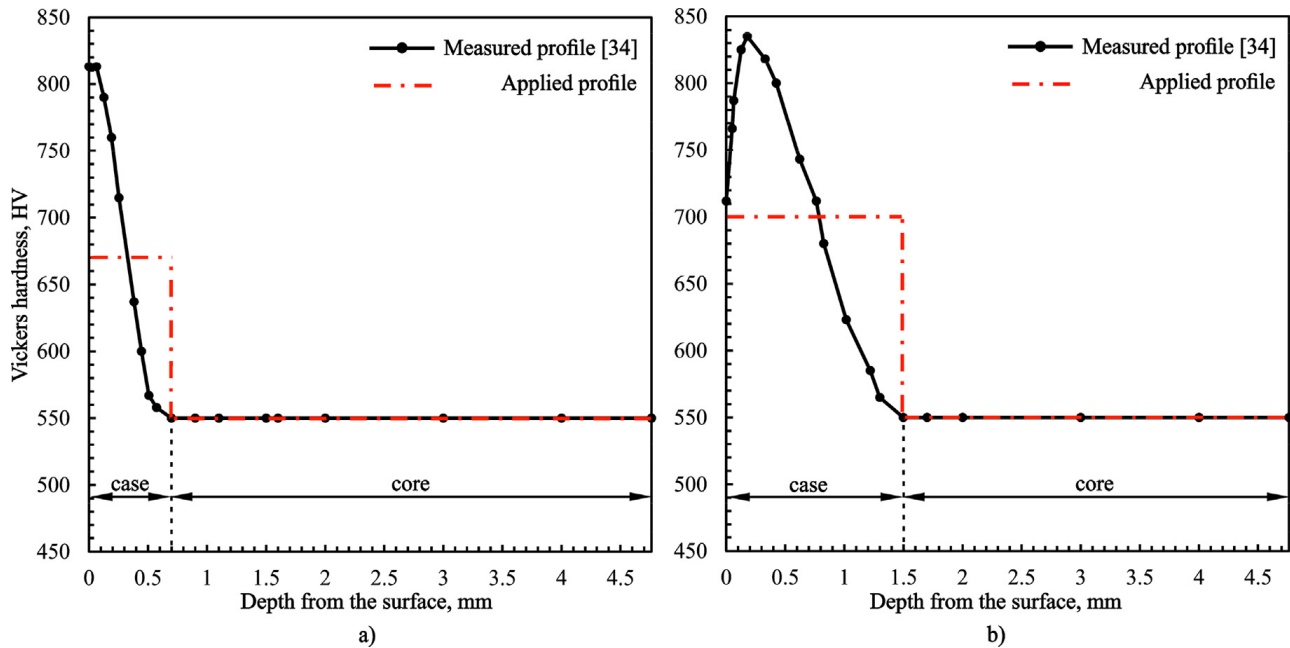
Fig. 4. Measured and applied hardness profiles for: (a) type A and (b) type B specimen.

Table 2
Strain-life fatigue properties for type A and B specimens.

Material parameter, symbol	Type A specimen		Type B specimen	
	Case layer	Core layer	Case layer	Core layer
Fatigue strength coefficient, σ'_f	2981.99 MPa	2396.75 MPa	2862.20 MPa	2396.75 MPa
Fatigue strength exponent, b	-0.09	-0.09	-0.09	-0.09
Fatigue ductility coefficient, ε'_f	0.05	0.12	0.06	0.12
Fatigue ductility exponent, c	-0.56	-0.56	-0.56	-0.56
Modulus of elasticity, E	210 GPa	210 GPa	210 GPa	210 GPa

data. Residual stress values for case and core layers of type A and type B specimens are presented in Table 3.

Four-point fully reversed pure bending tests with surface strain control were conducted on a specially designed servo-hydraulic four-point bending apparatus where failure was defined as complete fracture of the carburized specimen [35]. By employing strain-life fatigue properties from Table 2 and Eqs. (2.11) to (2.13), cyclic stress-strain curves for case and core layers of type A and type B specimens are obtained. RoM is then applied to find average cyclic stress-strain curves. Case, core and averaged cyclic stress-strain curves for type A and B specimens are presented in Fig. 5. It should be noted that in the absence of data for material properties, modulus of elasticity is assumed as $E = 210$ GPa for both case and core layers. Therefore, averaged cyclic stress-strain curve is very similar to case and core layer curves for lower values of true stresses and strains. For higher true stress and strain values, elasticity modulus is altered due to the presence of plastic strains (Fig. 5). When simulating material behaviour of carburized specimen by employing data from actual specimens representing case and core regions, somewhat different values for modulus of elasticity are expected for each layer [27]. However, averaged modulus of elasticity for carburized steel specimens in linear elastic region would still be approximately $E \approx 210$ GPa, as is assumed in this paper.

Averaged cyclic stress-strain curves are then used to obtain ε_a^{be} from ε_a^{ax} via Neuber's rule. Neuber's rule is typically employed for notched components. However, it has shown to provide best true stress-strain estimations [39] when compared to Glinka's equivalent strain energy density method [40] and Hofmann and Seeger's generalized Neuber approach [41] in the presence of low stress concentration factors. Hence, it is used in this investigation since both types of specimens are notch-free ($K_f = 1$). Due to the absence of a notch, minor localized plasticity in specimens is expected. However, it should still be considered when predicting bending fatigue

Table 3
Average residual stress values for case and core layers of type A and B specimens.

	Type A specimen		Type B specimen	
	Case layer	Core layer	Case layer	Core layer
Average residual stress, σ_{res} [MPa]	-160.81	27.46	-90.96	12.64
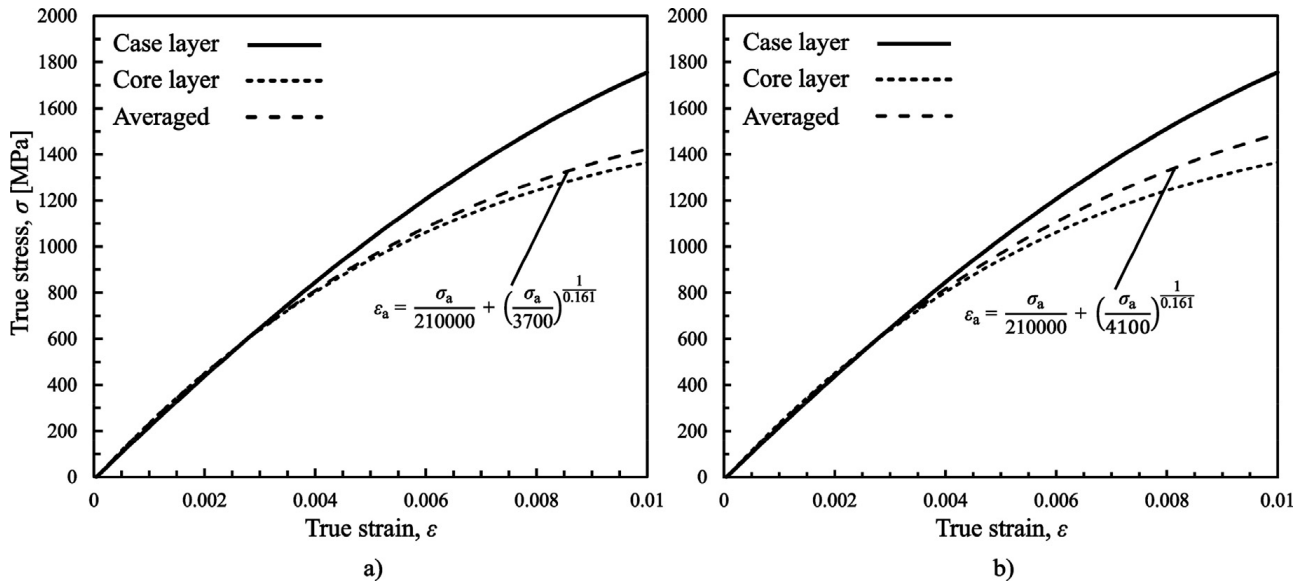
Fig. 5. Cyclic stress-strain curves predictions based on hardness method for: (a) type A and (b) type B specimen.

life, given that minor alteration of strain values in the presence of localized plasticity can produce significant shift in fatigue lives [33]. For fully reversed bending test with surface strain control, nominal stress range is equal to

$$\Delta S = 2 \cdot S_{\max} \tag{3.3}$$

Since experimental investigation was conducted under assumption of pure bending load, value of $C_L = 0.9$ was initially chosen. Preliminary results of the comparison between prediction model and experimental results have shown good correlation but over-estimated actual bending fatigue lives. By taking a closer look to the experimental results from [35], axially loaded carburized specimens have shown superior fatigue behavior when compared with carburized specimens under bending load in high cycle fatigue region, whereas the opposite is expected. According to experimental investigation [35], at 10^6 cycles, the observed ratio of fatigue strength of axial to bending specimens is approximately equal to 1.11. Even for non-carburized specimens, axially loaded round specimens have exhibited superior fatigue strength at 10^6 cycles when compared to rectangular bending specimens. This effect was found to be highly unusual and inconsistent with the research data of typical fatigue behavior of materials under different types of loading. Hence, to properly conduct an initial validation of the prediction model, this effect had to be accounted for. Thus, for validation of the analytical model in this paper, correction factor $C^* = C_L k_f = 1.11$ instead of $C^* = C_L = 0.9$ was used. This factor accounts for both C_L and additional miscellaneous effects, k_f, which were difficult to precisely determine due to lack of information from [35].

For case and core layers of type A and type B specimens, modified strain-life curves for bending fatigue life prediction are

Fig. 6. Estimated ratio $\varepsilon_a^{ax}/\varepsilon_a^{be}$ for: (a) type A specimen and (b) type B specimen.

obtained according to procedure schematically depicted in Fig. 3. Layer with lower bending fatigue life is denoted as critical and the corresponding number of cycles until failure is recorded.

4. Results and discussion

4.1. Ratio of total axial and bending fatigue strain amplitudes

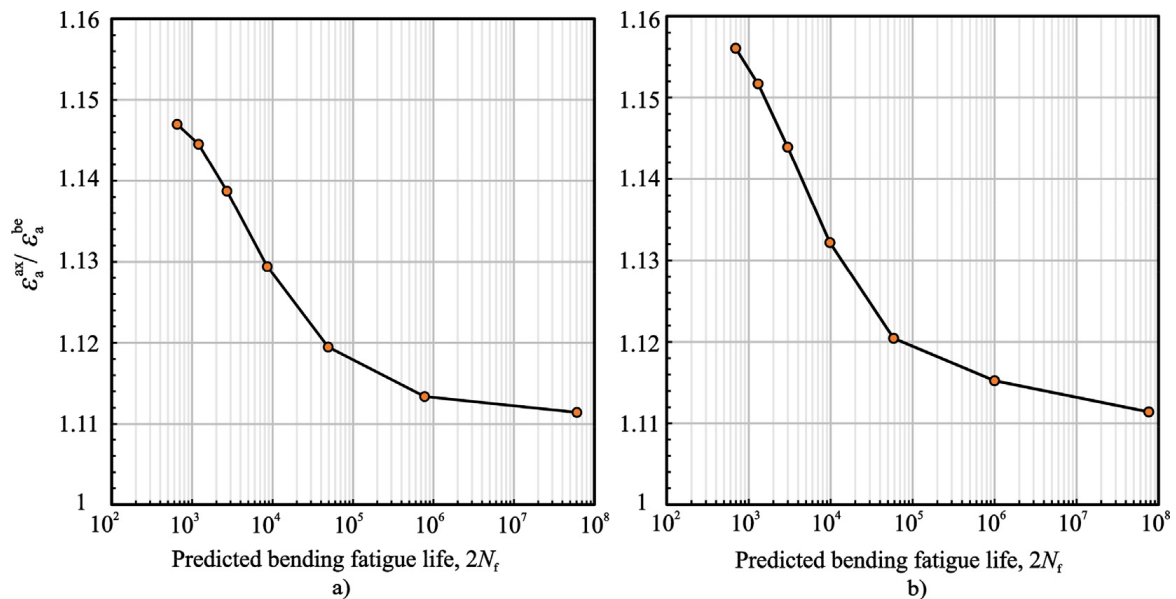Estimated ratio $\varepsilon_a^{ax}/\varepsilon_a^{be}$ is depicted in Fig. 6 for type A and type B specimens with regard to predicted bending fatigue life. For discussion purposes, low cycle fatigue region is defined as less than 10^4 cycles until failure, while high cycle fatigue region is defined as more than 10^4 cycles until failure [42].

In the high cycle fatigue regime where predominantly linear elastic behavior of material is present, for given fatigue life, ratio of total strain amplitude under axial load, ε_a^{ax}, to total strain amplitude under bending load, ε_a^{be}, is approximately equal to $C^* = 1.11$, as expected. However, in low cycle fatigue regime, it is slightly higher. This effect is shown in Fig. 6 and is also noticed in [29] for stress-life (*S–N*) fatigue data. In addition, higher $\varepsilon_a^{ax}/\varepsilon_a^{be}$ values are observed for type B specimen in low cycle fatigue when compared to type A specimen. This indicates that for given fatigue life in low cycle fatigue regime, specimens with greater carburizing depths (type B specimens) have lower bending fatigue life, which is in accordance with the experimental data from [35]. The aforesaid could be due to relatively greater carburized region when compared to type A specimens, whose brittle behavior and residual stress relaxation result with inferior low cycle fatigue properties.

4.2. Bending fatigue life predictions

Modified strain-life curves for bending fatigue predictions of type A and type B specimens are shown in Fig. 7. Strain-life fatigue properties and averaged residual stress values are taken from Tables 2 and 3. According to the approach schematically represented in Fig. 3, best agreement of bending strain-life curves with ε_a^{be} for corresponding bending fatigue life is obtained when $X_e = 1/C^*$, where $C^* = 1.11$ for 10^6 cycles. The aforesaid is true for case and core layer bending strain-life curves for both type A and type B specimens. However, X_p, which modifies plastic strain amplitude, was found to provide best estimation for bending strain-life curve by being somewhat lower that X_e, presumably due to localized plasticity effects and difference in estimated $\varepsilon_a^{ax}/\varepsilon_a^{be}$ ratios. For case layer of both type A and type B specimens, $X_p = 0.7$, while for core layer of type A and type B specimens, $X_p = 0.8$.

If reciprocal value of C^* at 10^6 cycles is chosen for both X_e and X_p, such that:

$$X_e = X_p = \frac{1}{C^*} \tag{4.1}$$

the equation (2.17) can be written as

$$C^* \varepsilon_a^{be} = \frac{(\sigma_f' - \sigma_m - \sigma_{res})}{E}(2N_f)^b + \varepsilon_f'(2N_f)^c \tag{4.2}$$

which suggests that bending strain-life curve (Fig. 3) with modification of total strain amplitude can be used to predict axial fatigue lives and vice-versa. This would be reasonable approximation in high cycle fatigue region where predominantly linear elastic material behaviour is exhibited. However, for low cycle bending fatigue predictions, accuracy of the results would be decreased due to localized plasticity and consequently different values of X_p.
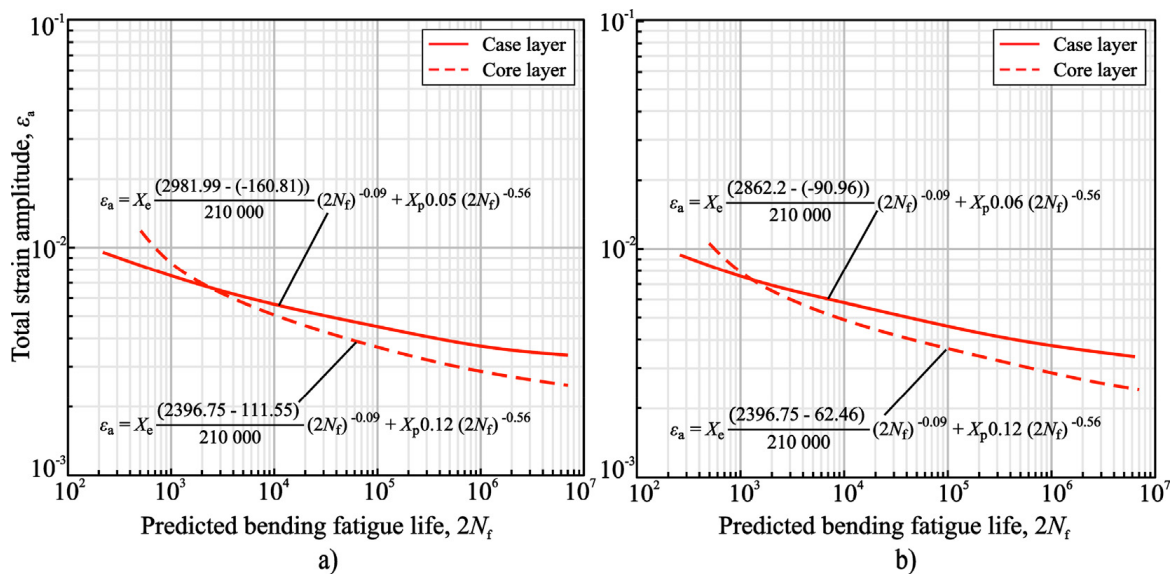

Fig. 7. Modified strain-life curves for bending fatigue life prediction: (a) type A specimen and (b) type B specimen.

Comparison of the experimental and predicted bending fatigue lives for type A and type B specimens with the corresponding scatter factor of three are plotted in Fig. 8. Surface and subsurface failure location is also depicted. Predicted failure location roughly corresponds to reported crossover point of surface-subsurface failure initiation [35]. Moreover, it is in accordance with the recognized effect of failure initiation shift from surface to subsurface in carburized specimens during high cycle fatigue [10,25,43]. Pinpointing failure location could possibly be improved by employing more than two layers.

4.2.1. Low cycle fatigue region

For type A specimens, predicted results are somewhat conservative in the LCF region, whereas for type B specimens good correlation of predicted and experimental results is observed. This could be due to the hardness method itself, which was originally proposed to predict experimental fatigue investigations with failure criterion of 50% load drop [18], as opposed to complete fracture criterion used within the scope of this research. In general, even though crack growth time is often relatively short when compared to crack initiation time in the HCF region, in the LCF region it can take up substantial portion of total fatigue life. This explains somewhat conservative results for type A specimen in the LCF region, whereas good correlation of type B specimen results in the LCF region can be attributed to relatively large and brittle carburized region, through which rapid crack growth occurs [44]. Hence, for brittle behavior of type B specimens, crack growth time in the LCF region is possibly negligible.

4.2.2. High cycle fatigue region

For type A specimens, bending fatigue predictions in the HCF region are slightly overestimating experimental data. This could be the result of residual stress approximations according to Eqs. (3.1) and (3.2) due to the absence of actual residual stress data. Since HCF region is characterized by predominantly linear elastic material behavior, residual stresses are unable to completely relax and as such can influence bending fatigue lives. For type B specimens, good correlation between predicted and experimental results is observed in the HCF region.

Some factors which may have influenced the accuracy of the results should also be mentioned. The hardness method was originally proposed for steels with hardness between 150 HB and 700 HB, while hardness for the carburized AISI 4027 specimens can reach somewhat higher values in the near-surface region. Furthermore, Neuber's rule is more conservative when compared to other methods of true stress and strain estimation. This results in lower stress and strain values in low cycle fatigue regime, producing conservative predictions. Lastly, even though the experimental results used in this paper are adequate for the initial validation of the prediction model, additional experimental data should be used to validate the model on a more statistically significant sample.

5. Conclusion

In this paper, analytical model for bending fatigue prediction of carburized gear steel specimens based on strain-life approach was proposed for low and high cycle fatigue regimes. Hardness method and multilayer method were used to acquire strain-life fatigue properties of material layers. Through rule of mixture, average cyclic stress-strain curves for carburized specimens were obtained. In addition, an approach was suggested for translating axial to bending fatigue data through Neuber's rule and modifying factors.

The following conclusions are derived:

- Nearly all the predicted bending fatigue lives fall within the scatter factor of three when compared to the experimental results, while overall good correlation is observed between predicted and experimental data.
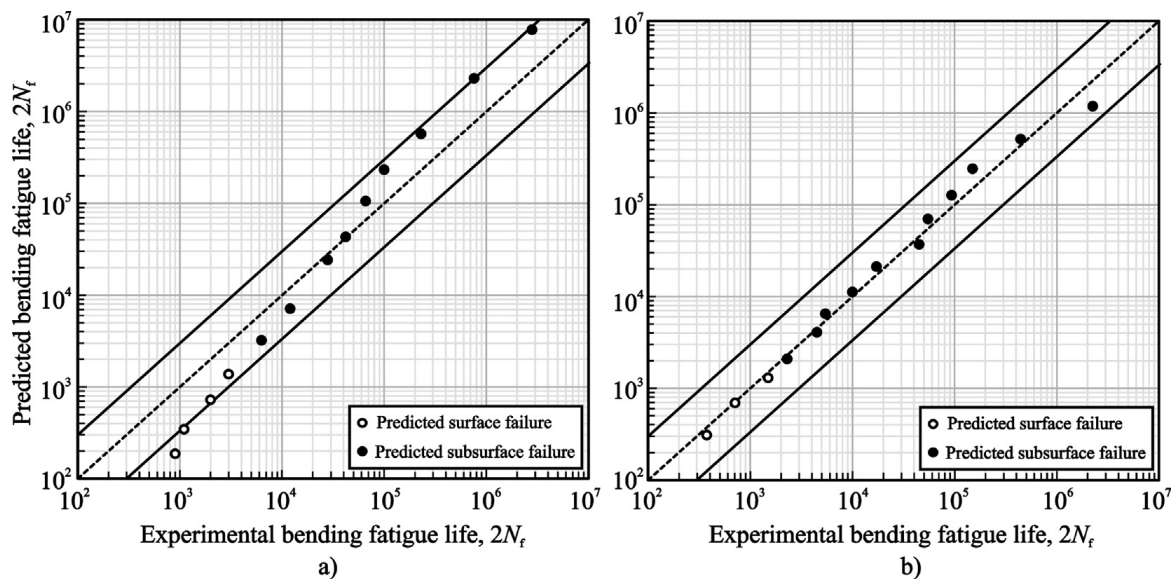

Fig. 8. Comparison of experimental and predicted bending fatigue lives for: (a) type A specimens and (b) type B specimens.

- For specimens with lower carburizing depths, low cycle fatigue predictions are conservative, while specimens with greater carburizing depths shows good data correlation. Data indicates that with a decrease in carburizing depth, more conservative results are expected in the low cycle fatigue region, whilst good correspondence between experimental and predicted data is expected for the high cycle fatigue regimes.
- Rough agreement of predicted failure location is observed with the reported shift from surface to subsurface failure. The predicted shift is in accordance with the recognized effect of subsurface failure initiation in bending fatigue of carburized materials.

In future studies, additional analytical bending fatigue life investigations of carburized specimens are planned while considering various carburizing depths, where accuracy of the multilayer model on predictions will be evaluated. Furthermore, to validate the prediction model on a more statistically relevant sample, additional four-point bending experimental investigations of carburized gear steel specimens will be performed. The effect of specimens under axial load showing superior fatigue strength when compared to bending ones will be investigated in detail. Finally, the applicability of the proposed approach in combination with multilayer and finite element method, while considering mean, residual and multiaxial stress effects will be evaluated for bending fatigue life prediction of carburized spur gears.

Declaration of Competing Interest

The authors declare that they have no conflict of interest.

References

[1] T. Tobie, F. Hippenstiel, H. Mohrbacher, Optimizing gear performance by alloy modification of carburizing steels, Metals 7 (415) (2017) 20, https://doi.org/10.3390/met7100415.
[2] ISO 6336:2006. Calculation of load capacity of spur and helical gears.
[3] G. Meneghetti, C. Dengo, F.L. Conte, Bending fatigue design of case-hardened gears based on test specimens, J. Mech. Eng. Sci. (2017) 17, https://doi.org/10.1177/0954406217712278.
[4] K. Genel, M. Demirkol, Effect of case depth on fatigue performance of AISI 8620 carburized steel, Int. J. Fatigue 21 (1999) 207–212.
[5] V. Gaur, V. Doquet, E. Persent, C. Mareau, E. Roguet, J. Kittel, Surface versus internal fatigue crack initiation in steel: influence of mean stress, Int. J. Fatigue 82 (2015) 437–448, https://doi.org/10.1016/j.ijfatigue.2015.08.028.
[6] P. Liu, W. Li, A. Nehila, Z. Sun, H. Deng, High cycle fatigue property of carburized 20Cr gear steel under axial loading, Metals 6 (246) (2016) 14, https://doi.org/10.3390/met6100246.
[7] W. Li, H. Deng, P. Liu, Interior fracture mechanism analysis and fatigue life prediction of surface-hardened gear steel under axial loading, Materials 9 (843) (2016) 14, https://doi.org/10.3390/ma9100843.
[8] H. Deng, W. Li, H. Zhao, T. Sakai, Multiple fatigue failure behaviors and long-life prediction approach of carburized Cr-Ni steel with variable stress ratio, Materials 10 (1084) (2017) 21, https://doi.org/10.3390/ma10091084.
[9] C. Dengo, G. Meneghetti, M. Dabala, Experimental analysis of bending fatigue strength of plain and notched case- hardened gear steels, Int. J. Fatigue 80 (2015) 145–161, https://doi.org/10.1016/j.ijfatigue.2015.04.015.
[10] H. Deng, W. Li, T. Sakai, Z. Sun, Very high cycle fatigue failure analysis and life prediction of Cr-Ni-W gear steel based on crack initiation and growth behaviors, Materials 8 (2015) 8338–8354, https://doi.org/10.3390/ma8125459.
[11] J. John, K. Li, H. Li, Fatigue performance and residual stress of carburized gear steels part II: fatigue performance, SAE Int. J. Mater. Manuf. 1 (1) (2008) 709–717.
[12] J.J. Spice, D.K. Matlock, Optimized carburized steel fatigue performance as assessed with gear and modified brugger fatigue tests, SAE Tech. Papers 111 (5) (2002) 9.
[13] Y. Liu, M. Wang, J. Shi, W. Hui, G. Fan, H. Dong, Fatigue properties of two case hardening steels after carburization, Int. J. Fatigue 31 (2) (2008) 292–299, https://doi.org/10.1016/j.ijfatigue.2008.08.010.
[14] C. Zhou, M. Wang, W. Hui, H. Dong, L. Wang and R. Wu, "Rotating bending fatigue properties of two case hardening steels after nitriding treatment," vol. 46, pp. 539-545, 2013. doi:10.1016/j.matdes.2012.08.061.
[15] A.J. Baumel, T. Seeger, The influence of residual stresses and surface strenghtening on components fatigue life, Fatigue 1 (90) (1990) 311–316.
[16] N. Shamsaei, S.A. McKelvey, Multiaxial life predictions in absence of any fatigue properties, Int. J. Fatigue 67 (2014) 62–72, https://doi.org/10.1016/j.ijfatigue.2014.02.020.
[17] V. Troshchenko, L. Khamaza, Strain-life curves of steels and methods for determining the curve parameters. Part1. Conventional methods, Strength Mater. 42 (6) (2010) 647–659.
[18] M. Roessle, A. Fatemi, Strain-controlled fatigue properties of steels and some simple approximations, Int. J. Fatigue 22 (2000) 495–511.
[19] U. Muralidharan, S. Manson, A modified universal slopes equation for estimation of fatigue characteristics of metals, J. Eng. Mater. Technol. 110 (1) (1988) 55–58.
[20] K. Kim, X. Chen, C. Han, H. Lee, Estimation methods for fatigue properties of steels under axial and torsional loading, Int. J. Fatigue 24 (7) (2002) 783–793.
[21] A.J. Bäumel, T. Seeger, Metals data for cyclic loading, supplement I, Elsevier Science Publishers, Amsterdam, 1990.
[22] A. Ince, G. Glinka, A modification of Morrow and Smith–Watson–topper mean stress correction models, Fatigue Fract. Eng. Mater. Struct. 34 (2011) 854–867, https://doi.org/10.1111/j.1460-2695.2011.01577.x.
[23] J. Morrow, Fatigue Properties of metals, Warrendale, SAE, PA, 1968.
[24] K. Smith, P. Watson, T. Topper, A stress-strain function for the fatigue of materials, J. Mater. 5 (1970) 767–778.
[25] B. Jo, S. Sharifimehr, Y. Shim, A. Fatemi, Cyclic deformation and fatigue behavior of carburized automotive gear steel and predictions including multiaxial stress states, Int. J. Fatigue 100 (2016) 454–465, https://doi.org/10.1016/j.ijfatigue.2016.12.023.
[26] F. Yin, A. Fatemi, Fatigue behaviour and life predictions of case-hardened steels, Fatigue Fract. Eng. Mater. Struct. 32 (3) (2009) 197–213.
[27] B. Jo, Y. Shim, S. Sharifimehr, A. Fatemi, Deformation and fatigue behaviors of carburized automotive gear steel and predictions, Frattura ed Integrità Strutturale 37 (2016) 28–37, https://doi.org/10.3221/IGF-ESIS.37.05.
[28] K.-S. Lee, J.-H. Song, Estimation methods for strain-life fatigue properties from hardness, Int. J. Fatigue 28 (2006) 386–400, https://doi.org/10.1016/j.ijfatigue.2005.07.037.
[29] Y.-L. Lee, J. Pan, R. Hathaway, M. Barkey, Fatigue Testing and Analysis (Theory and Practice), Elsevier Butterworth-Heinemann, Burlington, 2005.
[30] Richard G Budynas, J. Keith Nisbett, Shigley's Mechanical Engineering Design, (10th Edition),, McGraw-Hill, Education, New York, 2015.
[31] H. Neuber, Theory of stress concentration for shear strained prismatical bodies with arbitrary non-linear stress strain law, J. Appl. Mech. 28 (1961) 544–550.
[32] K. Vučković, I. Galić, Ž. Božić, S. Glodež, Effect of friction in a single-tooth fatigue test, Int. J. Fatigue 114 (2018) 148–158, https://doi.org/10.1016/j.ijfatigue.2018.05.005.

[33] R. Stephens, A. Fatemi, R. Stephens, H. Fuchs, Metal Fatigue in Engineering, Second Edition, John Wiley and Sons, inc., New York, 1981.

[34] G. Massing, "Eigenspannungen und verfestigung beim messing (Self stretching and hardening for brass)," in Proceedings of the 2nd Int. Congress for Applied Mechanics, Zurich, 1926.

[35] R. Landgraf, R. Richman, Fatigue Behavior of Carburized Steels, Fatigue Comp. Mater., ASTM STP 159 (1975) 130–144.

[36] J. Bayer, »Steel bars for automotive applications,« Advanced Materials & Processes, pp. 46-49, 2003.

[37] A. International, E 140 - 02: Standard Hardness Conversion Tables for Metals Relationship Among Brinell Hardness, Vickers Hardness, Rockwell Hardness, Superficial Hardness, Knoop Hardness and Scleroscope Hardness, 2002.

[38] T. Hertter, Rechnerischer Festigkeitsnachweis der Ermüdungstragfähigkeit vergüteter und einsatzgehärteter Stirnräder, TU München, Fakultät für Maschinenwesen, München, 2003.

[39] S. Visvanatha, P. Straznicky, R. Hewitt, Influence of strain estimation methods on life predictions using the local strain approach, Int. J. Fatigue 22 (2000) 675–681.

[40] K. Molski, G. Glinka, Elasto-plastic plane strain analysis of stresses and strains at the notch root, J. Eng. Mater. Technol. 110 (3) (1988) 195–204.

[41] M. Hoffmann, T. Seeger, A generalized method for estimating multiaxial elastic-plastic notch stresses and strains, parts 1 and 2, J. Eng. Mater. Technol., Transac. ASME 107 (1985) 250–260.

[42] L.O.A. Affonso, Machinery Failure Analysis Handbook, Gulf Publishing Company, Houston, 2007.

[43] Š. Major, Š. Hubálovský, J. Šedivý, J. Bryscejn, Fatigue life of carburized steel specimens under push-pull loading, Int. J. Mater. 1 (2014) 99–104.

[44] T.H. Courtney, Mechanical Behavior of Materials, second edition, Long Grove, Waveland Press Inc, Illinois, 2005.

Paper II

The manuscript shown within this thesis published in:

Contributions of the Ph.D. candidate:

- employing the previously established numerical model to investigate the adjacent tooth effect
- interpreting and discussing the results
- establishing the modifying factor
- writing the manuscript

Numerical model for bending fatigue life estimation of carburized spur gears with consideration of the adjacent tooth effect

Krešimir Vučković, Ivan Čular [*], Robert Mašović, Ivica Galić, Dragan Žeželj

University of Zagreb, Faculty of Mechanical Engineering and Naval Architecture, I. Lučića 5, 10000 Zagreb, Croatia

A B S T R A C T

In this paper, a computational model for bending fatigue failure prediction of case hardened spur gears is proposed. The model consists of finite element gear and fatigue failure models, and it accounts for the actual stress–strain state at the tooth root by accounting for local elastic–plastic correction. By employing the proposed model, the effect of the adjacent tooth on bending fatigue lives is investigated. It is observed that bending fatigue lives can vary by approximately 22% when accounting for the adjacent tooth effect. Therefore, this effect should be considered when estimating bending fatigue lives of spur gears.

1. Introduction

Metal gears are one of the most commonly employed power transmission machine elements. During their operating life, gears are subjected to cyclic loading. In carburized spur gears, the tooth root represents a more critical potential failure location. Since this area is accompanied by cyclic and variable stresses, material fatigue occurs in the tooth root region (more commonly known as bending fatigue). Consequently, material fatigue may result in crack initiation, propagation, and eventually tooth breakage. If one is to consider that gear drives are often used in heavy machinery power transmission devices such as helicopters, gear failure can even result in an injury or possibly loss of human life. To prevent such events and contribute to the cost-effectiveness of the gear design, it is of great importance to accurately estimate the bending fatigue lives of gears.

In recent years, due to the relatively high costs and complexity of experimental investigations, numerical methods are often used to simulate gear power transmission. Miscellaneous effects, due to their negligible influence on actual tooth root stresses and strains, are often omitted. This might be justified if one is to observe only stresses and strains. However, when fatigue is considered, a relatively small amount of stress modification can significantly affect the fatigue life of a component [1]. Therefore, when estimating the bending fatigue lives of spur gears, the most notable yet often neglected phenomenon such as the effect of the adjacent tooth should be properly accounted for. Currently, one of the most accurate and relatively simple numerical methods for gear drive simulation is the quasi-static simulation. In this type of

simulation, gear rotation is achieved by separating the complete process into a finite number of frames, with each frame representing a static loading case. Zhan et al. [2] proposed a quasi-static model based on the finite element method (FEM) to analyze the time-varying load capacity of the gear system. The authors compared the results of contact and tooth-root stresses against the results obtained via AGMA (American Gear Manufacturers Association) standard [3]. They concluded that AGMA contact stress results agree with the FEM model, while tooth root ones do not. It should also be mentioned that the authors specifically noted that compressive stresses should be determined when estimating the bending fatigue of gears. In other words, the adjacent tooth effect, which results in a certain amount of compressive stresses in the tooth root, should be considered in such instances. Further work on FEM simulations of gear drives was conducted by Lias et al. [4]. The authors developed a quasi-static spur gear model and analyzed the time-varying strength of the spur gear system by comparing the results against analytical equations. They concluded that the proposed model was in good agreement with the analytical model. Manojkumar et al. [5] investigated fatigue life of aluminum alloy and SAE (Society of Automotive Engineers) material spur gears in mating conditions based on finite element (FE) analysis under fully reversed load conditions. Unlike quasi-static simulations, the authors simulated a single contact between two teeth of the gear pair. Similar to the previous case, the authors stated that a more realistic simulation would have been achieved by accounting for the mean stress due to the adjacent tooth effect. Jabbour and Asmar [6] presented a method for calculating tooth root and contact stresses for spur and helical metal gears. The authors verified their method against finite element results for maximum contact and tooth-

---

Nomenclature

a	center distance of a spur gear pair
b	fatigue strength exponent
C_{ATE}	adjacent tooth effect modifying factor
C_m	adjacent tooth effect modifying factor for mean linear-elastic bending stress obtained via FE analysis
C_ε	adjacent tooth effect modifying factor for linear-elastic strain amplitude obtained via FE analysis
c	fatigue ductility exponent
E	modulus of elasticity
K'	cyclic strength coefficient
K_t	theoretical stress concentration factor
K_{sf}	surface finish correction factor
N_f	number of cycles until failure
N_f*	number of cycles until failure modified to account for the adjacent tooth effect
n'	cyclic strength exponent
S	nominal stress in Neuber's elastic–plastic correction
T	driven gear torque
$\Delta\varepsilon^a$	actual strain range
$\Delta\varepsilon_e$	elastic strain range in Basquin-Coffin-Manson's equation
$\Delta\varepsilon_e^*$	elastic strain range in Basquin-Coffin-Manson's equation modified to account for the adjacent tooth effect
$\Delta\varepsilon_p$	plastic strain range in Basquin-Coffin-Manson's equation
$\Delta\varepsilon_p^*$	plastic strain range in Basquin-Coffin-Manson's equation modified to account for the adjacent tooth effect
$\Delta\sigma^a$	actual stress range
$\Delta\sigma_a$	stress amplitude modification in linear-elastic bending stress cycle
$\Delta\sigma_m$	mean stress modification in linear-elastic bending stress cycle
ε^a	actual bending strain
ε_a^a	actual bending strain amplitude
ε_{max}^a	maximum value of actual bending strain
ε_{min}^a	minimum value of actual bending strain
ε_{a*}^a	actual bending strain amplitude modified for the adjacent tooth effect
ε_{aFE}^e	linear-elastic bending strain amplitude obtained via FE analysis
ε_{aFE}^{e*}	linear-elastic bending strain amplitude obtained via FE analysis modified for the adjacent tooth effect
ε_{max}^e	maximum value of linear-elastic bending strain
ε_f'	fatigue ductility coefficient
σ	bending stress for linear elastic material behavior (principal stress tangential to the observed root fillet)
σ^a	actual bending stress
σ_m^a	actual mean bending stress
σ_m^{a*}	actual mean bending stress modified for the adjacent tooth effect
σ_{max}^a	maximum value of actual bending stress
σ_{min}^a	minimum value of actual bending stress
σ_{ATE}	supplementary factor which describes the relationship between mean stress from FE analysis, fatigue strength coefficient, and residual stress
σ^e	linear-elastic bending stress
σ_{aFE}^e	linear-elastic bending stress amplitude obtained via FE analysis
σ_{aFE}^{e*}	linear-elastic bending stress amplitude obtained via FE analysis and modified for the adjacent tooth effect
σ_{max}^e	maximum value of linear-elastic bending stress
σ_m	mean bending stress for linear-elastic material behavior
σ_f'	fatigue strength coefficient
σ_n	principal normal stress
σ_{res}	residual stress
σ_φ	principal stress tangential to the observed tooth root fillet for a specific node
ϑ	angle of rotation of the driving gear
μ	coefficient of friction
ν	Poisson's factor

root stress regions. They concluded that good agreement exists between the two methods, but no adjacent tooth effect was considered within the investigation. It should be noted that there are some investigations where the adjacent tooth effect is considered. Thirumurugan et al. [7] proposed a numerical model for high contact ratio asymmetric spur gear drive with consideration of the adjacent tooth load. The authors concluded that the adjacent tooth effect influences the bending strength of gear and should be accounted for when designing a gear drive. Furthermore, Jiang et al. [8] proposed numerical mesh stiffness models for cracked spur gears with consideration of both crack and the adjacent tooth effect. The authors observed that both the crack and the adjacent tooth influence the total mesh stiffness. Even though the adjacent tooth effect is considered in some investigations, its effect on bending fatigue lives where quasi-static gear mesh is simulated is still not investigated.

When investigating material fatigue in gear transmission, the choice of appropriate methods significantly contributes to the accuracy of the results. He et al. [9] proposed a damage-coupled elastic–plastic contact fatigue model for a wind turbine gear based on CDM (continuous damage mechanics) and user subroutine. The authors concluded that the contact fatigue of the gear is dominated by the elastic damage. He et al. [10] investigated rolling contact fatigue crack propagation by employing the FEM with consideration of various lubrication conditions, initial cracks, and loading conditions. The authors observed that the lubricating pressurization dominates the surface-initiated rolling contact fatigue. Glodež et al. [11] proposed a computational model for

evaluating the service life of gears with regard to bending fatigue life. The authors employed FEM to investigate both crack initiation based on Coffin-Manson relation and crack propagation based on Paris' law. They concluded that the proposed model is in good agreement with the experimental results. Liu et al. [12] developed a numerical model for contact fatigue life a wind turbine gear pair. The authors investigated both contact fatigue crack initiation and propagation, while investigating the effect of multiple multiaxial stress state criteria on estimated lives. Lastly, the explored the effect of residual stress distribution on contact fatigue lives. Lin et al. [13] investigated bending crack initiation and propagation lives of a spur gear by employing the finite element analysis and the power density method. By using the fatigue test rig, the authors concluded that the power density method is more accurate when compared to the Miner rule when predicting fatigue lives. The aforementioned methods are mostly based on numerical simulations. In addition, they are mostly employed for gear contact fatigue investigations, which is characterized by different stress – strain state and failure criteria as opposed to gear tooth root fatigue. Thus, the most appropriate method for bending fatigue investigation of carburized spur gears has to be chosen.

To summarize, multiple studies exist where the adjacent tooth effect is considered in spur gear meshing. However, it is limited only to tooth root stresses and strains, not bending fatigue lives. Moreover, when bending fatigue lives are being estimated while considering the adjacent tooth effect, gear meshing is not simulated. In this paper, a

computational bending fatigue life estimation model of spur gears is proposed. First, a quasi-static FEM model of a spur gear pair is established and compared against the existing standard. Then, the fatigue model based on the strain-life (ε – N) approach, which was already validated in a previous investigation, is employed. Finally, the effect of the adjacent tooth on the bending fatigue life of spur gear is evaluated and the results are discussed. In this study, gear bending fatigue life is equalized with the crack initiation life, as recommended for case-hardened gears in [14]. Moreover, surface fatigue crack initiation is assumed for comparison purposes, although a fatigue crack may initiate below the surface in case-hardened materials [15-17].

2. FE and fatigue models

In Fig. 1, a schematic flowchart of the proposed computational bending fatigue life estimation model, which is separated into four steps, is shown.

In the first step, quasi-static FE analysis based on actual gear pair geometry, material properties, and boundary conditions is conducted. Linear-elastic tooth root stresses (σ^e) are provided as the analysis output, and FE model results are compared against the relevant standard [14].

In the second step, to account for localized plasticity effects on tooth root stresses and strains, elastic–plastic correction of linear-elastic stresses is performed based on predetermined cyclic stress–strain parameters of gear material. In addition, surface finishing quality is considered. Hence, actual stresses, σ^a, and strains, ε^a, at the tooth root fillet are obtained.

In the third step, bending fatigue life (N_f) of spur gear is estimated via strain-life (ε – N) approach based on the predetermined actual stress–strain state in the tooth root fillet and known strain-life parameters. Here, residual stresses due to surface hardening treatments and mean stresses due to the adjacent tooth effect are accounted for. Together, the 2nd and 3rd steps form the fatigue model, whose accuracy has already been validated in the previous investigation conducted by the authors [18]. It should be noted that this fatigue model is part of the computational model proposed in [18] for estimating the bending fatigue lives of a single tooth bending fatigue (STBF) test. The other part of the computational model was the FE analysis used to obtain linear-elastic bending stresses of an STBF test. However, actual gears meshing, as opposed to the pulsating load acting upon the tooth flank, is simulated in this paper, while the same fatigue model (described in Section 2.2) is employed as in [18].

Finally, in the fourth step, a computational bending fatigue life estimation model is obtained. The adjacent tooth effect on bending fatigue lives is investigated and the results are discussed. In addition, a modifying factor is proposed which can be applied to account for the adjacent tooth effect when estimating bending fatigue lives of spur gears.

2.1. Finite element model

FE analysis is carried out via commercially available software Abaqus-Standard [19] to obtain cyclic tooth root stresses for the linear-elastic material behavior. For the driving gear, a specimen from [20] is chosen. To ensure the accuracy of the FE gear model following the grinding process, specimen data and fillet profile are modified in accordance with [21]. It should be mentioned that the same specimen was employed as a part of bending fatigue model validation in the previous work conducted by the authors f18]. As mentioned in the final paragraph of the introductory section, this already validated bending fatigue model is used for bending fatigue life estimation in this paper. The geometrical parameters of the driving gear are presented in Table 1.

For simplicity purposes, identical gear is selected as the driven gear. Lastly, the spur gear center distance is taken as $a = 88.9$ mm [21]. According to Pehan et al. [22], plane stress can be assumed if the gear module is higher than one-sixth of its face width. Therefore, to reduce computational requirements, a two-dimensional FE analysis is carried out. Schematic representation of the finite element model with boundary conditions is shown in Fig. 2.

Reference points RP_1 and RP_2 are constrained via *kinematic coupling* to the gear hub of the driving and the driven gear, respectively. Contact between five pairs of gear teeth (initial contact pair to the final contact pair according to Fig. 2) is established as *normal behavior, hard contact*. Under the assumption of fully lubricated operating conditions resulting in relatively low coefficients of friction between teeth flanks [23,24], the effect of friction is not accounted for within this paper. The observed tooth root fillet for all simulations is chosen on the middle tooth of the driven gear between the initial and final contact pair (Fig. 2).

The simulation itself is separated into two steps:

1. Application of torque, T.
2. Rotation of the gears about their respective reference points by an angle ϑ while maintaining the applied load.

In the first step, degrees of freedom of the driving gear are restricted in all directions. For the driven gear, only rotational displacement about RP_2 is allowed, while its radial displacement is restricted. Then, torque T is applied to the RP_2 in the clockwise direction.

In the second step, boundary conditions of the driven gear are kept the same, i.e., radial displacement is restricted, rotation about RP_2 is

Table 1
Geometrical parameters of the driving gear.

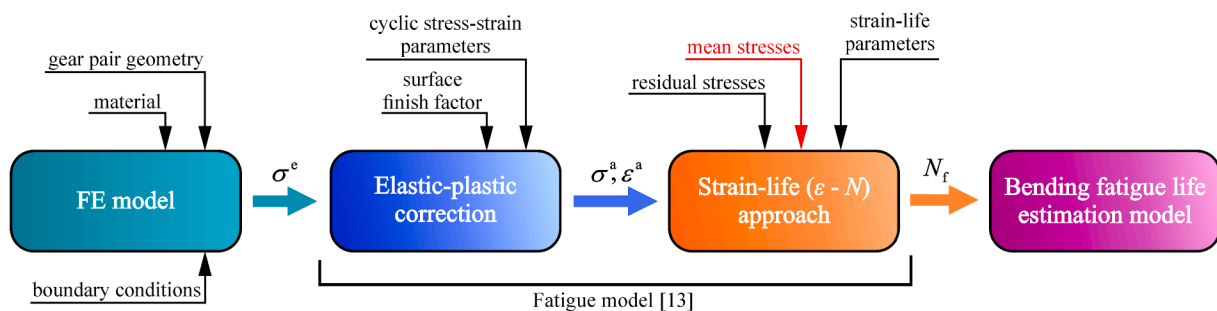| Parameter	Value	Parameter	Value
Number of teeth	28	Tip relief (at tooth tip)	0.013 mm
Module	3.175 mm	Root fillet radius of the basic rack	0 mm
Profile shift coefficient	−0.05	Addendum of the basic rack	3.334 mm
Face width	6.35 mm	Dedendum of the basic rack	4.286 mm
Pressure angle of the basic rack	20°	Tip diameter	95.25 mm

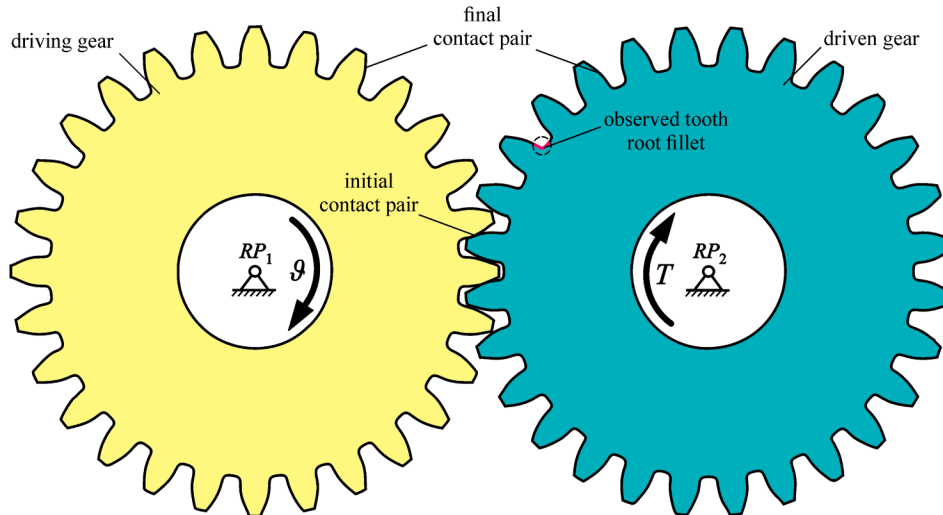**Fig. 1.** Flowchart of computational bending fatigue life estimation model.

Fig. 2. Boundary conditions of the finite element model.

allowed, and constant torque T is applied. Rotation of the driving gear about RP_1 is enabled while its radial displacement remains restricted. The driving gear rotates by an angle of $\vartheta = 1$ rad, i.e., $\vartheta \approx 57.3°$. *Nonlinear geometry* (NLGEOM) option is turned on within Abaqus to account for the effect of geometric nonlinearity due to large displacements induced by the incremental rotation of the gears. To ensure adequate resolution of the obtained stress cycles, the second step is separated into 500 time frames, with each frame representing a static loading case. Thus, a quasi-static simulation is achieved.

Both driving and driven gears are discretized via four-node plane stress quadrilateral elements, designated as CPS4 within Abaqus-Standard. The finite element mesh with the region of interest is shown in Fig. 3.

To increase the accuracy of the results, finite element mesh is refined in the tooth-root region. Multiple analyses were conducted to ensure convergence of the results. The final model used for the analysis consists of 107 062 finite elements and 109 682 nodes, while the tooth root region at the observed fillet consists of 900 finite elements and 961 nodes. Both gears are made of AISI 9310 steel, whose modulus of elasticity and Poisson's ratio are equal to $E = 207$ GPa and $\nu = 0.3$, respectively [21]. The material is assumed as homogeneous, isotropic, and linear-elastic.

Following the FE analysis, stresses and strains for linear-elastic material behavior are analyzed at the observed tooth root fillet. To account for actual stress and strain values, elastic–plastic correction is applied to linear-elastic stresses and strains within the fatigue model described in the following section.

2.2. Fatigue model

Linear-elastic stresses and strains are employed as input parameters for the bending fatigue model, which is based on the strain-life ($\varepsilon - N$) approach. This approach is founded on the assumption that the bending fatigue life of a node at the tooth root fillet can be estimated by a smooth material specimen subjected to the same cyclic loading conditions (Fig. 4a).

As previously mentioned, plane stress can be assumed in the tooth root of a spur gear if its face width is sufficiently small. Principal stresses for an arbitrarily chosen node on the tooth root fillet are shown in Fig. 4b. Since surface crack initiation is assumed, principal stress in the normal direction to the root fillet tangent, σ_n, is equal to zero. Maximum principal stress appears in the direction tangential to the root fillet (σ_φ). Given that this is also the only principal stress (hereinafter referred to as
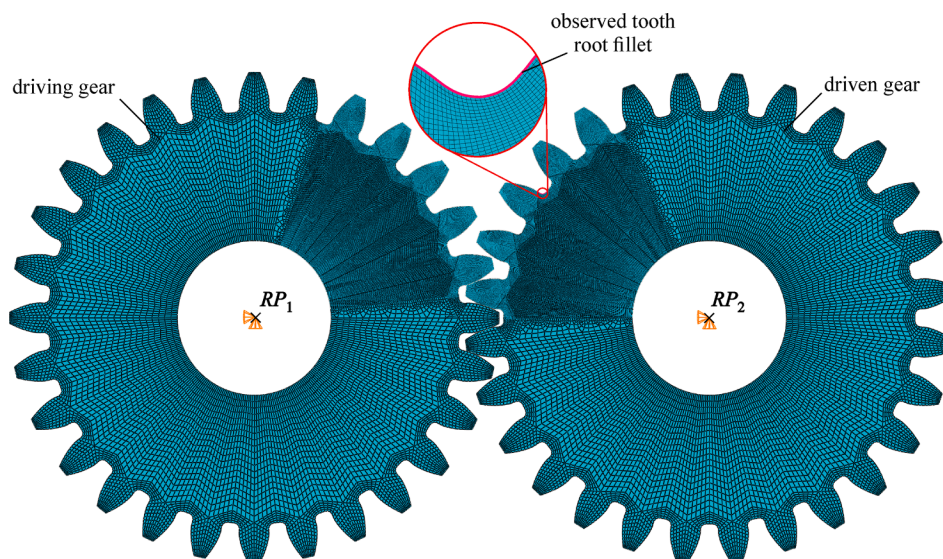

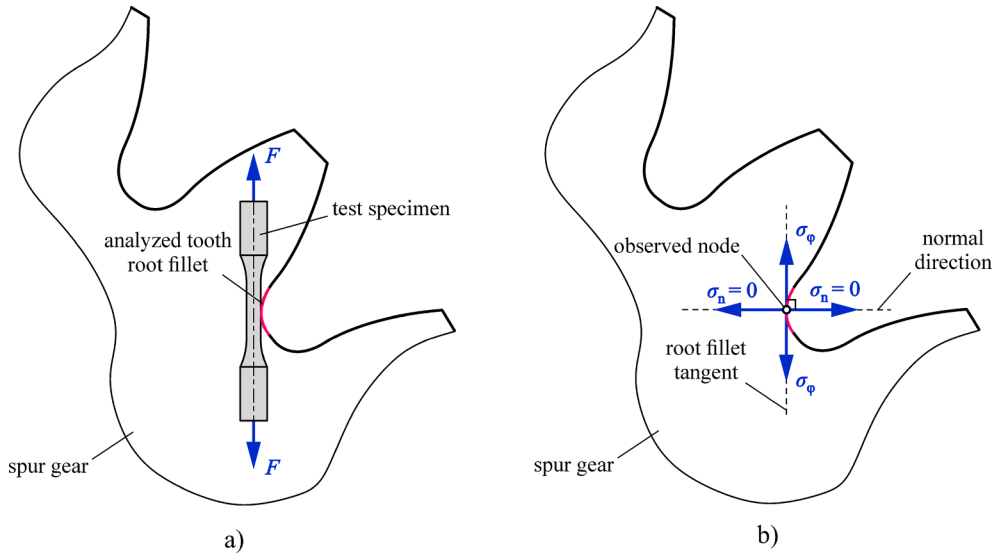**Fig. 3.** Finite element model with the applied mesh.

Fig. 4. Loading and stresses at the analyzed tooth root fillet: a) similarity principle between a smooth specimen and tooth-root nodes, and b) principal stresses for a specific fillet node.

the *bending stress* and denoted as σ), bending fatigue life can be estimated based on the uniaxial stress similarity principle between a smooth specimen and tooth-root nodes.

In Section 2.1, bending stresses under the assumption of linear-elastic behavior were obtained via FE analysis. However, due to the notch-like geometry of the tooth root fillet, stress concentration may result in a localized plasticity zone controlled by the relatively large encompassing elastic field. Therefore, actual bending stress and strain values accounting for elastic–plastic material behavior have to be obtained to accurately model bending fatigue behavior.

Neuber's rule [25] is one of the most widely employed notch stress/strain models which demonstrates favorable agreement with plane stress conditions [1]. Although it was initially formulated for grooved shafts subjected to torsional loading conditions, it is often employed for spur gear tooth root fillets subjected to plane stress conditions [26-28]. Neuber's rule equalizes the actual total strain energy at the notch tip with the elastic material behavior strain energy [29]. For uniaxial stress state, Neuber's rule can be expressed as:

$$\frac{(K_t \cdot S)^2}{E} = \sigma^a \cdot \varepsilon^a \tag{1}$$

where K_t represents the theoretical stress concentration factor, S represents nominal stress value (without consideration of geometric discontinuities), E is the modulus of elasticity, σ^a is the actual bending stress, and ε^a is the actual bending strain at the notch tip. Since linear-elastic bending stresses and strains are obtained via FE analysis on the actual gear geometry, the stress concentration factor is already accounted for. In other words:

$$K_t \cdot S = \sigma^e \tag{2}$$

where σ^e is the bending stress for linear-elastic material behavior obtained via FE analysis. By substituting Eq. (2) into Eq. (1), it can be rewritten as:

$$\frac{(\sigma^e)^2}{E} = \sigma^a \cdot \varepsilon^a \tag{3}$$

Factor K_{sf} is introduced to account for surface finish effects in the spur gear tooth root, such that:

$$\frac{(K_{sf} \cdot \sigma^e)^2}{E} = \sigma^a \cdot \varepsilon^a \tag{4}$$

where K_{sf} is a dimensionless surface finish correction factor that

depends on the material's ultimate tensile strength and surface roughness [30].

Schematic representation of acquiring actual bending stresses and strains via Neuber's rule is shown in Fig. 5. Within Fig. 5 and for the remainder of this paper, superscripts "a" and "e" stand for actual and linear-elastic values, respectively.

To employ Neuber's rule for elastic–plastic correction, a stable cyclic stress–strain curve (also known as Ramberg-Osgood curve) is determined first:

$$\varepsilon_{max}^a = \frac{\sigma_{max}^a}{E} + \left(\frac{\sigma_{max}^a}{K'}\right)^{\frac{1}{n'}} \tag{5}$$

where ε_{max}^a is the maximum actual bending strain, σ_{max}^a is the maximum actual bending stress, K' is the cyclic strength coefficient, and n' is the cyclic strength exponent. For maximum linear-elastic and actual bending stresses and strains, Eq. (4) can be rewritten as:

$$\frac{(K_{sf} \cdot \sigma_{max}^e)^2}{E} = \sigma_{max}^a \cdot \varepsilon_{max}^a \tag{6}$$

where σ_{max}^e is the maximum linear-elastic bending stress. Eq. (4) is schematically depicted in Fig. 5 as Neuber's hyperbola. By solving Eq. (6) for ε_{max}^a and substituting into Eq. (5), the following expression is obtained:

$$\frac{(K_{sf} \cdot \sigma_{max}^e)^2}{E \cdot \sigma_{max}^a} = \frac{\sigma_{max}^a}{E} + \left(\frac{\sigma_{max}^a}{K'}\right)^{\frac{1}{n'}} \tag{7}$$

Eq. (7) is represented in Fig. 5 by an intersection point between the cyclic stress–strain curve and Neuber's hyperbola. Since parameters K_{sf}, E, K', and n' are known material parameters, and σ_{max}^e is taken directly from the FE analysis, σ_{max}^a is the only unknown parameter. Once σ_{max}^a is found, ε_{max}^a can be obtained. Thus, maximum actual bending stress and strain values for the loading cycle are found.

The hysteresis loop curve of the material is employed to attain minimum actual bending stress and strain values and the end of the unloading cycle. Massing-type behavior [31] can be assumed as an adequate approximation in the absence of actual data [1], where a stable cyclic stress–strain curve is expanded by a factor of two. Hence, the hysteresis loop curve can be expressed as:

$$\Delta \varepsilon^a = \frac{\Delta \sigma^a}{E} + 2 \cdot \left(\frac{\Delta \sigma^a}{2 \cdot K'}\right)^{\frac{1}{n'}} \tag{8}$$
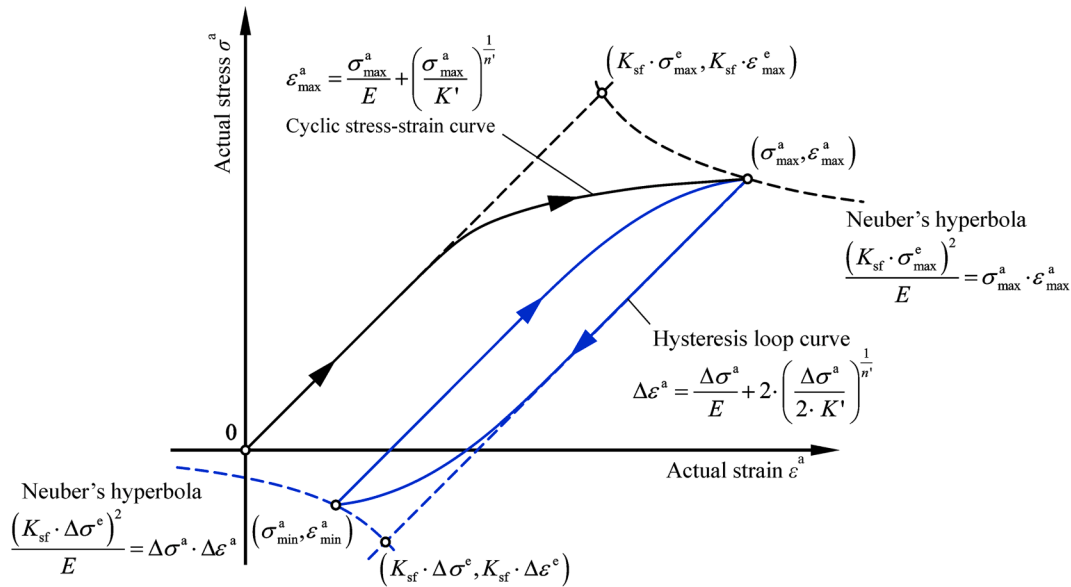
Fig. 5. Neuber's rule for constant amplitude cyclic loading.

where $\Delta\varepsilon^a$ is the actual bending strain range and $\Delta\sigma^a$ is the actual bending stress range. Analogous to the procedure described in Eqs. (5)–(7), minimum actual cyclic bending stress and strain can be obtained by intersecting the hysteresis loop curve and the Neuber's hyperbola, which are equal to:

$$\sigma_{min}^a = \sigma_{max}^a - \Delta\sigma^a \tag{9}$$

$$\varepsilon_{min}^a = \varepsilon_{max}^a - \Delta\varepsilon^a \tag{10}$$

Thus, actual bending stresses and strains are found based on linear-elastic ones by applying the elastic–plastic correction via Neuber's rule.

As previously mentioned, the strain-life approach ($\varepsilon - N$) is used in this paper to estimate the bending fatigue lives of spur gear [18]. In this approach, the relation between the actual strain amplitude and fatigue life for a fully reversed loading (stress ratio of $R = -1$) is expressed by the Basquin-Coffin-Manson equation:

$$\varepsilon_a^a = \frac{\Delta\varepsilon_e}{2} + \frac{\Delta\varepsilon_p}{2} = \frac{\sigma_f'}{E}\cdot(N_f)^b + \varepsilon_f'\cdot(N_f)^c \tag{11}$$

where ε_a^a is the actual total strain amplitude, $\frac{\Delta\varepsilon_e}{2}$ and $\frac{\Delta\varepsilon_p}{2}$ are elastic and plastic strain amplitudes, respectively, σ_f' is the fatigue strength coefficient, N_f is the number of cycles until fatigue failure, b is the fatigue strength exponent, ε_f' is the fatigue ductility coefficient, and c is the fatigue ductility exponent. Parameters σ_f', E, b, ε_f', and c are material properties, while ε_a^a is the output of the FE analysis and elastic–plastic correction via Neuber's rule. Therefore, an estimated number of cycles for bending fatigue failure, N_f, can be found. It should be mentioned that, as demonstrated in the introductory section [9-13], many methods for fatigue life estimation exist. However, since the fatigue model proposed in this paper is based on Basquin-Coffin-Manson equation which was already experimentally validated [18], it is also employed in this investigation. Otherwise, additional experimental validation of the obtained results would be required. Furthermore, in this paper, gear bending fatigue life is equalized with the crack initiation life, as recommended for case-hardened gears in [14]. Since Basquin-Coffin-Manson's equation is used for fatigue live estimation with regard to crack initiation as opposed to total fracture (which also includes propagation), it is also one of the reasons why this method is employed in this paper.

The bending stress cycle of a typical spur gear cannot be represented by a fully reversed loading. Ergo, mean stresses have to be accounted for. Furthermore, these mean stresses are modified due to the adjacent tooth effect. Such modification in the bending stress cycles can be accounted for by employing Smith-Watson-Topper (SWT) [32] or Morrow [33] mean stress correction methods, which are one of the most popular ones in engineering fields. Both methods have found successful applications for steel materials. However, Morrow's mean stress correction has demonstrated slightly better results than the SWT's one. Therefore, it is recommended for steel materials [30,34]. As a result, it is chosen as the mean stress correction method employed in this paper [17,18]. According to [30], Eq. (11) can be rewritten to account for mean and residual stresses:

$$\varepsilon_a^a = \frac{\sigma_f' - \sigma_m^a - \sigma_{res}}{E}\cdot(N_f)^b + \varepsilon_f'\cdot(N_f)^c \tag{12}$$

where σ_m^a is the actual mean stress and σ_{res} is the residual stress due to additional treatments such as surface hardening or surface finishing. Since residual stresses are regarded as pre-existing stresses within the material, no elastic–plastic correction is applied to them. Furthermore, mean and residual stresses are applied only to the elastic section of the Basquin-Coffin-Manson equation. In this way, stress relaxation due to plastic deformation, which is more prominent in low cycle fatigue regions, is simulated. In high cycle fatigue, mean and residual stresses are most often unable to completely relax due to insufficient plastic deformation. Hence, mean and residual stress effects are more evident in high cycle fatigue regimes.

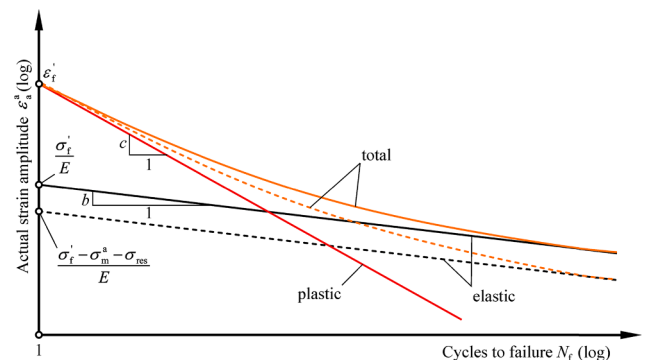The strain-life approach based on the Basquin-Coffin-Manson

Fig. 6. Schematic representation of strain-life approach with Morrow's mean stress correction.

equation and Morrow correction accounting for the effect of both mean and residual stresses is schematically depicted in Fig. 6.

According to Fig. 6, actual strain amplitude, ε_a^a, consist of the elastic strain amplitude, $\frac{\Delta\varepsilon_e}{2}$, and plastic strain amplitude, $\frac{\Delta\varepsilon_p}{2}$. It can be noticed that the plastic strain amplitude is more prominent in low-cycle fatigue region, whereas the elastic strain amplitude is more significant in high-cycle fatigue region. This is in accordance with the recognized effect of localized plasticity which contributes to a decrease of fatigue lives in low-cycle fatigue regions. The dashed lines in Fig. 6 represent Morrow's mean stress correction. As previously mentioned, this correction affects the elastic strain amplitude and consequently the total strain amplitude, while the plastic strain amplitude remains unaltered.

The computational model described in Section 2, which consists of FE and fatigue analysis, is applied to all nodes located at the observed tooth root. Node with the lowest estimated bending fatigue life, which is consequently the bending fatigue life of the entire spur gear, is denoted as the critical one and its location is recorded. As suggested in [14], the location of critical nodes, or for that matter any node at the observed tooth root fillet, is denoted by an angle φ. This angle is defined by two lines. The first line is the centerline of the gear tooth. The second line is tangent to the observed node at the root fillet (Fig. 7).

Due to the relative complexity of the aforementioned procedure, commercially available fatigue analysis software FE-Safe [30] is employed for estimating the location and required number of cycles for bending fatigue failure.

3. Results and discussion

3.1. Comparison of FE results with ISO 6336–3 standard

As previously mentioned, the fatigue model has already been successfully validated against experimental results in [18]. However, before employing the proposed computational bending fatigue model, the accuracy of the FE model has to be determined. Here, the maximum linear-elastic bending stress value is compared against analytical results obtained according to ISO 6336–3 standard [14]. An arbitrarily chosen torque value of $T = 350$ N•m is applied to the driven gear. It should be mentioned that the standard does not account for gear meshing, corresponding elastic tooth deformation, and migration of the contact point on the tooth flank. Furthermore, the location at the tooth root fillet with maximum linear-elastic bending stress is not the same as the one assumed by the standard. Lastly, due to tooth profile modifications described in the previous section, minor geometric dissimilarities exist between the standard tooth profile and the one employed within the numerical model. As a result, FE values are slightly lower than analytical values. Comparison between maximum bending stress values obtained via analytical and FE methods is presented in Fig. 8.

Maximum linear-elastic bending stress obtained according to ISO 6336–3 is equal to $\sigma_{max} = 1459.7$ MPawhile the one obtained via FE analysis is equal to $\sigma_{max}^e = 1413.4$ MPa. The difference between the obtained values is equal to 3.28%. Based on these results, it can be

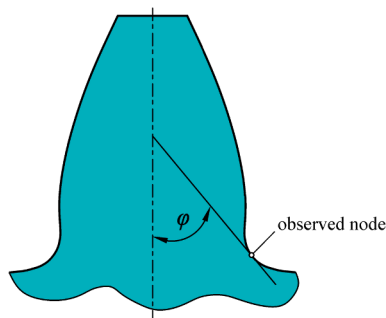**Fig. 7.** Location of a specific node at the observed tooth root fillet.
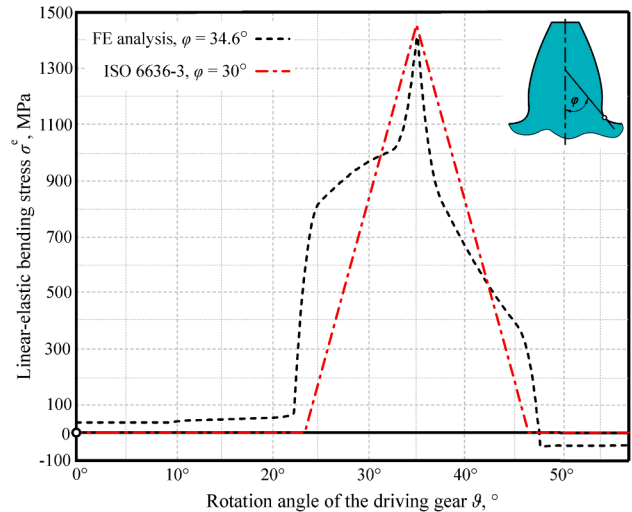
Fig. 8. Comparison of maximum linear-elastic bending stresses between the standard and the numerical model.

concluded that the accuracy of the FE analysis is adequate.

3.2. Fatigue model material properties

Before bending fatigue lives can be obtained and the effect of the adjacent tooth can be discussed, material parameters required for the fatigue model described in Section 2.2 have to be provided. For surface hardened steel materials, each material layer (case hardened and case layer) contains individual fatigue properties [35]. However, even though core material fatigue properties can be experimentally obtained via pulsating tests of specimens, case layer fatigue properties are relatively complicated to come by. In such instances, other approximation methods, whose effectiveness has already been demonstrated can be employed [17,36]. Therefore, strain-life properties required for the fatigue analysis are obtained according to the Hardness method proposed by Roesle and Fatemi [37]:

$$\sigma_f' = 425 \cdot HB + 225 \tag{13}$$

$$\varepsilon_f' = \frac{0.32 \cdot (HB)^2 - 487 \cdot HB + 191\,000}{E} \tag{14}$$

$$b = -0.56 \tag{15}$$

$$c = -0.09 \tag{16}$$

where HB is the averaged Brinell hardness for a specific layer. For the case layer, the hardness profile was obtained from [21] and its width is assumed as equal to the nominal case depth of 0.9652 mm [20]. According to the common practice when estimating hardness or residual stress value for a single layer [16,17,35], the average hardness of the case layer is estimated as 59.6 HRC [18]. Rockwell hardness is converted to Brinell hardness according to hardness conversion tables in [38], and it is approximately equal to 646 HB. As previously mentioned, only surface crack initiation is assumed in this paper. Thus, core layer properties are not provided here. In addition to strain-life properties, cyclic stress–strain properties required for elastic–plastic correction via Neuber's rule can be estimated as [1]:

$$K' = \frac{\sigma_f'}{\left(\varepsilon_f'\right)^{n'}} \tag{17}$$

$$n' = \frac{b}{c} \tag{18}$$

Finally, strain-life and cyclic stress–strain properties are obtained and presented in Table 2.

The surface finish quality of the gear tooth is specified as a maximum Ra value of 0.366 μm [20], which is accounted for within FE-Safe in the form of the surface finish correction factor K_{sf}. Lastly, according to [39] and analogous to the aforementioned procedure used for obtaining the case layer hardness, residual stress value within the case layer due to carburization is estimated as $\sigma_{res} = $ -415 MPa.

Once the FE model is verified and fatigue model parameters are provided, the proposed computational model is employed to investigate the effect of the adjacent tooth on bending fatigue lives of spur gears. To cover both low and high cycle fatigue regimes, torque values in the range of $T = 350$ N•m to $T = 600$ N•m with an interval of 50 N•m are applied to the driven gear for all subsequent analyses.

3.3. Effect of the adjacent tooth on bending fatigue lives

During gear meshing, the observed tooth root fillet of the driven gear experiences primarily tensile bending stresses (Fig. 9a). However, once the corresponding tooth of the observed fillet exits the mesh and tensile bending stresses are no longer present at the observed fillet, compressive bending stresses due to the contact between the following tooth (the adjacent tooth) and its corresponding tooth on the driving gear become dominant (Fig. 9b) [40-42].

The effect of the adjacent tooth on the linear-elastic bending stress cycle for an arbitrarily chosen root fillet node is schematically depicted in Fig. 10.

If the adjacent tooth effect is accounted for, the linear-elastic bending stress cycle represented in Fig. 10 is not entirely tensile; it also contains a compressive stress zone. This is manifested as mean stress modification, $\Delta\sigma_m$, and consequently a change in the stress amplitude of the cycle, $\Delta\sigma_a$.

A possible significant reason for not accounting for the adjacent tooth effect in the existing investigations can be found by considering a two-dimensional stress tensor for an arbitrarily chosen node at the observed tooth root fillet (Fig. 11).

When the observed tooth of the driven gear meshes with the corresponding tooth of the driving gear, the maximum principal stress of an arbitrarily chosen node at the observed fillet is tensile (mathematically positive value) and tangential to the fillet. According to Section 2 and Fig. 4, this stress is also the only non-zero principal stress at the observed tooth root fillet (as previously mentioned, it is referred to as the *bending stress* and denoted as σ). This is schematically depicted in Fig. 11a.

Once the observed tooth of the driven gear exists the mesh, bending stress changes its direction and becomes compressive (mathematically negative value) due to the adjacent tooth effect (Fig. 9b, Fig. 11b). For plane stress conditions, principal stress in the normal direction, σ_n, becomes the maximal principal stress even though its value is zero.

Since material fatigue is often associated with maximum tensile stresses, the effect presented in Fig. 11 tends to be overlooked [43] when estimating the bending fatigue lives of spur gears. For example, Abaqus-Standard software, which was employed for obtaining linear-elastic bending stresses in this paper, offers to plot three different types of principal stresses: maximum principal stress, minimum principal stress, and absolute maximum principal stress.

Maximum principal stress option plots linear-elastic bending stress cycle which is represented by the solid line in Fig. 10. This corresponds to a principal stress tensor depicted in Fig. 11a). *The minimum principal stress* option plots the linear-elastic bending stress cycle which is represented only by the dashed line in Fig. 10. This corresponds to a principal stress tensor depicted in Fig. 11b). As the name itself says, *absolute maximum principal stress* plots absolute values of principal stresses throughout the entire gear rotation cycle. This cycle can be seen in Fig. 10 by combining the solid black line and the dashed red line, and it is the most representative linear-elastic stress state among the three options.

As already mentioned in the introductory section, some researchers have considered the adjacent tooth effect when investigating bending stresses of spur gears. However, the effect of the adjacent tooth on the bending fatigue life of a spur gear undergoing actual gear meshing has not yet been investigated. Hence, bending fatigue lives of spur gears are obtained for different values of the applied torque with and without consideration of the adjacent tooth effect.

When the adjacent tooth effect is neglected, the minimum bending stress value for all root fillet nodes is zero, which occurs before the observed tooth enters and after it leaves the contact. Therefore, bending fatigue failure will occur at the node with the maximum linear-elastic bending stress. If the adjacent tooth effect is accounted for, the node with the maximum bending stress may not also be the critical one. This might transpire if the compressive stress zone of another node is large enough to result in a higher stress amplitude than the stress amplitude of the node with the maximum bending stress value. This is exactly the case in this investigation. Node with the maximum bending stress (located at $\varphi = 34.6°$) is critical when the adjacent tooth effect is not considered. However, when the adjacent tooth effect is accounted for, node located at $\varphi = 39.5°$ becomes the critical one even though its maximum value is slightly lower than the one at $\varphi = 34.6°$. This is demonstrated for the load of $T = 350$ N•m in Fig. 12 and Fig. 13.

According to Fig. 12, it can be observed that both nodes have almost identical maximum stress values. However, the node at $\varphi = 39.5°$ has a lower minimum stress value. Therefore, its stress amplitude is greater than the one of the node located at $\varphi = 34.6°$. Even though the critical node at $\varphi = 39.5°$ has lower mean bending stress (which by itself increases the fatigue life), an increase in the stress amplitude is still more significant than a decrease in the mean stress. This eventually leads to lower bending fatigue life of a spur gear. It should be mentioned that both critical locations are relatively close to each other, i.e., no significant shift in the failure location site is observed. However, a more considerable change in both failure location and corresponding fatigue lives might be observed in thin-rimmed gears, whose bending stress cycles are characterized by relatively large compressive stress zones [44,45]. This will be investigated in future works.

The effect of the adjacent tooth on bending fatigue lives for the applied torque range of $T = 350$ N•m to $T = 600$ N•m with an interval of 50 N•m is shown in Fig. 14. Maximum linear-elastic bending stress values for each corresponding torque are also provided for comparison purposes. It should be noted that these bending stress values are, as previously mentioned, very similar for both nodes ($\varphi = 39.5°$ and $\varphi = 34.6$, i.e., with and without the adjacent tooth effect). In other words, for a single torque value two bending stress values would have to be provided. To maintain figure simplicity, only maximum linear-bending stress values are provided for each torque, which always occur when the adjacent tooth effect is not accounted for ($\varphi = 34.6$).

Node located at $\varphi = 34.6°$ represents critical bending fatigue location for all applied torques when the adjacent tooth effect is not considered. Similarly, the node located at $\varphi = 39.5°$ is the critical one for all applied torques when the adjacent tooth effect is considered. The comparison depicted in Fig. 14 is also presented as numerical values in Table 3.

Although the presented differences in fatigue cycles might not be drastic, they are certainly not negligible. Moreover, consideration of the adjacent tooth effect results in conservative fatigue life predictions,

Table 2
Fatigue model parameters.

Parameter, symbol	Value	Parameter, symbol	Value
Fatigue strength coefficient,σ_f'	2970.5 MPa	Fatigue ductility exponent, c	−0.09
Fatigue strength exponent, b	−0.56	Cyclic strength coefficient,K'	4838.95 MPa
Fatigue ductility coefficient,ε_f'	0.048015	Cyclic strength exponent,n'	0.160714
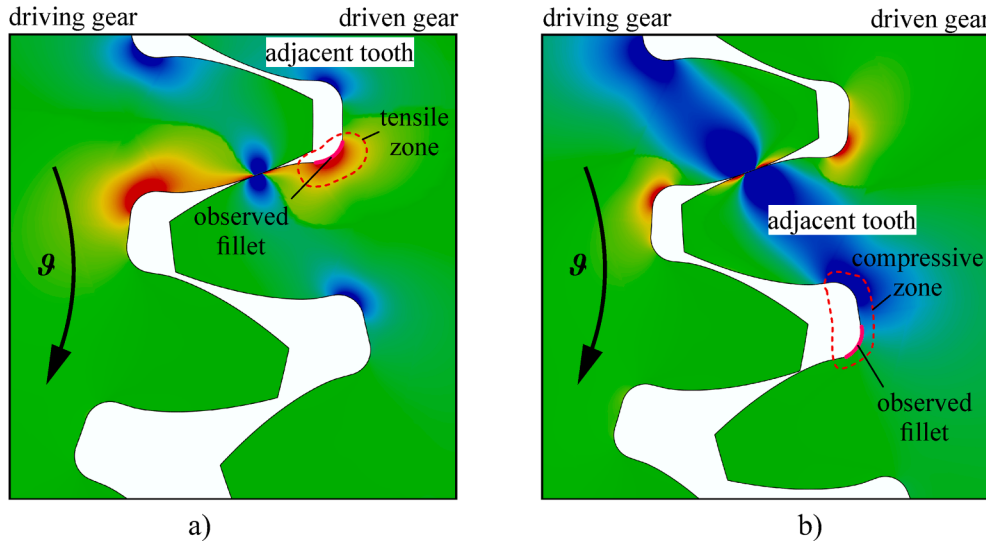
Fig. 9. Effect of the adjacent tooth on linear-elastic bending stresses: a) tensile stress zone at the observed fillet during gear mesh, and b) compressive stress zone at the observed fillet after meshing due to adjacent tooth contact.
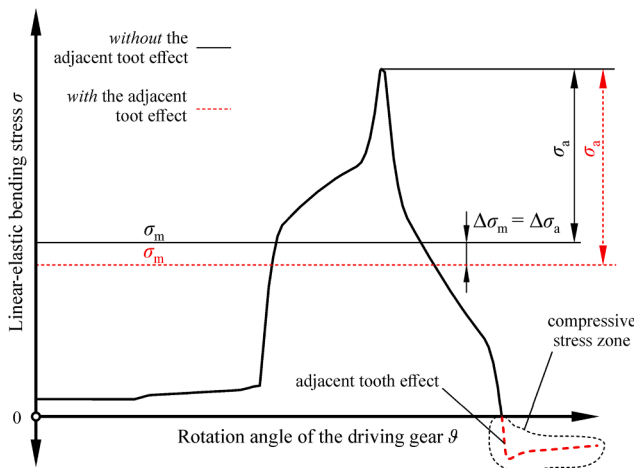
Fig. 10. The effect of the adjacent tooth on linear-elastic bending stress cycle.
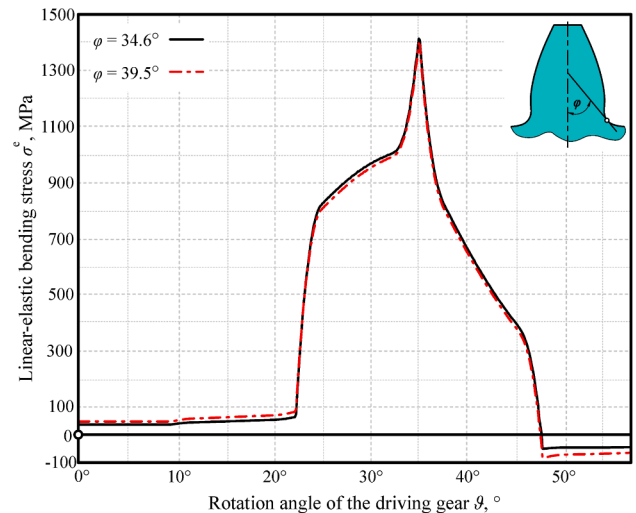
Fig. 12. Comparison of linear-elastic bending stress cycles between $\varphi = 34.6°$ and $\varphi = 39.5°$ for $T = 350$ N•m.

which adds to the safety of fatigue life predictions. Based on the provided results, it can be concluded that this effect should be accounted for when estimating the bending fatigue lives of spur gears.

Furthermore, according to the data provided in Table 3, an interesting effect can be observed. Regardless of the applied load, a roughly constant percentage difference exists between estimated bending fatigue lives with and without consideration of the adjacent tooth effect, which is approximately equal to 22%. This is not a common phenomenon in material fatigue since the high cycle fatigue region is more susceptible to a change in the applied load. In other words, a higher percentage difference in bending fatigue lives is expected in high cycle fatigue when the applied load is linearly increased. Therefore, it would be interesting to further investigate the exact cause of this phenomenon. More specifically, whether a modifying factor can be applied which accounts for the adjacent tooth effect when estimating bending fatigue lives.

Fig. 11. Principal stresses for an arbitrarily chosen surface node at the observed tooth root fillet: a) stress tensor during meshing of the observed tooth, and b) stress tensor once the observed tooth exits the mesh.
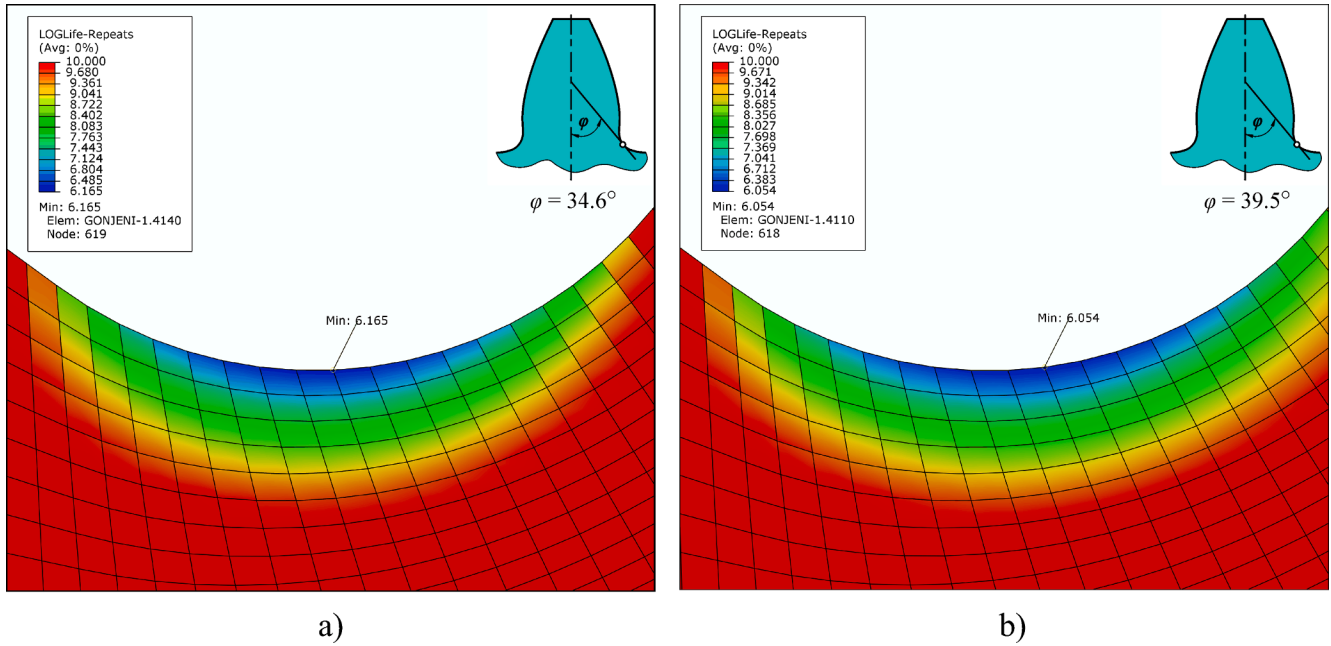
Fig. 13. Bending fatigue life of spur gear for $T = 350$ N•m: a) *without* consideration of the adjacent tooth effect, and b) *with* consideration of the adjacent tooth effect.
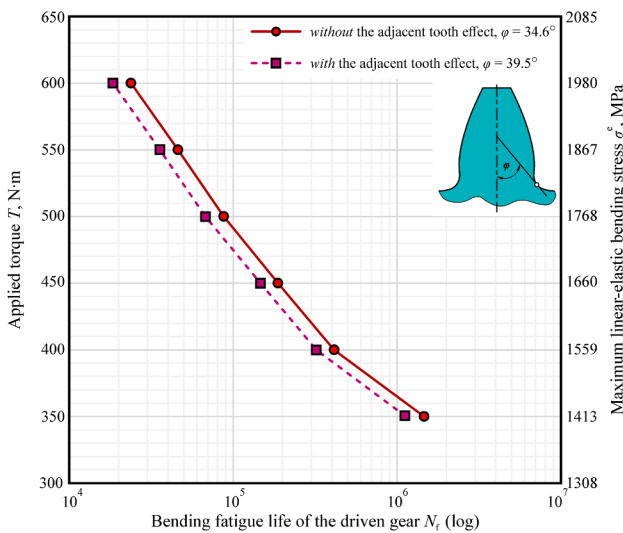
Fig. 14. Effect of the adjacent tooth on bending fatigue lives.

Table 3
Effect of the adjacent tooth on bending fatigue lives – numerical values.

Driven gear torque T, N•m	Bending fatigue life *without* the adjacent tooth effect, cycles	Bending fatigue life *with* the adjacent tooth effect, cycles	Difference
350	1 462 487	1 132 936	22.53%
400	412 884	321 819	22.06%
450	187 849	146 755	21.88%
500	87 582	67 647	22.75%
550	46 044	35 775	22.30%
600	23 814	18 439	22.57%

3.4. Adjacent tooth effect modifying factor C_{ATE}

As described in Section 2, bending fatigue lives without consideration of the adjacent tooth effect ($R = 0$) can be calculated according to the following expression:

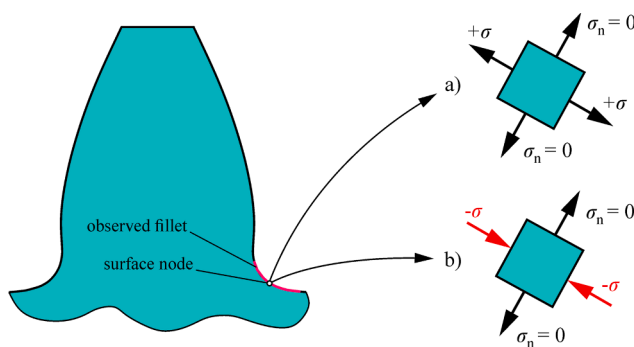$$\varepsilon_a^a = \frac{\Delta\varepsilon_e}{2} + \frac{\Delta\varepsilon_p}{2} = \frac{\sigma_f' - \sigma_m^a - \sigma_{res}}{E}\cdot(N_f)^b + \varepsilon_f'\cdot(N_f)^c \tag{19}$$

According to Fig. 10 and Fig. 12, the adjacent tooth effect influences both actual mean stress σ_m^a and actual strain amplitude ε_a^a. Thus, Eq. (19) can be written as:

$$\varepsilon_a^{a*} = \frac{\Delta\varepsilon_e^*}{2} + \frac{\Delta\varepsilon_p^*}{2} = \frac{\sigma_f' - \sigma_m^{a*} - \sigma_{res}}{E}\cdot\left(N_f^*\right)^b + \varepsilon_f'\cdot\left(N_f^*\right)^c \tag{20}$$

where superscript * represents parameters that include the adjacent tooth effect. Modifying factors C_ε and C_m are applied to define the ratio between actual strain amplitudes and actual mean stresses with and without consideration of the adjacent tooth effect, such that:

$$\varepsilon_a^{a*} = \varepsilon_a^a\cdot C_\varepsilon \tag{21}$$

$$\sigma_m^{a*} = \sigma_m^a\cdot C_m \tag{22}$$

By combining Eqs. (21) and (22) with Eq. (20), the following expression is obtained:

$$C_\varepsilon\cdot\varepsilon_a^a = C_\varepsilon\cdot\left(\frac{\Delta\varepsilon_e}{2} + \frac{\Delta\varepsilon_p}{2}\right) = \frac{\sigma_f' - C_m\cdot\sigma_m^a - \sigma_{res}}{E}\cdot\left(N_f^*\right)^b + \varepsilon_f'\cdot\left(N_f^*\right)^c \tag{23}$$

According to Table 3, a roughly constant difference between calculated bending fatigue lives with and without consideration of the adjacent tooth effect is observed. In other words:

$$\frac{N_f^*}{N_f} \approx C_{ATE} \tag{24}$$

where C_{ATE} is a modifying factor accounting for the change in bending fatigue lives due to the adjacent tooth effect. Modifying factor

C_{ATE} can be obtained by solving for N_f and N_f^* in Eqs. (19) and (23), respectively, and finding their ratio according to Eq. (24). However, these expressions are relatively complex to solve for their respective fatigue lives, which implies that additional simplifications of the aforementioned relations are required.

Eqs. (19) and (23) could be further simplified by assuming the negligible effect of plastic strain amplitude, $\frac{\Delta \varepsilon_p}{2}$. For that purpose, the effect of plastic deformation on actual strain amplitudes used in bending fatigue life estimation is investigated for the highest value of the applied torque, $T = 600$ N•m. When the adjacent tooth effect is not considered, a difference of approximately 0.5% is obtained between linear-elastic strain amplitude taken directly from the FE analysis, $\varepsilon_{\text{aFE}}^e$, and the actual (corrected by Neuber's rule) elastic–plastic strain amplitude, ε_a^a. When the adjacent tooth effect is considered, this difference is approximately equal to 0.68%. Based on these two differences, a reasonable approximation can be made by omitting the elastic–plastic correction via Neuber's rule only to obtain a modifying factor C_{ATE}. Therefore, Eqs. (19) and (23) can be rewritten as:

$$\varepsilon_{\text{aFE}}^e = \frac{\sigma_f' - \sigma_m - \sigma_{\text{res}}}{E} \cdot (N_f)^b \tag{25}$$

$$C_\varepsilon \cdot \varepsilon_{\text{aFE}}^e = \frac{\sigma_f' - C_m \cdot \sigma_m - \sigma_{\text{res}}}{E} \cdot \left(N_f^*\right)^b \tag{26}$$

Consequently, modifying factors C_ε and C_m described in Eqs. (21) and (22) are also modified:

$$\varepsilon_{\text{aFE}}^{e*} = \varepsilon_{\text{aFE}}^e \cdot C_\varepsilon \tag{27}$$

$$\sigma_m^* = \sigma_m \cdot C_m \tag{28}$$

Since the effect of elastic–plastic correction is neglected, actual mean stress σ_m^a becomes linear-elastic mean stress σ_m taken directly from the FE analysis. By equalizing linear-elastic strain amplitudes $\varepsilon_{\text{aFE}}^e$ provided by Eqs. (25) and (26), the following expression is obtained:

$$\frac{\sigma_f' - \sigma_m - \sigma_{\text{res}}}{E} \cdot (N_f)^b = \frac{\sigma_f' - C_m \cdot \sigma_m - \sigma_{\text{res}}}{C_\varepsilon \cdot E} \cdot \left(N_f^*\right)^b \tag{29}$$

Modifying factor C_{ATE} can then be written as:

$$C_{\text{ATE}} = \frac{N_f^*}{N_f} = \left(\frac{\frac{\sigma_f' - \sigma_m - \sigma_{\text{res}}}{E}}{\frac{\sigma_f' - C_m \cdot \sigma_m - \sigma_{\text{res}}}{C_\varepsilon \cdot E}} \right)^{\frac{1}{b}} \tag{30}$$

By rewriting Eq. (30), modifying factor C_{ATE} is finally defined as:

$$C_{\text{ATE}} = \left[\frac{C_\varepsilon \cdot (1 - \sigma_{\text{ATE}})}{1 - C_m \cdot \sigma_{\text{ATE}}} \right]^{\frac{1}{b}} \tag{31}$$

where a supplementary factor σ_{ATE} is applied for simplicity, which is a constant value equal to:

$$\sigma_{\text{ATE}} = \frac{\sigma_m}{\sigma_f' - \sigma_{\text{res}}} \tag{32}$$

In Eq. (32), σ_f' and σ_{res} are material properties defined in Section 3.2 for the observed tooth root fillet, while σ_m is the mean linear-elastic bending stress taken from FE analysis without consideration of the adjacent tooth effect ($R = 0$). Since stresses (instead of strains) are usually preferred as the output of FE analyses, Eq. (27) can be modified to express the modifying factor C_ε as:

$$C_\varepsilon = \frac{\varepsilon_{\text{aFE}}^{e*}}{\varepsilon_{\text{aFE}}^e} = \frac{\frac{\sigma_{\text{aFE}}^{e*}}{E}}{\frac{\sigma_{\text{aFE}}^e}{E}} = \frac{\sigma_{\text{aFE}}^{e*}}{\sigma_{\text{aFE}}^e} \tag{33}$$

where σ_{aFE}^{e*} and σ_{aFE}^e are linear-elastic bending stress amplitudes obtained via FE analysis with and without consideration of the adjacent tooth effect, respectively.

Lastly, the modifying factor C_m is equal to:

$$C_m = \frac{\sigma_m^*}{\sigma_m} \tag{34}$$

Based on Eqs. (31)–(34), modifying factor C_{ATE} which alters the estimated bending fatigue lives to account for the adjacent tooth effect can be obtained. However, as suggested by Eqs. (33) and (34), the relationship between linear-elastic bending stress amplitudes and mean stresses obtained via FE analysis has to be determined for each value of the applied torque.

As already demonstrated in the example in Fig. 12 for $T = 350$ N•m, both maximum and minimum linear-elastic bending stresses are disproportionally modified when the adjacent tooth effect is accounted for. In other words, factors C_ε and C_m are separately determined for each value of the applied torque. However, it was observed that maximum linear-elastic bending stresses with and without the adjacent tooth effect are very similar for each applied torque (Fig. 12), with the difference being approximately equal to 1%. Hence, only to obtain the modifying factor C_{ATE}, it is assumed that the adjacent tooth effect does not influence maximum linear-elastic bending stresses.

If $R = 0$ stress cycle with arbitrarily chosen values is taken as an example, lowering its minimum stress value while keeping its maximum value constant will increase the stress amplitude and proportionally decrease the mean stress value. In other words, if the stress amplitude increases by a factor of C_ε (as is the case in the adjacent tooth effect), mean stress will decrease by a factor of $C_m = 1 - (C_\varepsilon - 1) = 2 - C_\varepsilon$. Therefore, Eq. (31) can be further simplified as:

$$C_{\text{ATE}} = \left[\frac{C_\varepsilon \cdot (1 - \sigma_{\text{ATE}})}{1 - \sigma_{\text{ATE}} \cdot (2 - C_\varepsilon)} \right]^{\frac{1}{b}} \tag{35}$$

Modifying factor C_{ATE} calculated according to Eqs. (31) and (35) is applied to bending fatigue life cycles without consideration of the adjacent tooth effect (2nd column in Table 3). The results are then compared against the number of cycles with consideration of the adjacent tooth effect from Table 3 (3rd column) obtained by the computational model. The comparison is depicted in Fig. 15. Analogous to the description provided for Fig. 14, maximum linear-elastic bending stress values for each corresponding torque are also provided for comparison purposes.

According to Fig. 15, a good correlation is observed between bending fatigue lives obtained by the computational model and the ones obtained by applying the modifying factor C_{ATE}. More specifically, a maximum difference of approximately 4% is observed when C_{ATE} according to Eq. (31) is applied, while the maximum difference of approximately 10% is observed when employing a simplified expression of C_{ATE} according to

Fig. 15. Estimated bending fatigue lives with consideration of the adjacent tooth effect based on the computational model and modifying factor C_{ATE}.

Eq. (35). These differences are with respect to bending fatigue lives obtained by the computational model that considers the adjacent tooth effect. Since both types of C_{ATE} result in conservative yet relatively accurate approximations, it can be concluded that the proposed modifying factor may be suitable in accounting for the adjacent tooth effect when estimating bending fatigue lives of carburized spur gears.
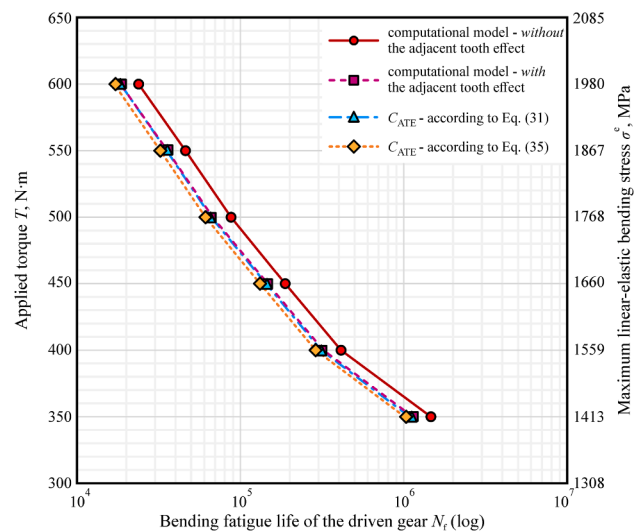
However, this modifying factor is proposed for higher cycle fatigue regions which are characterized by predominantly linear-elastic material behavior. Thus, its applicability in low cycle fatigue ($\langle 10^4$) has to be further investigated. Moreover, the relationship between maximum and minimum linear-elastic bending stress values should be predetermined within the corresponding finite element software. This relationship depends upon multiple parameters, such as the gear pair geometry, tooth profile, and the shape of the tooth root fillet. Lastly, to possibly provide additions to the existing gear load capacity standards, the application of the proposed modification factor for other gear materials has to be further investigated. Therefore, additional investigations should be conducted to determine the nature of this relationship with adequate accuracy.

4. Conclusions

In this paper, a computational model for bending fatigue life estimation of case hardened spur gears, which is comprised of finite element and fatigue model, was proposed. Gear meshing was simulated via finite element analysis, which was compared against the results from the existing standard. Fatigue lives were estimated according to the previously validated fatigue model via strain – life ($\varepsilon – N$) approach, where actual bending stress–strain state was obtained by employing elastic–plastic correction based on Neuber's rule. The effect of the adjacent tooth on bending fatigue lives was investigated by employing the presented model. Lastly, the modifying factor C_{ATE} was proposed which modifies bending fatigue lives to account for the adjacent tooth effect. The following conclusions are made:

- Good agreement was observed between the linear-elastic tooth root stresses obtained via finite element method and ISO 6336 standard. Combined with the previously validated fatigue model, it can be concluded that the proposed computational model reasonably estimates bending fatigue lives of spur gears under the assumption of surface crack initiation.
- The adjacent tooth effect influences both mean bending stress and bending stress amplitude of a spur gear. Based on the computational model, bending fatigue lives were decreased by approximately 22% when compared to instances where no adjacent tooth effect was considered. Furthermore, a shift in the failure location was observed, i.e., it was no longer at the location with the maximum stress value.
- A modifying factor C_{ATE} and its simplified form were proposed which modify bending fatigue lives based on numerical data to account for the adjacent tooth effect. By comparing the corrected bending fatigue lives with the ones obtained by the computational model, a maximum decrease of roughly 4% is observed when C_{ATE} is applied and 10% when simplified C_{ATE} is employed. Since both types of modifying factors result in conservative yet adequate estimations, C_{ATE} can be used to account for the adjacent tooth effect when estimating bending fatigue lives of carburized spur gears under the assumption of surface failure.

In future studies, subsurface bending fatigue crack initiation will be investigated by considering both case and core layers of a case hardened spur gear. Furthermore, the proposed model will be modified and applied to spur gears with greater thickness as well as helical gears. Lastly, to further simplify the proposed modifying factor, a more detailed investigation of the relationship between maximum and minimum linear-elastic bending stresses obtained via finite element analysis will be conducted.

Declaration of Competing Interest

The authors declare that they have no known competing financial interests or personal relationships that could have appeared to influence the work reported in this paper.

References

[1] Stephens R, Fatemi A, Stephens R, Fuchs H. Metal Fatigue in Engineering. 2nd Edition. John Wiley & Sons, inc.; 2001.

[2] Zhan J, Fard M, Jazar R. A quasi-static FEM for estimating gear load capacity. Measurement 2015;75(2015):40–9. https://doi.org/10.1016/j.measurement.2015.07.036.

[3] 2001-D04, Fundemental Rating Factors and Calculation Methods for Involute Spur and Helical Gear Teeth, Alexandria: American Gear Manufacturers Association, 2004.

[4] Lias M, Sharif Z, Awang M, Jailani A, Warap H. Quasi-static modeling of spur gear time varying strength analysis. Journal of Engineering and Applied Sciences 2017; 12(6):1938–47.

[5] Manojkumar D, Sravani SK, Bharghavi B. Comparative Fatigue Life Prediction of Spur Gear Under Fully Reversed Loading by Using Finite Element Analysis. International Journal of Research in Mechanical Engineering & Technology 2016;6 (2):12–7. https://doi.org/10.29002/asujse.498344.

[6] Jabbour T, Asmar G. Tooth stress calculation of metal spur gears and helica gears. Mech Mach Theory 2015;92:375–90. https://doi.org/10.1016/j.mechmachtheory.2015.06.003.

[7] Thirumurugan R, Deepak CCC, Karthieeban K. Effect of Adjacent Teeth Load on Bending Strength of High Contact Ratio Asymmetrical Spur Gear Drive. International Journal of Vehicle Structures & Systems 2017;9(1):32–5. https://doi.org/10.4273/ijvss.9.1.07.

[8] Jiang H, Liu F. Analytical models of mesh stiffness for cracked spur gears considering gear body deflection and dynamic simulation. Meccanica 2019;54 (2019):1889–909. https://doi.org/10.1007/s11012-019-01053-9.

[9] He H, Liu H, Zhu C, Wei P, Sun Z. Study of rolling contact fatigue behavior of a wind turbine gear based on damage-coupled elastic-plastic model. Int J Mech Sci 2018;141:512–9. https://doi.org/10.1016/j.ijmecsci.2018.03.044.

[10] H. He, H. Liu, C. Zhu and A. Mura, "Numerical study on fatigue crack propagation behaviors in lubricated rolling contact," Chinese Journal of Aeronautics, In Press, 2021. DOI: 10.1016/j.cja.2021.03.012.

[11] Gloděz S, Abersek B, Flašker J, Kramberger J. Evaluation of the Service Life of Gear in Regard to Bending Fatigue in a Gear Tooth Root. Key Eng Mater 2003;251–252: 297–302. https://doi.org/10.4028/www.scientific.net/KEM.251-252.297.

[12] H. Liu, H. Liu, C. Zhu, H. He and P. Wei, "Evaluation of Contact Fatigue Life of a Wind Turbine Gear Pair Considering Residual Stress," Journal of Tribology, vol. 140 (4), 2018. DOI: 10.1115/1.4039164.

[13] Lin Y, Liu S, Zhao X, Mao E, Cao C, Steve Suh C. Fatigue life prediction of engaging spur gears using power density. Journal of Mechanical Engineering Science 2018; 232(23):4332–41. https://doi.org/10.1177/0954406217751557.

[14] ISO 6336-3, Calculation of Load Capacity of Spur and Helical Gears – Part 3: Calculation of tooth bending strength, Geneva: International Standard Organization, 2006.

[15] Savaria V, Bridier F, Bocher P. Predicting the effects of material properties gradient and residual stresses on the bending fatigue strength of induction hardened aeronautical gears. Int J Fatigue 2016;85:70–84. https://doi.org/10.1016/j.ijfatigue.2015.12.004.

[16] Jo B, Sharifimehr S, Shim Y, Fatemi A. Cyclic deformation and fatigue behavior of carburized automotive gear steel and predictions including multiaxial stress states. Int J Fatigue 2017;100(2):454–65. https://doi.org/10.1016/j.ijfatigue.2016.12.023.

[17] Čular I, Vučković K, Žeželj D, Gloděz S. Analytical approach for low and high cycle bending fatigue life prediction of carburized gear steel specimens. Eng Fail Anal 2020;108:104328. https://doi.org/10.1016/j.engfailanal.2019.104328.

[18] Vučković K, Galić I, Božić Ž, Gloděz S. Effect of friction in a single-tooth fatigue test. Int J Fatigue 2018;114:148–58. https://doi.org/10.1016/j.ijfatigue.2018.05.005.

[19] ABAQUS Version 6.13, Dassault Systems (2013).

[20] Handschuh R, Krantz T, Lerch B, Burke C. Low-Cycle Bending Fatigue of AISI 9310 Steel Spur Gears. NASA/TM-2007-214914 2007.

[21] D. Lewicki, Crack Propagation Studies to Determine Benign or Catastrophic Failure Modes For Aerospace Thin-Rim Gears, Ph.D. Thesis, Cleveland, Ohio: NASA TM-107170, ARL–TR–971, 1996.

[22] Pehan S, Hellen T, Flašker J, Gloděz S. Numerical methods for determining stress intensity factors vs crack depth in gear tooth roots. Int J Fatigue 1997;19(10): 677–85. https://doi.org/10.1016/S0142-1123(97)00101-1.

[23] Hohn B, Michaelis K, Doleschel A. Frictional behaviour of synthetic gear lubricants. Tribology Series 2001;39:759–68. https://doi.org/10.1016/S0167-8922(01)80156-5.

[24] Martins R, Seabra J, Brito A, Seyfert C, Luther R, Igartua A. Friction coefficient in FZG gears lubricated with industrial gear oils: Biodegradable ester vs. mineral oil. Tribol Int 2006;39(6):512–21. https://doi.org/10.1016/j.triboint.2005.03.021.

[25] Neuber H. Theory of Stress Concentration for Shear Strained Prismatical Bodies with Arbitrary Non-Linear Stress Strain Law. J Appl Mech 1961;28(4):544–50.

[26] Glodež S, Šraml M, Kramberger J. A Computational Model for Determination of Service Life of Gears. Int J Fatigue 2002;24(10):1013–20. https://doi.org/10.1016/S0142-1123(02)00024-5.

[27] Kramberger J, Šraml M, Glodež S, Flašker J, Potrč I. Computational model for the analysis of bend- ing fatigue in gears. Comput Struct 2004;82(23–26):2261–9. https://doi.org/10.1016/j.compstruc.2003.10.028.

[28] Podrug S, Jelaska D, Glodež S. Influence of different load models on gear crack path shapes and fatigue lives. Fatigue & Fracture of Engineering Materials Structures 2008;31(5):327–39. https://doi.org/10.1111/j.1460-2695.2008.01229.x.

[29] Singh MNK, Glinka G, Dubey RN. Elastic-plastic stress-strain calculation in notched bodies subjected to non-proportional loading. Inernational Journal of Fracture 1986;76(1):39–60. https://doi.org/10.1007/BF00034029.

[30] FE-SAFE Version 6.5, User guide, Safe technology limited, 2014.

[31] G. Massing, "Eigenspannungen und verfestigung beim messing (Self stretching and hardening for brass)," in Proceedings of the 2nd Int. Congress for Applied Mechanics, Zürich, 1926.

[32] Smith K, Watson P, Topper T. A stress-strain function for the fatigue of materials. Journal of Materials 1970;5:767–78.

[33] J. Morrow, "Fatigue Properties of Metals," in Fatigue Design Handbook, Warrendale, PA, SAE, 1968.

[34] Dowling N., "Mean Stress Effects in Stress-Life and Strain-Life Fatigue," in 2nd SAE Brasil International Conference on Fatigue, Sao Paulo, Brasil, 2004. DOI: 10.4271/2004-01-2227.

[35] Yin F, Fatemi A. Fatigue behaviour and life predictions of case-hardened steels. Fatigue Fract Eng Mater Struct 2009;32(3):197–213. https://doi.org/10.1111/j.1460-2695.2009.01326.x.

[36] Lee K, Song J. Estimation methods for strain-life fatigue properties from hardness. Int J Fatigue 2006;28(4):386–400. https://doi.org/10.1016/j.ijfatigue.2005.07.037.

[37] Roessle ML, Fatemi A. Strain-Controlled Fatigue Properties of Steels and Some Simple Approximations. Int J Fatigue 2000;22(6):495–511. https://doi.org/10.1016/S0142-1123(00)00026-8.

[38] ASTM E140, Standard Hardness Conversion Tables for Metals Relationship Among Brinell Hardness, Vickers Hardness, Rockwell Hardness, Superficial Hardness, Knoop Hardness, Scleroscope Hardness, and Leeb Hardness, West Conshohocken, PA: ASTM International, 2012.

[39] T. Krantz, "The Influence of Roughness on Gear Surface Fatigue," in Nasa Technical Reports Server, BiblioGov, 2013.

[40] Linke H, Borner J. The influence of neighboring teeth on the tooth root capacity. Angew Chem Int Ed 1967;6(11):177–82.

[41] D.R. McPherson and S.B. Rao, "Methdology for Translating Single-Tooth Bending Fatigue Data to be Comparable to Running Gear Data", Gear Technology, March/April, 2008.

[42] H. Linke, J. Börner, and R. Heß, "Cylindrical Gears: Calculation – Materials – Manufacturing", Hanser, Munich, 2016.

[43] Concli F, Fraccaroli L, Maccioni L. Gear Root Bending Strength: A New Multiaxial Approach to Translate the Results of Single Tooth Bending Fatigue Tests to Meshing Gears. Metals 2021;11:863. https://doi.org/10.3390/met11060863.

[44] M. Opalić, K. Vučković, D. Žeželj and S. Risović, "Prediction of thin-rim gears bending fatigue crack initiation life," in PROCEEDINGS - The 7th International Scientific Conference - Research and Development of Mechanical Elements and Systems, Zlatibor, Serbia, 2011.

[45] Yilmaz T, Kalay O, Karpat F. Stress analysis of thin rimmed asymmetric spur gears. International Journal of Advances on Automotive and Technology 2018;2(3):143–50. https://doi.org/10.15659/ijaat.18.09.991.

Paper III

The manuscript shown within this thesis is published in:

Contributions of the Ph.D. candidate:

- establishing the computational model
- validating the model against experimental results
- interpreting and discussing the results
- writing the manuscript

Computational model for bending fatigue prediction of surface hardened spur gears based on the multilayer method

Ivan Čular [a],[*], Krešimir Vučković [a], Srečko Glodež [b], Zdenko Tonković [a]

[a] University of Zagreb, Faculty of Mechanical Engineering and Naval Architecture, I. Lučića 5, 10000 Zagreb, Croatia
[b] University of Maribor, Faculty of Mechanical Engineering, Smetanova ul. 17, 2000 Maribor, Slovenia

A B S T R A C T

A computational model for predicting both the location and the required number of cycles for bending fatigue failure in surface hardened spur gears is proposed. Linear elastic stresses and strains in a single tooth bending fatigue test are corrected for elastic–plastic material behavior. The tooth root region of spur gear is divided into layers. Fatigue properties are assigned to each layer via the hardness method. Based on the multiaxial fatigue criteria, fatigue failure location and corresponding fatigue lives are estimated. Predicted fatigue lives, failure locations, and transition from surface to subsurface fatigue failure show good agreement with the experimental results.

1. Introduction

Metal gears are one of the most widely utilized mechanical components for power transmission. Due to their geometric characteristics and loading conditions, the tooth root region of a gear experiences cyclic loading. This type of loading results in material fatigue in the tooth root region, which is more commonly known as bending fatigue. Bending fatigue may also result in the appearance of cracks. With the continuation of cyclic loading, these cracks may propagate and cause tooth breakage and consequently complete failure of a gear. Typically, if gear design is properly done according to the existing standards [1,2] while keeping in mind the operating conditions of gear, the probability of bending fatigue can be significantly reduced. However, metal gears are often surface hardened by additional thermal or mechanical processes, such as carburizing and shot peening [3]. Even though induced residual stresses by the aforementioned processes are beneficial for suppressing surface fatigue failure, they may promote subsurface failure typical for higher cycle fatigue regions. Since subsurface cracks are not easily detectable during regular service intervals, they may often go unnoticed. These cracks may rapidly propagate through a relatively brittle surface hardened layer and result in complete failure of the tooth and consequently, the gear.

Due to the relative geometric complexity of gears, many researchers have often investigated subsurface fatigue failure on simple surface hardened specimens made of typical gear steel material. Yin and Fatemi

[4] experimentally and analytically investigated monotonic and cyclic deformations of case-hardened gear steel specimens under axial loading by employing the multilayer method. The authors observed that the predicted cyclic stress–strain curves were higher than the experimental ones. Jo et al. [5] investigated the fatigue behavior of carburized gear steel specimens under axial loading. They applied a two-layer method to obtain the required number of cycles and location (surface vs. subsurface) of fatigue failure and concluded that the results are comparatively similar to the experimental data. To investigate the effect of mean stress on fatigue failure location, Gaur et al. [6] conducted axial stress-controlled tests on 2.5 %Cr-1 %Mo steel. The authors observed that surface crack occurred for almost all values of stress ratio R, while subsurface crack initiation was only achieved for $R = 0.25$. Yin et al. [7] also employed the multilayer method to investigate surface and subsurface fatigue crack initiation in axially loaded case hardened gear steel specimens. In addition, they discussed the role of residual stresses in fatigue failures. The authors have concluded that the obtained results correspond well with the experimental ones. The existing investigations that employ surface hardened gear steel specimens are almost all conducted for axial loading. This is not an accurate representation of the actual stress cycle experienced by the gear tooth root, which is mainly the result of bending moment due to the normal force acting upon the tooth flank. Therefore, Čular et al. [8] have proposed an analytical multilayer method for estimating both low and high cycle bending fatigue of typical gear steel specimens subjected to fully reversed bending loading. The obtained bending fatigue life results showed good

---

<table>
<tbody>
<tr><td colspan="2">Nomenclature</td><td>ε_3^e</td><td>minor linear elastic principal strain amplitude</td></tr>
<tr><td></td><td></td><td>ε_{max}^e</td><td>maximum value of linear elastic strain amplitude</td></tr>
<tr><td></td><td></td><td>ε_{min}^e</td><td>minimum value of linear elastic strain amplitude</td></tr>
<tr><td>b</td><td>fatigue strength exponent</td><td>σ_f'</td><td>fatigue strength coefficient</td></tr>
<tr><td>c</td><td>fatigue ductility exponent</td><td>σ_1</td><td>major principal stress</td></tr>
<tr><td>E</td><td>modulus of elasticity</td><td>σ_2</td><td>intermediate principal stress</td></tr>
<tr><td>Fp</td><td>pulsating force acting on the loading anvil</td><td>σ_3</td><td>minor principal stress</td></tr>
<tr><td>K'</td><td>cyclic strength coefficient</td><td>σ_1^a</td><td>major actual principal stress amplitude</td></tr>
<tr><td>Ksf</td><td>surface finish correction factor</td><td>σ_2^a</td><td>intermediate actual principal stress amplitude</td></tr>
<tr><td>Nf</td><td>number of reversals until failure</td><td>σ_3^a</td><td>minor actual principal stress amplitude</td></tr>
<tr><td>2Nf</td><td>number of reversals until failure</td><td>σ_{max}^a</td><td>maximum value of actual stress amplitude</td></tr>
<tr><td>n'</td><td>cyclic strength exponent</td><td>σ_{min}^a</td><td>minimum value of actual stress amplitude</td></tr>
<tr><td>$\Delta\varepsilon^a$</td><td>actual strain range</td><td>σ_1^e</td><td>major linear elastic principal stress amplitude</td></tr>
<tr><td>$\Delta\varepsilon^e$</td><td>elastic strain range in Baquin-Coffin-Manson's equation</td><td>σ_2^e</td><td>intermediate linear elastic principal stress amplitude</td></tr>
<tr><td>$\Delta\varepsilon^p$</td><td>plastic strain range in Baquin-Coffin-Manson's equation</td><td>σ_3^e</td><td>minor linear elastic principal stress amplitude</td></tr>
<tr><td>$\Delta\sigma^a$</td><td>actual stress range</td><td>σ_{max}^e</td><td>maximum value of linear elastic stress amplitude</td></tr>
<tr><td>ε_a</td><td>strain amplitude in Baquin-Coffin-Manson's equation</td><td>σ_{min}^e</td><td>minimum value of linear elastic stress amplitude</td></tr>
<tr><td>ε_f'</td><td>fatigue ductility coefficient</td><td>σ_m</td><td>mean load-induced stress in Baquin-Coffin-Manson's equation</td></tr>
<tr><td>ε_1^a</td><td>major actual principal strain amplitude</td><td>σ_m^a</td><td>actual load-induced mean stress</td></tr>
<tr><td>ε_2^a</td><td>intermediate actual principal strain amplitude</td><td>σ_{max}</td><td>maximum actual value of load-induced stress</td></tr>
<tr><td>ε_3^a</td><td>minor actual principal strain amplitude</td><td>σ_{res}</td><td>residual stress</td></tr>
<tr><td>ε_{max}^a</td><td>maximum value of actual strain amplitude</td><td>μ</td><td>coefficient of friction</td></tr>
<tr><td>ε_{min}^a</td><td>minimum value of actual strain amplitude</td><td>ν</td><td>Poisson's ratio</td></tr>
<tr><td>ε_1^e</td><td>major linear elastic principal strain amplitude</td><td></td><td></td></tr>
<tr><td>ε_2^e</td><td>intermediate linear elastic principal strain amplitude</td><td></td><td></td></tr>
</tbody>
</table>

agreement with the experimental results. Moreover, both surface and subsurface failure were accurately predicted. This investigation represented a first step towards estimating the location and number of cycles required for bending fatigue failure in surface hardened spur gears.

In addition to the relatively simple geometry of gear steel specimens, many investigations can also be found where actual gears were employed. Lv et al. [9] investigated the fatigue behavior of W6Mo5Cr4V2 steel gear following the micro-shot peening treatment. The authors concluded that the treatment improves the fatigue strength of the gear. Furthermore, the authors observed that residual stress relaxation promotes the occurrence of fatigue crack initiation. Peng et al. [10] investigated the effect of laser shock peening on the bending performance of AISI 9310 steel spur gears. The authors conducted single tooth bending fatigue (STBF) tests and concluded that laser shock peening significantly increases the bending fatigue life of the gear. Fuchs et al. [11] conducted STBF and running gear tests of shot-peened and carburized gears. The authors observed that lower cycle fatigue regions are characterized by surface failure, while failure location shifts to the subsurface region during higher cycle fatigue regimes. It should be mentioned that subsurface failure did not occur at the case-core transition layer, as is typically the case for axially loaded gear steel specimens [4–7]. On the contrary, subsurface failure was still located within the case layer. This phenomenon, which will be discussed in detail within this paper, was also observed in other bending fatigue investigations of surface hardened spur gears [12–14]. As demonstrated by the conducted literature overview, subsurface bending fatigue failure is a possibility in surface hardened spur gears. Therefore, a model should be provided that can accurately estimate both the location and the number of cycles required for bending fatigue failure.

Since experimental investigations are often costly, relatively complicated, and time-consuming, an increasing number of researchers are gravitating towards computational simulations. The same goes for bending fatigue modeling of surface hardened spur gears. Concli et al. [15] conducted an experimental and numerical investigation of carburized and shot-peened spur gears. The authors performed STBF tests accompanied by the corresponding finite element method (FEM) simulations and concluded that fatigue limits are increased for surface

hardened gears. Fuchs et al. [12] investigated the effect of nonmetallic inclusions in the steel matrix of surface hardened spur gears on the tooth root strength. The authors observed that, for surface hardened gears made of high-strength steel, cracks tend to initiate more frequently within the material matrix (subsurface initiation) than at the surface. Lastly, the authors proposed a model that combines the cleanliness of gear steels and the resulting tooth load-carrying capacity. Guntner et al. [14] investigated the effect of residual stress distribution in surface hardened shot-peened gears on their load capacity. In addition to experimental investigations, Guntner et al. employed FEM to simulate STBF tests. Zhang et al. [16] used three-dimensional finite element analysis to study the mechanics of high cycle subsurface fatigue crack nucleation in carburized and shot-peened steel. Vučković et al. [17] proposed an alternative STBF test to minimize the effect of friction on bending fatigue results. Authors employed FEM and fatigue analysis under the assumption of surface crack initiation to obtain the number of cycles required for bending fatigue crack initiation in an actual STBF test and an alternative one.

To adequately explore fatigue behavior in the tooth root region of gears, an accurate stress–strain state of the entire region should be determined. Due to the relative geometric complexity of gears, researchers tend to employ numerical methods to determine stresses and strains required for fatigue analyses. Lias et al. [18] proposed a quasi-static FEM model to analyze the time-varying strength of spur gears. The authors found their results to be in good agreement with the analytical ones. Thirumurugan et al. [19] employed FEM software ANSYS to explore maximum bending stress levels of asymmetric spur gears and investigate the effect of the adjacent tooth on the loading cycle. Additional research on the adjacent tooth effect was done by Vučković et al. [20], who investigated its effect on not only the stress cycle but also on the fatigue lives of surface hardened spur gears under the assumption of surface crack initiation. Similar to [8], research conducted in [20] represents a second step towards obtaining the computational model for bending fatigue life prediction of surface hardened spur gears that predicts both surface and subsurface failure. The third step, which investigates both surface and surface bending fatigue failure in an STBF test, is the subject of this paper.
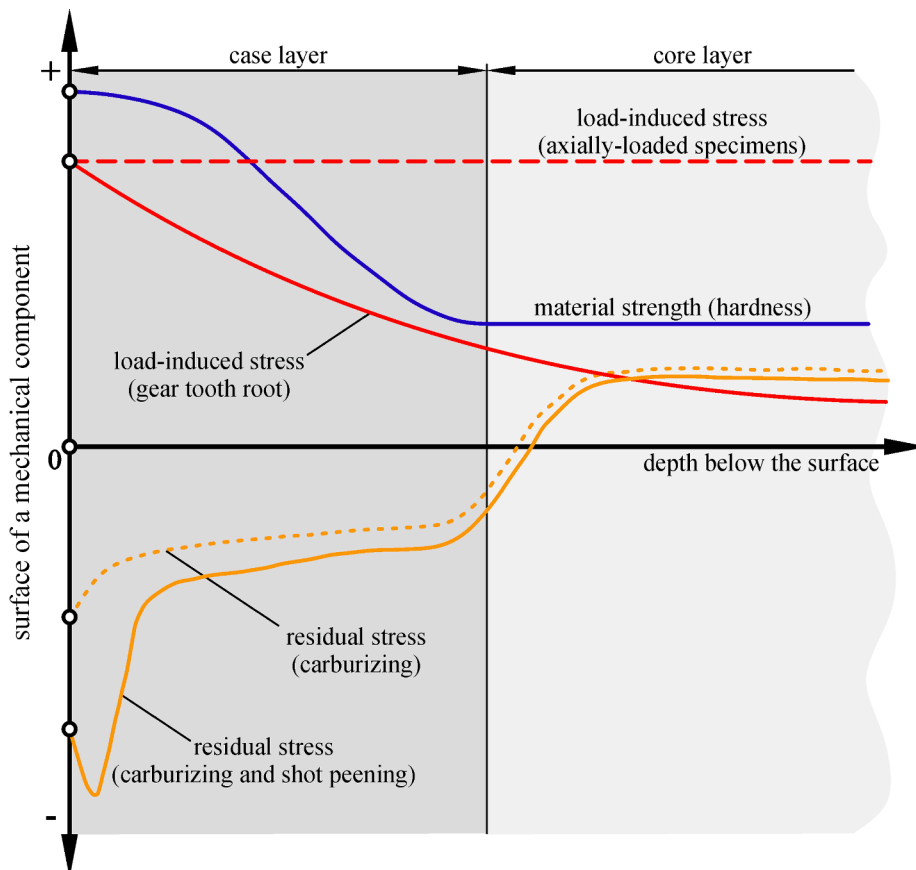
Fig. 1. Distribution of load-induced stresses, material strength, and residual stresses across the depth of surface hardened mechanical components.

By conducting a thorough literature overview, many investigations (mostly experimental) are found that deal with the effect of surface hardening treatments and the resulting residual stresses on bending fatigue lives of surface hardened gears. However, no model was found that estimates both the location (surface vs. subsurface) and the required number of cycles for bending fatigue failure. In this paper, a model based on the multilayer method and strain–life ($\varepsilon - N$) approach is proposed that predicts both the location and the required number of cycles for bending fatigue failure in surface hardened spur gears. In the absence of experimental fatigue data, the hardness method is employed to obtain fatigue parameters for each layer. Linear elastic stresses and strains, which serve as an input for the fatigue model, are obtained by FE simulations. Lastly, principal strain analysis is used to predict bending fatigue lives. The obtained results are validated against STBF experimental results from the available literature.

It should be noted that subsurface failure in surface hardened gears is typically a result of unfavorable material strength, residual stress, and load-induced stress profiles combined with subsurface inclusions or impurities such as aluminum or sulfide oxides. In this paper, the proposed model that estimates potential critical locations for both surface and subsurface bending fatigue failure is based on a macroscopic level, i. e., it does not consider specific irregularities and their distribution (microscopic modeling). In other words, it is assumed that irregularities due to the manufacturing processes are equally likely to occur at both surface and subsurface regions of the gear tooth root. The effect of the specific distribution of such irregularities (impurities, inclusions, and dislocations) will be investigated in future work.

The remainder of this paper is organized as follows.

In Section 2, the fatigue model based on the multilayer method, strain – life ($\varepsilon - N$) approach, hardness method, and principal strain analysis is proposed. This model requires an input of linear elastic stresses and strains typically obtained via a finite element simulation.

In Section 3, an STBF test from the available literature is employed to establish the finite element model. This model is used to obtain linear elastic stresses and strains in the tooth root region. The fatigue model and finite element model are then combined into a computational model that estimates both the location and the required number of cycles for bending fatigue failure in the tooth root of a gear.

In Section 4, the obtained results from the previous section are shown and discussed. Both the location and the number of cycles required for bending fatigue failure are compared against experimental results from the literature. Lastly, some disadvantages and possible improvements of the method are discussed.

In Section 5, the paper is summarized, main conclusions are drawn, and future work is discussed.

2. The fatigue model

It is well established that, for surface hardened metal components, fatigue failure is dictated by three main parameters: induced loads, material strength (typically associated with material hardness), and residual stresses [13]. Generally, lower fatigue lives are obtained for higher loads, lower material strength, and higher (tensile) residual stresses. On the contrary, higher fatigue lives are obtained for lower loads, higher material strength, and lower (compressive) residual stress values. In Fig. 1, typical distributions of load-induced stresses, material strength, and residual stresses for surface hardened components are schematically presented [13,14,21]. It should be noted that load-induced stresses for the gear tooth root shown in Fig. 1 are only a schematic representation of maximum principal stresses that exist within the material.

Material hardness, which is directly related to the material strength, is usually considered to distinguish the case from the core layer in surface hardened materials [8]. In other words, as shown in Fig. 1, the core
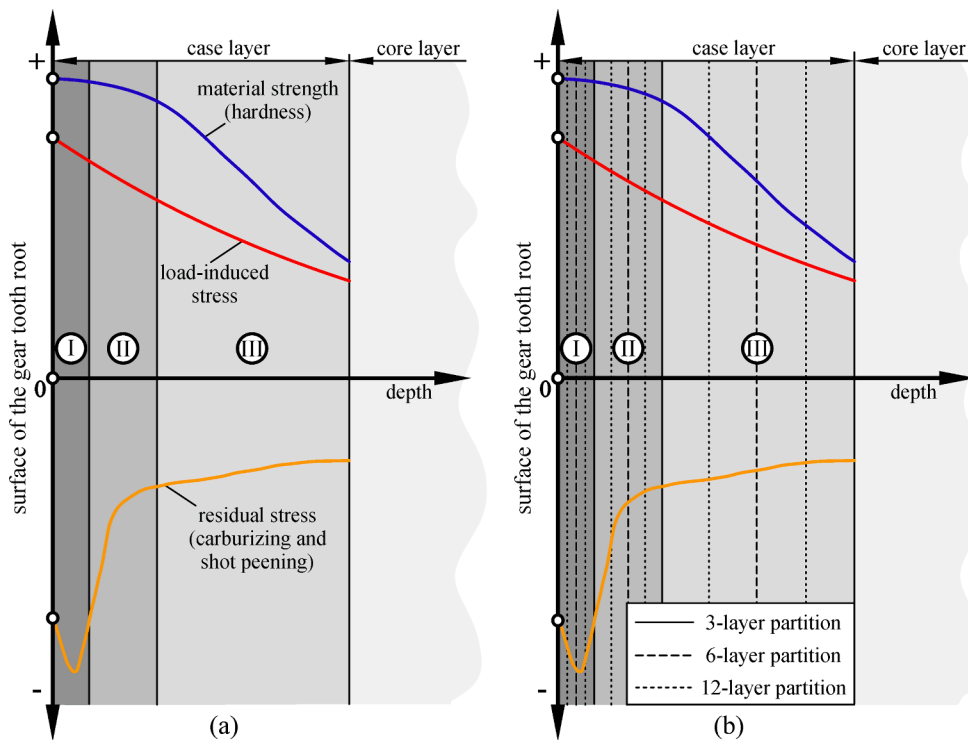
Fig. 2. Multilayer method applied to the case layer of a surface hardened gear: (a) initial 3-layer partition, and (b) 3, 6, and 12-layer partition.

layer is typically defined as the region of constant hardness. As previously mentioned in the introductory section, for axially-loaded specimens, subsurface failure initiates at the case-core transition. On the other hand, in surface hardened gears, subsurface failures are usually found within the case layer. This is subsequently explained by observing the distributions shown in Fig. 1.

In notch-free axially-loaded specimens with constant cross-section, load-induced stress (red dashed line) is also a constant value. In other words, every point within the specimen depth is equally loaded (apart from the specimen surface due to surface roughness parameters). Therefore, the relationship between material strength and residual stresses is crucial for determining possible fatigue failure locations. In low-cycle fatigue (high loads), localized plastic deformation partially relaxes beneficial compressive residual stresses. Coupled with the fact that the surface roughness causes stress concentration, fatigue cracks tend to originate at the surface. In high-cycle fatigue (low loads), the case layer is "protected" due to high material strength and low (compressive) residual stresses, both of which prolong fatigue lives. Therefore, fatigue failure shifts to the core layer. More specifically, to the region characterized by the highest (tensile) residual stresses, i.e., the case-core transition region.

In the tooth root of surface hardened gears, load-induced stress (red solid line) has a gradient that is highest at the surface and lowered with depth. Similar to the axially loaded specimens, the surface is once again a potential critical location due to the highest load-induced stresses, surface roughness, and partial relaxation of favorable compressive stresses. Unlike axially loaded specimens, the core region is no longer critical since load-induced stresses are significantly reduced. However, the possibility of subsurface failure in surface hardened gears still exists and is greatly dependent on residual stress distribution. In Fig. 1, two typical residual stress distributions for surface hardened materials are shown: carburizing and carburizing with shot peening.

For carburized gears (without shot peening), no significant changes in residual stresses within the case layer exist, i.e., no drastic change is observed from the surface to the lower limit of the case layer. Since the lower limit of the case layer is also characterized by lower load-induced stresses, the surface is once again a critical location for fatigue failure

[13].

For carburized and additionally shot-peened gears, a significant drop in residual stress values can be observed near the surface. Even though this drop is partially relaxed in the presence of higher loads (therefore causing a surface failure), it maintains its form in the presence of low loads (high-cycle fatigue). As such, it "protects" the surface and shifts the fatigue failure further down the case layer, more specifically to the region where load-induced stresses are still relatively high, but a sudden rise in residual stresses is observed [12–14].

2.1. The multilayer method

As demonstrated in the previous section, subsurface fatigue failure of surface hardened spur gears usually occurs within the case layer. Since the case layer is usually obtained by diffusing carbon atoms in the steel matrix of the original gear material, it is inhomogeneous. Therefore, the multilayer method [22], which assumes homogenous material behavior within each layer, is employed in this paper to separate the case layer into multiple layers. Within each layer, constant material strength and residual stress values are assumed. Due to the relative complexity of gear geometry, load-induced stresses are obtained via numerical simulations and are not constant within each layer. Additional information regarding the load-induced stresses and strains at the tooth root region is provided in Sections 2.3-2.5.

According to the multilayer method, the case layer of surface hardened gear is divided into a specific number of layers. By observing the distribution of induced-load stresses, material strength, and residual stresses, multilayer partitioning is suggested according to Fig. 2. The explanation for the suggested layer partitioning is provided after Fig. 2. It should be noted that a relatively complicated multiaxial stress–strain state exists at the gear tooth root region (Sections 2.3 and 2.4). For simplicity purposes, load-induced stress in Fig. 2 only depicts maximum principal stress behavior. As such, it is not entirely accurate, but can still be employed to gain the general impression of load-induced stresses at the gear tooth root.

It should be noted that residual stress distribution in Fig. 2 is taken for carburized and shot-peened gears as opposed to only carburized
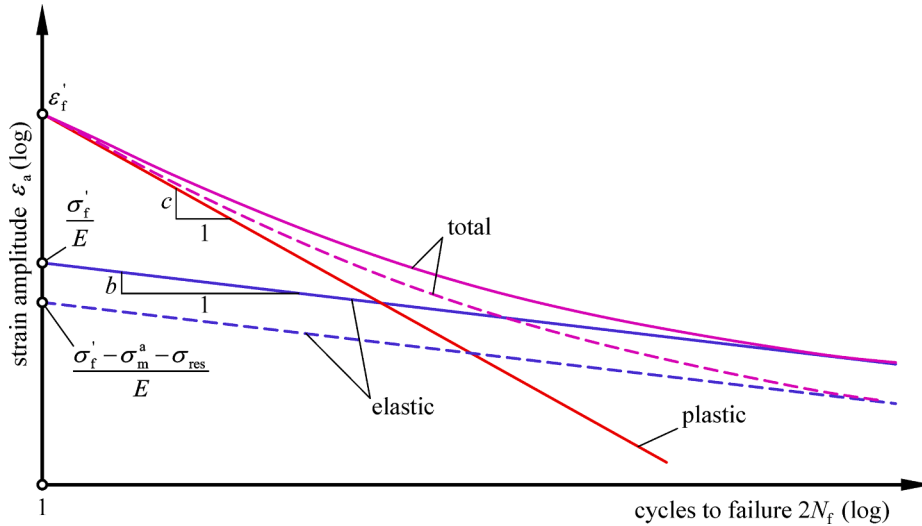
Fig. 3. Schematic representation of strain-life approach with Morrow's mean stress correction method.

ones. This is done because, as previously mentioned, only surface failure is observed in gears that have undergone carburization without additional surface hardening treatments such as shot peening [13]. Furthermore, the multilayer partition shown in Fig. 2 represents a suggestion based on typical (but not always the same) distributions in surface hardened gears. For an actual gear with a measured tooth root residual stress profile, layer partitioning will likely be somewhat different than the presented one, but it will still follow the same logic. The same goes for the hardness profile which is, as demonstrated later in the paper, required for obtaining fatigue parameters.

According to Fig. 2a), the most significant changes in profiles are observed for residual stresses, while material strength and load-induced stress are not significantly altered with an increase in depth. Therefore, the first two layers are defined predominantly based on the residual stress distribution.

- Layer I is defined from the surface to the point where the residual stress value is approximately equal to the surface one. This region represents the surface layer typically characterized by the highest stresses, but also the most resistant one to fatigue due to high material strength and compressive residual stresses.
- Layer II is defined from the lower limit of Layer I to the approximate point where a sudden increase in residual stresses is gradually slowed down. Within this layer, a sudden increase in residual stresses (an adverse effect for fatigue resistance) is more prominent than any changes observed in load-induced stress or material strength curves.
- Layer III is defined from the lower limit of Layer II to the nominal case depth. It should be noted that the lower limit of Layer III is not of great importance for the proposed method. This is because residual stresses after Layer II are retained at approximately the same compressive level, while load-induced stresses are significantly decreased (Fig. 1), thus avoiding potential fatigue failures. This is demonstrated in Section 3 when predicting bending fatigue failure on actual gears. Nevertheless, since fatigue parameters and residual stresses have to be averaged within each layer, the outer limit of Layer III has to be defined. Therefore, in this paper, it is taken as the nominal case depth.

To lower the averaging error and increase the accuracy of results of both predicted bending fatigue lives and failure locations, each layer is evenly divided into two additional layers. Thus, a 6-layer partitioning is obtained (Fig. 2b). Finally, to further increase the accuracy, each of the six layers is once again evenly divided into two additional layers (12-layer partition).

As previously mentioned, the multilayer method employs constant fatigue parameters and residual stresses within each layer. To predict the bending fatigue in surface hardened gears based on predetermined linear elastic stresses and strains, a certain fatigue estimation method has to be employed. In this paper, the strain–life ($\varepsilon - N$) approach is employed for fatigue life prediction, while the necessary fatigue parameters for this method are obtained via the hardness method.

2.2. Estimating strain-life properties of layers according to the hardness method

Similar to the previous investigations conducted by the authors for surface fatigue failure in gears [17,20], the strain-life approach is also employed in this paper. The main difference, however, is that the approach is applied to both surface and subsurface regions of the tooth root. Within the strain-life approach, the relationship between the actual strain amplitude and the estimated fatigue life for a fully reversed loading (stress ratio of $R = -1$) can be expressed by the Basquin-Coffin-Manson relation:

$$\varepsilon_a = \frac{\Delta\varepsilon^e}{2} + \frac{\Delta\varepsilon^p}{2} = \frac{\sigma_f^{'}}{E}(2N_f)^b + \varepsilon_f^{'}(2N_f)^c \tag{1}$$

where ε_a is the total strain amplitude, $\frac{\Delta\varepsilon^e}{2}$ is the elastic strain amplitude, $\frac{\Delta\varepsilon^p}{2}$ is the plastic strain amplitude, $\sigma_f^{'}$ is the fatigue strength coefficient, N_f is the number of reversals until fatigue failure, b is the fatigue strength exponent, $\varepsilon_f^{'}$ is the fatigue ductility coefficient, and c is the fatigue ductility exponent. Since the typical bending stress cycle of a spur gear also contains mean stresses [20], they can be accounted for by employing one of the most popular mean stress correction methods for steel materials [23]: Morrow's [24] and Smith-Watson-Topper's (SWT) [25]. Even though both methods are accurate, Morrow's mean stress correction provides slightly better results for materials characterized by high hardness. Therefore, it is recommended for high-strength steels [26,27]. Lastly, according to [26], residual stresses can also be accounted for by modifying Eq. (1):

$$\varepsilon_a = \frac{\sigma_f^{'} - \sigma_m - \sigma_{res}}{E}(2N_f)^b + \varepsilon_f^{'}(2N_f)^c \tag{2}$$

where σ_m is the mean stress and σ_{res} is the residual stress due to surface hardening treatments such as carburizing, shot peening, or surface finishing. Eq. (2) is schematically depicted in Fig. 3.

Strain-life properties shown in Eq. (1) are typically obtained by experimental testing. In the absence of experimental data, estimation
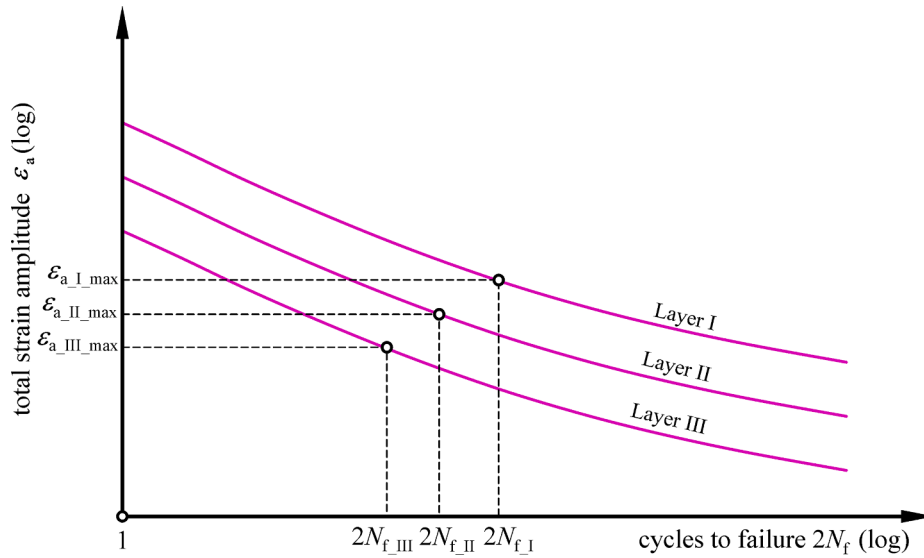
Fig. 4. Schematic representation of 3-layer partition fatigue life estimation with Morrow's mean stress correction.

methods such as the hardness method [28], which has already been proven effective for high-strength gear steels [8,17,20], can be employed. According to the hardness method, material hardness can be used to approximate strain-life properties:

$$\sigma_f^{'} = 4.25 \cdot HB + 225 \tag{3}$$

$$\varepsilon_f^{'} = \frac{0.32 \cdot HB^2 - 487 \cdot HB + 191000}{E} \tag{4}$$

$$b = -\ 0.09 \tag{5}$$

$$c = -\ 0.56 \tag{6}$$

where HB is the averaged Brinell hardness for each layer and E is the modulus of elasticity. Cyclic stress–strain properties can also be estimated as [29]:

$$K^{'} = \frac{\sigma_f^{'}}{\left(\varepsilon_f^{'}\right)^{n^{'}}} \tag{7}$$

$$n^{'} = \frac{b}{c} \tag{8}$$

where $K^{'}$ is the cyclic strength coefficient and $n^{'}$ is the cyclic strength exponent.

Based on the hardness profile in the gear tooth root and averaged hardness values, each layer within the multilayer method is characterized by constant strain-life properties. In other words, each layer has its corresponding strain-life curve. Furthermore, according to Eqs. (5) and (6), strain-life curves for each layer are also parallel. The aforementioned is schematically depicted for a 3-layer partition in Fig. 4. Within the figure, $2N_{f\_I}$, $2N_{f\_II}$, and $2N_{f\_III}$ represent estimated fatigue lives of each layer for the corresponding maximum total strain amplitudes within each layer $\varepsilon_{a\_I\_max}$, $\varepsilon_{a\_II\_max}$, and $\varepsilon_{a\_III\_max}$, respectively. These strains are directly related to load-induced stresses schematically depicted in Figures Fig. 1 and Fig. 2, which are gradually lowered with depth below the surface.

By observing Fig. 4, a significant problem can be noticed. For an arbitrarily chosen total strain amplitude shown in Fig. 4 and establish strain-life curves of each layer, Layer III will always be the critical one due to the lowest estimated fatigue life. This is not in accordance with the already established phenomenon of surface–subsurface transition of fatigue failure in surface hardened components. Therefore, if the hardness method is to be applied for bending fatigue life estimation, the same mean stress correction method (in this case Morrow's) cannot be
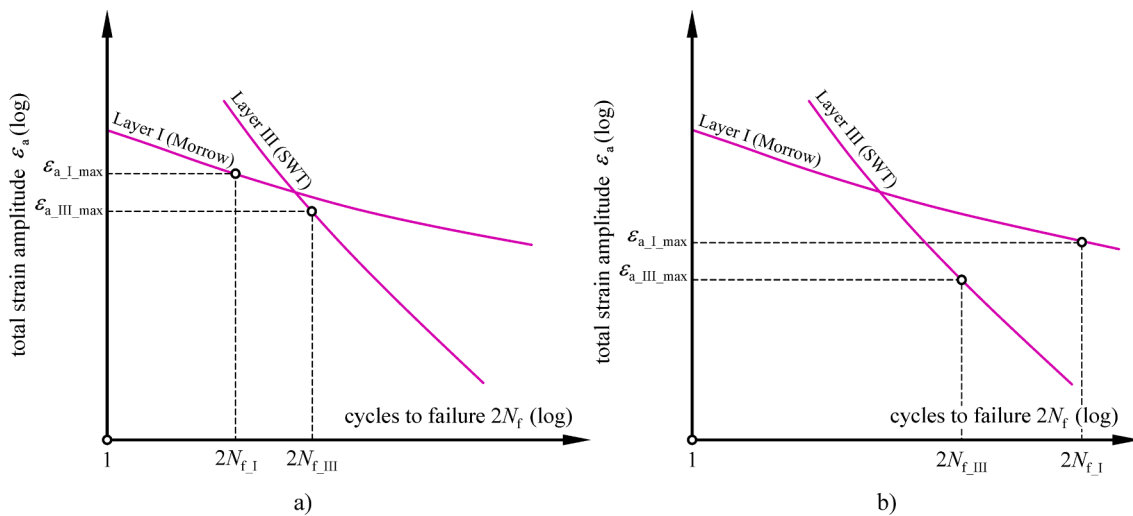

Fig. 5. Schematic representation of 3-layer partition fatigue life estimation based on Morrow's and SWT's mean stress correction: a) low cycle fatigue, and b) high cycle fatigue.
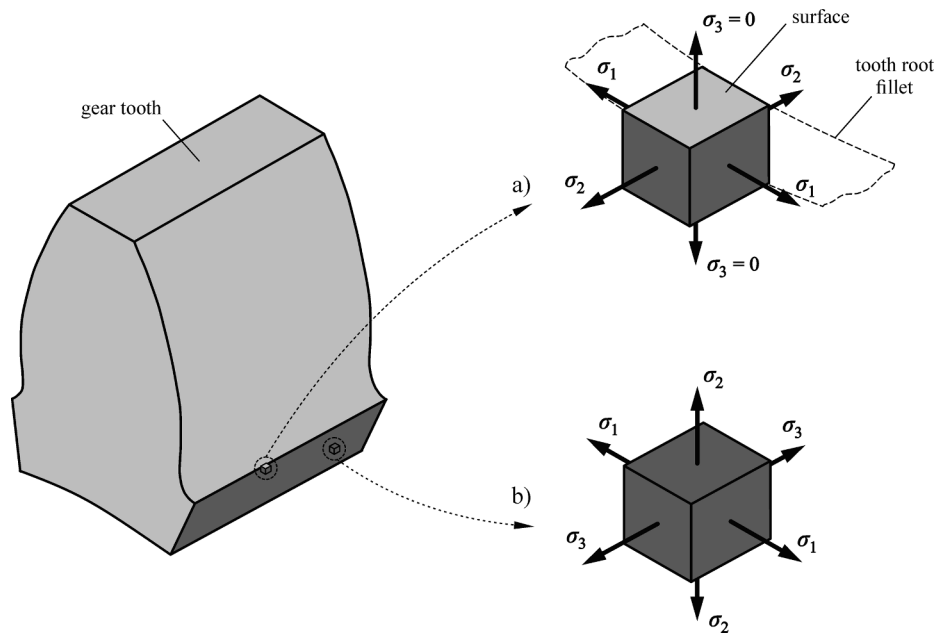
Fig. 6. Principal stresses at the gear tooth root: a) surface element, and b) subsurface element.

employed to all layers.

SWT's mean stress correction method is also often employed for steel materials. Strain-life approach with SWT correction can be expressed as [25,26]:

$$\varepsilon_a(\sigma_{max} + \sigma_{res}) = \frac{\left(\sigma_f'\right)^2}{E}(2N_f)^{2b} + \sigma_f'\varepsilon_f'(2N_f)^{b+c} \qquad (9)$$

In Eq. (9), $\sigma_{max} = \sigma_a + \sigma_m$, where σ_a is the load-induced stress amplitude. As previously mentioned, both Morrow's and SWT's mean stress correction methods can be applied to steel materials. However, with an increase in the strength of steel material (often associated with hardness), Morrow's method provides somewhat more accurate results. In addition, by assigning residual stresses to the elastic section of Eq. (2), Morrow's mean stress method accounts for partial residual stress relaxation in the presence of higher stress and strains as well as notches, i.e., the surface of the tooth root. On the other hand, SWT's mean stress correction method does not distinguish between the effect of residual stresses in the presence of higher loads (low-cycle fatigue) and lower loads (high-cycle fatigue). As such, the SWT's mean stress method is applied to subsurface layers since lower stresses and strains are not sufficient to relax subsurface residual stresses.

Therefore, in this paper, it is suggested that strain-life parameters of the first layer in 3-layer partitioning are corrected according to Morrow's mean stress method. This also applies to all additional layers that are created once the surface layer is further divided into 2 additional layers (6-layer partitioning) or 4 additional layers (12-layer partitioning), as shown in Fig. 2. The SWT's mean stress correction method is applied to all remaining subsurface layers. The results are schematically depicted in Fig. 5 for Layers I and III. To avoid cluttering the image, Layer II is not plotted.

Firstly, it can be observed that the curves intersect each other. Moreover, an SWT strain-life curve resembles typical fatigue curves for the subsurface region, while Morrow strain-life curve resembles typical fatigue curves for the surface region of surface hardened components [8,30].

During low-cycle fatigue (Fig. 5a), Layer I will most likely be the critical location for fatigue failure ($2N_{f\,I} < 2N_{f\,III}$). On the other hand, during high-cycle fatigue (Fig. 5b), the subsurface layer (Layer III) will most likely be the critical one ($2N_{f\,III} < 2N_{f\,I}$). It should be noted that Fig. 5 is only a schematic representation of a relatively simple

surface–subsurface failure transition. The actual situation is much more complex due to a higher number of layers, variable residual and mean stresses, material hardness, and multiaxial stresses and strains in the tooth root region, which are described in detail in Sections 2.3 and 2.4.

Up to this point, a method for determining fatigue properties (material strength) was defined. The tooth root region was separated into multiple layers and strain-life properties were applied to each layer based on the averaged hardness values. Moreover, a distinction between surface and subsurface failure was made by employing either Morrow's or SWT's mean stress correction method. In summary, strain-life curves of each layer required for fatigue life estimation were determined.

However, fatigue lives cannot be estimated without the applied load (represented in the form of total applied total strain amplitude ε_a). Therefore, in the next section, load-induced stresses and strain in the tooth root region of surface hardened spur gears are discussed.

2.3. Load-induced stresses and strains at the tooth root region in spur gears

As previously mentioned, the proposed fatigue model requires a linear elastic stress–strain state in the tooth root region that can be obtained via numerical simulations [17,20]. The simulation itself and the corresponding boundary conditions are not discussed in this section. However, numerical simulation is required for the validation of the proposed model. Therefore, it is described in detail in Section 3. For the purposes of this section (the fatigue model), it is assumed that linear-elastic stresses and strains in the gear tooth root region are already obtained.

In this paper, maximum principal strain (normal strain) analysis, which is suggested for multiaxial fatigue of brittle steels [26], is employed to predict bending fatigue lives of surface hardened spur gears. Its effectiveness in brittle materials, such as surface hardened spur gears, has already been demonstrated in previous investigations [8,17,20]. To employ principal strains for fatigue life estimation, principal stresses have to be first obtained. In Fig. 6, load-induced principal stresses in an STBF test for an arbitrarily chosen surface and subsurface differential elements at the spur gear tooth root are shown.

For the surface element, major principal stress (σ_1) is always tangential to the tooth root fillet. Since the main cause of this stress is the bending moment due to the tooth flank contact, it is called the bending
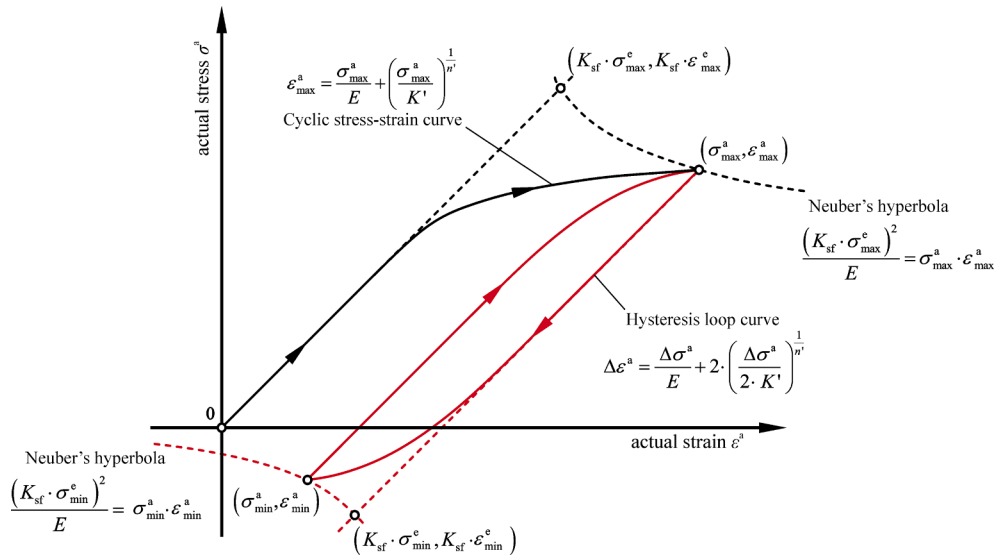
Fig. 7. Elastic-plastic correction of linear elastic stresses and strains via Neuber's rule.

stress in the literature and is often denoted as σ_φ. Intermediate principal stress σ_2 is oriented in the direction of the gear width and can usually be neglected in sufficiently thin gears [31]. Lastly, minor principal stress σ_3 does not exist since the observed differential element is located at the surface. Since principal stress σ_3 is normal to the tooth root fillet tangent, it is often called the normal stress and denoted as σ_n.

For the subsurface element and proportional loading (such as the STBF test loading), major principal stress is still σ_1 and parallel to the tooth root fillet. However, unlike the surface element, principal stress normal to the tooth root fillet tangent is not zero. Since it is typically higher than the principal stress in the gear width direction for typical spur gears, it is designated as intermediate principal stress σ_2. Minor stress σ_3 now becomes the lowest principal stress below the surface, which is precisely the one oriented in the direction of the gear width. It should be mentioned that σ_2 and σ_3 might be swapped depending upon the gear width (for extremely wide gears σ_3 might be higher than σ_2).

As previously mentioned, principal stresses for linear elastic material behavior (denoted as σ_1^e, σ_2^e, and σ_3^e) can be obtained by numerical simulations. Since maximum principal strain analysis (normal strain) is employed in this paper, the aforementioned principal stresses are first converted to principal strains according to Hooke's law. Thus, linear elastic principal strains (denoted as ε_1^e, ε_2^e, and ε_3^e), are acquired.

2.4. Multiaxial elastic–plastic correction of linear-elastic principal stresses and strains

In the presence of relatively high loads, actual stresses and strains might be somewhat different than linear elastic ones due to the elastic–plastic deformation of the material. Actual principal stresses (denoted as σ_1^a, σ_2^a, and σ_3^a in this paper), as well as actual principal strains (denoted as ε_1^a, ε_2^a, and ε_3^a in this paper), can be obtained via elastic–plastic correction by Neuber's rule [32]. Even though it was originally proposed for grooved shafts under torsional loading, Neuber's rule is often applied to spur gears [33–35]. A schematic representation of Neuber's elastic–plastic correction is shown in Fig. 7.

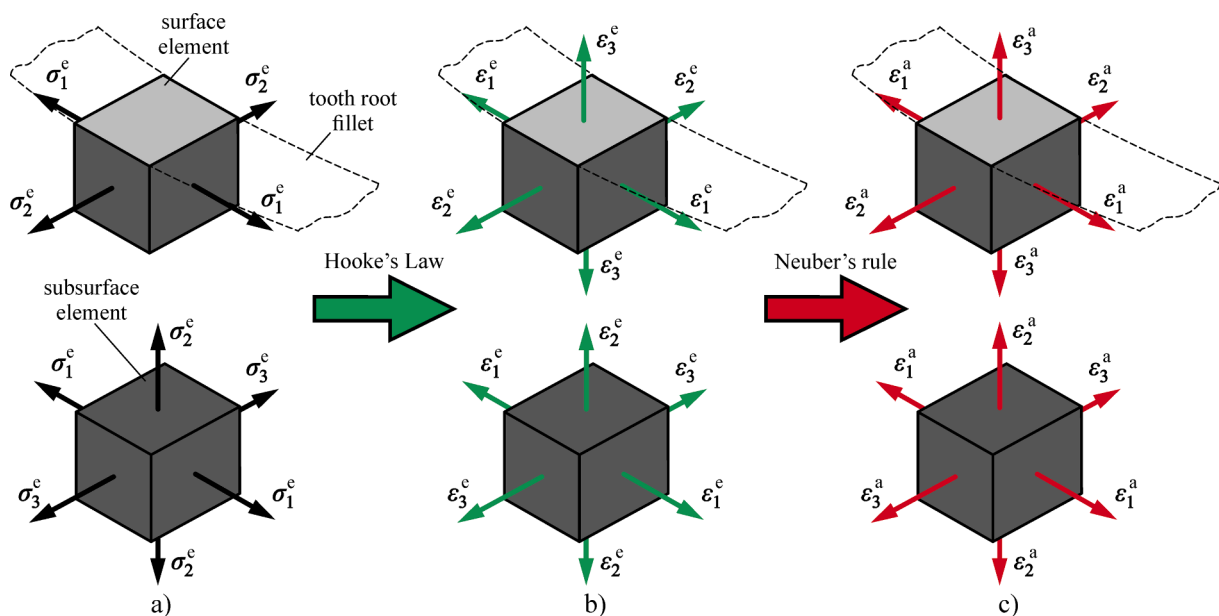Within the figure, ε_{max}^a is the actual maximum strain, σ_{max}^a is the

Fig. 8. Multiaxial elastic–plastic correction via Neuber's rule for surface and subsurface element in the tooth root region: a) principal stresses for linear elastic material behavior, b) principal strains for linear elastic material behavior, and c) actual principal strains.
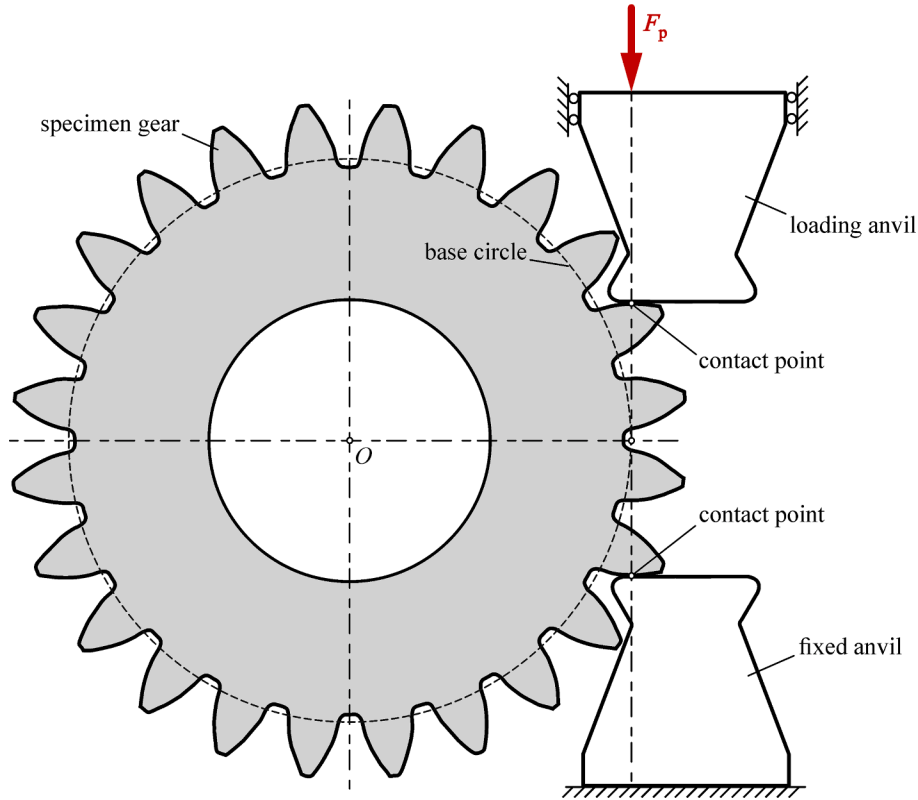
Fig. 9. Schematic representation of an STBF test.

actual maximum stress, K' is the cyclic strength coefficient, n' is the cyclic strength exponent, K_{sf} is a dimensionless surface finish correction factor, σ_{max}^e is the maximum linear elastic stress, ε_{max}^e is the maximum linear elastic strain, $\Delta\varepsilon^a$ is the actual strain range, $\Delta\sigma^a$ is the actual stress range, σ_{min}^a is the minimum actual stress, and ε_{min}^a is the minimum actual strain.

A detailed step-by-step explanation of Neuber's rule can be found in previous bending fatigue investigations of spur gears, such as [17] and [20]. Given that the strain-life approach based on maximum principal strain analysis is employed in this paper, actual strain values in the tooth root region have to be obtained. Since multiaxial stresses and strains are considered in this paper (Fig. 6), multiaxial Neuber's rule is applied (according to Fig. 7) to obtain actual principal stresses (and more importantly strains) that consider elastic–plastic material behavior. The entire process starting from linear elastic principal stresses to actual principal strains is schematically depicted in Fig. 8.

2.5. The procedure for predicting the bending fatigue failure location and number of cycles

The entire procedure for estimating the bending fatigue failure location and the corresponding number of cycles described in Sections 2.1-2.4 is summarized by the following steps:

1. According to the multilayer method, the gear tooth root region is divided into 3, 6, or 12 layers (Fig. 2). Based on the hardness and residual stress profiles, averaged hardness and residual stress values are applied to each layer. According to Eqs. (3) – (8), averaged hardness value is employed to obtain strain-life and cyclic stress–strain properties for each layer.
2. A numerical model representing actual gear loading conditions is generated by employing the finite element software Abaqus [36]. To apply the multilayer method, uniform finite element sets are defined in the tooth root region within the numerical model. By carrying out

the numerical simulation, principal linear elastic stresses (σ_1^e, σ_2^e, and σ_3^e) and strains (ε_1^e, ε_2^e, and ε_3^e) for each node in the tooth root region of a surface hardened spur gear are obtained.
3. Averaged multilayer values from step 1 for the 3, 6, and 12-layer partitioning are assigned to finite element sets defined in step 2. Surface roughness at the tooth root fillet is also accounted for.
4. Principal linear elastic stresses and strains of each node obtained via numerical simulation are corrected for elastoplastic material behavior via Neuber's rule to obtain actual principal stresses (σ_1^a, σ_2^a, and σ_3^a) and strains (ε_1^a, ε_2^a, and ε_3^a). This process is schematically depicted in Fig. 8. It should be noted that actual load-induced means stresses, σ_m^a, are obtained from maximum and minimum load-induced stresses that are corrected for elastoplastic material behavior. However, no elastoplastic correction is applied to residual stresses, σ_{res} [26].
5. The maximum principal strain (normal strain) analysis is applied to each node in the tooth root region. Total strain amplitude, ε_a, shown in Eqs. (1), (2), and (9), is substituted with the major actual (corrected by Neuber's rule) principal strain amplitude:

$$\varepsilon_a = \frac{\Delta\varepsilon_1^a}{2} \tag{12}$$

where $\Delta\varepsilon_1^a$ is the range of the major actual principal strain amplitude.

A total number of cycles for bending fatigue failure is calculated based on the strain-life ($\varepsilon - N$) approach:

- If the node is located in the surface layer, Morrow's mean stress correction is employed.
- If the node is located in one of the subsurface layers, SWT's mean stress correction is employed.

6. The procedure described in step 5 is repeated for each node at the tooth root region. To summarize, for the region defined as the surface layer in 3-layer partitioning, bending fatigue lives, $2N_f$, are calculated according to Morrow's mean stress correction method:

Table 1
Geometrical, material, and surface hardening parameters of the specimen gear.

Parameter	Value	Parameter	Value
Number of teeth	24	Tip diameter	134 mm
Module	5 mm	Base material	18CrNiMo7-6
Profile shift coefficient	0.11	Modulus of elasticity	210 GPa
Face width	30 mm	Poisson's ratio	0.3
Normal pressure angle	20°	Surface hardening treatment	Quenched, carburized to the nominal case depth of 0.7 mm, and shot-peened

$$\frac{\Delta \varepsilon_1^a}{2} = \frac{\sigma_f' - \sigma_m^a - \sigma_{res}}{E}(2N_f)^b + \varepsilon_f'(2N_f)^c \qquad (13)$$

For the remaining subsurface layers, bending fatigue lives, N_f, are calculated according to SWT's mean stress correction method:

$$\frac{\Delta \varepsilon_1^a}{2}(\sigma_a + \sigma_m^a + \sigma_{res}) = \frac{(\sigma_f')^2}{E}(2N_f)^{2b} + \sigma_f'\varepsilon_f'(2N_f)^{b+c} \qquad (14)$$

7. Node with the lowest bending fatigue life is designated as critical and its location is recorded. Due to the relative complexity of the procedure, computational software FE-Safe [37], which requires an input of linear elastic stresses and strain from Abaqus, is employed to carry out steps 3 – 7.

3. Validation of the computational model

The proposed computational model is validated against experimentally available STBF results [11], where a bending fatigue pulsator test rig was employed by symmetrically clamping the specimen gear between two anvils (Fig. 9).

A pulsating load, F_p, is applied via the loading anvil to the specimen gear. This pulsating load is directly translated to the gear tooth flank, which is once again translated across the specimen gear to the fixed anvil. Due to the involute tooth profile, the pulsating force is tangent to the base circle of the specimen gear. Since the setup shown in Fig. 9 requires no support at point O, a certain preload has to be applied to clamp the gear between the anvils. This preload should not be higher than 10% of the maximum applied load [14]. Geometrical, material, and surface hardening parameters of the specimen gear are taken from [38] and [39] and shown in Table 1.

The averaged hardness profile of the specimen gear is taken from [12] and the corresponding averaged residual stress profile is taken from [13]. They are both shown in Fig. 10, where the multilayer method is applied according to Section 2.1 to obtain 3, 6, and 12-layer partitioning.

For each layer in 3, 6, and 12-layer partitioning, averaged Vickers hardness (HV1) is first obtained, which is converted to Brinell hardness (HB) according to the hardness conversion tables provided in [40]. It should be mentioned that Brinell hardness values obtained by the conversion are obtained for an indenter with 10 mm in diameter and the force of 3 000 kgf. Then, strain-life properties σ_f', ε_f', b, and c, as well as cyclic stress–strain properties K' and n' are calculated according to Eqs. (3) – (8). Lastly, averaged residual stress values are obtained based on the actual residual stress profile. The aforementioned values are shown in the Appendix in Table 2. This concludes the first step of the procedure defined in Section 2.5.

The second step is conducting a numerical simulation of an STBF test by employing a finite element software Abaqus [36]. According to Pehan et al. [31], plane stress can be assumed if the gear width is equal to or lower than six times its module, which is the case in this paper according to Table 1. Therefore, to reduce computational costs, a two-dimensional (2D) finite element analysis is carried out based on the boundary conditions provided in Fig. 9. Plane stress quadrilateral elements designated within Abaqus as CPS4 are applied to the entire model. It should be noted that, since 2D finite element analysis is employed,

linear elastic stresses (σ_3^e) in the direction of the gear width are nullified, therefore simplifying the procedure defined in Section 2.5. The numerical model used for bending fatigue analysis is shown in Fig. 11.

The specimen gear is modeled according to the data shown in Table 1. To reduce computational costs, only the four gear teeth clamped between the anvils as well as two adjacent ones are modeled (Fig. 11a). According to the instructions provided in [11], the specimen gear is symmetrically clamped between four teeth. Moreover, it is ensured that the contact points between the loading anvil, fixed anvil, and the specimen gear create a vertical line that is tangent to the base circle. Since no information regarding the geometry or material of anvils is provided, they are roughly modeled based on the existing STBF test rigs. Furthermore, it is assumed the anvils are made of the same material as the gear. Structured and refined quadrilateral element mesh is applied to the observed tooth root region (Fig. 11b) to ensure the uniform layer distribution required for assigning the averaged multilayer values.

Reference points RP_1, RP_2, and RP_3 are constrained via *kinematic coupling* to the inner gear surface, the top surface of the loading anvil, and the bottom surface of the fixed anvil, respectively. Contact between the loading anvil, fixed anvil, and the corresponding gear teeth is defined as *normal behavior, hard contact*. In the absence of actual lubrication data, dry friction contact is assumed. The coefficient of friction is taken as $\mu = 0.15$, which best predicts STBF lives in dry friction
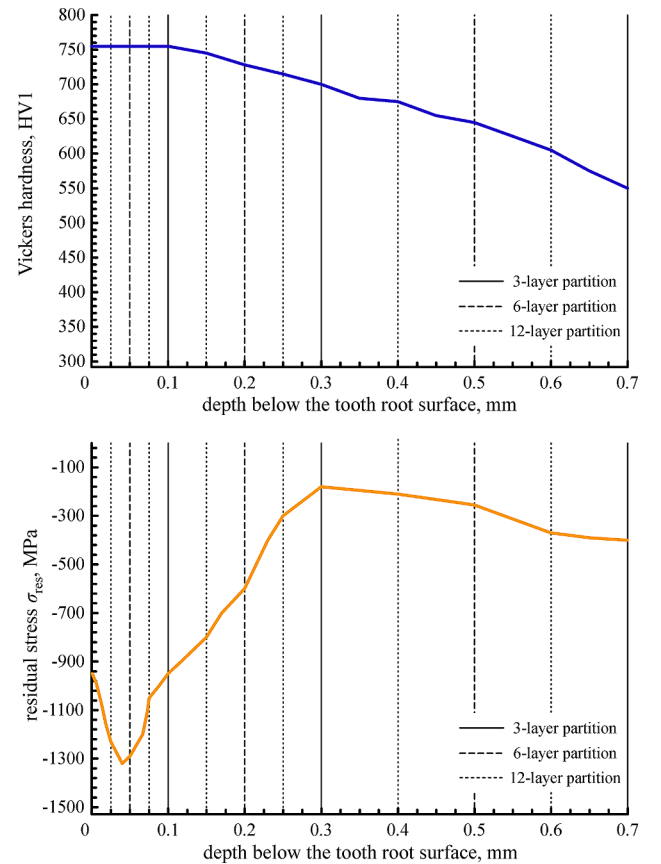

Fig. 10. Averaged hardness and residual stress profiles of the specimen gear with multilayer partitioning.
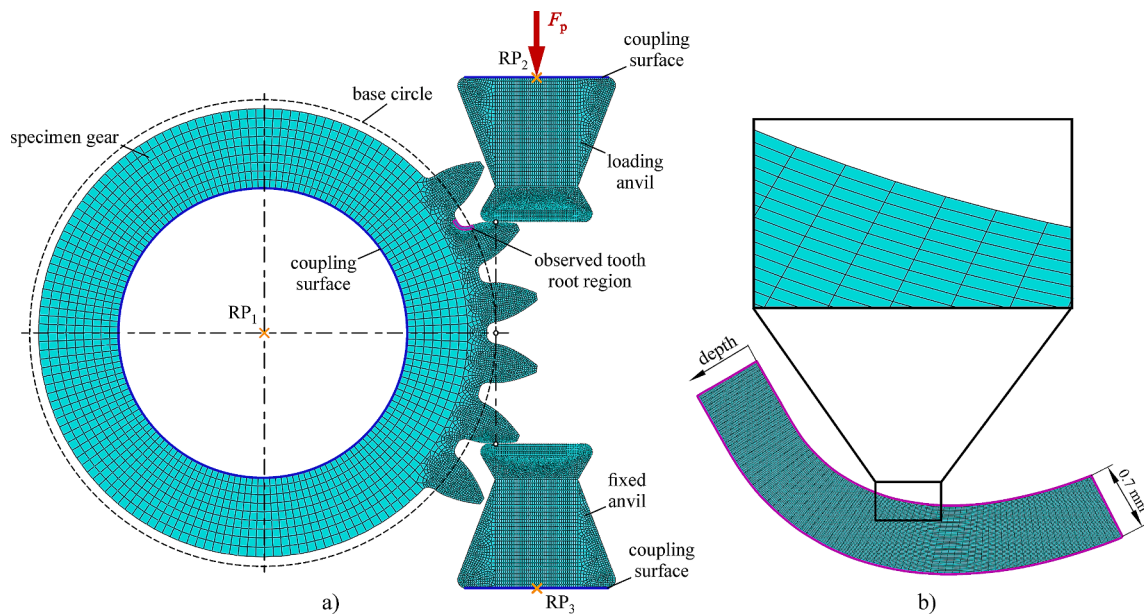
Fig. 11. Numerical simulation model of an STBF test: a) boundary conditions, and b) a close up of the observed tooth root region.
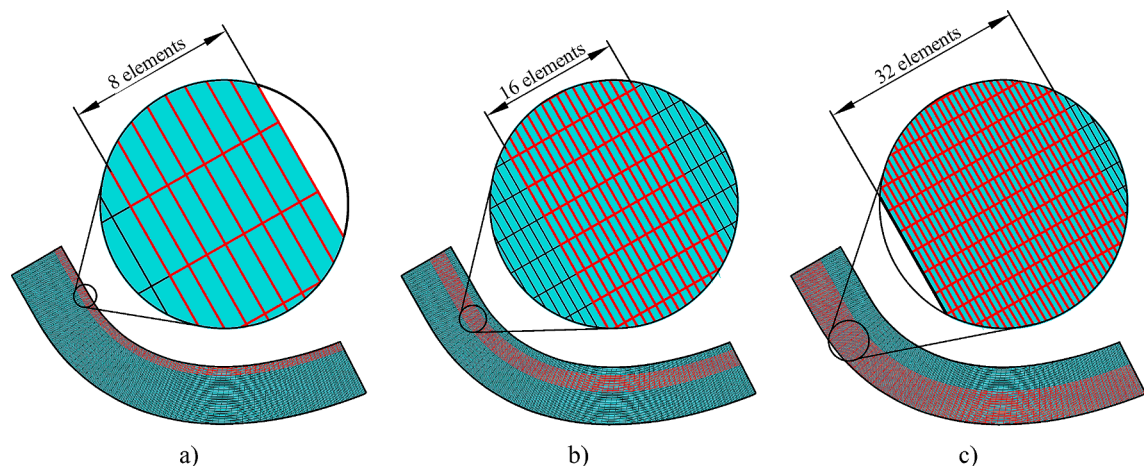

Fig. 12. 3-layer mesh partitioning of the observed tooth root region: a) the first layer, b) the second layer, and c) the third layer.

conditions [17]. Therefore, *tangential behavior* with the *penalty* option is employed to assign the coefficient of friction.

According to step 2 described in Section 2.5, finite element sets are defined in the observed tooth root region. As previously mentioned, the depth of the observed tooth root region is taken as the nominal case depth, i.e., 0.7 mm (Table 1). The exact number and dimensions of quadrilateral elements should be chosen based on the actual hardness and residual stress profiles as well as layer partitioning (Fig. 10). For the 3-layer partitioning, the depth of each layer is defined by an even number of finite elements. This is done to ensure that each layer in 3-layer partitioning can be equally separated two more times (6 and 12-layer partitioning). Due to proportional differences in layer size, for the 3-layer partitioning, 8 elements are assigned to the first layer in the depth direction, 16 elements to the second layer, and 32 elements to the third layer (Fig. 12). In other words, a total of 56 elements are assigned to the observed tooth root region in the depth direction, where the width of each element is $0.7/56 = 0.0125$ mm. In the direction of the tooth root fillet, 75 elements are assigned. As a result, a total of $56·75 = 4200$ finite elements are assigned to the observed tooth root region. The accuracy of mesh refinement in the tooth root region was confirmed by conducting multiple convergence analyses.

Once finite element sets have been defined, the numerical simulation

can be carried out to obtain linear elastic principal stresses and strains. The numerical simulation is conducted in three steps:

1. Step 1. Horizontal and vertical displacement restriction is applied to RP_1 to fix the specimen gear, while its rotation is allowed. This simulates a safety pin that is used to position the gear and establish contact with the anvils. An arbitrarily chosen vertical displacement of 0.001 mm is applied to RP_2 to establish the contact between the loading anvil and the corresponding gear tooth. The horizontal displacement of RP_2 is restricted. Lastly, to fix the lower anvil, degrees of freedom for RP_3 are restricted. Hence, contact between the loading anvil, fixed anvil, and the corresponding gear teeth is established.

2. Step 2. Displacement restrictions are removed from RP_1 and an arbitrarily chosen preload of 50 N is applied to the loading anvil via RP_2. This step represents the removal of the gear safety pin and application of preload to clamp the specimen gear between the anvils.

3. Step 3. Pulsating load, F_p, is applied via RP_2 as shown in Fig. 11 via sinusoidal form separated into 20 equal time increments. The maximum value of the pulsating load is taken from experimental results [11].
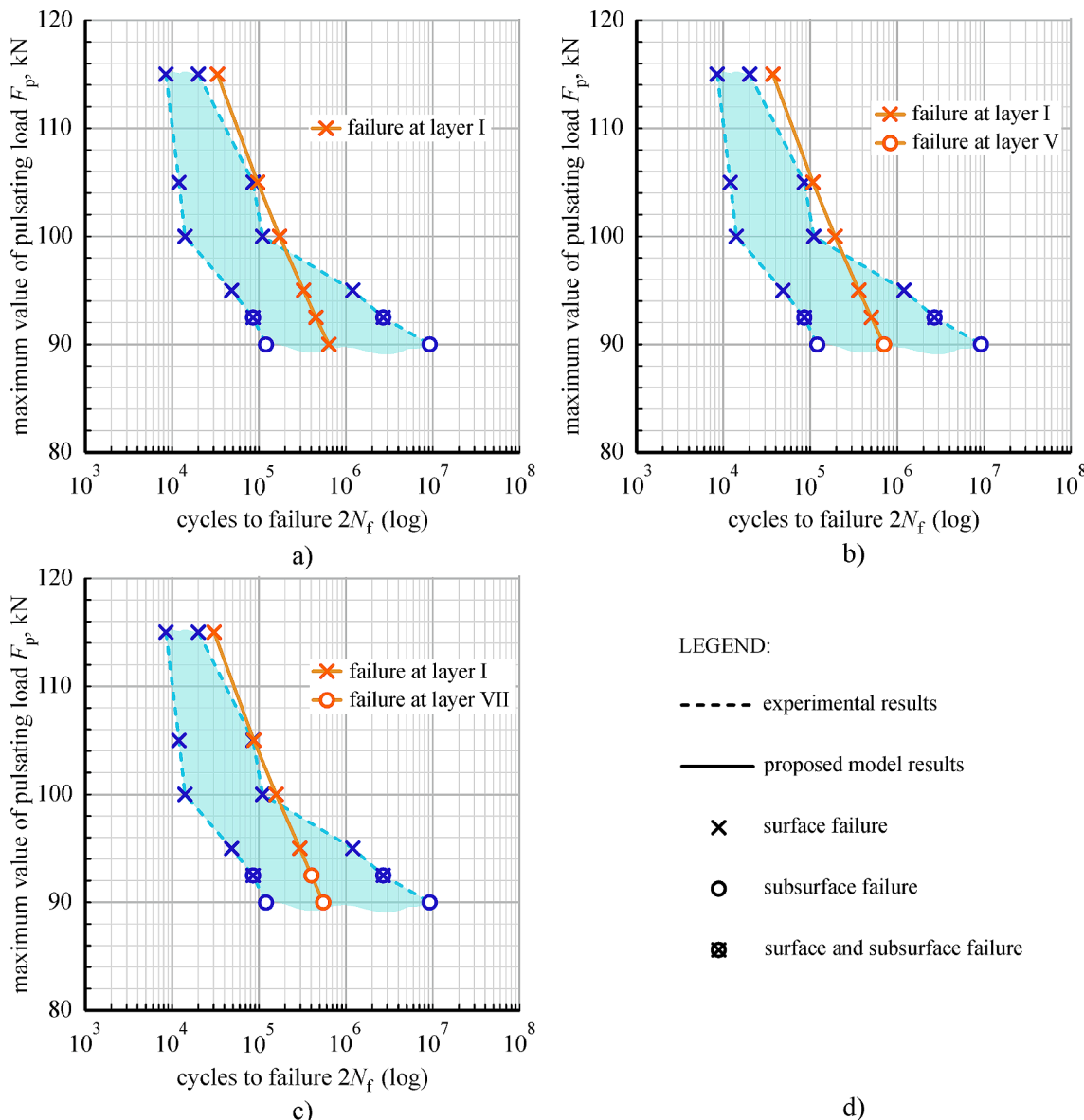
Fig. 13. Comparison of bending fatigue lives and failure locations between experimental results and the proposed model: a) 3-layer partitioning, b) 6-layer partitioning, c) 12-layer partitioning, and d) legend.

Following the numerical simulation, stresses (σ_1^e, σ_2^e, and σ_3^e) and strains (ε_1^e, ε_2^e, and ε_3^e) for linear elastic material behavior at each node within the tooth root region of a surface hardened spur gear are obtained. This concludes the second step of the procedure defined in Section 2.5.

The remaining steps (3 – 7) defined in Section 2.5 are, as previously mentioned, carried out by employing the computational software FE-Safe. Lastly, based on the specimen gear surface roughness of Ra ≈ 0.87 μm [14], dimensionless surface finish correction factor K_{sf} shown in Fig. 7 is taken as 1.1 [26]. The entire procedure is repeated for 3, 6, and 12-layer partitioning.

4. Results and discussion

4.1. Validation of the proposed computational model

In this section, bending fatigue prediction results obtained by the proposed model are compared against experimental ones [11]. In Fig. 13, a comparison between predicted and experimental bending

fatigue lives and failure locations is shown. Since experimental tests are conducted multiple times for a single pulsating load, only the minimum and maximum bending fatigue lives are shown. It should be noted that the transition from surface to subsurface failure is first observed for F_p = 92.5 kN in experimentally tested gears (denoted by both surface and subsurface failure marks in Fig. 13).

Bending fatigue lives

According to Fig. 13, good agreement with the experimental results is observed in higher cycle fatigue regions, while somewhat overestimating results are obtained in the lower cycle fatigue region. Furthermore, it can be concluded that additional layer partitioning has a negligible effect on estimated bending fatigue lives. Nevertheless, the most accurate results are obtained for 12-layer partitioning.

Surface to subsurface failure transition

For 3-layer partitioning, only surface failure is obtained by the proposed model. With an increase in the number of layers, the predicted failure shifts from surface to the subsurface in the presence of lower loads. By employing 12-layer partitioning, the predicted transition from surface to subsurface failure occurs at F_p = 92.5 kN. This value
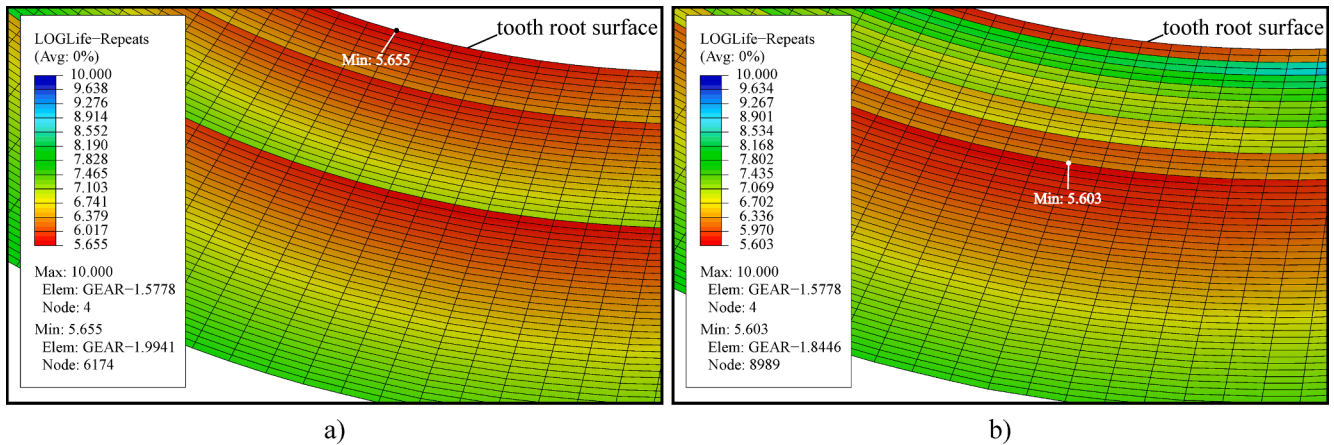
Fig. 14. An example of observed tooth root region results obtained by the proposed model for F_p = 92.5 kN and: a) 3-layer partitioning, and b) 12-layer partitioning.
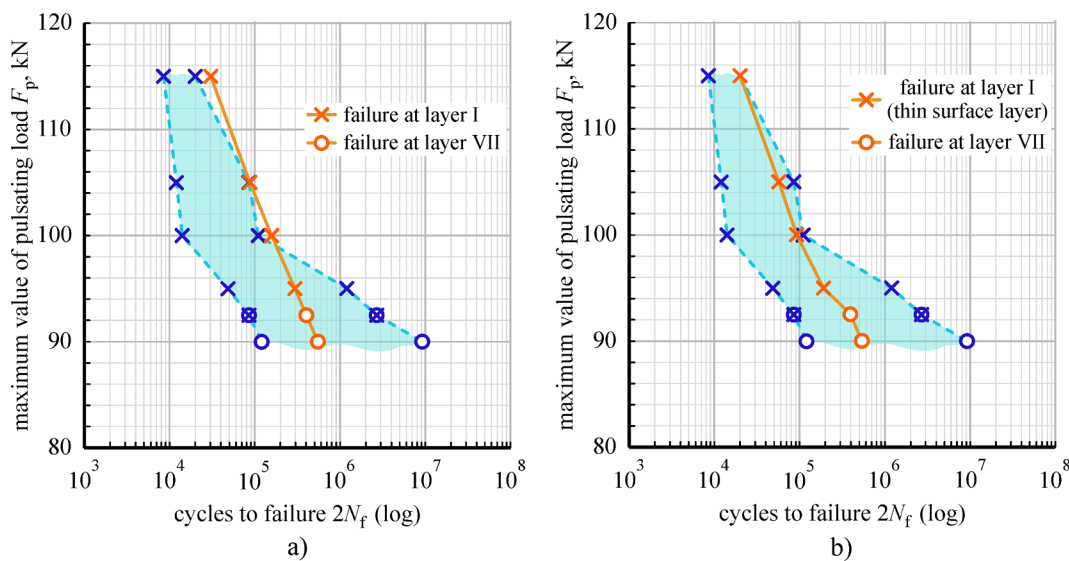

Fig. 15. Comparison of bending fatigue lives and failure locations between experimental results and the proposed model: a) 12-layer partitioning, and b) modified 12-layer partitioning with a thin surface layer.

corresponds to the load at which subsurface failure is first observed in experimental results (denoted by both surface and subsurface failure marks in Fig. 13). Therefore, it can be concluded that the proposed model accurately predicts the surface to subsurface failure transition.

Subsurface failure location

For 6-layer partitioning, the critical subsurface failure location is layer V (Fig. 13), which is defined from 300 μm to 500 μm below the tooth root fillet according to Fig. 10. For 12-layer partitioning, the critical subsurface failure location is Layer VII, which is defined from 200 μm to 250 μm below the tooth root fillet. Within experimental results [11], it is stated that subsurface failures always occurred at the region of non-metallic inclusions, which is located at an average distance of 225 μm ± 50 μm below the tooth root fillet [12]. Therefore, it can be concluded that the results obtained by the proposed model show good agreement with experimental ones regarding the subsurface failure location prediction.

An example of predicted bending fatigue lives and failure locations

obtained by the proposed model for F_p = 92.5 kN is shown in Fig. 14.

To summarize, the predicted model shows good agreement with experimental results when estimating the required number of cycles for bending fatigue failure in high cycle fatigue. In addition, predictions of surface-to-subsurface failure transition, as well as subsurface failure location, also show good agreement with the experimental observations. However, the predicted number of cycles for bending fatigue failure in low cycle fatigue tends to overestimate the actual results.

Nevertheless, estimated low cycle bending fatigue lives can be improved by further increasing the number of layers (higher than 12). This results in additional complications when creating the fatigue model since finite elements within each layer have to be manually selected. The tooth root surface is always a critical fatigue failure location due to the highest load-induced stresses and surface finishing. Hence, an extremely thin layer with the width of a single finite element can be employed as the surface layer. Then, averaged surface hardness and residual stress values that are insignificantly different from actual ones (since the layer

thickness is extremely small) can be assigned to the layer. Consequently, the prediction error due to averaging can be lowered.

The aforementioned is not done for subsurface failure since it is characterized by relatively complicated multiaxial load-induced stresses and strains, as well as variable residual stresses and hardness. Therefore, it is not immediately clear at which depth below the surface will the failure occur. In other words, where exactly below the surface should the layer with a single finite element thickness be placed cannot be easily determined. This problem will be tackled in future investigations.

Due to its highest accuracy, 12-layer partitioning is once again employed. A total of 200 elements (instead of the previous 56) are assigned to the observed tooth root region in the depth direction, where the width of each element is $0.7/200 = 0.0035$ mm. In the direction of the tooth root fillet, 75 elements are once again assigned. As a result, a total of $200 \cdot 75 = 15000$ finite elements are assigned to the observed tooth root region. Then, a thin surface layer with the width of a single finite element (0.0035 mm) is created at the tooth root surface. According to Fig. 10, the surface hardness of HV 755 and surface residual stress $\sigma_{res} = -950$ MPa are assigned to the layer. Finally, to lower the averaging error and improve predicted surface bending fatigue lives, the procedure described by steps 1 – 7 in Section 2.5 is repeated only for the newly created surface layer. Since they are characterized by surface fatigue failure and overestimated fatigue lives, only the first four pulsating loads ($F_p = 115$ kN, 105 kN, 100 kN, and 95 kN) are considered. Subsurface failure results for $F_p = 92.5$ kN and 90 kN are not modified. The results are shown in Fig. 15.

When modified 12-layer partitioning is employed, all bending fatigue prediction lives fall within the shaded region between the experimental results. Therefore, good agreement is observed between estimated and actual results.

Lastly, some parameters that may have affected the obtained results should be mentioned. To reduce computational costs, a 2D numerical simulation was conducted to obtain linear elastic principal stresses and strains. As previously mentioned, this is justified since the gear width is not greater than six times its module (Table 1) [31]. However, two-dimensional approximation of actual three-dimensional stress–strain state inevitably results in some approximation errors, i.e., the stresses and strains are somewhat lower for the 2D case. Consequently, higher bending fatigue lives are obtained. If a 3D numerical analysis is carried out, estimated bending fatigue lives would be lower. Hence, even better agreement with the experimental results would be achieved. Lastly, a finer layer partition may be employed to additionally increase the accuracy of subsurface failure location prediction. Since the obtained results are in good agreement with the experimental investigation, the layers were not further partitioned due to increased complexity and computational costs.

In addition, the hardness method, which was used to obtain strain-life properties, is an approximation method used in the absence of actual experimental data. As such, it also results in some prediction errors. A better option would be to utilize actual fatigue data acquired by testing specimens made of the material as the gear. However, this is problematic since the case layer of a surface hardened gear is not homogenous and its hardness varies with depth, while test specimens usually have a uniform material cross-section.

5. Conclusions

In this paper, a fatigue model based on the multilayer method and strain–life (ε – N) approach was proposed to predict both the location and the required number of cycles for bending fatigue failure in surface hardened spur gears. The tooth root region of the gear was separated into 3, 6, or 12 layers. According to the hardness method, constant strain-life properties and residual stresses were assigned to each layer. Finite element simulation was employed to obtain linear elastic stresses and strains in the tooth root region, which were corrected for elastic–plastic material behavior via Neuber's rule. Bending fatigue failure predictions were obtained by using the principal strain analysis. The obtained results were validated against experimental results from the available literature and good agreement was observed.

The following conclusions can be drawn:

- A good correlation between the bending fatigue lives obtained by the proposed model and experimental ones is observed in the high cycle fatigue region. On the other hand, the proposed model tends to overestimate bending fatigue lives in the low cycle fatigue region. This can be improved by introducing a thin layer with a thickness of a single element at the tooth root surface. Then, all of the results obtained by the proposed model show good agreement with the experimental results. Lastly, it should be noted that the number of employed layers (3, 6, or 12) has a negligible effect on estimated bending fatigue lives.

- With an increase in the number of employed layers, a more accurate transition point from surface to subsurface fatigue failure is obtained. When 12 layers are assigned, the aforementioned transition point coincides with the one obtained by experimental testing. Hence, it can be concluded that the proposed model accurately estimates the transition point from surface to subsurface fatigue failure.

- With an increase in the number of layers, a more accurate subsurface failure location is obtained. When 12 layers are assigned, the proposed model predicts that subsurface failure will occur at 200 μm – 250 μm below the surface. According to experimental results, subsurface failure always appeared at 225 μm ± 50 μm below the surface. Therefore, it can be concluded that the proposed model is accurate in estimating the subsurface failure location.

In future work, a two-dimensional STBF numerical simulation will be replaced by a three-dimensional one to improve the accuracy of the results. Then, the plan is to employ the proposed model to investigate the effect of carburizing depth and shot peening parameters on both the location (surface vs subsurface) and the required number of cycles for bending fatigue failure in surface hardened spur gears. Last but not least, a quasi-static numerical simulation of a running gear pair will be conducted, where non-proportional load-induced stresses and strains are present in the tooth root region. The proposed fatigue model will then be utilized to predict the location and number of cycles required for bending fatigue failure of a running gear pair.

Declaration of Competing Interest

The authors declare that they have no known competing financial interests or personal relationships that could have appeared to influence the work reported in this paper.

Acknowledgment

Appendix

Table 2

Table 2
Averaged hardness values, strain-life properties, cyclic stress–strain properties, and residual stresses for each layer in 3, 6, and 12-layer partitioning.

Total number of layers	Layer	HV	HB	σ'_f, MPa	ε'_f	b	c	K', MPa	n'	σ_{res}, MPa
3	I	755	699	3195	0.037	−0.09	−0.56	5438	0.161	−1109
	II	728	677	3104	0.042			5170		−592
	III	625	592	2742	0.078			4131		−301
6	I	755	699	3195	0.037			5438		−1144
	II	755	699	3195	0.037			5438		−1098
	III	742	688	3151	0.039			5309		−790
	IV	708	661	3036	0.047			4967		−396
	V	673	633	2914	0.058			4608		−215
	VI	598	568	2638	0.093			3866		−354
12	I	755	699	3195	0.037			5437		−1080
	II	755	699	3195	0.037			5437		−1280
	III	755	699	3195	0.037			5437		−1160
	IV	755	699	3195	0.037			5437		−1000
	V	750	695	3179	0.037			5391		−883
	VI	737	684	3134	0.040			5259		−700
	VII	722	673	3084	0.043			5110		−450
	VIII	708	661	3036	0.047			4967		−240
	IX	688	645	2967	0.053			4762		−195
	X	660	622	2869	0.062			4481		−233
	XI	625	592	2742	0.078			4313		−313
	XII	578	550	2562	0.105			3679		−387

References

[1] "ISO 6336:2006, Calculation and load capacity of spur and helical gears," 2006.
[2] "ANSI/AGMA 2101-D04, Fundamental rating factors and calculation methods for involute spur and helical gear teeth," 2004.
[3] Rego R, Löpenhaus C, Gomes J, Klocke F. Residual stress interaction on gear manufacturing. J Mater Process Technol 2018;252:249–58. https://doi.org/10.1016/j.jmatprotec.2017.09.017.
[4] Yin F, Fatemi A. Monotonic and cyclic deformations of case-hardened steels including residual stress effects. Strain 2011;47(SUPPL. 1):74–83. https://doi.org/10.1111/j.1475-1305.2008.00504.x.
[5] Jo B, Sharifimehr S, Shim Y, Fatemi A. Cyclic deformation and fatigue behavior of carburized automotive gear steel and predictions including multiaxial stress states. Int J Fatigue 2017;100:454–65. https://doi.org/10.1016/j.ijfatigue.2016.12.023.
[6] Gaur V, Doquet V, Persent E, Mareau C, Roguet E, Kittel J. Surface versus internal fatigue crack initiation in steel: Influence of mean stress. Int J Fatigue 2015;82: 437–48. https://doi.org/10.1016/j.ijfatigue.2015.08.028.
[7] Yin F, Fatemi A, Bonnen J. Variable amplitude fatigue behavior and life predictions of case-hardened steels. Int J Fatigue 2010;32(7):1126–35. https://doi.org/10.1016/j.ijfatigue.2009.12.009.
[8] Čular I, Vučković K, Žeželj D, Glodež S. Analytical approach for low and high cycle bending fatigue life prediction of carburized gear steel specimens. Eng Fail Anal 2020;108:104328.
[9] Lv Y, Lei L, Sun L. Effect of microshot peened treatment on the fatigue behavior of laser-melted W6Mo5Cr4V2 steel gear. Int J Fatigue 2017;98:121–30. https://doi.org/10.1016/j.ijfatigue.2017.01.017.
[10] Peng C, Xiao Y, Wang Y, Guo W. Effect of laser shock peening on bending fatigue performance of AISI 9310 steel spur gear. Opt Laser Technol 2017;94:15–24. https://doi.org/10.1016/j.optlastec.2017.03.017.
[11] Fuchs D, Schurer S, Tobie T, Stahl K. On the determination of the bending fatigue strength in and above the very high cycle fatigue regime of shot-peened gearsZur Bestimmung der Zahnfußfestigkeit kugelgestrahlter Zahnräder im Bereich erhöhter Lastspielzahlen. Forsch im Ingenieurwesen/Engineering Res 2022;86(1):81–92.
[12] Fuchs D, Schurer S, Tobie T, Stahl K. A model approach for considering nonmetallic inclusions in the calculation of the local tooth root load-carrying capacity of high-strength gears made of high-quality steels. Proc Inst Mech Eng, Part C: J Mech Eng Sci 2019;233(21-22):7309–17.
[13] Bretl N, Schurer S, Tobie T, Stahl K, Höhn BR. Investigations on tooth root bending strength of case hardened gears in the range of high cycle fatigue. Am Gear Manuf Assoc Fall Tech Meet 2013;2013:103–18.
[14] Güntner C, Tobie T, Stahl K. Influences of the Residual Stress Condition on the Load-Carrying Capacity of Case-Hardened Gears, no. August, pp. 60–69, 2018.
[15] Gorla C, Rosa F, Conrado E, Concli F. Bending fatigue strength of case carburized and nitrided gear steels for aeronautical applications. Int J Appl Eng Res 2017;12 (21):11306–22.
[16] Zhang J, Prasannavenkatesan R, Shenoy MM, McDowell DL. Modeling fatigue crack nucleation at primary inclusions in carburized and shot-peened martensitic steel. Eng Fract Mech 2009;76(3):315–34. https://doi.org/10.1016/j.engfracmech.2008.10.011.

[17] Vučković K, Galić I, Božić Ž, Glodež S. Effect of friction in a single-tooth fatigue test. Int J Fatigue 2018;114(May):148–58. https://doi.org/10.1016/j.ijfatigue.2018.05.005.
[18] Lias MR, Sharif Z, Awang M, Jailani A, Warap H. Quasi-static modeling of spur gear time varying strength analysis. ARPN J Eng Appl Sci 2017;12(6):1938–47.
[19] Thirumurugan R, Deepak CCC, Karthieeban K. Effect of adjacent teeth load on bending strength of high contact ratio asymmetrical spur gear drive. Int J Veh Struct Syst 2017;9(1):32–5. https://doi.org/10.4273/ijvss.9.1.07.
[20] Vučković K, Čular I, Mašović R, Galić I, Žeželj D. Numerical model for bending fatigue life estimation of carburized spur gears with consideration of the adjacent tooth effect. Int J Fatigue 2021;153:106515.
[21] Chen Z, Jiang Y, Tong Z, Tong S. Residual stress distribution design for gear surfaces based on genetic algorithm optimization. Materials (Basel) 2021;14(2): 1–17. https://doi.org/10.3390/ma14020366.
[22] Baumel AJ, Seeger T. The influence of residual stresses and surface strengthening on components fatigue life. Fatigue 1990;90:311–6.
[23] Ince A, Glinka G. A modification of Morrow and Smith-Watson-Topper mean stress correction models. Fatigue Fract Eng Mater Struct 2011;34(11):854–67. https://doi.org/10.1111/j.1460-2695.2011.01577.x.
[24] Morrow J. Fatigue Properties of Metals. Warrendale, PA: SAE, 1968.
[25] Smith K, Watson P, Topper T. A stress-strain function for the fatigue of materials. J Mater 1970;5:767–78.
[26] S. technology Limited, "FE-SAFE Version 6.5, User Guide." 2014.
[27] Dowling NE. Mean stress effects in stress-life and strain-life fatigue. SAE Tech. Pap., vol. 2, no. 1, 2004, doi: 10.4271/2004-01-2227.
[28] Roessle ML, Fatemi A. Strain-controlled fatigue properties of steels and some simple approximations. Int J Fatigue 2000;22(6):495–511. https://doi.org/10.1016/S0142-1123(00)00026-8.
[29] Fuchs HO, Stephens RI, Saunders H. Metal Fatigue in Engineering 1980.
[30] Landgraf R, Car- FB. Fatigue behavior of carburized steel, pp. 130–142, 2018.
[31] Pehan S, Hellen TK, Flasker J, Glodez S. Numerical methods for determining stress intensity factors vs crack depth in gear tooth roots. Int J Fatigue 1997;19(10): 677–85. https://doi.org/10.1016/S0142-1123(97)00101-1.
[32] Neuber H. Theory of stress concentration for shear-strained prismatical bodies with arbitrary nonlinear stress-strain law. J Appl Mech Trans ASME 1960;28(4):544–50. https://doi.org/10.1115/1.3641780.
[33] Glodež S, Šraml M, Kramberger J. A computational model for determination of service life of gears. Int J Fatigue 2002;24(10):1013–20. https://doi.org/10.1016/S0142-1123(02)00024-5.
[34] Kramberger J, Šraml M, Glodež S, Flašker J, Potrč I. Computational model for the analysis of bending fatigue in gears. Comput Struct 2004;82(23–26):2261–9. https://doi.org/10.1016/j.compstruc.2003.10.028.
[35] Podrug S, Jelaska D, Glodež S. Influence of different load models on gear crack path shapes and fatigue lives. Fatigue Fract Eng Mater Struct 2008;31(5):327–39. https://doi.org/10.1111/j.1460-2695.2008.01229.x.
[36] SIMULIA, "Abaqus 6.13," Analysis User's Guide, Dassault Systems. 2013.
[37] "FE Safe version 6.5." Dassault Systemes, 2014.
[38] Fuchs D, Schurer S, Tobie T, Stahl K. Investigations into non-metallic inclusion crack area characteristics relevant for tooth root fracture damages of case carburised and shot-peened high strength gears of different sizes made of high-quality steelsUntersuchungen zu Rissflächencharakteristiken nicht-metallischer

Einschlüsse maßgeblich für Zahnfußbrüche von einsatzgehärteten und kugelgestrahlten hochtragfähigen Zahnrädern unterschiedlicher Größe aus hochreinen Stählen. Forsch im Ingenieurwesen/Engineering Res 2019;83(3): 579–87.

[39] Winkler KJ, Schurer S, Tobie T, Stahl K. Investigations on the tooth root bending strength and the fatigue fracture characteristics of case-carburized and shot-peened gears of different sizes. Proc Inst Mech Eng Part C J Mech Eng Sci 2019;233 (21–22):7338–49. https://doi.org/10.1177/0954406219841650.

[40] ASTM. E140-07 Standard hardness conversion tables for metals relationship among brinell hardness, vickers hardness, rockwell hardness, superficial hardness, knoop hardness, and scleroscope hardness. Astm 2007:1–21.

Paper IV

The manuscript shown within this thesis is published in:

Contributions of the Ph.D. candidate:

- establishing the computational model
- validating the model against experimental data
- interpreting and discussing the results
- writing the manuscript

Computational model for bending fatigue life and failure location prediction of surface-hardened running gears

Ivan Čular [*], Krešimir Vučković, Ivica Galić, Dragan Žeželj

University of Zagreb, Faculty of Mechanical Engineering and Naval Architecture, I. Lučića 5, 10000 Zagreb, Croatia

ARTICLE INFO

ABSTRACT

In this paper, a numerical model is proposed to predict the location and the number of cycles for bending fatigue failure of surface-hardened gears. The predictions are validated against experimental results. Linear-elastic stresses and strains obtained by a finite element simulation are imported into the fatigue model. Bending fatigue lives at the observed tooth root region are estimated based on the multilayer method, hardness method, and strain-life approach. The critical plane approach is employed due to non-proportional loading. Good agreement between actual and predicted bending fatigue lives was observed, as well as between the estimated and actual subsurface failure location.

1. Introduction

Steel gears are one of the key components in mechanical power transmission. Due to the variable and cyclic loading nature, material fatigue might occur in the tooth root of a gear (more commonly known as *bending fatigue*). For metal gears additionally hardened via heat treatments such as carburizing, bending fatigue is typically more problematic than tooth flank fatigue (*contact fatigue*). Furthermore, metal gears are often additionally shot-peened to induce a beneficial, fatigue-resistant, compressive residual stress at the surface. However, even though this might improve the surface bending fatigue resistance, fatigue crack initiation may shift to a subsurface area. These cracks are hard to detect and may not be noticed during regular service intervals. As a result, once the gear pair is returned to normal operating conditions, a subsurface crack may rapidly grow and propagate through a relatively brittle surface-hardened layer. Consequently, complete tooth breakage due to bending fatigue may occur. The existing analytical methods according to relevant standards such as ISO 6336 [1] or ANSI/ AGMA 2101 [2] do not account for the effects such as subsurface bending fatigue failure, tooth deformation, or the adjacent tooth effects on the bending stress cycle (in this paper *bending stress* is defined as the major principal surface stress on the tooth root fillet). Therefore, the researchers often tend to gravitate towards experimental or numerical investigations to explore bending fatigue failure of gears.

Since experimental investigations involving a running gear pair are relatively complicated and expensive, bending fatigue of gears is often explored by employing single tooth bending fatigue (STBF) tests. Concli et al. [3] proposed a new multiaxial approach to translate STBF results to be comparable to the running gear pair results. The authors modified the correction factor that translates STBF results. Moreover, they concluded that the relevant standards are more conservative when translating the results but may lead to underestimating the actual gear performance. Bonaiti and Gorla [4] conducted STBF tests to obtain the modified *S—N* curve and account for the statistical behavior and different load history that characterizes the running gear pair. Argoud et al. [5] investigated the bending fatigue of jet engine gears made of 16NiCrMo13 steel via STBF tests. Moreover, they proposed an alternative plane-bending method to substitute the STBF test method. Conrado et al. [6] compared the bending fatigue strength of carburized and nitrided gears used in industrial applications by employing a custom-made STBF rig. The authors concluded that the bending fatigue strength of nitrided gears is comparable to the bending fatigue strength of carburized gears. Hong et al. [7] developed a new experimental method for evaluating the bending fatigue lives of a running gear pair under different loading conditions. Even though bending fatigue is the subject of this paper, it should be also mentioned that running gear pair tests are also used for contact fatigue investigations [8].

Contrary to the experimental methods, numerical methods are more frequently used in bending fatigue investigation due to their relative simplicity, low cost, and continuous accuracy improvement over the years. Vučković et al. [9] established a numerical finite element model of an STBF test. The authors proposed a different test approach to minimize the effect of friction on the bending fatigue lives of a gear.

Nomenclature

b	fatigue strength exponent
c	fatigue ductility exponent
E	modulus of elasticity
F_p	pulsating force acting on the loading anvil
h_{aP}	addendum of a gear
K'	cyclic strength coefficient
K_A	application factor
$K_{F\alpha}$	transverse load factor
$K_{F\beta}$	face load factor
K_{SC}	scale factor used to modify linear-elastic stresses and strains
K_{sf}	surface finish correction factor
K_V	internal dynamic factor
m	gear's module
N_f	number of reversals until failure
n'	cyclic strength exponent
T	torque at the test gear
x	profile shift coefficient of a gear
Z_1	driving gear (test gear)
Z_2	driven gear
ΔS_{ij}^e	incremental change in the linear-elastic stress
ΔS_{ij}^a	incremental change in the actual stress
Δe_{ij}^e	incremental change in the linear-elastic strain
Δe_{ij}^a	incremental change in the actual strain
$\Delta\varepsilon^e$	elastic strain range in Baquin-Coffin-Manson's equation
$\Delta\varepsilon^p$	plastic strain range in Baquin-Coffin-Manson's equation
ε_a	strain amplitude in Baquin-Coffin-Manson's equation
ε_f'	fatigue ductility coefficient
ε_n	strain amplitude normal to the critical plane
ε_1^a	major actual principal strain amplitude
ε_2^a	intermediate actual principal strain amplitude
ε_3^a	minor actual principal strain amplitude
σ_f'	fatigue strength coefficient
σ_F	maximum tooth root stress
σ_{F0}	maximum nominal tooth root stress
σ_1	major principal stress (commonly refered to as *bending stress* for surface nodes)
σ_a	load-induced stress amplitude used in SWT's mean stress correction
σ_m	mean load-induced stress in Baquin-Coffin-Manson's equation
σ_m^a	actual load-induced mean stress
σ^e	linear-elastic bending stress
σ_{max}^e	maximum linear-elastic bending stress in a single cycle
σ_{min}^e	minimum linear-elastic bending stress in a single cycle
σ_{res}	residual stress
φ	critical plane rotation angle about z-axis
θ	critical plane rotation angle with respect to the major actual principal strain
ν	Poisson's ratio

Čular et al. [10] proposed an STBF computational model for estimating bending fatigue lives and failure location (surface vs subsurface fatigue failure). The results were experimentally validated, and good agreement between the results was observed. Vučković et al. [11] established an additional numerical model that estimates the bending fatigue lives of a running gear pair under the assumption of surface failure. Moreover, the authors investigated the effect of the adjacent tooth on bending fatigue lives. He et al. [12] proposed a damage-coupled numerical model to investigate gear fatigue that accounts for the initial residual stress effect. The authors explored both contact and bending fatigue and concluded that initial tensile residual stress reduces while initial compressive residual stress prolongs the fatigue life. Lias et al. [13] established a quasi-static numerical model of spur gears and compared the time-varying strength of gears with analytical equations. Thirumurugan et al. [14] investigated the effect of the adjacent tooth load on the tooth root stresses of a spur gear. The authors concluded that the maximum tooth root stress level during a single stress cycle is increased when the adjacent tooth is considered. Savaria et al. [15] proposed a three-dimensional (3D) fatigue model that accounts for the microstructure variation, residual stresses, and surface roughness to predict the bending endurance limit. The authors experimentally validated the results and concluded that residual stress could significantly affect bending fatigue. Therefore, it is important to determine residual stress distribution accurately when investigating surface-hardened components [15].

Based on the existing literature, it can be observed that the issue of surface-to-subsurface bending fatigue failure is not yet sufficiently investigated, at least not from the perspective of numerical modeling. However, some researchers have experimentally explored the aforementioned phenomenon. Fuchs et al. [16] explored the effect of non-metallic inclusions on subsurface bending fatigue failure and proposed an analytical model as a first step in a prediction model. The authors concluded that surface strengthening and high cleanliness of gear steels have become important aspects in mechanical engineering. However, this results in frequent bending fatigue crack initiation below the tooth root's surface. Winkler et al. [17] investigated the bending fatigue of

case-carburized and shot-peened gears. For such gears, the authors concluded that bending fatigue failure in a high-cycle regime is significantly affected by subsurface fatigue failures instead of surface ones. Guntner et al. [18] explored the effect of residual stress distribution on the load-carrying capacity of case-hardened and/or additionally shot-peened gears. The authors concluded that, for shot-peened gears, subsurface failure mode might limit the tooth root bending strength as well as positive effects of shot peening. Fuchs et al. [19] further investigated the effect of the area of non-metallic inclusions on the bending fatigue strength of surface-hardened gears. The authors concluded that the measured elliptical area of the subsurface failure site (the so-called *fish eye*) is proportional to the distance from the surface of a non-metallic inclusion. Moreover, the authors stated that cracks in surface-hardened gears that are additionally shot-peened more often initiate below the tooth root surface. Fuchs et al. [20] continued their investigation by employing STBF and running pair gear tests to investigate the high and very high cycle fatigue behavior of shot-peened gears. The authors concluded that no bending fatigue limit is expected for such gears since a failure was observed up to $5 \bullet 10^7$ cycles.

Based on the conducted literature overview of the most relevant and most recent investigations, the following conclusion can be made. The phenomenon of surface–subsurface bending failure transition in surface-hardened spur gears is adequately experimentally investigated. However, no model can be found that jointly accounts for as many as possible real-time effects, such as considering the running gear pair (as opposed to STBF tests), adjacent tooth effect [11], and surface-to-subsurface bending failure transition [10]. Therefore, in this paper, a numerical model that accounts for the aforementioned effects is proposed. The model is comprised of a quasi-static finite element (FE) simulation of a running gear pair conducted in Abaqus [21] and the fatigue model [10] that was previously established and experimentally validated on an STBF test. Linear-elastic FE stresses and strains are corrected for elastic–plastic behavior via Neuber's rule [22]. Bending fatigue lives are estimated based on the strain-life method ($\varepsilon - N$) with either Morrow's [23] or Smith-Watson-Topper's (SWT) [24] mean stress correction

methods. In the absence of actual fatigue data, fatigue properties are obtained via the hardness method [25]. The multilayer method [26] is employed to assign averaged residual stresses and fatigue properties, as well as to distinguish between surface and subsurface failure. Lastly, the predicted bending fatigue lives and potential failure locations are validated against the available experimental results from the literature.

2. Finite element model of a running gear pair

In this section, a quasi-static FE model of a running gear pair is established to obtain linear-elastic stresses and strains at the tooth root of the gear. This model is based on the existing running gear pair tests that will be later used to validate the numerical model proposed in this paper. Moreover, a scale factor is introduced to account for additional effects not considered within the FE model. Geometric and material parameters of the running gear pair are taken from [17] and shown in Table 1. Both gears are made of 18CrNiMo7-6 steel, and the material is assumed as homogenous, isotropic, and linear-elastic.

It should be noted that, apart from the profile shift coefficient, addendums of each gear were additionally modified from the standard value of $h_{aP} = (1 + x)m$, where h_{aP} is the addendum of the gear, x is the profile shift coefficient, and m is the gear's module. Therefore, atypical values of tip diameter were obtained, as shown in Table 1. It is assumed that this was done to increase the center distance and consequently tooth root stresses, which lowers the experimentally obtained fatigue lives, thereby reducing the total required time for the experiment.

First, a quasi-static finite element model, whose accuracy was already confirmed in previous investigations [10,27,28], is established via the numerical simulation software Abaqus. Both gears were modeled according to the parameters shown in Table 1. Boundary conditions of the running gear pair with the corresponding mesh are shown in Fig. 1.

The running gear pair consists of the driving gear (test gear), Z_1, and the driven gear, Z_2. A two-dimensional (2D) finite element analysis is carried out to reduce computational costs. Only nine gear teeth are modeled on both gears to further simplify the simulation. Reference points RP_1 and RP_2 are connected via *kinematic coupling* constraint to the inner surfaces of the driving gear and the driven gear, respectively. The simulation is divided into two steps.

In the first step, fixed boundary conditions are applied to RP_2 to fix the driven gear. Only the rotation of the driving gear is enabled by applying horizontal and vertical displacement restrictions on RP_1. Then, to establish contact between gears, torque T is applied to RP_1 in the counterclockwise direction (as shown in Fig. 1). Values of the applied torque are taken directly from the experimental investigation [20] used for subsequent validation of the proposed model and are equal to 230 Nm, 210 Nm, 190 Nm, 170 Nm, and 150 Nm. *Normal behavior, hard contact* option is chosen to define interaction properties between gear teeth, and *primary* and *secondary* surfaces are defined for each contact pair within the model, i.e., a total of nine pairs of contact surfaces. By assuming fully lubricated operating conditions and consequently low friction coefficients between teeth flanks [29,30], friction is not considered in this paper.

In the second step, the driven gear is rotated by an angle of $\vartheta = 50°$ to ensure that the observed tooth root region experiences the entire load-induced stress cycle. The second step is separated into 500 increments

(time frames) to obtain an accurate resolution of the results, where each time frame is solved as a static loading case. Hence, a quasi-static simulation is established. Lastly, *non-linear geometry* (NLGEOM) is activated due to geometric nonlinearity induced by large displacements resulting from incremental rotation of the gears.

According to Pehan et al. [31], plane stress can be assumed when the gear's face width is lower than six times its normal module, which is true according to Table 1. Therefore, the assembly is meshed by combining four-node quadrilateral plane stress finite elements (CPS4) and three-node triangular plane stress finite elements (CPS3). However, only CPS4 elements are used to structurally mesh the observed tooth region (Fig. 1b). This is done to ensure the uniform layer distribution required for the multilayer method, which is part of the fatigue model (Section 3). Only the tooth root region is selected in the *field output request* to reduce the output file size. Lastly, the lower boundary of the observed tooth root region is taken as the nominal case depth of the test gear (0.35 mm according to Table 1).

2.1. Additional factors that affect tooth root stresses

By employing the quasi-static FE simulation, stresses and strains for linear-elastic material behavior are obtained for each node within the observed tooth root region. However, before the obtained values can be input into the fatigue model, additional factors that affect tooth root stresses and were not accounted for within the FE model must be considered.

According to ISO 6336 [1], the maximum nominal tooth root stress σ_{F0} is modified by four additional factors to obtain the maximum tooth root stress, σ_F, as follows:

$$\sigma_F = \sigma_{F0} \cdot K_A \cdot K_V \cdot K_{F\alpha} \cdot K_{F\beta} \tag{1}$$

where K_A is the application factor that compensates for incremental gear loading from external sources, and K_V is the internal dynamic factor that accounts for the effects of gear tooth accuracy grade with respect to speed and load. Parameter $K_{F\alpha}$ is the transverse load factor for tooth root stress that considers the effect of non-uniform transverse load distribution between several pairs of simultaneously contacting gear teeth, and $K_{F\beta}$ is the face load factor that accounts for non-uniform load distribution effects over the gear face width on tooth root stress values. To simplify Eq. (1), a "combined factor" denoted as K_C is introduced in this paper:

$$K_C = K_A \cdot K_V \cdot K_{F\alpha} \cdot K_{F\beta} \tag{2}$$

According to [1], K_C can be obtained by different methods. However, some running gear pair parameters have to be known, such as accuracy and tolerances of the manufactured gears, operating speed, alignment of axes of rotation, bearing clearances, running-in effects, and lubricant properties.

Due to calculation simplifications, ISO 6336 standard tends to overestimate the maximum nominal tooth root stress, σ_{F0}, while more accurate results are obtained by employing the FE method [11,32]. Therefore, the K_C is used to modify linear-elastic stresses and strains obtained by the FE model (denoted as σ^e) instead of the maximum nominal tooth root stress, σ_{F0}, obtained via the ISO 6336 standard.

In Fig. 2, a schematic representation of the linear-elastic major

Table 1
Parameters of the running gear pair according to [17].

| Parameter	Driving gear, Z_1 (test gear)	Driven gear, Z_2	Parameter	Driving gear, Z_1 (test gear)	Driven gear, Z_2
Number of teeth	59	61	Tip diameter	91.5 mm	96 mm
Normal module	1.5 mm		Center distance	91.5 mm	
Profile shift coefficient	− 0.125	0.186	Modulus of elasticity	210 GPa	
Face width	8 mm		Poisson's ratio	0.3	
Normal pressure angle	20°		Surface hardening treatment	Quenched, carburized to the nominal case depth of 0.35 mm, and shot-peened	
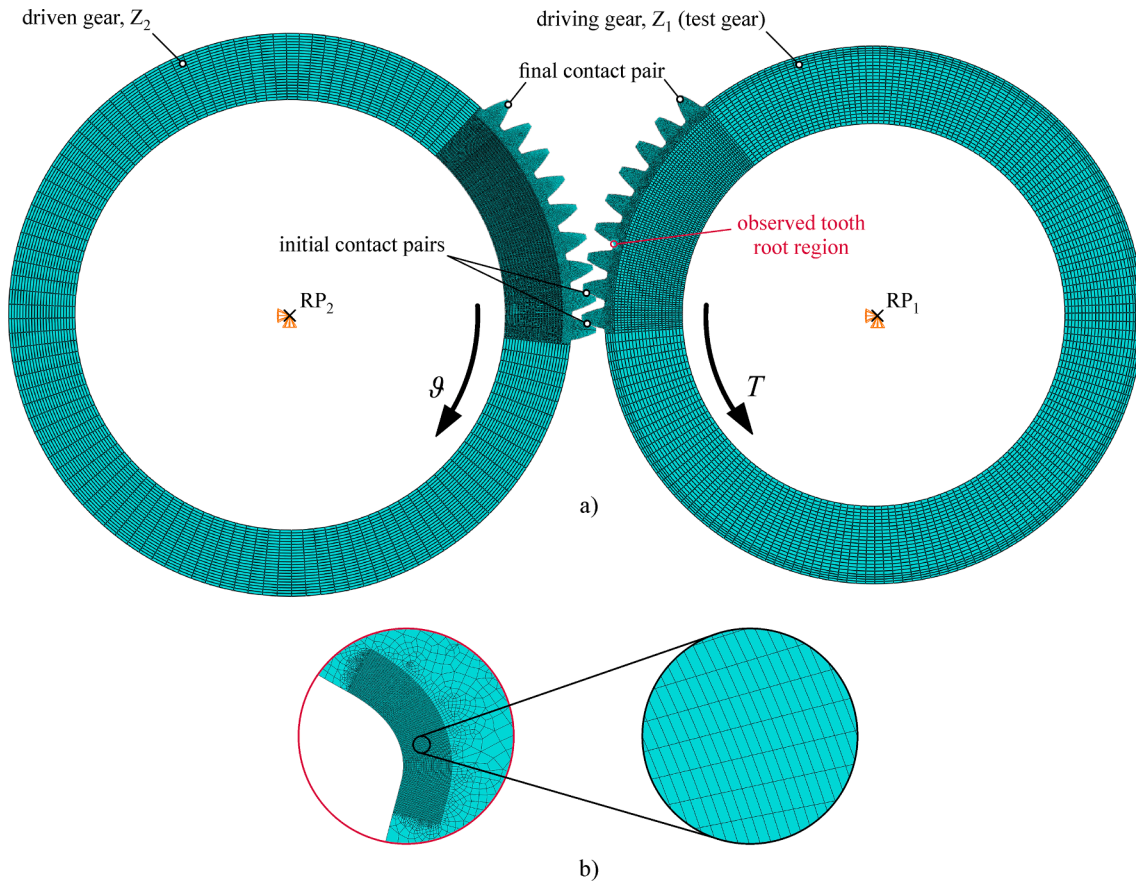
Fig. 1. Finite element model of the running gear pair: (a) boundary conditions and mesh, and (b) a close-up of the observed tooth root region.
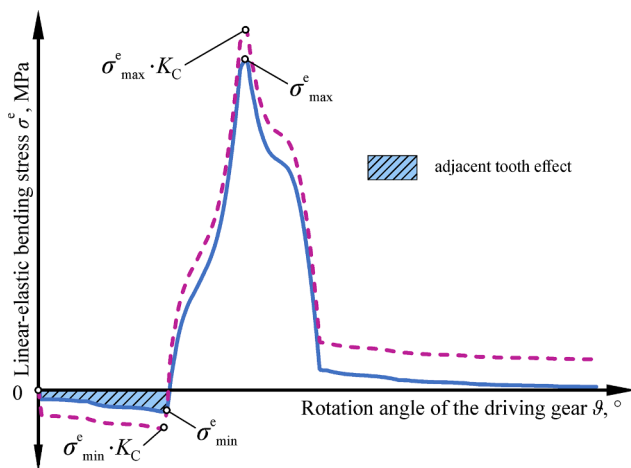

Fig. 2. Schematic representation of linear-elastic bending stress cycle with the adjacent tooth effect and modified cycle.

principal stress cycle obtained by the FE simulation is shown for an arbitrarily chosen node on the tooth root fillet. The adjacent tooth effect [11] and modification of the linear elastic major principal stress cycle by employing the combined factor K_C are presented.

As previously mentioned, bending fatigue life predictions obtained in this paper are compared against experimental results from the available literature [20]. Unfortunately, since insufficient data regarding the experimental rig is provided in [20], the combined factor K_C could not be manually calculated according to Eq. (2). However, tooth root stresses, σ_F, required to estimate the combined factor calculated

according to ISO 6336 [1] are directly provided in [20]. Since σ_{F0} can be calculated according to [1], Eq. (1) can be employed to finally obtain the value of K_C, as shown in Table 2.

The combined factors are then applied to all linear-elastic stresses and strains at the observed tooth root region obtained by the FE simulation. The new (modified) values of linear-elastic stresses and strains are then input into the fatigue model.

3. The fatigue model of a running gear pair

In this section, linear elastic stresses and strains are used as an input for the already established fatigue model, which is briefly summarized. However, due to non-proportional loading and non-proportional multiaxial stresses at the tooth root of the gear, two additions to the fatigue model are made. First, incremental Neuber's rule is applied to account for elastic–plastic stresses and strain correction. Second, the critical plane method is employed.

The fatigue model used in this paper was already established and experimentally validated in the previous investigation conducted by the

Table 2
Combined factors used to modify linear-elastic stresses and strains obtained via the FE simulation.

Torque at the test gear T, Nm	Maximum tooth root bending stress σ_F, MPa, [1,20]	Maximum nominal tooth root bending stress σ_{F0}, MPa, [1]	Combined factor $K_C = \sigma_F/\sigma_{F0}$
230	1773	1489	1.191
210	1630	1360	1.199
190	1489	1230	1.211
170	1366	1100	1.242
150	1213	971	1.249

authors [10] for an STBF test. Therefore, it will not be explained in detail but instead summarized. However, certain changes to the fatigue model have to be made due to the non-proportional loading characteristic for the running gear pair as opposed to STBF tests (which can typically be considered as proportional loading even though slight non-proportionality might occur due to friction forces [9]).

3.1. Obtaining fatigue properties via the hardness method and multilayer partitioning of the observed tooth root region

As previously mentioned, the strain-life ($\varepsilon - N$) method is used to predict bending fatigue lives. Fatigue properties required for the strain-life approach are obtained according to the hardness method [25]:

$$\sigma_f' = 4.25 \cdot HB + 225 \tag{3}$$

$$\varepsilon_f' = \frac{0.32 \cdot HB^2 - 487 \cdot HB + 191000}{E} \tag{4}$$

$$b = -0.09 \tag{5}$$

$$c = -0.56 \tag{6}$$

where σ_f' is the fatigue strength coefficient, HB is the averaged value of Brinell hardness for each layer, ε_f' is the fatigue ductility coefficient, E is the modulus of elasticity, b is the fatigue strength exponent, and c is the fatigue ductility exponent.

Cyclic Ramberg-Osgood stress–strain properties can also be estimated as [33]:

$$K' = \frac{\sigma_f'}{\left(\varepsilon_f'\right)^{n'}} \tag{7}$$

$$n' = \frac{b}{c} \tag{8}$$

where K' is the cyclic strength coefficient and n' is the cyclic strength exponent.

Hardness and residual stress profiles for the test gear are obtained from [16,34], respectively, and shown in Fig. 3 along with the initial 3, 6, and 12-layer partitioning. According to [10], the most accurate bending fatigue predictions were obtained for 12-layer partitioning. Therefore, the same partitioning is used in this paper. It should be noted that additional 6 and 12-layer partitioning is not shown for the first layer (the surface layer) in Fig. 3 to avoid cluttering the image. Instead, specific corresponding values are provided in Table 3.

The first of the initial three layers is defined from the surface to the subsurface point where approximately equal residual stress as the one on the surface is present. The second layer is defined up to the point where residual stresses are no longer rapidly decreasing. Lastly, the third of the initial three layers is represented by the remainder of the profile up to the nominal case depth.

A detailed description for the initial 3-layer partitioning can be found in [10]. Once the initial three layers are obtained, the final 12-layer partitioning is achieved by equally partitioning each of the three layers two more times.

Averaged hardness, residual stresses, and layer boundaries for 12-layer partitioning are shown in Table 3. Since the hardness profile taken from the available literature is expressed in HV1, these values are converted to Brinell hardness (HB) to ensure that Eqs. (3)–(6) can be employed. This is done according to the hardness conversion tables from [35]. Lastly, it should be mentioned that the converted Brinell hardness values are acquired for an indenter with 10 mm in diameter and the force of 3000 kgf.
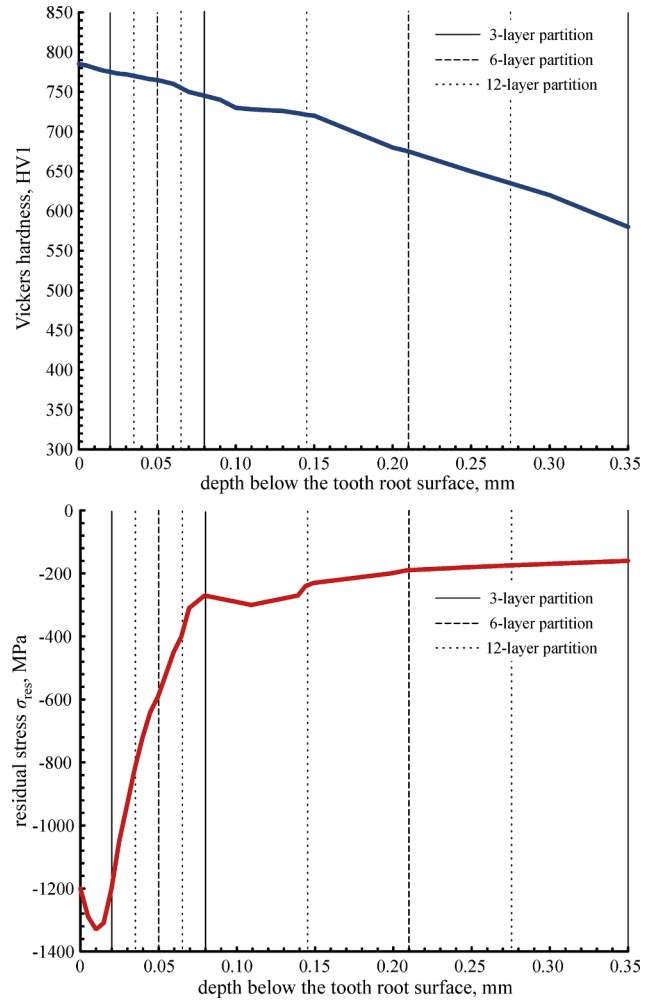

Fig. 3. Hardness and residual stress profiles of the specimen gear with multilayer partitioning.

3.2. Defining sets within the finite element model for the multilayer method

Before the employment of the strain-life method to predict bending fatigue lives is further discussed, the observed tooth root region shown in Fig. 1 has to be divided into 12 layers. This is done to assign layer parameters (fatigue properties and residual stresses) to each layer. According to the range of each layer shown in Table 3, the width of a single finite element is chosen as 5 μm. Therefore, a total of $350/5 = 70$ finite elements are assigned in the depth direction in a single column. In the tooth root fillet direction, 85 elements are assigned in a single row, i.e., a total number of finite elements in the observed tooth root region is $70 \times 85 = 5950$.

3.3. The strain-life approach with different mean stress corrections

The relationship between the actual strain amplitude and the estimated number of cycles for a fully reversed loading ($R = -1$) can be expressed according to Basquin-Coffin-Manson's (BCM) equation:

$$\varepsilon_a = \frac{\Delta\varepsilon^e}{2} + \frac{\Delta\varepsilon^p}{2} = \frac{\sigma_f'}{E}\left(2N_f\right)^b + \varepsilon_f'\left(2N_f\right)^c \tag{9}$$

where ε_a is the total strain amplitude, $\frac{\Delta\varepsilon^e}{2}$ is the elastic strain amplitude, $\frac{\Delta\varepsilon^p}{2}$ is the plastic strain amplitude, and N_f is the number of reversals until fatigue failure. BCM's equation is schematically presented in Fig. 5.

Table 3
Averaged hardness, fatigue properties, and residual stress values for 12-layer partitioning.

Layer No.	Layer range, μm	HV1	HB	σ'_f, MPa	ε'_f	b	c	K', MPa	n'	σ_{res}, MPa
1	0–5	784	721	3288	0.030	− 0.09	− 0.56	5787	0.161	−1245
2	5–10	782	719	3280	0.030			5766		−1310
3	10–15	779	717	3271	0.030			5744		−1320
4	15–20	776	715	3263	0.030			5719		−1255
5	20–35	773	712	3252	0.031			5689		−1001
6	35–50	767	708	3235	0.031			5641		−693
7	50–65	760	703	3211	0.032			5575		−480
8	65–80	750	695	3179	0.034			5479		−327
9	80–145	730	679	3112	0.037			5279		−278
10	145–210	699	655	3007	0.044			4960		−215
11	210–275	653	617	2845	0.059			4485		−182
12	275–350	612	580	2692	0.077			4066		−168

Within the proposed model [10], the BCM's equation for the first four layers of 12-layer partitioning (Fig. 4a–d) is modified according to Morrow's mean stress correction, i.e.:

$$\varepsilon_a = \frac{\sigma'_f - \sigma_m - \sigma_{res}}{E}(2N_f)^b + \varepsilon'_f(2N_f)^c \qquad (10)$$

where σ_m is the mean stress and σ_{res} is the residual stress.

The remaining eight layers (Fig. 4c–l) are modified according to SWT's mean stress correction:

$$\varepsilon_a(\sigma_{max} + \sigma_{res}) = \frac{(\sigma'_f)^2}{E}(2N_f)^{2b} + \sigma'_f\varepsilon'_f(2N_f)^{b+c} \qquad (11)$$

Within Eq. (11), $\sigma_{max} = \sigma_a + \sigma_m$, where σ_a is the load-induced stress amplitude.

Lastly, it should be mentioned that the fatigue model taken from [10] and used in this paper employs the maximum principal strain (normal strain) criterion for bending fatigue failure. This criterion is suggested for multiaxial fatigue involving brittle steels (such as surface-hardened spur gears) [36].

According to the existing STBF model [10] and in addition to the obtained fatigue properties and residual stresses shown in Table 3, load-induced stresses and strains obtained via the FE simulation for linear-elastic material behavior have to be corrected for elastic–plastic material behavior, which may appear due to geometric notches (such as the tooth root fillet). Therefore, Neuber's rule was originally used to obtain actual stresses and strains. Since running gear pair is characterized by non-proportional cyclic load histories, an incremental form of Neuber's
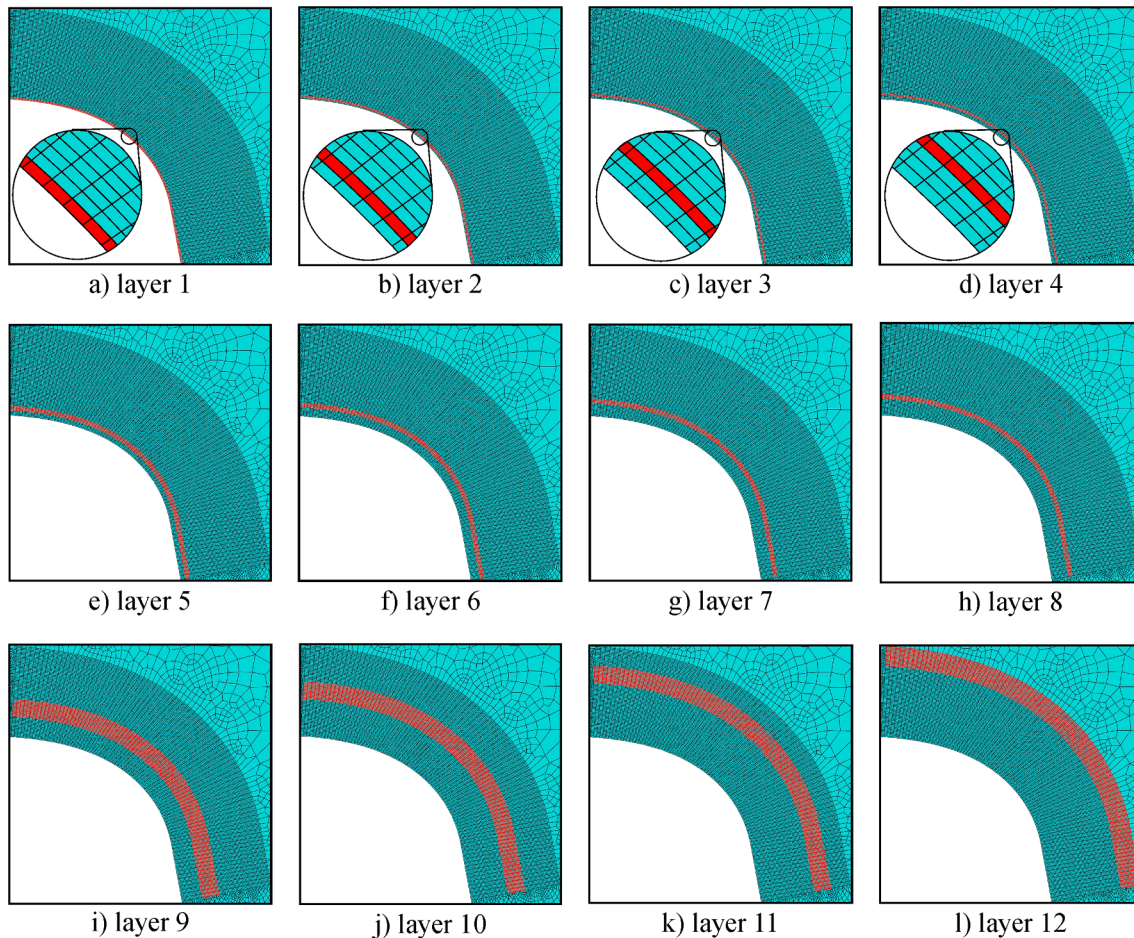

a) layer 1   b) layer 2   c) layer 3   d) layer 4

e) layer 5   f) layer 6   g) layer 7   h) layer 8

i) layer 9   j) layer 10   k) layer 11   l) layer 12

Fig. 4. Defined layers within Abaqus according to Table 3 from: (a) layer 1 to (l) layer 12.
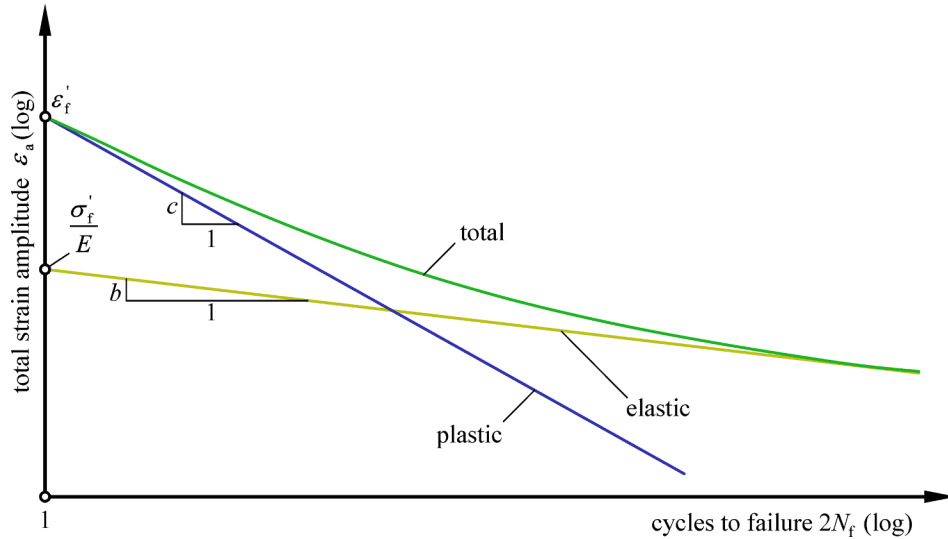
Fig. 5. Schematic representation of BCM's strain-life approach.

rule [37] is applied. Moreover, one of the most widely applied approaches employed in multiaxial fatigue, the critical plane method [38], is employed.

3.4. Non-proportional loading of a running gear pair: incremental Neuber's rule and the critical plane method

In this section, non-proportional loading and the resulting tooth root stresses are discussed. Then, two additions to an already established STBF model are discussed: the incremental Neuber's rule and the critical plane method.

3.4.1. Non-proportional loading of a running gear pair

In Fig. 6, a comparison between the major tooth root principal stress, σ_1, of the running gear pair and the STBF test is shown. The driving gear acts with torque T on the test gear. As a result, a normal force, F_n, is applied on the tooth flanks in contact. Within an STBF test, F_P denotes the pulsating force acting on the tooth. The gear pair in Fig. 6(a) is positioned in a single-tooth contact region, i.e., only a single pair of teeth is in contact.

The observed tooth root region for both the running gear pair and an STBF test is characterized by similar stresses for a fixed time increment. For an arbitrarily chosen node at the tooth root surface, the major principal stress in both cases is tangential to the tooth root fillet (dashed
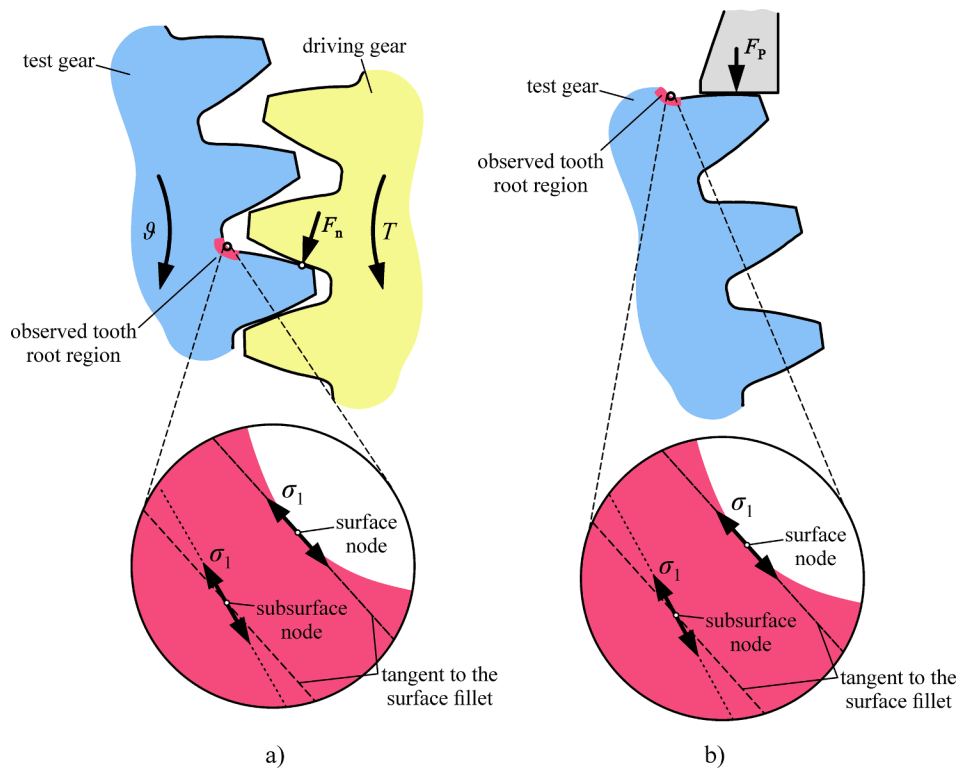

Fig. 6. Comparison between major tooth root principal stresses of the running gear pair and STBF test: (a) running gear pair with single pair of teeth in contact, and (b) the STBF test.

lines denote directions of the major principal stress vectors). On the other hand, the major principal stress vectors for subsurface nodes are not strictly tangential to the root fillet. Contrary to the surface node, where only single principal stress is present (uniaxial stress state), subsurface nodes are characterized by two principal stresses. As a result, the major principal stress direction is slightly altered.

As the STBF test continues, the pulsating load F_P gradually increases. Hence, the magnitude of major principal stresses in the observed tooth root region increases. However, the direction of their vectors stays the same (if minor tooth deformation is assumed as negligible and an experimental platform is employed that allows for negligible friction assumption [9]). This phenomenon is denoted by increasing the length of major principal stress vectors in Fig. 7b).

As the running gear pair test is continued, the test gear rotates by an angle of ϑ. Consequently, two pairs of gear teeth are now in contact (Fig. 7a), and two normal forces, F_n, act on the corresponding teeth of the test gear. Even though its magnitude will be altered, the major principal stress vector for the surface node will remain tangential to the root fillet. However, the major principal stress at the subsurface node will change its magnitude and direction, as shown in Fig. 7a). This effect is referred to as non-proportional stress due to non-proportional loading since the normal force, F_n, changes both its location on the tooth flank and its amplitude.

The effect shown in Figs. 6 and 7 is also demonstrated by employing the running gear pair FE model established in this paper and comparing the results with the previously established FE model of an STBF test [10] (Fig. 8). For both the running gear pair and the STBF numerical models, an arbitrarily chosen column of finite elements (from the tooth root surface to the nominal case depth) is chosen to demonstrate the non-proportional loading effects.

According to Fig. 8(c) and (d), major principal stresses remain approximately tangent to the fillet at the tooth root surface with an increase in depth regardless of the applied pulsating load (a change in the values of F_P represents a sinusoidal loading cycle typical for STBF tests).

However, according to Fig. 8(a) and (b), it can be observed that both the magnitude and direction of major principal stresses are modified with an increase in depth below the tooth root surface. In other words, even though the major principal surface stress maintains its direction while changing its magnitude as the gear pair rotates (proportional stress), the major principal subsurface stress changes both its magnitude and direction (non-proportional stress).

3.4.2. Incremental Neuber's rule

Once the non-proportionality of major principal stresses at the observed tooth root region has been demonstrated, incremental Neuber's rule [37] should be applied to correct linear-elastic stresses and strains obtained via FE simulation while simultaneously accounting for non-proportional stresses and strains. Incremental Neuber's rule is schematically depicted in Fig. 9.

In Fig. 9, ΔS represents an incremental change in the stress value and Δe represents an increment change in the strain value. Superscript e denotes linear-elastic, while superscript a denotes actual (elastic-plastic) material behavior. Lastly, for a general state characterized by three-dimensional stresses and strains, subscripts i and j are equal to $i, j = 1, 2, 3$. A detailed description of incremental Neuber's rule can be found in [37].

3.4.3. The critical plane method

Once the linear-elastic stresses and strains have been corrected for elastic–plastic material behavior via incremental Neuber's rule, Eqs. (10) and (11) can be employed to estimate bending fatigue lives. As previously mentioned, the maximum principal strain (normal strain) criterion is employed to estimate fatigue lives. Moreover, each node at the observed tooth root region experiences non-proportional principal stresses and strains (apart from the nodes located at the tooth root surface). Hence, an appropriate method must be applied to account for these effects. In this paper, one of the most widely used multiaxial fatigue methods, the critical plane method [38], is employed. A schematic
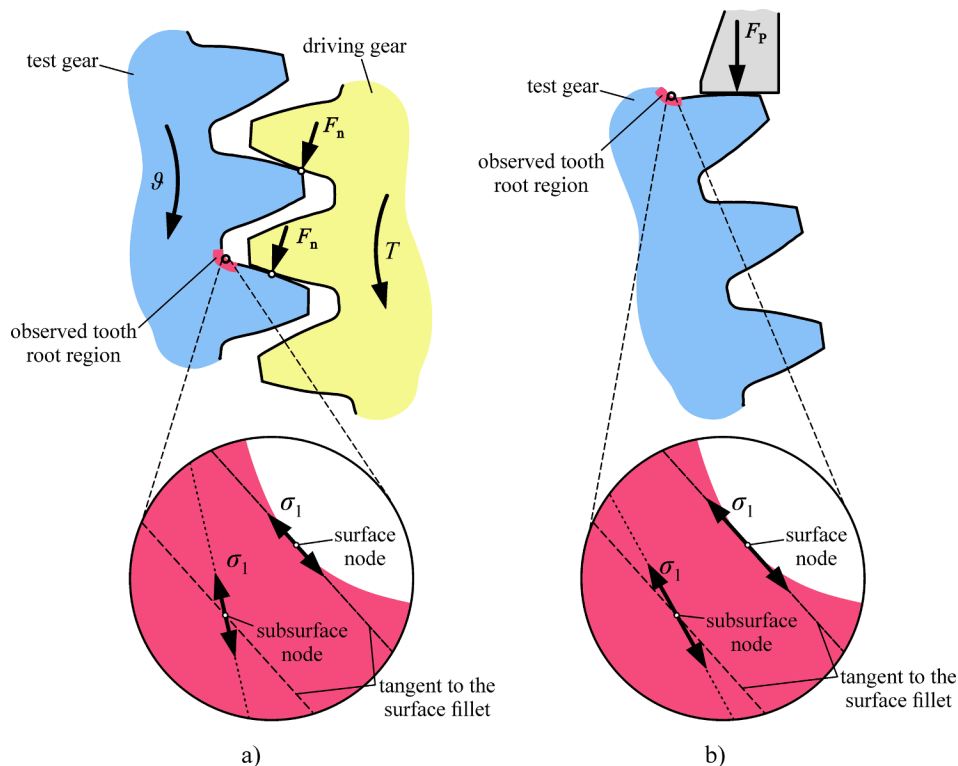

Fig. 7. Comparison between major tooth root principal stresses of the running gear pair and STBF test: (a) running gear pair with two pairs of teeth in contact, and (b) the STBF test.
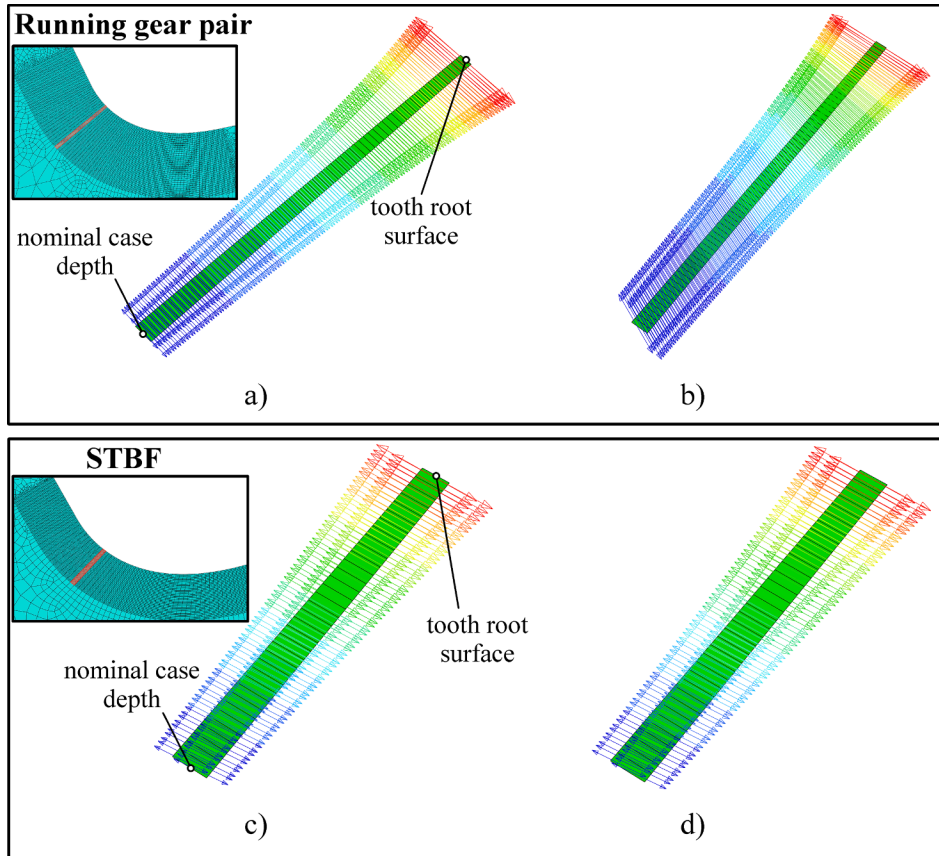
Fig. 8. The direction of major principal stresses with respect to the depth below the tooth root surface: (a) running gear pair during single-tooth contact, (b) running gear pair during double-tooth contact, (c) STBF for low F_P values, and (d) STBF for peak F_P values.
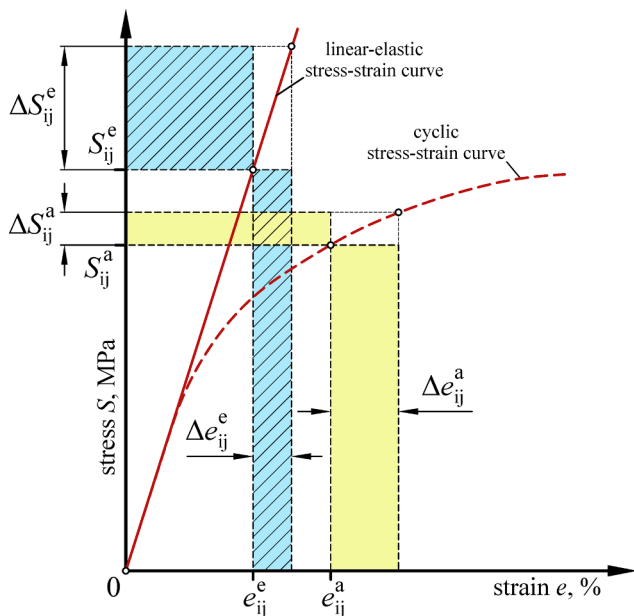

Fig. 9. Schematic representation of incremental Neuber's rule.

representation of the critical plane method applied to surface and sub-surface nodes is shown in Fig. 10.

The critical plane method is based on locating the plane upon which fatigue failure is most likely to initiate. A possible critical plane is defined via two angles: φ and θ (Fig. 10). The critical plane is initially (during the first loading increment) positioned perpendicular to the

actual major principal strain, ε_1^a. For surface nodes (Fig. 10a), since ε_1^a is tangent to the tooth root fillet, the critical plane is initially positioned perpendicular to the surface. For subsurface nodes, the initial direction of ε_1^a is not necessarily perpendicular to the surface, as shown in Fig. 8b). Hence, the corresponding initial position of the critical plane will also not necessarily be perpendicular to the surface. The planes are incrementally rotated by angles φ and θ, and total fatigue damage is obtained for each plane based on the maximum principal (normal) strain criterion. The critical plane with the highest accumulated damage and consequently lowest fatigue life is denoted as critical, and the corresponding node is recorded.

3.5. A step-by-step procedure for predicting the bending fatigue lives of each node within the observed tooth root region

Based on the previously described methods and criteria in Sections 2 and 3, the procedure for estimating bending fatigue lives in the tooth root of surface-hardened spur gears is summarized as follows:

1. The finite element model of a running gear pair is established, and a quasi-static analysis is conducted to obtain linear-elastic stresses and strains at the observed tooth root region (Fig. 1). Simultaneously, finite elements are assigned to 12 individual sets (Fig. 4) to enable subsequent assignment of fatigue properties and residual stresses.
2. Based on the existing hardness profile shown in Fig. 3 and Eqs. (3)–(8), averaged strain-life properties and residual stress values are obtained for each layer (Table 3).
3. From this point onward, due to the relative complexity of the analytical procedure, a computational program for fatigue calculation FE-Safe is employed [36]. The finite element results are input
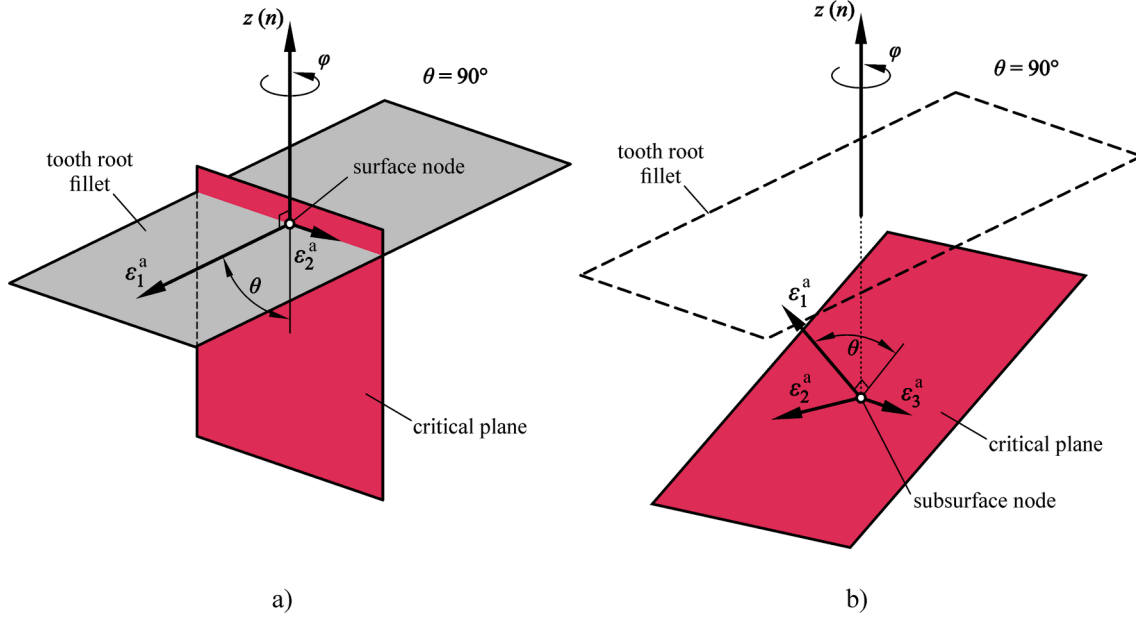
Fig. 10. Initial critical plane positions for: (a) surface nodes, and (b) subsurface nodes.

into FE-Safe, where strain-life properties and residual stresses are assigned to each layer.

4. Linear-elastic stresses and strain obtained via the FE simulation are first modified according to the combined factor K_C (Table 2 in Section 2).

5. A surface finish correction factor K_{sf} is applied only to the surface layer (the first of 12 layers) to account for the surface finishing effects on fatigue lives. According to [34], the specimen gears have a surface roughness of $Rz = 2.27$ μm, which is equal to $Ra \approx 0.57$ μm. Therefore, within FE-Safe, a predefined range of 0.2 μm $< Ra <$ 0.6 μm is chosen for the surface layer.

6. A single node at the observed tooth root region is chosen to describe the procedure in this step. Since the maximum principal strain criterion (normal strain) is used in this paper, the critical plane is positioned perpendicular to the direction of the major principal strain in the first rotational increment (as shown in Fig. 10). The remaining steps, starting with the first rotational increment, are defined as follows:

6.1 Modified linear-elastic stresses and strains (Fig. 2) are corrected for elastic–plastic material behavior via incremental Neuber's rule. Since the maximum principal (normal) strain criterion is used, the normal strain (strain perpendicular to the critical plane and denoted as ε_n) is then obtained based on actual strains.

6.2 Step 6.1 is repeated for all 500 rotational increments of an observed node. Hence, a normal strain cycle (corrected for elastic–plastic material behavior) for the observed node and the fixed (initial) position of the critical plane is obtained. Consequently, normal strain amplitude, $\frac{\Delta\varepsilon_n}{2}$, and actual mean stress, σ_m^a, are acquired.

6.3 If the node is located within the first four layers (which represents the original surface layer of 3-layer partitioning), Morrow's mean stress correction is employed according to Eq. (12):

$$\frac{\Delta\varepsilon_n}{2} = \frac{\sigma_f' - \sigma_m^a - \sigma_{res}}{E}(2N_f)^b + \varepsilon_f'(2N_f)^c \tag{12}$$

6.4 If the node is located within the bottom eight layers, SWT's mean stress correction is employed according to Eq. (13).

$$\frac{\Delta\varepsilon_n}{2}\left(\sigma_a + \sigma_m^a + \sigma_{res}\right) = \frac{\left(\sigma_f'\right)^2}{E}(2N_f)^{2b} + \sigma_f'\varepsilon_f'(2N_f)^{b+c} \tag{13}$$

6.5 The number of required cycles for bending fatigue failure, $2N_f$, is then calculated.

6.6 The critical plane is rotated by a default value of 10° [36], and steps 6.1–6.5 are repeated.

7. Step 6 is repeated for all nodes at the observed tooth root region. The critical plane with the lowest bending fatigue life $2N_f$ and the corresponding node are recorded.

4. Results and discussion

In this section, a comparison between estimated and experimental bending fatigue lives is shown. Moreover, the predicted and actual bending fatigue failure initiation locations are also discussed. Lastly, some parameters not accounted for within the proposed model that would have affected the estimated fatigue lives are mentioned, and their influence is discussed.

4.1. Comparison between experimental and numerical bending fatigue lives

A comparison between the bending fatigue lives obtained by the proposed model and experimental results from [20] is shown in Fig. 11.

Contrary to the typical logarithmic representation of fatigue lives, a box-and-whisker plot is chosen to show the results. This is done because multiple experimental tests are carried out for a single torque T at the test gear. Consequently, multiple fatigue lives are obtained for a single load. Hence, to more accurately represent the obtained results and improve the discussion of results, the statistical distribution of experimental results was taken into account by employing the box-and-whisker plots. It should be noted that the arrow symbol in Fig. 11 represents gear specimens that reached the limiting number of cycles, i.e., they did not fail due to bending fatigue. For higher loads ($T = 230$ Nm, 210 Nm, and 190 Nm), the limiting number of cycles was set to $3 \bullet 10^7$. For lower loads ($T = 170$ Nm and 150 Nm), the limiting number of cycles was set to $5 \bullet 10^7$. For consistency, the same criteria were applied to the numerical model.

For $T = 230$ Nm, the experimental results vary within the range of approximately $3.5 \bullet 10^5$ to $3 \bullet 10^7$ cycles, whereas no failure was observed for the latter (indicated by the blue arrow). The limits of this range are represented by vertical black lines, i.e., "whiskers". The
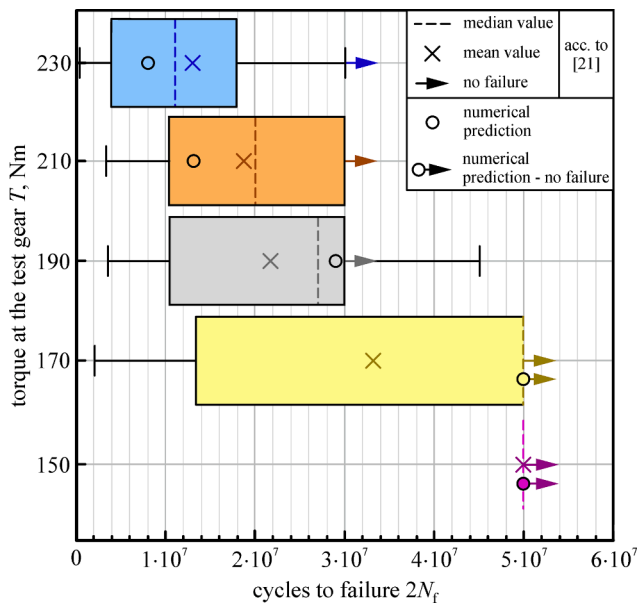
Fig. 11. Comparison between numerical and experimental bending fatigue lives.

interquartile range (area in which 50 % of all data points are located) is represented by a blue "box", and it ranges from roughly $4 \bullet 10^6$ to $1.8 \bullet 10^7$ cycles. Since the mean value (blue x-mark) and the median value (blue dashed line) are relatively close, it can be concluded that experimental bending fatigue lives are relatively evenly distributed. Lastly, it can be observed that the predicted bending fatigue life (denoted as a blue circle) is within the blue box and somewhat lower than both mean and median experimental values, i.e., slightly conservative.

For $T = 210$ Nm, the experimental lives are also evenly distributed (indicated by the relative proximity of mean and median values). The experimental results are distributed from the minimum value of almost $4 \bullet 10^6$ to $3 \bullet 10^7$ (no failure) cycles. The interquartile range spans from approximately $1 \bullet 10^7$ to $3 \bullet 10^7$ cycles. Once again, the predicted fatigue lives are slightly conservative and within the boxed range of experimental results.

For $T = 190$ Nm, the width of the box plot, as well as the lower boundary, are relatively similar to the values for $T = 210$ Nm. However, the mean and median values have shifted to the right, indicating that most experimental results are now located at higher fatigue lives. This is confirmed by the highest obtained bending fatigue life of roughly $4.5 \bullet 10^7$ cycles. Consequently, the predicted bending fatigue life of nearly $3 \bullet 10^7$ cycles is also shifted towards higher fatigue lives. Even though the predicted fatigue life is no longer conservative, it is still located within the boxed area and relatively close to the median experimental fatigue lives.

For $T = 170$ Nm, an interesting effect can be observed. The median value is approximately $5 \bullet 10^7$ cycles, the same limit at which the test was stopped due to a lack of bending fatigue failure. This means that most experimental results were terminated since no failure occurred. Nevertheless, some specimens still failed within the range of $2 \bullet 10^6$ to $5 \bullet 10^7$ cycles (otherwise, no box plot would be present). Based on these observations, it is reasonable that the predicted fatigue life indicates that failure will occur after $5 \bullet 10^7$ cycles.

Lastly, for $T = 150$ Nm, none of the tested specimens experienced bending fatigue failure. In other words, the corresponding tests were terminated once the specimens reached $5 \bullet 10^7$ cycles. The predicted bending fatigue life is once again also higher than $5 \bullet 10^7$ cycles.

According to Fig. 11, it can be observed that all predicted bending fatigue lives are within the range obtained by experimental testing. More importantly, the predicted fatigue lives are within the boxed areas,

i.e., within 50 % of all data points. For higher loads ($T = 230$ Nm and 210 Nm), the predicted results are located inside the second quartile of the box and whisker plots and are relatively close to mean and median experimental values. For $T = 190$ Nm, numerical predictions are also relatively close to the median experimental value but are no longer conservative. For lower loads ($T = 170$ Nm and 150 Nm), no failure is predicted up to $5 \bullet 10^7$ cycles, which is in good agreement with the experimental results.

4.2. Comparison between experimental and numerical bending fatigue failure locations

According to the experimental results [20], subsurface failure was the most frequent type of failure for conducted tests. As reported, this subsurface failure always occurred at 150 μm ± 75 μm. According to the proposed model, subsurface failure was also predicted for all values of the applied torque. This failure was always at the same location (layer 9), as shown in Fig. 12. According to Table 3, layer 9 is defined from 80 μm to 145 μm. Since the actual subsurface failure always occurred in the range of 75–225 μm, it can be concluded that a relatively good agreement exists between the numerical and experimental results.

Furthermore, it can be observed that the subsurface failure occurs in the region where residual stresses are sharply increased (Fig. 3). Hence, the subsurface layers are no longer "protected" by highly compressive and fatigue-resistant residual stresses. Since material hardness (and consequently fatigue properties) are not significantly altered within the first nine layers, the load-induced stresses and residual stresses are mostly governing the surface-to-subsurface failure transition. At the surface layer, load-induced stresses are the highest. However, residual stresses are also the lowest (Fig. 3), thereby providing a beneficial effect for fatigue resistance. The applied loads result in high-cycle fatigue lives (according to Fig. 11, the lowest number of experimentally obtained fatigue cycles is approximately equal to $3.5 \bullet 10^5$). Therefore, the localized plasticity at the tooth root surface is not sufficient to relax the residual stresses, which would result in the surface area being critical. Consequently, the critical failure location shifts below the surface, specifically in the region where load-induced stresses are still relatively high and residual stresses have suddenly increased.

According to the obtained results, it can be observed that two parameters govern the probability of subsurface bending fatigue failure on a macroscopic level: the gradient of load-induced stresses and the residual stress profile. The former can be influenced by changing the geometry of the gear [16,39], while the latter can be modified by increasing the nominal case depth, i.e., increasing the carburization time to induce additional compressive residual stresses at the critical region. This will be investigated in future work.

Lastly, a few parameters and simplifications that affected the obtained results should be mentioned. First, a 2D instead of 3D finite element analysis was carried out to improve computational efficiency. Even though the test gears are sufficiently thin to assume plane-stress conditions, this still resulted in some errors. Moreover, a quasi-static FE analysis was carried out since insufficient experimental data was available to conduct a dynamic FE analysis. If dynamic FE analysis was carried out, the obtained stresses and strains could be directly imported into FE-Safe, i.e., without the combined factor K_C. This would also affect the results. Furthermore, ideal gear geometry was assumed, whereas actual gear geometry would have modified the stresses and strains at the tooth root. Lastly, since the numerical model is proposed on a macroscopic scale, it does not account for the effect of specific inclusions (impurities) and their distribution, which typically calls for microscopic modeling. In other words, the proposed model assumes equal likelihood of fatigue failure for each gear tooth on a specimen gear.

5. Conclusions

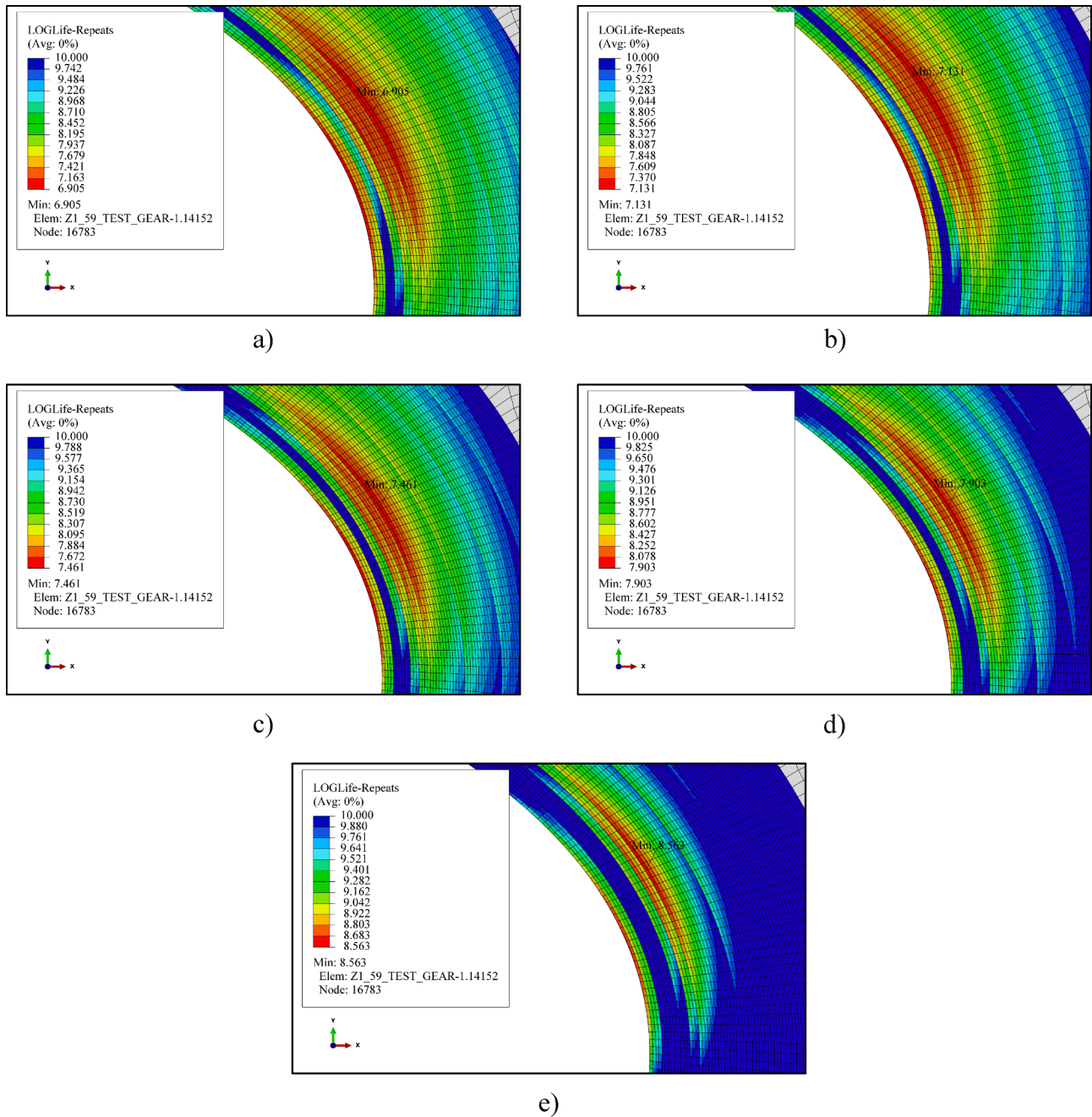In this paper, a numerical model for bending fatigue prediction of

Fig. 12. Critical estimated locations for bending fatigue failure: (a) $T = 230$ Nm, (b) $T = 210$ Nm, (c) $T = 190$ Nm, (d) $T = 170$ Nm, and (e) $T = 150$ Nm.

surface-hardened running spur gears was proposed. Quasi-static finite element simulation with consideration of the adjacent tooth effect was conducted to obtain linear-elastic stresses and strains. These values were then modified to account for additional running gear parameters and input into the fatigue model, where the multilayer method, hardness method, and strain-life approach with different mean stress corrections were employed. As a result, bending fatigue lives, and the corresponding locations below the tooth root surface were obtained. The following conclusions are drawn:

- Good agreement between the predicted and experimentally obtained bending fatigue lives is observed for all values of the applied load. However, for higher loads, the results are slightly conservative. The results are somewhat higher than the mean and median experimental values for lower loads but still within the 50 % data range.

- Good agreement is also observed between the estimated and actual failure locations for bending fatigue. According to the proposed model, subsurface bending fatigue failure should occur between 80 μm and 145 μm, whereas the actual failure occurs between 75 μm and 225 μm.

- It is observed that subsurface failure tends to occur in the region characterized by the sharpest increase in residual stresses. Within this region, the load-induced stresses are still relatively high, but the lack of highly compressive ("protective") residual stresses contributes to subsurface failure.

In future work, the proposed model will be applied to various running gear pairs for further validation. Moreover, a 3D numerical simulation will be conducted to improve the accuracy of the results. The proposed model will be modified and applied to other types of surface-

hardened machine elements, such as helical gears or axles. Lastly, the effect of carburization time and modification of the gear geometry on the probability of subsurface bending fatigue crack initiation will be investigated.

Declaration of Competing Interest

The authors declare that they have no known competing financial interests or personal relationships that could have appeared to influence the work reported in this paper.

Data availability

Data will be made available on request.

Acknowledgement

References

[1] ISO. ISO 6336:2006, Calculation and load capacity of spur and helical gears; 2006.

[2] AGMA. ANSI/AGMA 2101-D04. Fundamental rating factors and calculation methods for involute spur and helical gear teeth; 2004.

[3] Gears M. Gear root bending strength: a new multiaxial approach to meshing gears; 2021.

[4] Bonaiti L, Gorla C. Estimation of gear SN curve for tooth root bending fatigue by means of maximum likelihood method and statistic of extremes. Int J Fatigue 2021;153(July):106451. https://doi.org/10.1016/j.ijfatigue.2021.106451.

[5] Argoud V, Morel F, Pessard E, Bellett D, Thibault S, Gourdin S. Fatigue behaviour of gear teeth made of case hardened steel: From competing mechanisms to lifetime variability. Proc Struct Integr 2019;19:719–28. https://doi.org/10.1016/j.prostr.2019.12.078.

[6] Conrado E, Gorla C, Davoli P, Boniardi M. A comparison of bending fatigue strength of carburized and nitrided gears for industrial applications. Eng Fail Anal 2017;78:41–54. https://doi.org/10.1016/j.engfailanal.2017.03.006.

[7] Hong IJ, Kahraman A, Anderson N. A rotating gear test methodology for evaluation of high-cycle tooth bending fatigue lives under fully reversed and fully released loading conditions. Int J Fatigue 2020;133(November 2019):105432. https://doi.org/10.1016/j.ijfatigue.2019.105432.

[8] Li W, Deng S, Liu B. Experimental study on the influence of different carburized layer depth on gear contact fatigue strength. Eng Fail Anal 2020;107:104225. https://doi.org/10.1016/j.engfailanal.2019.104225.

[9] Vučković K, Galić I, Božić Ž, Glodež S. Effect of friction in a single-tooth fatigue test. Int J Fatigue 2018;114(May):148–58. https://doi.org/10.1016/j.ijfatigue.2018.05.005.

[10] Čular I, Vučković K, Glodež S, Tonković Z. Computational model for bending fatigue prediction of surface hardened spur gears based on the multilayer method. Int J Fatigue 2022;161:106892.

[11] Vučković K, Čular I, Mašović R, Galić I, Žeželj D. Numerical model for bending fatigue life estimation of carburized spur gears with consideration of the adjacent tooth effect. Int J Fatigue 2021;153:106515.

[12] He H, Liu H, Zhu C, Tang J. Study on the gear fatigue behavior considering the effect of residual stress based on the continuum damage approach. Eng Fail Anal 2019;104(July 2018):531–44. https://doi.org/10.1016/j.engfailanal.2019.06.027.

[13] Lias MR, Sharif Z, Awang M, Jailani A, Warap H. Quasi-static modeling of spur gear time varying strength analysis. ARPN J Eng Appl Sci 2017;12(6):1938–47.

[14] Thirumurugan R, Deepak CCC, Karthieeban K. Effect of adjacent teeth load on bending strength of high contact ratio asymmetrical spur gear drive. Int J Veh Struct Syst 2017;9(1):32–5. https://doi.org/10.4273/ijvss.9.1.07.

[15] Chen Z, Jiang Y, Tong Z, Tong S. Residual stress distribution design for gear surfaces based on genetic algorithm optimization. Mater (Basel) 2021;14(2):1–17. https://doi.org/10.3390/ma14020366.

[16] Fuchs D, Schurer S, Tobie T, Stahl K. A model approach for considering nonmetallic inclusions in the calculation of the local tooth root load-carrying capacity of high-strength gears made of high-quality steels. Proc Inst Mech Eng, Part C: J Mech Eng Sci 2019;233(21–22):7309–17.

[17] Winkler KJ, Schurer S, Tobie T, Stahl K. Investigations on the tooth root bending strength and the fatigue fracture characteristics of case-carburized and shot-peened gears of different sizes. Proc Inst Mech Eng Part C J Mech Eng Sci 2019;233 (21–22):7338–49. https://doi.org/10.1177/0954406219841650.

[18] Güntner C, Tobie T, Stahl K. Influences of the residual stress condition on the load-carrying capacity of case-hardened gears; 2018. no. August, pp. 60–69.

[19] Fuchs D, Schurer S, Tobie T, Stahl K. Investigations into non-metallic inclusion crack area characteristics relevant for tooth root fracture damages of case carburised and shot-peened high strength gears of different sizes made of high-quality steelsUntersuchungen zu Rissflächencharakteristiken nicht-metallischer Einschlüsse maßgeblich für Zahnfußbrüche von einsatzgehärteten und kugelgestrahlten hochtragfähigen Zahnrädern unterschiedlicher Größe aus hochreinen Stählen. Forsch im Ingen/Eng Res 2019;83(3):579–87.

[20] Fuchs D, Schurer S, Tobie T, Stahl K. On the determination of the bending fatigue strength in and above the very high cycle fatigue regime of shot-peened gearsZur Bestimmung der Zahnfußfestigkeit kugelgestrahlter Zahnräder im Bereich erhöhter Lastspielzahlen. Forsch im Ingen/Eng Res 2022;86(1):81–92.

[21] SIMULIA, "Abaqus 6.13, Analysis user's guide, dassault systems; 2013.

[22] Neuber H. Theory of stress concentration for shear-strained prismatical bodies with arbitrary nonlinear stress-strain law. J Appl Mech Trans ASME 1960;28(4):544–50. https://doi.org/10.1115/1.3641780.

[23] Morrow J. Fatigue properties of metals. Warrendale, PA: SAE; 1968.

[24] Smith K, Watson P, Topper T. A stress-strain function for the fatigue of materials. J Mater 1970;5:767–78.

[25] Roessle ML, Fatemi A. Strain-controlled fatigue properties of steels and some simple approximations. Int J Fatigue 2000;22(6):495–511. https://doi.org/10.1016/S0142-1123(00)00026-8.

[26] Baumel AJ, Seeger T. The influence of residual stresses and surface strengthening on components fatigue life. Fatigue 1990;90:311–6.

[27] Vučković K, Čular I, Risović S. Effects of finite element type, mesh size and friction on spur gear nominal tooth root stress results. in: Proceedings of the 3rd international scientific conference "conference on mechanical engineering technologies and applications" COMETa, 2016; 2016. p. 185–90.

[28] Čular I, Vučković K, Miler D, Žeželj D. Numerical bending fatigue analysis of a surface hardened spur gears. In: 18th international conference on new trends in fatigue and fracture; 2018. p. 55–8.

[29] Martins R, Seabra J, Brito A, Seyfert C, Luther R, Igartua A. Friction coefficient in FZG gears lubricated with industrial gear oils: Biodegradable ester vs. mineral oil. Tribol Int 2006;39(6):512–21. https://doi.org/10.1016/j.triboint.2005.03.021.

[30] Höhn BR, Michaelis K, Doleschel A. Frictional behaviour of synthetic gear lubricants. Tribol Ser 2001;39:759–68. https://doi.org/10.1016/s0167-8922(01)80156-5.

[31] Pehan S, Hellen TK, Flasker J, Glodez S. Numerical methods for determining stress intensity factors vs crack depth in gear tooth roots. Int J Fatigue 1997;19(10): 677–85. https://doi.org/10.1016/S0142-1123(97)00101-1.

[32] Zhan J, Fard M, Jazar R. A quasi-static FEM for estimating gear load capacity. Meas J Int Meas Confed 2015;75:40–9. https://doi.org/10.1016/j.measurement.2015.07.036.

[33] Fuchs HO, Stephens RI, Saunders H, Fatigue M. Metal Fatigue Eng 1980.

[34] Schurer S. Einfluss nichtmetallischer Einschlüsse in hochreinen Werkstoffen auf die Zahnfußtragfähigkeit [eng.: influence of non-metallic inclusions in ultra-clean materials on the tooth root load-carrying capacity]. Technical University of Munich; 2016.

[35] Astm. E140-07 Standard hardness conversion tables for metals relationship among brinell hardness, vickers hardness, rockwell hardness, superficial hardness, knoop hardness, and scleroscope hardness. Astm 2007:1–21.

[36] S. technology Limited. FE-SAFE Version 6.5, user guide; 2014.

[37] Buczynski A, Glinka G. An analysis of elasto-plastic strains and stresses in notched bodies subjected to cyclic non-proportional loading paths. Eur Struct Integr Soc 2003;vol. 31, no. C:265–83. https://doi.org/10.1016/S1566-1369(03)80015-8.

[38] Fatemi A, Socie DF. a Critical plane approach to multiaxial fatigue damage including out of phase loading. Fatigue Fract Eng Mater Struct 1988;11(3):149–65. https://doi.org/10.1111/j.1460-2695.1988.tb01169.x.

[39] Bretl N, Schurer S, Tobie T, Stahl K, Höhn BR. Investigations on tooth root bending strength of case hardened gears in the range of high cycle fatigue. Am Gear Manuf Assoc Fall Tech Meet 2013;2013:103–18.